Physics in the extreme: X-ray and optical studies of magnetic white dwarfs and related objects

Mark Kennedy
BSc
109482792

NATIONAL UNIVERSITY OF IRELAND, CORK

School of Science

Department of Physics

Thesis submitted in partial fulfilment of the requirement for the degree of Doctor of Philosophy

March 2017

Head of Department:	Prof. John McInerney
Supervisors:	Prof. Paul Callanan Prof. Peter Garnavich
External Examiner:	Dr. Chris Watson Queen's University Belfast
Internal Examiner:	Dr. Asaf Pe'er University College Cork

Research supported by The Naughton Foundation

Contents

List of Figures

List of Tables

I, Mark Kennedy, certify that this thesis is my own work and I have not obtained a degree in this university or elsewhere on the basis of the work submitted in this thesis.

Signed:_____

Date:_____

Abstract

In this thesis, we present results from optical and X-ray studies of compact binary systems. These observations are used to constrain orbital parameters - mainly periods and inclinations for several cataclysmic variables - and examine the accretion structures within the systems.

In Chapters 3 and 4, optical and X-ray studies of two interesting cataclysmic variables systems, Lanning 386 and MASTER OTJ192328.22+612413.5, are presented. The X-ray and optical data of these objects suggest that both systems have a high inclination and harbour weakly magnetic white dwarfs with spin periods 17-22 min.

There is also a strong focus on studying the long term behaviour in intermediate polars in this thesis. Chapter 5 presents results from *Kepler* observations of FO Aquarii taken over 69 consecutive days. The shape of the light curve is consistent with the outer edge of the accretion disc being eclipsed and the detected period is longer than the last reported period of 1254.284(16) s, suggesting that FO Aqr was now spinning down, and had a positive $\dot{P}$ at the time of the observations. Chapter 6 continues the work on FO Aquarii, and presents X-ray data taken during a low accretion state. The X-ray spectrum shows an increase in the ratio of the soft X-ray flux to the hard X-ray flux due to a change in the partial covering fraction of the white dwarf and a change in the hydrogen column density within the disc. *XMM-Newton* observations of FO Aqr during the subsequent recovery suggest that the system had not yet returned to its typical high state by November 2016. The spin period of the white dwarf in 2014 and 2015 is refined to 1254.3342(8) s.

Chapter 7 focuses on CSS120422:J111127+571239, an "evolved main-sequence" channel cataclysmic variable. We present spectroscopy of CSS120422:J111127+571239 using the COS FUV instrument on the Hubble Space Telescope and using the MODS spectrograph on the Large Binocular Telescope. The UV spectrum shows Si IV, N V and He II, but no detectable C IV. The anomalous nitrogen/carbon ratio is seen in a small number of other CVs and confirms a unique binary evolution. We also present and compare the optical spectrum of V418 Ser and advocate that it is also an evolved main-sequence system.

Finally, Chapter 8 presents results on UW Coronae Borealis, a low mass X-ray

binary that shows both Type 1 X-ray and optical bursts. The orbital period is refined to 110.97680(1) min. 17 optical bursts are presented, with 10 of these bursts being resolved temporally. The average e-folding time of 19 ± 3s for the bursts is consistent with the previously found value. Optical bursts are observed during a previously identified gap in orbital phase centred on $\phi = 0.967$, meaning the reprocessing site is not eclipsed as previously thought. Finally, the apparent P-Cygni profiles present in some of the atomic lines in the optical spectra are due to transient absorption, which suggests the origin of the absorption is not a wind from the primary.

Acknowledgements

Throughout the last 4 years, I've had the support of an enormous amount of people, whom without this PhD would never have been completed.

I've been fortunate to work for 2 great researchers during my PhD, Paul Callanan and Peter Garnavich. Paul, you've been inspiring me to study astrophysics for the last 8 years, and I have learnt a lot from your mentorship. Peter, you took a chance by agreeing to take on a student you have never met in 2013, and I will always be thankful that you took that risk. Working with you both has been an honour.

I would also like to thank the Naughton Family who, through the Martin and Carmel Naughton Graduate Fellowship, funded this PhD. Your generosity knows no bounds and, without your support, this work would never have happened.

I have been fortunate to experience PhD life in both Ireland and the US over the last few years, and there are many people in both countries who I have to thank for their support and friendship. In Ireland, I would like to thank my housemates - Danny, Anthony, and Michael - for the many late night gaming sessions and movie nights to help unwind after a hard day of work. Also, to my office mates - Owen, Hayret, Liam, Simon, and Selma - thank you for helping me with various problems and always being up for a chat in the office. To the other physics post graduate students - Bryan, Joe, Declan, Sebastian - thank you for the various lunch and tea breaks, and after work banter. Also, to Dee, Kate, Luke, Cian, Sarah O'C, Sarah R, Claire, Max, Ben M, Ben H, Brian, Dylan, Sarah W, Tom, Siobhán, Áine, Kieran, Noreen, Dan, thank you for the board game nights, movie nights, TV show nights, coffee breaks, tea breaks, and trips to Tramore, Dublin, and London over the last 4 years.

In the US, I would like to thank the people who made moving to a new country seem easy, and made my decision to spend a second summer in South Bend even easier. Gary, Antonis, Karly, Bryce, Laura, Evercita, Marwa, Kenton, Kelsey, Eamonn, Niraja, Pancho, Joel, Caleb, Erica, Erika, Sarah D, Vu, Nate, Jake - you are a truly remarkable group of people, and I can't wait to visit you all again. I also have to thank my office mates in Nieuwland Science Hall - Ben, Jason, Taylor, Erin, and Colin - for their help on various projects and creating such a great environment to work in.

A department only functions if it has great departmental staff, and to that end I'd like to thank the staff both in UCC and Notre Dame for the tremendous amount of time they spent on the paperwork involved with attending both colleges simultaneously.

I would also like to thank the various people I have worked with over the years including Paula Szkody, Tom Marsh, Danny Steeghs, Boris Gänsicke, Elmé

Breedt, Zhibin Dai, Mark Reynolds, Ivan Hubeny, Jerome Orosz, and Koji Mukai. The many email exchanges and conversations we had were incredibly important in developing the ideas in many of the chapters presented in this thesis.

Of course, where would I be without my family - Roger, Caroline, Chris, Andy, Michael and Joan. The 6 of you have constantly encouraged me to follow my goals, and have never questioned my choice to live with my head in the stars (well, nearly never). Thanks also to Dave, Jenny, Dee, and Emma for helping keep these people sane while they kept me sane. Also to my second family - George, Rioghnach, and Georgina - thank you for all of the support and amazing meals.

Finally, to Therese. You've been at my side, holding my hand and supporting me every step of the way. None of this would have been possible without you, and I can't wait for the next chapter in our lives.

Mark Kennedy
University College Cork
March 2017

For Matthew - the Universe awaits.

“If one is not moved by astrophysics, is one truly alive?”

- David Rea

1 Introduction

The study of compact objects (black holes, neutron stars or white dwarfs) in close binary systems has been on going for over a thousand years, with the earliest observations of a supernova associated with a compact object taken in the year 1006 (Winkler et al., 2003). Since then, compact objects in binary systems have been used to test general and special relativity by observing binary neutron stars (Hulse & Taylor 1975; this research was awarded the Nobel Prize in Physics in 1993) and as cosmological probes by observing the explosions of white dwarfs (Riess et al. 1998; Perlmutter et al. 1999; this research was awarded the Nobel Prize in Physics in 2011). Most recently, gravitational waves from a binary black hole merger were detected by the Laser Interferometer Gravitational-Wave Observatory (LIGO), the first direct detection of gravitational waves in history (Abbott et al., 2016).

Given this, it is easy to see why the study of compact binary star systems is important, as they provide a laboratory for testing physical processes under conditions that are impossible to replicate here on Earth. One of the most important physical processes that occurs in binary systems that harbour compact objects is accretion, which is not unique to binary systems, but also plays a vital role in powering the central engines of active galactic nuclei (Scaringi et al., 2015) and in the development of young stellar objects (Beltrán & de Wit, 2016). As such, understanding accretion and all of the processes involved with accretion is important in determining the evolution of the Universe.

Cataclysmic variables, which are binary systems that contain a primary which is a white dwarf star, are the most common type of binary system which undergoes accretion in the Universe with over 1,400 confirmed members as of 2015 (Ritter & Kolb, 2003). In comparison, the number of systems with either a neutron star or black hole primary (also known as, depending on the size of the companion, Low Mass or High Mass X-ray Binaries) is only 108 (Ritter & Kolb, 2003). As such, cataclysmic variables are often used to probe the accretion mechanisms that occur in binary systems.

In this thesis, I mainly focus on binary systems that have white dwarf primaries, and attempt to classify and characterise some of the more exotic white dwarf binary systems. In particular, I investigate what role the magnetic field of the white dwarf has on the accretion geometry (Chapters 3, 4, 5, and 6) and how the evolution of the secondary star affects the overall evolution of a system (Chapter 7). I also discuss a Low Mass X-ray binary system in Chapter

8.

1.1 Observational Properties of Binary Systems

The optical and X-ray light curves and spectra of any binary system can give hints about the nature of the underlying compact object. Below I discuss the most common classifications and their characteristics, starting with systems that contain white dwarf primaries, and concluding with neutron star binaries.

Close binary systems that harbour a white dwarf (WD) primary star, known as cataclysmic variables (CVs), are the longest studied members of compact binaries. The amount of variability differs between objects, and there are many different mechanisms associated with them. CVs can be classified by considering their optical variability, optical spectra and X-ray properties.

The most definitive way of classifying a CV is by the detection of a nova outburst. Classical nova outbursts are the largest amplitude variations observed in CVs, with objects brightening by between 8 and 20 mag within a few days (Strope et al., 2010). The appearance of these large amplitude outbursts requires the release of a tremendous amount of energy, and rarely are these witnessed to come from a system more than once. Only 10 objects have been observed to undergo multiple nova outbursts (the recurrent novae; Mukai 2015). The mechanism behind a nova outburst is discussed in Section 1.4.

Other than novae outbursts, there are several optical and X-ray phenomena that can be used to classify a CV. These phenomena normally distinguish between CVs which harbour non-magnetic and magnetic WDs or, alternatively, between systems which harbour simple accretion discs or a more complicated accretion structure.

1.1.1 Non-magnetic CVs

1.1.1.1 Dwarf Novae

Fig. 1.1 shows the general components of a non-magnetic CV, including a disk which is hottest close to the white dwarf and whose temperature falls of as $r^{-0.75}$, which will be discussed in Section 1.2.2.

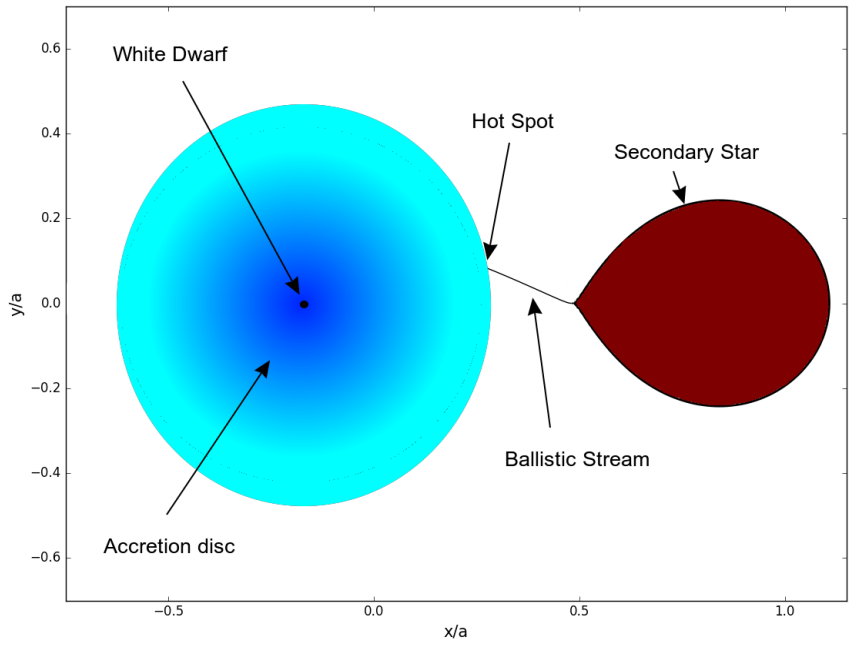

Figure 1.1: A schematic of a non-magnetic CV, with the hot spot, secondary star, ballistic stream, accretion disc and white dwarf highlighted. All components are scaled in units of a, the orbital separation. The disc has been assumed to extend out to a radius of $2r_{circ}$, which will be discussed in Section 1.2.2.

The most common identification of a cataclysmic variable comes from the detection of smaller amplitude outbursts in optical light curves, which are called dwarf nova outbursts. Dwarf nova outbursts occur multiple times within a system, and are characterised by their rise time to maximum light and decay time back to quiescence. Fig. 1.2 shows the light curve taken by the *Kepler* Space Telescope during the *K2* mission of HS Vir, a known CV. There are 3 well defined dwarf nova outbursts in the middle of the observation, along with a weak outburst at the start and a double outburst at the end. Systems which show dwarf nove outbursts are simply called dwarf novae.

The optical spectra of dwarf novae are typically dominated by a strong continuum and H and He emission lines. Fig. 1.3 a typical spectrum from a CV with the strongest emission lines marked. The double peaked structure of the emission lines is common for high inclination CVs which have an accretion disc.

The light curves of CVs also show periodic structures. The most common type of periodicity is from the orbital motion of the 2 stars around each other leading to eclipses in systems with high inclinations (conventionally, an

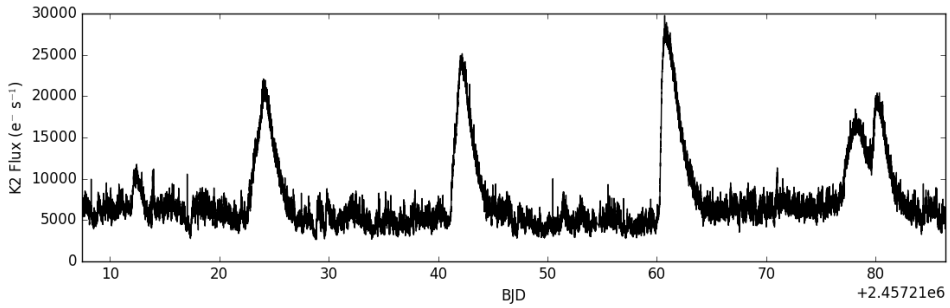

Figure 1.2: The (unpublished) light curve of the CV HS Vir, taken using the *Kepler* telescope during the *K2* mission. The light curve spans 79 days with a cadence of 1 min. There 3 clear regular outbursts, along with a weak outburst around 5 days after observations began, and a double outburst towards the end of the observation. The mechanism that causes the outbursts is thought to be due to a disc instability, which will be discussed in Section 1.4.

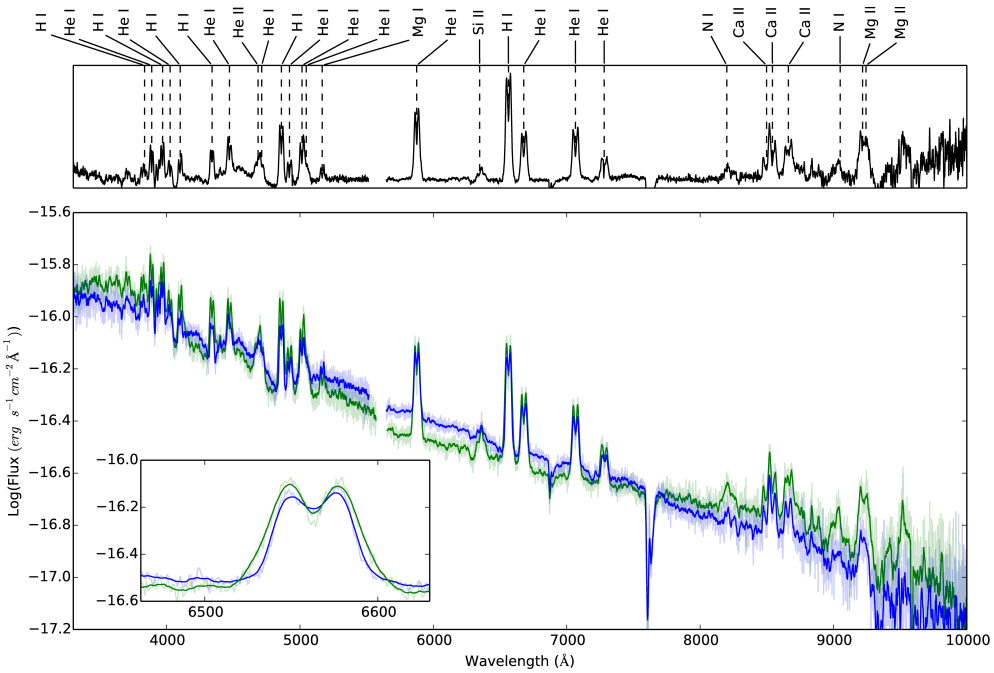

Figure 1.3: A CV spectrum with emission lines marked. This particular CV, CSS120422:J111127+571239, will be discussed in Chapter 7.

inclination of 0° is when an observer would have a top-down view of the system, and an inclination of 90° would be when an observer sees the system edge on). Fig. 1.4 shows a typical light curve of a cataclysmic variable which shows a strong hot spot and an eclipse.

Finally, dwarf novae are weak emitters of X-rays, with typical X-ray luminosities between $10^{28} - 10^{30}$ erg s^{-1} (Reis et al., 2013).

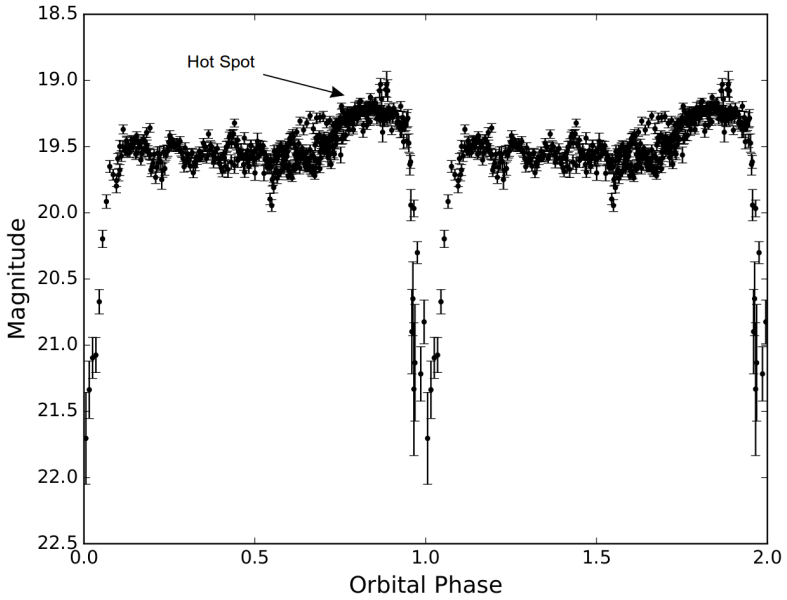

Figure 1.4: A typical light curve of a high inclination cataclysmic variable. The data has been plotted as a function of orbital phase, with the eclipse centred on phase 0. There is also a hump visible in the light curve, which peaks around orbital phase 0.8. This hump is called a hot spot. This particular light curve is of OTJ192328.22+612413.5, which will be discussed in Chapter 3.

1.1.1.2 Nova-likes

Nova-like (NL) CVs are (possibly) non-magnetic CVs that do not typically undergo classical nova or dwarf nova outbursts. There is a subset of nova-likes that can be identified through the appearance of superhumps in their optical light curves (the so-called permanent superhumpers; Osaki 1996). Superhumps are variations in the optical light curves which have periods slightly longer than the orbital period of the system, and are also detected in some dwarf nova during super-outbursts (the SU Uma systems), which are dwarf nova outbursts that occur during periods of high mass transfer rate (Osaki, 1996). As such, it is thought the permanent appearance of superhumps in nova-likes is related to an underlying constant high mass transfer rate (Patterson & Richman, 1991).

1.1.1.3 SW Sextantis Systems

Finally, of importance to this work is the SW Sextantis classification for CVs. SW Sextantis stars are a subclass of high accretion rate CVs. Their defining

features are: (1) they are nova-like CVs, with an orbital period $3 < P < 4$ hours; (2) they show He II λ4686 emission with a strength of half $H\beta$ or larger; (3) the radial velocities of the emission lines vary periodically, with the Balmer lines lagging behind the expected phase for a WD based on the eclipse; (4) absorption lines are only visible for a part of the orbit opposite the eclipse phase (Thorstensen et al., 1991). The emission lines of SW Sextantis stars are also single-peaked lines, making candidates easy to identify. SW Sextantis stars are now thought to be the dominant population of CVs with periods between 3 and 4 hours (Rodríguez-Gil et al., 2007). I have included the SW Sextantis class under the category of non-magnetic CVs as this such they were intially thought to be non-magnetic. However, this will be discussed further in Section 1.4.2.5.

1.1.2 Magnetic CVs

1.1.2.1 Polar (AM Her) Stars

Polars are CVs whose WDs have high magnetic fields (> 10 MG; Cropper 1990). AM Her, which is another commonly used name for polars, was the first of this class after Tapia (1977) proposed the compact object in the binary had a strong magnetic field. In these systems, the magnetic field of the WD is strong enough that the WD becomes tidally locked to the secondary, meaning the spin period of the WD is the same as the orbital period. The mechanism behind this is thought to be either Ohmic dissipation of currents in the secondary stars atmosphere due to the variable magnetic field from the WD Joss et al. (1979) or interaction of the WDs magnetic field with the plasma flow coming from the L1 point (Lamb et al. 1983; Andronov 1987). The magnetic field also affects the accretion geometry in these systems, which will be discussed further in Section 1.4.3. Polars have optical spectra that are dominated by cyclotron emission, instead of the normal continuum seen in dwarf novae and nova-likes. Additionally, instead of the strong H emission lines seen in dwarf novae, polars tend to have strong He I and He II lines. Finally, polars have a very high ratio of X-ray to optical flux, with typical values being $3 < F_X/F_{opt} < 300$ Warner (1995). There are a few cases where this is not true, and the spin period of the WD varies from the orbital period by a few %; Stockman et al. 1988). These systems are called asynchronous polars.

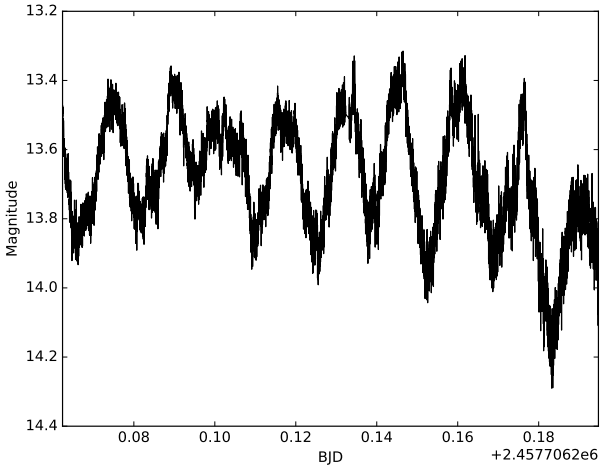

Figure 1.5: Optical pulses seen from FO Aquarii. The pulses have a period of 21 min. FO Aquaraii has the strongest optical pulses of any CV with an amplitude of 0.2 magnitudes.

1.1.2.2 Intermediate Polar (Dq Her) Stars

Intermediate polars (IPs), also called DQ Her systems after the first known member of this category, are normally identified by the detection of strong pulses in both their X-ray and optical light curves. Walker (1956) detected optical pulses with a period of 71.1 s from DQ Her and since then there have been 107 CVs observed which show these optical pulses. Fig. 1.5 shows an example of these pulses from FO Aquarii, the so-called 'King' of these systems. These pulses are thought to be related to the magnetic moment of the underlying white dwarf which is disrupting the accretion flow within the systems, leading to a light house effect which is very similar to the effect seen rotating neutron stars (also known as pulsars; Hewish et al. 1968). The affects on the accretion geometry shall be discussed in Section 1.4.4.

IPs are moderate X-ray emitters, with typical X-ray luminosities between $10^{31} - 10^{32}$ erg s^{-1} (Vogt et al. 1980; Patterson 1994; Xu et al. 2016).

1.1.3 Low Mass X-ray Binaries

Low Mass X-ray Binaries (LMXBs) are compact binary systems where the primary star is either a neutron star (NS) or black hole and the companion is a low mass main or near-main sequence star, similar to CVs. There are many systems that have been classified originally as a CV only to be later re-classified

as an LMXB, and vice-versa. This is due to the many similarities between the systems. The first confirmation of a NS primary in a binary system came from Giacconi et al. (1971) in relation to Cen X-3. While Shklovsky (1967) proposed the existence of a NS in Sco X-1 four years before Giacconi, their detection was based solely on the X-ray spectrum of the source. The discovery by Giacconi et al. (1971) was far more convincing due to the strong X-ray pulsations also detected in Cen X-3. The main method of determining whether the primary star is a neutron star (NS) is through the detection of strong, short X-ray bursts. These X-ray bursts were first observed from a binary system by Grindlay et al. (1976), who suggested the flashes were caused by thermonuclear runaway on the surface of the NS. Since then, there have been several binary systems that have been suggested to harbour black holes as the primary (the first was A0620-00 by McClintock & Remillard 1986). In this thesis, we present results on the long term optical monitoring of a single LMXB, UW Coronae Borealis.

LMXBs are very strong X-ray emitters, with typical X-ray luminosities of $10^{35} - 10^{38}$ erg s^{-1} (Grimm et al. 2002; Revnivtsev et al. 2011).

1.2 Roche lobe geometry of accreting systems

To understand what causes all of the above phenomena in the optical and X-ray light curves of CVs, the geometry of close binary systems and the processes behind mass transfer (accretion) must be considered.

The first thing to consider is the gravitational potential of the system. Consider 2 stars with masses M_1 and M_2, which are gravitationally bound and orbiting the centre of mass (C.O.M.) of the binary. The effective gravitational potential for a point mass of mass m which sits a distance s_1 from mass M_1 and s_2 from mass M_2 is then given by

$$\phi = -G\left(\frac{M_1}{s_1} + \frac{M_2}{s_2}\right) - \frac{1}{2}\omega^2 r^2 \tag{1.1}$$

where G is Newton's gravitational constant (6.67×10^{-11} m^3 kg^{-1} s^{-2}). The last term is related to the centrifugal force on the test mass which arises from viewing the problem in the rotating frame of the binary. In this term, ω is the angular velocity of the test mass and r is the distance from the test mass to the C.O.M (Frank et al., 2002). Taking the derivative of this equation, and looking

for local maxima, allows for the surfaces along which the gravitational forces exerted by the two stars are balanced by the centrifugal force within the binary to be found.

These surfaces have been derived by assuming that the orbits of M_1 and M_2 are circular, that M_2 is tidally locked, and that the masses are centrally condensed. The first assumption should be true for most binary systems, as the timescale on which eccentric orbits are circularised due to tidal interaction of the two stars is shorter than the timescale over which mass transfer will begin (Frank et al., 2002). The second assumption should be true for any systems where the secondary fills its Roche lobe. The third assumption is a good approximation for the WD and a main sequence secondary. Fig. 1.6 shows the gravitational equipotential for a binary system with $M_1 = 0.85M_\odot$ and $M_2 = 0.17M_\odot$. The five points marked are the five Lagrange points, which are the local maxima (L5 and L4) and saddle points (L1, L2, and L3) of the potential. L1 is also called the inner Lagrangian point. The points are named after Joseph-Louis Lagrange.

The masses chosen here are not random. Rather, the primary mass of $M_1 = 0.85M_\odot$ and secondary mass of $M_2 = 0.17M_\odot$ are consistent with the average mass of a WD and the companion star in a CV (Littlefair et al. 2008; Zorotovic et al. 2011). Actual measurements of the masses in CV are measured by looking for absorption features in the spectra of the binary which can be related to the secondary. The motion of these lines due to the orbital motion of the secondary can be combined with the inclination of a system (if known) to measure the mass of the secondary star (see McConnell et al. 2015 for an example of this technique).

Of particular interest for binary systems is the inner equipotential surface which contains the L1 point. If the orbital period and masses M_1 and M_2 of the system are known, then the binary separation, a, can be calculated from Keplers 3rd Law (Kepler, 1618):

$$\frac{P^2}{a^3} = \frac{4\pi^2}{G(M_1 + M_2)} \tag{1.2}$$

Consider a binary star system with a WD of mass $M_1 = 0.8M_\odot$, a main sequence star of mass $M_2 = 0.2M_\odot$ and a binary period of 4 hours. The binary separation in this case is 1.3 $R_\odot$. This separation is small enough that the radius of the secondary star would extend to the equipotential surface.

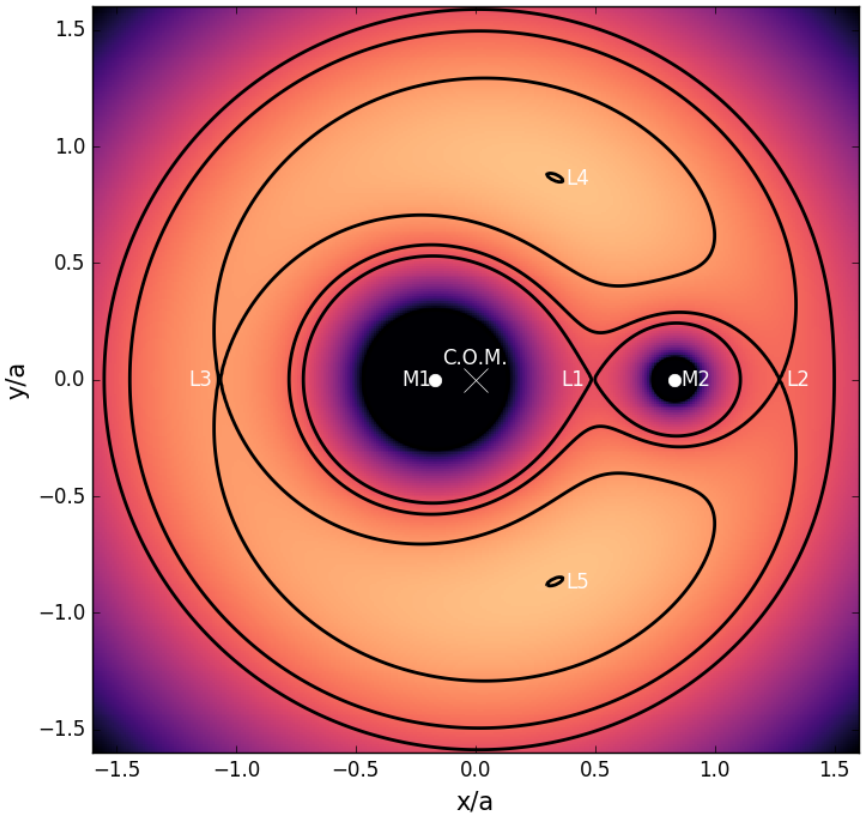

Figure 1.6: The colour plot represents the gravitational potential calculated using Eqn. 1.1, with darker colour showing regions of low potential. The two stars are at the centre of the 2 potential wells, and the C.O.M. is marked by a white cross. All 5 Lagrange points are marked. The equipotential surfaces are also shown as the solid lines. The x and y-axis have been scaled into units of a, which is the orbital separation of the system.

Edouard Roche was the first person to consider this, and it is after him the initial equipotential surface, the Roche lobes, are named.

If the secondary star fills its Roche lobe, then any material that is on the star's surface, which is also on the perimeter of the Roche lobe, will follow the surface to the L1 point, where it will then move into the Roche lobe of the primary star, and begin spiralling in towards the primary. This will be discussed further in Section 1.2.2.

1.2.1 X-ray Luminosity-Accretion Rate relation

Before we consider the structures that arise due to accretion, we can use the above geometry to make a crude estimate of the accretion rates within binary systems. Consider a test particle that falls from the L1 point onto the surface of a compact object (CO). When it impacts the surface of the CO, it will release the gravitational energy gained by falling into the potential well of

$$E_g \sim \frac{GM_1 m}{R_1} \tag{1.3}$$

for $R_1 << R_{L1}$ where R_{L1} is the distance from the CO to the L1 point. For example, a single atom of hydrogen which falls onto the surface of a $0.8 M_\odot$ WD would release approximately 174 keV. If all of this energy were released as a single photon (which assumes the particle does not lose any of its energy before striking the surface of the CO), that photon would be a very, very high energy X-ray. The luminosity from this accretion onto the CO should then be

$$L \sim \frac{GM_1 \dot{m}}{R_1}. \tag{1.4}$$

In practice, particles lost some of their energy before settling onto the surface of the CO through accretion discs or shocks. The X-ray luminosity from a system can be related to this overall luminosity by (Norton & Watson, 1989)

$$L_X = \eta L. \tag{1.5}$$

The η parameter is determined by how much energy particles may release through thermal and non-thermal process before reaching the CO. Warner (1996) determined $\eta = 0.03$ for intermediate polars and assuming $M_1 = 0.6 \mathrm{M}_\odot$. Using the observed $L_X \sim 10^{32}$ erg s^{-1} for an IP and combining equations 1.4 and 1.5 gives a rough handle on the accretion rates within these systems of $\dot{m} \sim 10^{16}$ g s^{-1}. The mass accretion rate in polars and non-magnetic CVs should be similar to that of $\dot{m}$ in IPs, with η varying between the objects and depending on the ratio of the X-ray luminosity to the optical luminosity of the different types of systems.

1.2.2 The Accretion Disc

As material falls in towards the primary star, it will still have a high specific angular momentum that will prevent it from falling directly onto the compact object (CO). Flannery (1975) gives the equations of motion for a particle moving in the Roche potential in the frame of the binary to be,

$$\ddot{x} = 2\dot{y} + x - \mu\left(\frac{x - x_1}{r_1^3}\right) - (1-\mu)\left(\frac{x - x_2}{r_2^3}\right),$$
$$\ddot{y} = -2\dot{x} + y - \frac{\mu y}{r_1^3} - (1-\mu)\left(\frac{y}{r_2^3}\right),$$

where $\mu = \frac{1}{1+q}$, $q = \frac{M_2}{M_1}$, and subscript 1 and 2 denote the x, y and r distances to star 1 and 2 respectively. These equations of motion are a solution to the 3 body problem, where it has been assumed that M_1 and M_2 are much larger than the mass of the particle, and that M_1, M_2, and the particle are confined to the same orbital plane. This is also called the restricted three-body problem.

Fig. 1.7 shows the trajectory for a particle found by numerically integrating these equations of motion, assuming the particle starts at the L1 point with an initial velocity similar to that used in Flannery (1975) and assuming $q = 0.8$.

Due to this the material will orbit the CO elliptically. This orbit will precess due to the motion of the secondary star, which will cause new material to interact with material that has already completed several orbits of the CO. This will circularise the material at a radius of

$$r_{circ} = a\left(0.500 - 0.227\log\left(\frac{M_2}{M_1}\right)\right)^4\left(1 + \frac{M_2}{M_1}\right) \tag{1.6}$$

(see Section 18.2 of Carroll & Ostlie 2006 or Section 4.5 of Frank et al. 2002). As more material settles into this orbit, the entire ring of material heats up (due to a combination of the collisions of particles, viscous dissipative processes, shocks etc.). This heating causes the material to radiate away more of its energy and so, to conserve energy, material must then move closer to the CO, further into the potential well. However, this comes at the expense of angular momentum, which is transported outwards through the material, causing some material to move further away from the CO (Pringle, 1981). The

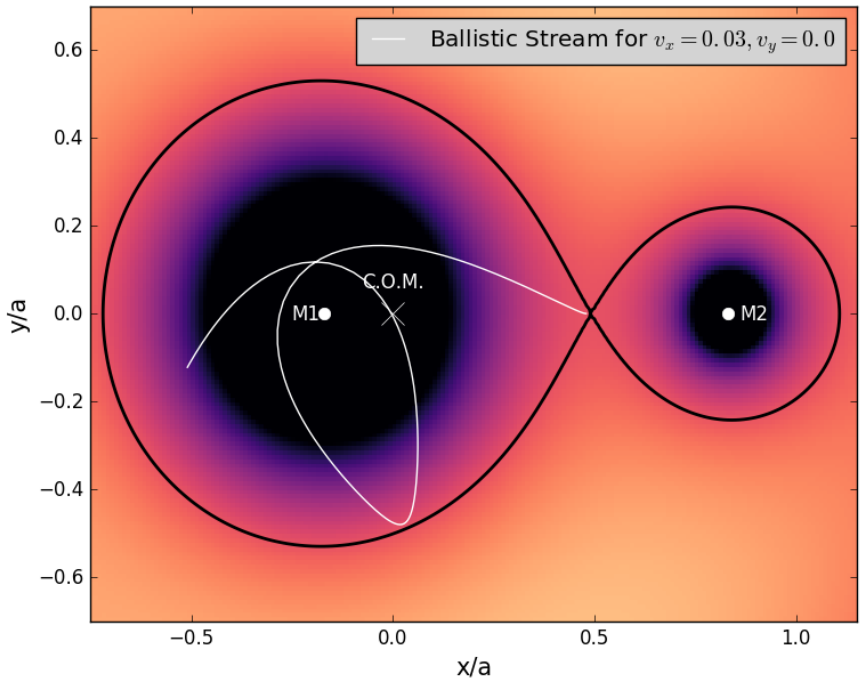

Figure 1.7: The results from numerically integrating the equations of motion given by Flannery (1975) which shows how particles which leave the L1 point with a non-zero velocity will loop around the CO. The black line is the Roche Lobe and the colour indicates the value of the binary potential.

entire structure eventually forms an accretion disc that spans (depending on the magnetic field strength of the CO, more on this later) from close to the surface of the CO (typically the accretion disc exists up until it is a distance b away from the surface, where $b << R_{CO}$. The area between the inner disc and the surface of the CO is called the boundary layer) out to an approximate radius of $2r_{circ}$ (this distance varies depending on mass ratio, accretion rate, magnetic field strength of the stars etc.) . Fig. 1.8 shows the evolution of a ring of matter into an accretion disc.

To understand how the accretion disc contributes to the spectrum of compact binary systems, the temperature profile of the disc must be estimated. Assume the material within the disc is moving in a near-Keplarian orbit (this is a good approximation for the so called “thin disc approximation”, where the self-gravitation of the accretion disc can be ignored when compared with the gravitational force exerted on the disc by the CO. Recently there has been work to show that this approximation can be applied to magnetised accretion discs also (Penna et al. 2010; Avara et al. 2016). The velocity of the material at any

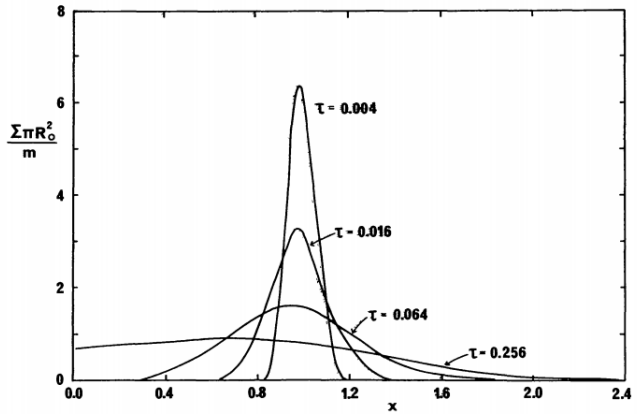

Figure 1.8: The viscous evolution of a ring of matter of mass m. The surface density Σ is shown as a function of the dimensionless radius $x = R/R_0$ (where R_0 is the initial radius of the ring), and of dimensionless time $\tau = 12\nu t/R_0^2$ (where ν is the viscosity). Adapted from Horne & Marsh (1986).

point in the disc should approximately be given by

$$v = \sqrt{\frac{GM_1}{R}} \tag{1.7}$$

where M_1 is the mass of the WD and R is the distance to the WD. This shows that, as expected, material closer to the WD will be moving much faster than material in the outer parts of the disc, which means it should be more energetic and have a hotter temperature associated with it. Mitsuda et al. (1984) give an approximate expression for the temperature profile of an optically thick geometrically thin accretion disc of

$$T(r) = \left(\frac{3GM_1\dot{m}}{8\pi r^3\sigma} \left(1 - \left(\frac{R_{in}}{r} \right)^{\frac{1}{2}} \right) \right)^{\frac{1}{4}} \tag{1.8}$$

where $\dot{m}$ is the mass transfer rate in the system, σ is the Stefan-Boltzmann constant and R_{in} is the inner radius of the accretion disc. This equation comes from imposing boundaries on the inner and outer radii of the accretion disc. The inner radius is limited by the size of the boundary layer between the CO and the disc. This boundary layer is assumed to be negligible in size relative to the radius of the CO. The outer radius of the disc can be bounded by considering at what radius the disc will begin to be tidally distorted by the secondary star. These two bounds can be combined with the rate at which energy should be generated in the disc by viscous shearing, and leads to the

above expression. This expression shows that the temperature profile goes as $T \propto r^{-3/4}$ when $r >> R_{in}$. Equation 1.8 has a maximum at $\frac{r}{R_{in}} = 1.361$, which corresponds to a temperature of

$$T_{max} = 0.488 \left(\frac{3GM_1\dot{m}}{8\pi R_{in}^3 \sigma} \right). \tag{1.9}$$

Taking a primary mass of $0.8M_{\odot}$, the inner accretion disc radius to be $R = 3R_{\oplus}$ and a mass accretion rate of $\dot{m} = 10^{16}$ g s^{-1} (in line with the mass accretion rate calculated in the previous Section) gives a maximum temperature in the accretion disc of 26,000 K. This means the accretion disc can be modelled as a collection of rings that emit as black bodies with a continuous temperature distribution, starting at 26,000 K and falling off as $r^{-3/4}$. Since the white dwarfs in binary systems tend to have very high temperatures (20,000-30,000 K) and emit most of their light in the UV (Sion 1999; Gänsicke 2000; Knigge et al. 2011) and the secondaries tend to be late-type main sequence stars with black body temperatures $<$ 3,000 K (Knigge et al., 2011) that emit in the far red to infrared wavelengths, it is the accretion discs which tend to dominate most of the optical spectrum in compact binary systems.

Identifying accretion discs around compact objects can be an easy task, depending on the inclination of the system. This is not just due to the dominance of the accretion discs in the optical spectrum, but also because of their impact on the shape of emission lines. Fig. 1.9 shows synthetic emission lines from an accretion disc for a variety of inclinations (conventionally, an inclination of 0° is when an observer would have a top-down view of the system, and an inclination of 90° would be when an observer sees an accretion disc edge on). The effect of the accretion disc on the shape of the line is quite apparent, particularly for higher inclination systems, where the emission line is split into a double-peaked structure. This is due to the fact that half of the accretion disc is moving towards the observer, generating the blue peak while half of the accretion disc is moving away, generating the red peak. How different parts of the accretion disc contribute to different parts of the emission line is shown in Fig. 1.10. This figure shows contours for constant velocities as seen by an observer at the bottom of the figure. This explains the double peaked lines shown in Fig. 1.11 for the system CSS120422:J111127+571239, which will be discussed in detail later in this thesis.

There are also other effects which can lead to changes in the shape of emission

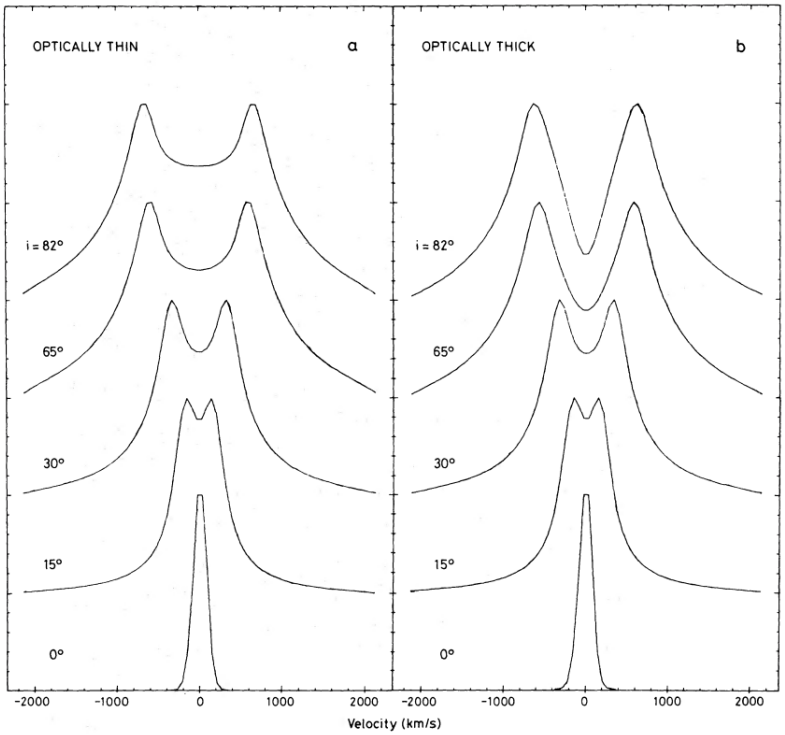

Figure 1.9: Emission lines from both a synthetic optically thin (left) and an optically thick (right) accretion disc for various inclination angles. Adapted from Horne & Marsh (1986)

lines. The most common effects are due to pressure broadening due to the collision of particles (which may happen inside of the disc, depending on the density), broadening due to absorption of photons by interstellar material, or broadening of the line due to gravitational redshift. This last effect is important when dealing with black holes due to their very compact nature, but is negligible for systems containing white dwarfs.

1.3 Formation of Cataclysmic Variables

The orbital period of CVs varies from as long as a few hours down to $\approx$ 78 min for systems with main sequence companions, and even shorter for systems with degenerate companions. The binary separation, spectral type of the companion and strength of the magnetic field of the WD tend to determine what type of accretion, if any, occurs within a cataclysmic variable.

The formation of a CV begins with 2 main sequence stars orbiting each other. Once one of the stars (typically the more massive star) has reached the end of its main sequence life, it will expand into a red giant. If the secondary is

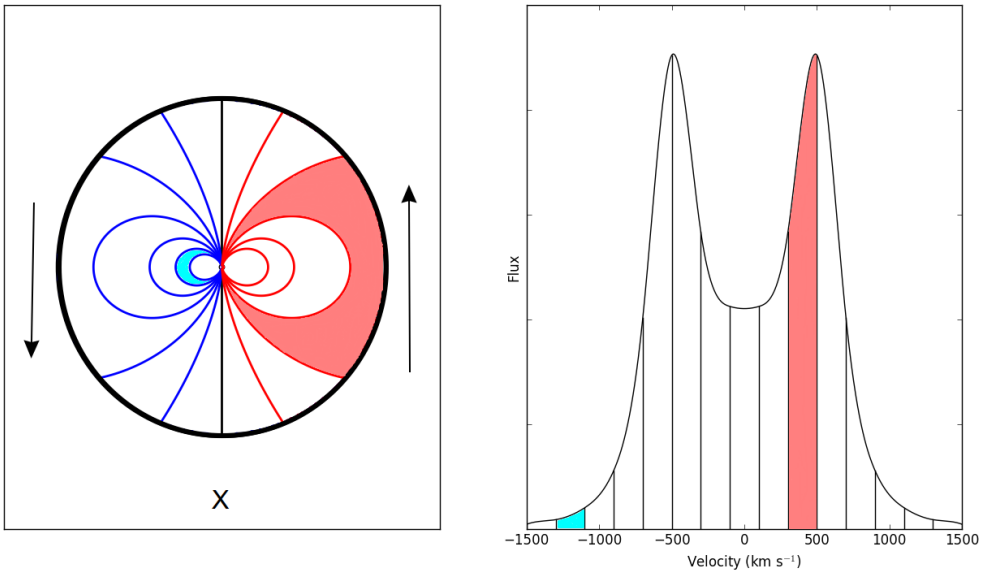

Figure 1.10: The left panel shows contours of constant radial velocity as seen by an observer who is viewing the disc from the position marked X. The arrows show the direction the disc is rotating. Blue contours represent material which is moving towards the observer, and hence has a negative velocity, while red contours are material that is moving away from the observer. The right panel shows the emission line seen by the observer due to the velocity shifts which are occurring in the disc. The highlighted regions in the disc contribute to the highlighted regions of the line, and show that there is very little high velocity material observed, which leads to a small contribution out in the wings.

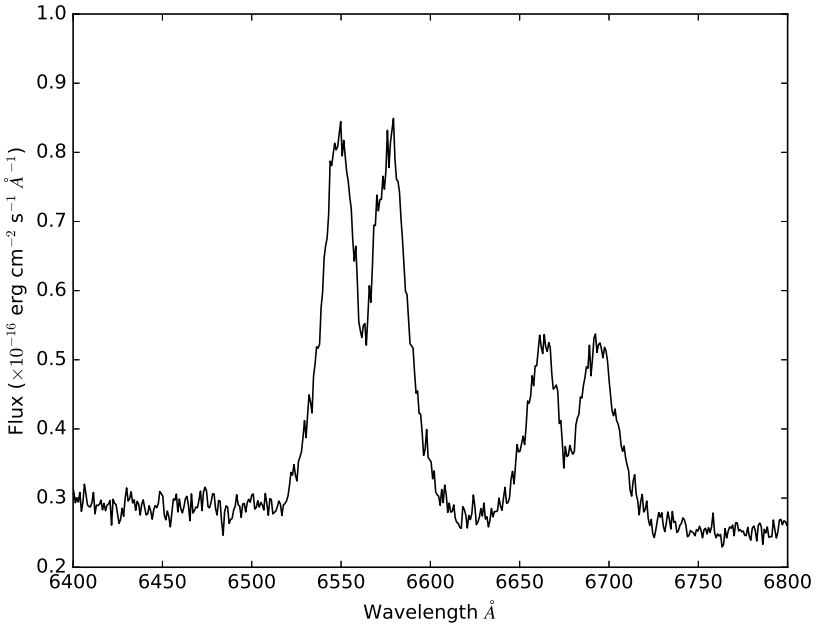

Figure 1.11: The Hα and He I emission lines from CSS120422:J111127+571239. These lines are an example of how an accretion disc gives emission lines their double peaked nature.

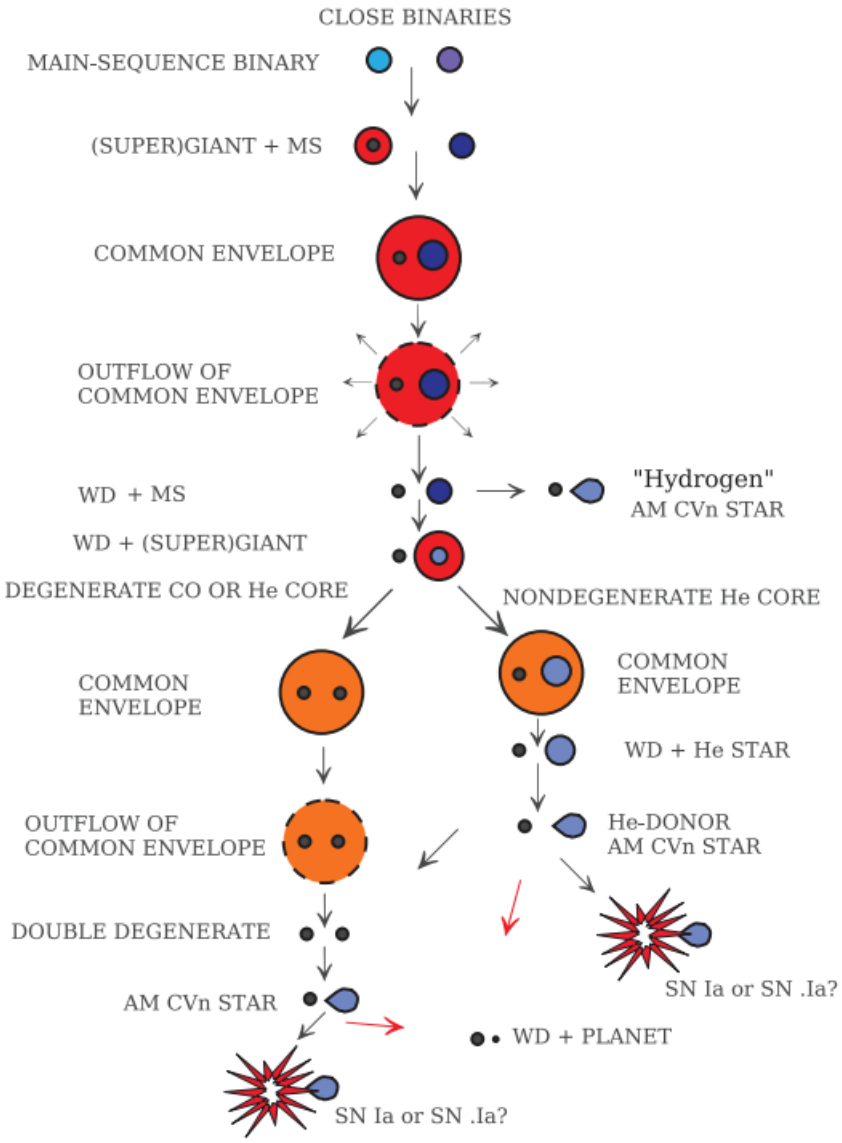

Figure 1.12: The basic steps in the evolution of AM CVn stars from close binaries to supernova explosions or a cooling white dwarf with a companion (prepared by L. Yungelson). Adapted from Solheim (2010).

orbiting close enough to be enveloped by the red giant, the system enters the common envelope stage. This common envelope stage causes the secondary star to spiral inwards towards the core of the red giant. After the common envelope has been ejected and the WD is left at the centre of the primary, the binary separation will continue to decrease (the mechanisms for this will be discussed in the following sections). Once this separation has reached around $1.7 R_{\odot}$, the secondary (which has a radius of ~ 0.5 R$_{\odot}$; Knigge et al. 2011) fills its Roche lobe and mass transfer begins. Fig. 1.12 shows this evolution track for AM CVn systems, which are a class of CVs.

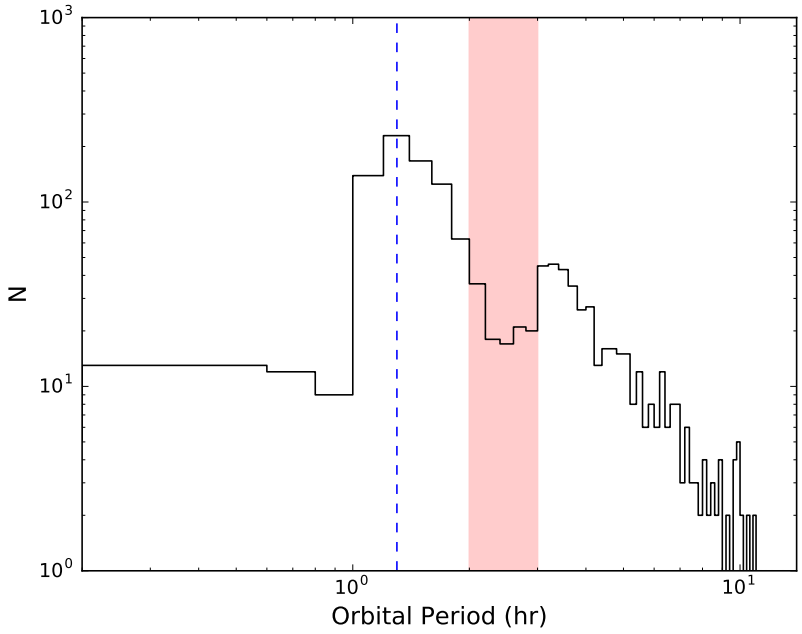

Figure 1.13: The distribution of orbital periods for all known CVs. The period gap is visible between $2\text{hr} < P < 3\text{hr}$ (and is highlighted in red), as well as the period minimum for main sequence companions around ≈ 78 min (the dashed blue line).

1.3.1 Period distribution of CVs

The Ritter & Kolb catalogue of CVs (Ritter & Kolb 2003, updated 2016) contains data for all known CVs, including (if known) their orbital periods (P), primary and secondary masses (M_1 and M_2), mass ratios ($q = M_2/M_1$), inclinations (i) and system classifications. Fig. 1.13 shows the number of known systems versus their orbital periods. There are 2 main features to this plot. The first is the low number of systems with orbital periods $2\text{hr} < P < 3\text{hr}$ and the second is the large number of CVs clustered around the orbtial period ≈ 78 min.

Before we discuss the 2 main features of Fig. 1.13, we will address the small number of systems detected with a period > 6 hr. The main source of optical light in a CV is the accretion disc, which is formed after the secondary comes into contact with its Roche lobe. However, for systems with typical masses and orbital periods > 6 hr, the binary separation is large enough that the secondary has not yet come into contact with the Roche lobe, and accretion is not occurring. Systems which are discovered with orbital periods above > 6 hr are called pre-CVs. As these systems age, they lose angular momentum (the

processes for losing this angular momentum will be considered in the next paragraph). As the systems lose angular momentum, their orbital periods and binary separations decrease. Eventually, the system will become compact enough that the secondary will fill its Roche lobe and mass transfer will begin. This occurs at (approximately) an orbital period of $5 - 6$ hours, which is why the number of known CVs begins to increase around these orbital periods.

As was already mentioned, as these systems age, they lose angular momentum to their surroundings. This is important as, if no angular momentum were lost from a system which is undergoing mass transfer, the process of mass transfer would cause the binary separation for increase, and the secondary would quickly lose contact with its Roche lobe as the Roche lobe expands. Hence, to keep the secondary in contact with its Roch lobe, the orbital separation must decrease, which requries the loss of angular momentum.

The main processes of angular momentum loss are thought to be magnetic braking of the secondary and gravitational radiation from the system as a whole. Magnetic braking is a process where charged particles are accelerated along open magnetic field lines coming from the star. Once these particles are lost from the system, they remove angular momentum. This concept was first used to help describe the different sections of the Hertzsprung-Russell diagram (Schatzman, 1962). Magnetic braking is important in CVs due to the magnetic activity of the secondary stars. Most secondary stars in CVs are tidally locked, meaning the secondary star is rotating with the same period as the orbital period. (There are exceptions to this. For example, there has been a small amount of differential rotation measured in AE Aqr; Hill et al. 2014.) This fast stellar rotation enhances stellar activity due to an increase in the efficiency of the secondary star's stellar dynamo. Tomograms of the secondary stars in several systems have shown large starspots on their surfaces, which supports this increase in stellar activity (Watson et al. 2006; Watson et al. 2007; Dunford et al. 2012; Hill et al. 2014; Hill et al. 2016). For a review on the role of magnetic braking in CVs, see Hussain (2011). Magnetic braking is thought to be particularly important for explaining the period gap around $2\mathrm{hr} < P < 3\mathrm{hr}$, which will be discussed in the next section.

Gravitational radiation is thought to also be responsible for angular momentum loss within CVs (Paczyński 1967; Webbink 1976; Andronov et al. 2003), and becomes particularly important below the period gap (Knigge et al., 2011).

1.3.1.1 The Period Gap

The decrease in the number of CVs with orbital periods between $2\text{hr} < P < 3\text{hr}$ (the period gap) is thought to be related to the convective status of the secondary star. In the "disrupted magnetic braking" evolution scenario for CVs (Rappaport et al. 1983; Paczynski & Sienkiewicz 1983; Spruit & Ritter 1983), magnetic braking plays an important role in angular momentum loss up until an orbital period of 3 hours. Up until this point in its evolution, the Roche lobe of the secondary has been shrinking faster than the time it takes for the secondary star to reach its thermal equilibrium radius after losing mass, which has kept the secondary in contact with its Roche lobe. However, at an orbital period of 3 hours, the secondary star has become small enough that it becomes fully convective, and the increased stellar activity which led to the efficient loss of angular momentum through magnetic braking is quenched. Once magnetic braking has ceased, the rate at which the Roche lobe shrinks slows (due to a lower amount of angular momentum loss from the system) and the star has enough time to reach a thermal radius which lies inside of its Roche lobe. During this time, accretion ceases, and the accretion disc, which would normally be dominant at optical wavelengths, dissipates. The system continues to lose angular momentum through gravitational radiation and, at an orbital period of 2 hours, the secondary once again comes in contact with its Roche lobe, and accretion resumes, allowing for the system to become easily detectable at optical wavelengths. The system then continues evolving to shorter periods as angular momentum is continually lost by gravitational radiation. However, as Fig. 1.13 shows, there are still a few systems detected within the period gap. These systems, which do not follow the conventional evolution paths of CVs, are discussed in Chapter 7.

1.3.1.2 The Period Minimum

The clustering of CVs around the orbital period of ≈ 78 min (known as the period minimum) is due to the evolution of main sequence stars as their radius is compressed. Up until an orbital period of ≈ 78 min, the loss of angular momentum through gravitational radiation causes the orbital period (and, by consequence of Kepler's 3rd law, binary separation) to decrease. This shrinks the Roche lobe of the secondary, and the secondary star continues to shrink due to mass loss. However, at approx a period of ≈ 78 min, the secondary star

becomes degenerate. The effect that this has on the orbital evolution of the system can be found by considering the mass-radius index of the secondary star which is given by Knigge et al. (2011) to be

$$\frac{\dot{M}_2}{M_2} = \frac{1}{\zeta}\left(\frac{\dot{R}_2}{R_2}\right) \tag{1.10}$$

where ζ is a constant which relates the mass and radius for a given stellar evolution state. For example, low mass main sequence stars have $\zeta \sim 0.8$, while for a brown dwarf $\zeta \sim -1/3$ (Chabrier et al., 2009).

The relation between the density of the secondary star and the orbital period of the system for a CV (for $q \leq 0.8$) is given by (King, 1988)

$$\rho_2 \sim \frac{115}{P^2}\mathrm{g\ cm^{-3}}, \tag{1.11}$$

By logarithmically differentiating this equation such that

$$\frac{\dot{\rho}_2}{\rho_2} = \frac{2\dot{P}_2}{P_2}, \tag{1.12}$$

and expressing equation 1.10 in terms of M_2, $\dot{M}_2$, ρ_2, and $\dot{\rho}_2$ (using $R_2 = \left(\frac{M_2}{4\pi\rho_2}\right)^{1/3}$), then these equations can be combined to give an expression which relates P, $\dot{P}$, M_2, and $\dot{M}_2$ by

$$\frac{\dot{P}_{orb}}{P_{orb}} = \frac{3\zeta - 1}{2}\left(\frac{\dot{M}_2}{M_2}\right). \tag{1.13}$$

Since $P_{orb} > 0$, $M_2 > 0$ and $\dot{M}_2 < 0$, the sign of $\dot{P}_{orb}$ is dependant on the value of ζ. (Knigge et al., 2011) shows that $\zeta \sim 0.8$ for the secondary stars in CVs which are just below the period gap, so $\dot{P}_{orb} < 0$. However, once the secondary has become degenerate, ζ approaches 0, which leads to a sign change in $\dot{P}_{orb}$.

Hence, once the secondary has become degenerate, the orbital period will increase (Paczynski 1981; Paczynski & Sienkiewicz 1981) due to mass loss. This leads to a large number of systems with periods close to ≈ 78 min. However, as Fig. 1.13 shows, there have been systems detected with periods less than the period minimum. These systems have companions which are not main sequence stars, and become degenerate at much shorter orbital periods. This will be discussed further in Chapter 7.

1.4 Classification of CVs revisited

Now armed with a basic overview of the components of a binary system, we can discuss what effects cause the variabilites in the various CV subtypes. By far the most important way of a classifying a CV is by considering the strength of the magnetic field of the WD, which also dictates the accretion geometry for the system. In the following section, I discuss the 2 magnetic classification of CVs (the so-called Polars and Intermediate Polars) along with the non-magnetic classification. But first, I will discuss the cause of classical nova outbursts.

1.4.1 Nova Outbursts

Novae are thought to be driven by runaway hydrogen fusion on the surface of the WD (Bode & Evans, 2008). Nova outbursts require a large amount of hydrogen to accumulate on the surface of the WD (between $10^{-5} - 10^{-3}$ $M_{\odot}$; Starrfield 1989) and have very long recurrence times. Systems which have only been observed to have a single outburst are called classical nova.

Starrfield et al. (2016) give an excellent review of classical novae and the mechanism behind the thermonuclear runaway. In essence, as material is accreted onto the WD, it forms a shell of nuclear fuel. The bottom of this shell becomes compressed due to the surface gravity of the WD, and eventually becomes degenerate, which works to prevent the material from expanding despite an increase in temperature in the material which is caused by pressure from the material lying above it and the small amount of fusion this material will be undergoing. Once the material has reached the Fermi temperature of the white dwarf $\sim 7 \times 10^7$ K, it will begin to expand rapidly. Here, the Fermi temperature is given by $T_f = \frac{E_f}{k}$ where k is Boltzmanns constant and E_f is the Fermi energy of the degenerate WD, which is the energy difference between the lowest and highest energy levels populated by fermions in the WD. This leads to the thermonuclear runaway which explodes the shell of fuel around the WD. The mass of the shell required to cause a novae eruption is mainly a function of the mass of the underlying WD, as higher mass WDs have higher surface gravities, which requires a lower shell mass for the material to reach the Fermi temperature, but also a function of the temperature of the WD and mass accretion rate Prialnik & Kovetz (1995).

There has been a lot of research into whether a nova event erodes or adds mass to the WD, as if it adds mass, novae events would be important in growing a WD to the Chandresekhar mass of 1.4 $M_{\odot}$. most sources currently agree that novae work to erode the WD mass, suggesting that CVs which undergo nova events will not reach the Chandrasekhar limit (MacDonald 1984; Gehrz et al. 1998; Starrfield et al. 2000). However, this will be discussed further in Chapter 7.

1.4.1.1 Recurrent Nova

Recurrent novae are systems which have been observed to undergo more than one nova outburst. The requirements for a system to show recurrent novae are simply. First, the mass of the WD should be close to the Chandraskehar limit. This will reduce the recurrence time for nova outbursts as a smaller shell must be accreted before the system meets the requirements to undergo thermonuclear runaway. The current lower limit on the WD mass required to produce a recurrent novae system is > 1.2 $M_{\odot}$. Second, the mass accretion rate must be high such that the shell gains enough mass to undergo a thermonuclear runaway in the observed recurrence times. See Schaefer (2010), Anupama (2013), and Mukai (2015) for excellent reviews on the known recurrent novae systems.

1.4.1.2 Low Mass X-ray Binaries

The previously mentioned X-ray bursts seen in LMXBs are analogous to the novae outbursts in CVs. In a CV, the amount of hydrogen required and the accretion rates in the system cause novae outbursts to be long, powerful and rare. However, in LMXBs, where the primary is a NS, the amount of material required before the surface of the NS erupts is significantly lower, meaning the Type 1 X-ray bursts happen far more frequently than novae outbursts, and only last between $10 < t < 200$ s, with the amplitude of the outburst being much smaller than a nova outburst. (It should also be noted that it is thought that a mix of H and He is the main fuel used in Type 1 X-ray bursts, as opposed to simply H; Strohmayer & Bildsten 2003.)

1.4.2 Non-magnetic CVs

When the WD in a CV has a low magnetic field, material that passes through the L1 point will fall ballistically towards the WD until it encounters the accretion disc. The point at which this incoming material strikes the accretion disc is known as the hot (or bright) spot, and is a source of strong optical emission. The accretion disc itself will extend down nearly to the surface of the WD.

Non-magnetic CVs are split into many different subtypes, depending on their accretion rates, light curve morphology and spectral properties.

1.4.2.1 Dwarf Novae

The mechanism by which dwarf nova outbursts occur has long been debated, but the currently accepted theory is that the outbursts are triggered by an instability within the accretion disc due to partial hydrogen ionisation (disc instability model, or DIM; Osaki 1974; see Cannizzo 1993, Osaki 1996, Lasota 2001 and Buat-Ménard et al. 2001a for excellent reviews on the topic).
Fig. 1.14 shows the typical S-curve which relates the surface density, Σ, to the effective temperature, T_{eff}, for an accretion disc in this model.

Consider a system which has a Σ and T_{eff} such that the system is at point A. The temperature in the disc is not hot enough for hydrogen to be fully ionised, and the viscosity in the disc is low. Since the viscosity is low, the amount of material entering the disc from mass transfer from the secondary ($\dot{M}_2$) is larger than the mass transfer rate through the disc. This means that Σ increases and, consequently, so does T_{eff}, until the disc reaches point B. Once it has reached B ($T_{eff} \sim 8000$ K), all of the hydrogen in the disc will become full ionised. T_{eff} will rapidly increase, as will the viscosity inside of the disc. The cause of this viscosity is not simple molecular viscosity, which does not give the required magnitude for these types of discs. One explanation for the the high viscosity is the Balbus-Hawley magneto-rotational instability (Balbus & Hawley, 1991). Once at point C, the disc begins to transfer material through it towards the WD faster than it is gaining material from the secondary, causing Σ and T_{eff} to decrease. Once the disc has reached point D, the disc has cooled enough that hydrogen will recombine, and the temperature and viscosity rapidly decrease again, returning the system to point A and starting the cycle over.

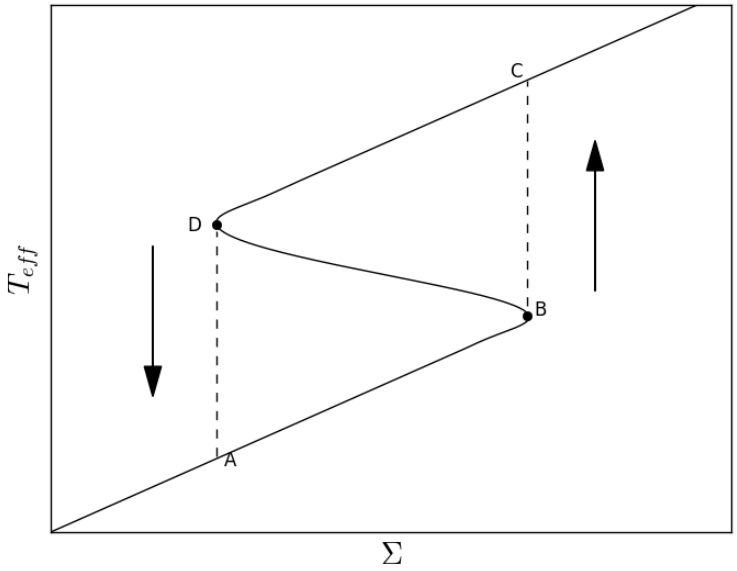

Figure 1.14: A schematic for how the 'S-curve' which relates the surface density of an accretion disc, Σ, to the effective temperature of the disc, T_{eff}. See the text for a full explanation.

The discovery of new DNe usually comes from all sky surveys that look for transient objects, such as the Mobile Astronomical System of Telescope-Robots (MASTER) survey, the Catalina Sky Survey (CSS) or the the All-Sky Automated Survey for Supernovae (ASAS-SN) survey.

1.4.2.2 SU UMa

The SU UMa systems are a subclass of dwarf novae. This is because of the large amplitude super-outbursts which are seen in their light curves alongside the typical dwarf nova outbursts. Fig. 1.15 shows the previously unpublished light curve of MLS035906+175034. Visible in this light curve are three normal dwarf nova outbursts followed by a super-outburst which is then followed by a further four normal outbursts.

The current theory for the mechanisms responsible for these super-outbursts is the thermal-tidal instability (TTI) model (Osaki, 1989). In this model, a normal outburst will cause the accretion disc to expand, and sequential outbursts will have an increasing amplitude. Once an outburst occurs which causes the radius of the disc to expand to the 3:1 orbital resonance, tidal interactions between the secondary star and the disc cause the disc to become

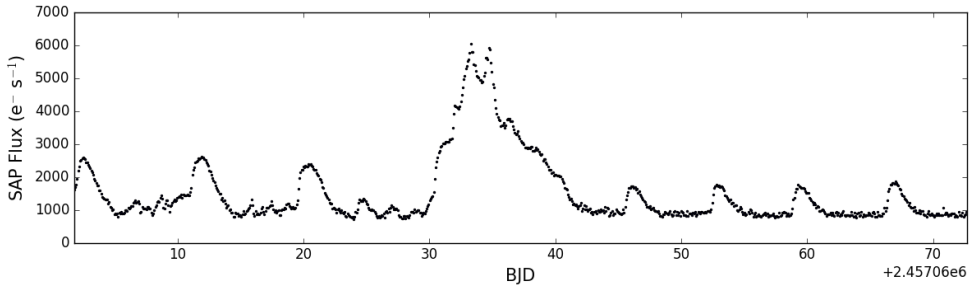

Figure 1.15: The previously unpublished light curve of MLS035906+175034 which was taken as part of the *Kepler K2* mission. The light curve shows 7 normal outbursts along with a single super-outburst.

eccentric. The disc then undergoes significant tidal dissipation, which causes most of the disc to accrete onto the WD. This is what causes the significant increase in brightness in the light curve. After the super-outburst, the normal outbursts have a much smaller amplitude, since the disc has been reduced in size. Eventually the disc will reach a point where another super-outburst will occur. The time between consecutive super-outbursts is called the super-cycle.

Recent *Kepler K2* observations of the SU UMa systems V1504 Cygni and V344 Lyrae suggest that the accretion disc radius does increase during a superoutburst as expected in the TTI model (Osaki & Kato, 2014).

1.4.2.3 Z Cam

Z Cam stars another subclass of dwarf novae. They exhibit the normal, nearly-periodic outbursts observed in dwarf nova systems, but also undergo long periods of standstill, where their brightness stays at a level between their normal quiescent brightness and their maximum brightness during outburst. These standstills can last from a few days up to more than 1,000 days. The standstills are thought to be related to a variable mass accretion rate. When the mass accretion rate is low, the accretion disc is unsteady and lies on the lower branch of the S-curve shown Fig. 1.14. The disc can then undergo dwarf nova outbursts. However, when the mass accretion rate from the secondary increases, the disc can enter the upper branch of the S-curve and stay there. This means the disc becomes hot and steady, and the system enters a standstill period (Buat-Ménard et al., 2001b).

1.4.2.4 Nova-likes

It is currently suspected that the non-detection of dwarf nova outbursts from nova-likes is due to an intrinsic high accretion rate within these systems that suppresses the disc instability and, essentially, keeps the disc in constant outburst (Dhillon, 1996). This means these systems lie on the upper branch of the 'S-curve' permanently. There are two main subcategories for nova-like systems.

RW Tri

The normal nova-like CVs are the RW Tri class, which are CVs that have pure emission line spectra with H , He I and He II lines in the optical and N V, Si IV and C IV in the UV (see Warner 1995 for a full definition).

UX UMa

The UX UMa subtype of nove-like CVs are identified through their peculiar optical spectra. These systems show weak, broad hydrogen absorption lines which come from optically thick discs and spend the majority (if not all) of their lifetimes in an outburst state (Ferguson et al., 1984). Superimposed on the weak hydrogen absorption lines are emission lines which are thought to arise from irradiation of the secondary stars in these systems (for example, see the work on RW Sex by Beuermann et al. 1992). These systems also show N V, Si IV and C IV in absorption in the UV.

1.4.2.5 SW Sextantis Systems

The SW Sextantis stars present one of the most complicated classes of CVs. Initially, this class was limited to CVs whose light curves showed deep eclipses (suggesting a high inclination) yet their emission lines were single peaked and only showed shallow eclipses. Additionally the radial velocity of the emission lines were out of phase with that of the WD and showed transient absorption features, which suggests that the lines originated in a part of the disc which was not close to the WD, or that they even originated outside of the disc. Currently, the SW Sextantis classification has been expanded to include low inclination CVs, and SW Sextantis stars now make up the majority of CVs

detected with an orbital period within the period gap (Rodríguez-Gil et al., 2007).

There have been several models created to explain the observed features of the SW Sextantis class. This includes the idea that SW Sextantis stars may be magnetic, which would give single-peaked emission lines which originate from material encountering a magnetic accretion curtain close to the surface of the white dwarf (Hoard et al. 2003; this is supported by the detection of circular polarisation from several SW Sextantis stars; Rodríguez-Gil et al. 2001). Other models include a disc wind, stream-overflow and obstruction of the central components of the system by the disc edge for high inclination systems. For a thorough review of the class, and the issues which arise from these models, see Dhillon et al. (2013).

1.4.3 Polar (AM Her) Stars

Accretion within polars does not occur through an accretion disc. Instead, in-falling material follows a ballistic stream from the L1 point until the magnetic pressure exerted by the magnetic field of the WD over comes the ram pressure within the accretion stream. When this occurs, the material couples to the magnetic field lines, rises out of the orbital plane and is funnelled onto the magnetic pole of the WD (Mukai, 1988). This is shown in the second panel of Fig. 1.16 (the top panel of Fig. 1.16 shows an example of the accretion geometry for a typical non-magnetic CV). The accreting material encounters a shock before the top of the WD, where hard (2-10 keV) X-rays are produced. Some of these hard X-rays, along with some material, can potentially pass through the shock and heat the surface of the WD to high enough temperatures to produce soft (0.3-2 keV) X-rays.

As previously stated, accretion disks are thought to be the dominant producers of optical light in CVs. Hence, the lack of an accretion disk in polars explains the high F_X/F_{opt} ratio observed in these systems.

1.4.4 Intermediate Polar (DQ Her) Stars

In IPs the white dwarf's magnetic field is high enough ($\sim$1-10 MG) that the material from the donor star is not accreted through a typical accretion disc extending close to the white dwarf. There are three current models for

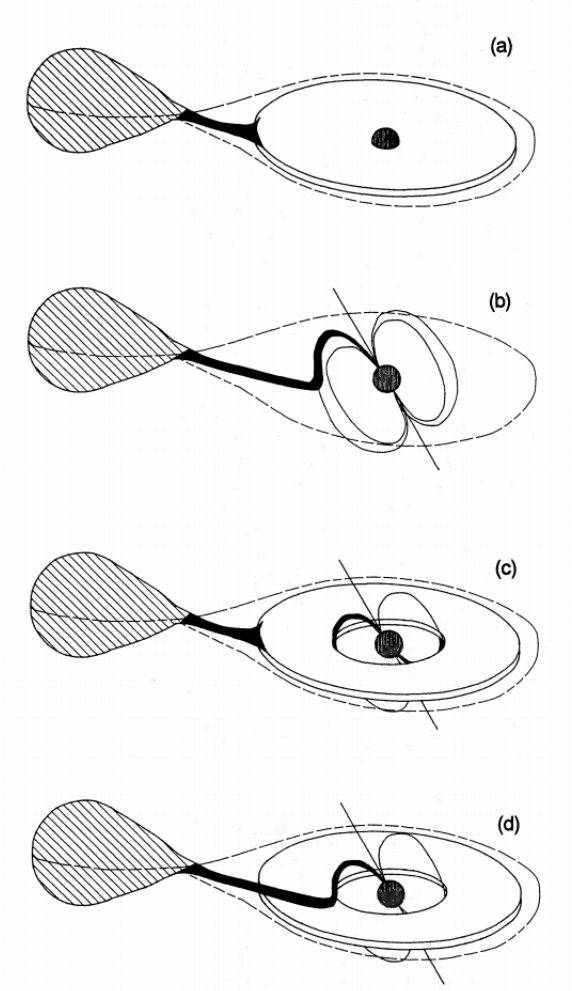

Figure 1.16: Schematic diagrams of accretion in cataclysmic variables, (a) Non-magnetic CV with no disruption of the accretion disc, (b) Stream-fed magnetic CV in which the formation of an accretion disc is prevented, (c) Disc-fed magnetic CV in which the accretion disc is disrupted at the magnetosphere boundary (which will be defined in Section 1.4.4), (d) Magnetic CV with non-accretion disc in which a disrupted disc exists, but in which (some of) the accreting material skims over the surface to impact the magnetosphere directly as in (b). Adapted from Norton (1993).

accretion in an IP, with the applicable model for any given IP depending on the magnetic moment of the WD and the mass accretion rate. The first is the disc-fed model, where an accretion disc is present in the system, and the inner edge of the accretion disc is truncated by the magnetic field of the WD at the point where the magnetic pressure from the WD,

$$P_{mag} = \frac{4\pi}{\mu_0}\frac{\mu^2}{8\pi r^6}, \tag{1.14}$$

where μ is the magnetic moment of the white dwarf and μ_0 is the permeability of free space and has a value of 1.25×10^{-6} m kg s^{-2} A^{-2}, exceeds the ram pressure of the disc,

$$P_{ram} = \rho v^2. \tag{1.15}$$

By equating these two expressions, and assuming spherically symmettric accretion such that $\dot{M} = 4\pi\rho v r^2$ and that infalling material has a velocity approximately equal to its freefall velocity of $v_{ff} = \sqrt{\frac{2GM_1}{r}}$ and then solving for r, we find this occurs at a radius of

$$r_M = 5.1 \times 10^8 \dot{M}_{16}^{-2/7} \left(\frac{M_1}{M_\odot}\right)^{-1/7} \mu_{30}^{4/7} \text{cm} \tag{1.16}$$

for material which was falling with a velocity close to its freefall velocity, where $\dot{M}_{16}$ is the mass accretion rate measured in units of 10^{16} g s^{-1} and μ_{30} is the magnetic moment of the WD in units of 10^{30} G cm^3. This radius is also called the Alfvén radius (Frank et al., 2002). Material then follows "accretion curtains" to the magnetic poles of the WD (Rosen et al. 1988; the third panel of Fig. 1.16).

The second accretion model is the stream-fed model, which has no accretion disc due to the magnetic field of the WD. In this model, the accretion stream entering the Roche lobe of the WD does not form a disc, but instead directly impacts the magnetosphere of the WD (Hameury et al., 1986), similar to the accretion geometry in the polars. The third model is a combination of the first two models, and is known as the "disc-overflow" model (Lubow 1989; Armitage & Livio 1996). In this model, material accretes via the "accretion curtains" of the disc fed model, but accretion can also occur from material in the accretion stream being caught by the magnetic field at the hot spot, following the stream-fed model (bottom panel of Fig. 1.16).

In all of the above models, the EUV and X-ray light created by the impact of material onto the WD is partially reprocessed into the optical by the accretion curtain, accretion disc or accretion stream. In the disc-fed and disc-overflow models, the material impacts onto both magnetic poles, while in the stream-fed model it impacts a single pole, and as these regions move into and out of our plane of sight, they give rise to modulations in the optical and X-ray light curve. Fig. 1.17 shows a model of these accretion curtains for a disc-fed system for various spin phases, showing how the modulation arises. In the disc-fed and disc-overflow models, this signal is detected at the spin period of

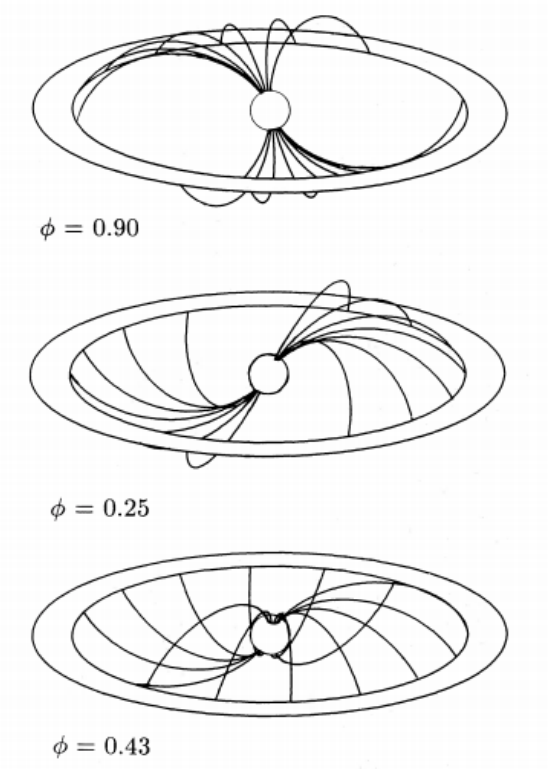

Figure 1.17: A three-dimensional illustration of the accretion curtains falling to the magnetic poles of an intermediate polar. The arch-shaped accretion curtain is azimuthally extended and has a footprint on the surface forming an arc around the magnetic pole covering only 1 per cent of the white-dwarf surface area. The variations in our view of the curtain with spin phase explain the spin-period behaviour of the X-rays, optical continuum and emission lines in intermediate polars. Spin-flux maximum (phase zero) occurs when the upper pole points away from the observer. Adapted from Hellier et al. (1991).

the WD $(2\pi/\omega_s)$ in the optical and X-ray wavelengths, while in the stream-fed model, the modulation is seen at spin period of the WD in the X-ray light curve and at the beat period $(2\pi/(\omega_s - \omega_o))$ in the optical, where $(2\pi/\omega_o)$ is the orbital period (for a review, see Patterson 1994).

1.5 Structure of Thesis

This thesis focuses on examining and characterising various cataclysmic variables based on the above categories. Chapter 2 details the basic reduction steps for the various datasets used throughout the thesis. Chapters 3 and 4 focus on two new cataclysmic variables, J1923 and Lanning 386, and how they defy easy characterisation. Lanning 386 was selected for X-ray observations based off of its unusal classification of part SW Sextantis star, part

normal dwarf novae star, while J1923 was selected after its discovery in 2014 as an unusual CV. Chapter 5 focuses on *Kepler* observations of the "King" of IPs, FO Aquarii, which are the first observations of an intermediate polar taken using the *Kepler* telescope. Chapter 6 focuses on the first ever low state observed in FO Aqr, and shows the X-ray behaviour of any intermediate polar during a low state for the first time in history. Chapter 7 presents the results on CSS120422:J111127+571239, a CV with an orbital period below the period minimum but with persistent hydrogen emission lines. This object may have followed an unusual evolutionary track, and may be part of a rare type of CV. Chapter 8 discusses the long term light curves of UW Coronae Borealis, an LMXB that displays bright, powerful optical bursts. This system was chosen for study as the optical bursts may be related to Type 1 X-ray bursts, which are similar to the novae eruptions seen in CVs but occur on a much faster timescale.. Finally, Chapter 9 sumarises the work, and presents future plans.

2 Data Reduction

Any data recorded using an electronic device is subject to instrumental and background noise. In this chapter, I discuss the most common methods for removing these effects from optical and X-ray data. In some cases, pipelines which have been developed by the institutions that run some of the telescopes have been used to reduce data. In these cases, I refer the reader to the handbooks for these pipelines, and attempt to give a general over view of the steps within the pipelines.

2.1 FITS Files

The typical file format for any astronomical image or dataset is the Flexible Imaging Transport System (.fits; Pence et al. 2010). In the following sections most of the data which are reduced and analsyed using the .fits format can be read directly by the reduction programs. These files can also be read in the programming language PYTHON by using the FITS module located in ASTROPY.IO.

2.2 Optical Photometry

The reduction of optical data taken with charged coupled devices (CCDs) is performed to remove instrumental effects from the raw images. The 3 most basic and necessary steps are removal of the bias current, which is inherent to the CCD and is related to the charge applied to each pixel such that the pixel can record a signal, removal of the dark current, which is the build up of charge within any pixel due to thermal noise, and flat fielding of the images, which removes pixel-to-pixel variations across the image due to the CCD response. In the following, the dark current effect was negligible since the CCDs on all telescopes were either cooled using liquid nitrogen or a thermoelectric cooler, which essentially eliminates the dark current. Fig. 2.1 shows a raw science image in the left panel, and a bias-corrected, flat fielded science image in the right panel. The packages used for reduction are all found in the CCDRED package within IRAF [*].

[*] IRAF is distributed by the National Optical Astronomy Observatory, which is operated by the Association of Universities for Research in Astronomy (AURA) under cooperative agreement with the National Science Foundation

Figure 2.1: An example of the difference between a raw and a reduced science image. The left shows a typical raw image taken using the CCD on the 1m C2PU telescope, while the right shows the same image after bias subtraction and flat fielding.

2.2.1 Bias Correction

After converting the analog signal from the CCD to a digital signal, the distribution of values for a pixel that did not detect a photon should be centred on 0, with a small distribution around 0. To avoid any negative counts, which are unphysical, and to allow for the counts to be amplified correctly, a constant count is typically added to each pixel in the CCD to lift the mean to approximately 1000. This bias level must be subtracted off before analysis of the data.

There are 2 steps to correct for a bias current, depending on the age of the CCD. For older CCDs, the first step is to use an overscan region. With older CCDs the bias level (which should be constant between frames) was found to vary between frames, meaning it was important to have a way to bias correct every frame independently. The overscan region, which was a region on the CCD (typically a row or column of pixels) that are not exposed to the sky, was used for this. At the end of each exposure, this overscan region was fitted with a low order polynomial as a function of row number, and this function was subtracted from each row of the exposed image.

The second step, and only step that really affects modern CCDS, is to generate a master bias frame from a series of 0 s exposures. The median of these 0 s exposures, called the master bias frame, then represents the underlying bias current which is present in any image taken by the CCD. Since modern CCDs

are very stable, with bias levels that are constant across observing runs, this master bias frame can be used to correct every image taken during a single night. As such, each science exposure has this median bias frame subtracted from it to remove the bias current.

2.2.2 Flat field Correction

In order to account for pixel-to-pixel variations in the CDD due to the detector and for "doughnuts" that might appear on images due to dust on filters or the dewar window, a series of flat field images are taken. A flat field image is an image of a source that is uniformly illuminated, such that an image of the source taken with the CCD will highlight the defects within the CCD, any "doughnuts" caused by dust, or vignetting (which is where images typically get fainter towards the edge of the CCD and is related to the shape of the mirrors/lenses used in the telescope). Typically, a flat field image will be taken during astronomical twilight, when the sky is illuminated by the sun, but it is not bright enough for the CCD to be saturated. Flat field images for each observational filter used must be taken, since the CCD response may vary between filters. A master flat for each filter is then generated by median combining the individual exposures together. The master flat field image is then normalised such that the average charge value throughout the image is 1. The science image is then divided by this normalised master flat to remove pixel-to-pixel variations. Fig. 2.2 shows a typical flat field taken using the CCD on the C2PU telescope in the V-band filter, and shows how vignetting affects the image.

2.3 Optical Spectroscopy

Along with the standard reduction applied to photometry images, optical spectroscopy require several additional steps before a spectrum is ready for analysis. Mainly, the raw spectrum has to be extracted, wavelength calibrated and flux calibrated. Reduction of optical spectra were carried out using the SPECRED package within IRAF.

Figure 2.2: Flat field image taken from the C2PU telescope, which shows how vignetting affects the image.

2.3.1 Spectral Extraction

The first step in reducing any spectra is to convert from the raw 2 dimensional spectrum recorded on the CCD to a 1 dimensional spectrum. The gratings used in taking optical spectra disperse the light from a star across the CCD, so there are 2 important directions when talking about raw spectra - the dispersion direction and the slit direction. The dispersion direction is the direction that light is split into after passing through a grating, while the slit (or spatial) direction is perpendicular to the dispersion direction. The dispersion direction will be converted to wavelength in future steps, while the second dimension, across the slit direction, is summed across to give the flux along the dispersion direction.

After bias subtraction and flat fielding, the raw spectrum must be extracted from the CCD image by tracing the spectrum across this dispersion direction, which is typically across the columns of the CCD (see Fig. 2.3 for an example of the dispersed spectrum of CSS120422:J111127+571239 taken using the MODS (Multi-Object Double Spectrograph) instrument on the Large Binocular Telescope). The task APALL was used to trace the spectrum across the dispersion direction, and extract the spectrum across the aperture by summing the flux within the aperture across the slit direction. A background spectrum is extracted by calculating the median flux across the slit direction for an

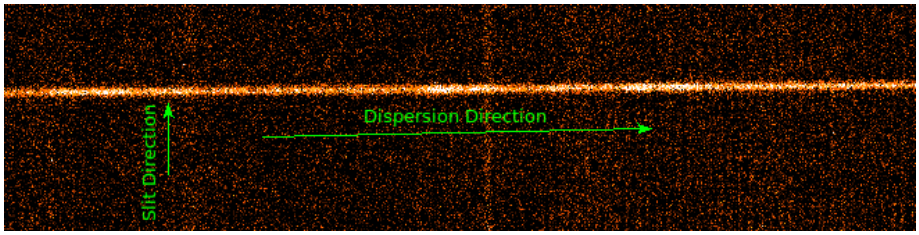

Figure 2.3: The raw 2-d spectrum of CSS120422:J111127+571239 taken using the MODS instrument on the Large Binocular Telescope, showing the dispersion direction and the slit direction.

aperture running parallel to the aperture used for the object spectrum, and the resulting background spectrum is then subtracted from the object spectrum.

2.3.2 Wavelength Calibration

The next step in calibrating any spectra is to wavelength calibrate the extracted spectrum. Wavelength calibration gives a relation between the pixel number in the dispersion direction and the wavelength of the spectrum. Wavelength calibration is done by taking exposures of arclamps which contain gases that emit at known wavelengths. A raw spectrum is then extracted of the arclamp exposure using the same aperture used to extract the object spectrum. The arclamp spectrum is then analysed using IDENTIFY, which allows for identification of the lines in the extracted spectrum and produces a solution between pixel number and wavelength. This solution is then applied to each science exposure using DISPCOR.

Arclamp exposures should be taken before and after every science exposure. This is to account for the fact that the wavelength solution for the data is likely to change over the course of the night due to changes in the telescope and instrument temperatures, or changes in the air pressure above the telescope, which will affect how the grating disperses the light from the object. However, this can be quite time consuming, and is normally only done if velocity resolutions of less than a few km s^{-1} are required in the extracted spectra. Otherwise, arclamps from the beginning and end of the night should suffice, unless observing conditions vary dramatically over the course of the night.

2.3.3 Flux Calibration

The final step in calibrating spectra is to convert the flux from electron charge s^{-1} $Å^{-1}$ to the more physical units of erg cm^{-2} s^{-1} $Å^{-1}$. This is done by taking spectra of stars that have a known, flux calibrated spectra. These flux calibration exposures are extracted and wavelength calibrated in the same way as the science exposures. Finally, the flux calibration exposures are compared to their known spectra using STANDARD and SENSFUNC, which gives a flux calibration for the science exposures. This calibration is then applied to the science exposures using CALIBRATE.

2.4 *Hubble Space Telescope* Cosmic Origins Spectrograph Data

The Cosmic Origins Spectrograph (COS; Green et al. 2012) onboard the *Hubble Space Telescope* (HST) is a spectrograph designed to work in the near (1700-3200 Å) to far (1150-2050 Å) ultraviolet. It was installed on the HST during STS-125 in May 2009.

Data reduction of COS data is carried out by the CALCOS pipeline, which was developed by the Space Telescope Science Institute (STScI). The pipeline performs the above reduction for spectra (bias correcton, flat fielding, extraction, and wavelength and flux calibration) along with various other tasks associated with taking data from space such as correcting for temperature fluctuations over the spacecraft, removing bad data, and correcting the exposure times to the time at the barycentre (centre of mass) of the solar system. The full list of the steps carried out by CALCOS can be found in the COS Data Handbook (Fox & et al., 2015). The output files of the pipeline are available at the Mikulski Archive for Space Telescopes (MAST)[†]. The output files are basic FITS files, and containing both spectral and timing information for the observations.

[†]`https://archive.stsci.edu/`

2.5 *Kepler* Data

During the initial *Kepler* mission, the *Kepler Space Telescope* (Howell et al., 2014) pointed at a single field on the sky, centred on 19h 22m 40s (right ascension), +44 30' 00" (declination). The spacecraft was supposed to continue observing this single field for the duration of the mission, until the telescope failed or ran out of fuel (predicted to happen in 2019). No oppurtunities were given to observe targets which did not lie in the field of view of the telescope when centred on this field. However, in 2013, a second reaction wheel failed, and the spacecraft could no longer keep itself pointing at its original field. *Kepler* was re-purposed such that the radiation pressure exerted by the Sun on *Kepler* could act as a temporary fly wheel, balancing the spacecraft long enough to allow it to observe areas of the ecliptic for a period of 3 months at a time with a level of precision close to the original *Kepler* mission (see Fig. 2.4 for a diagram of how this works). This mission has been called *K2*. This mission varies from the original mission in that it provides an opportunity to investigate objects which are located around the ecliptic using the high precision photometry instruments on-board *Kepler*, as opposed to just objects which were located in the original field, but for a significantly shorter time period of time (the *K2* mission views different fields for periods of 3 months at a time, while the initial *Kepler* mission observed the original field uninterrupted for 4 years). One of the objects observed during the *K2* mission which was not in the original field for the initial *Kepler* mission was an intermediate polar, with a cadence of 1 min over 69 days. These observations will be discussed in Chapter 5.

The photometry instrument on *Kepler* is composed of 42 individual CCDs, and each CCD has 2200×1024 pixels (Koch et al., 2004). Due to the size of a full frame image from *Kepler* and the bandwidth between Earth and the spacecraft, the entirety of the field of view is never downloaded. Instead, objects that fall onto *Kepler's* instrument are chosen prior to the beginning of any *K2* observation, and the pixels surrounding that object are downloaded. Observations can be requested at 2 different cadences - either long cadence (29.4 min) or short cadence (58.89 s).

Once the observation of a field has concluded, the data for an object is released as a Target Pixel File (TPF). This TPF is then analysed using the PYKE software package (Still & Barclay, 2012) for IRAF. The TPF is a table where

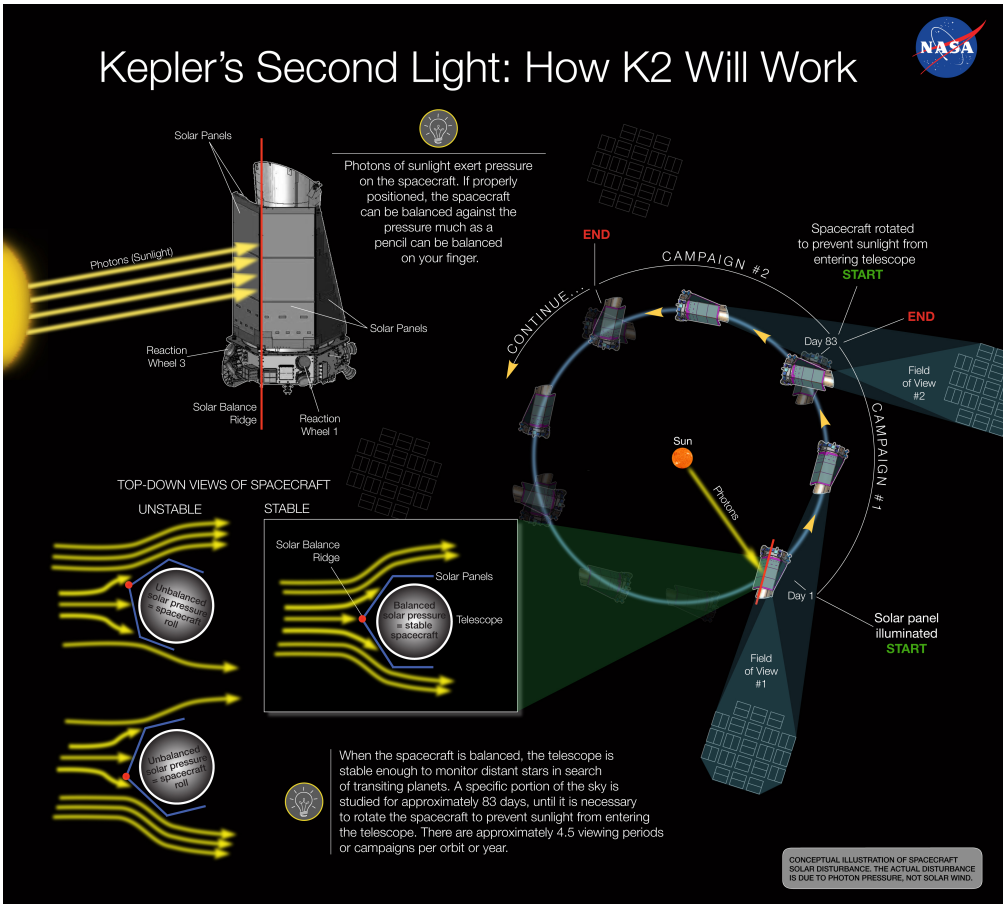

Figure 2.4: How the *K2* mission uses photon pressure from the Sun to temporarily balance the spacecraft. **Image Credit: NASA Ames/W Stenzel**

each row contains a timestamp, photometric measurements and data quality flags for each pixel in the TPF. The task KEPPIXSERIES is used to plot the flux versus time for each pixel in a TPF. Fig. 2.5 shows an example of the result of running KEPPIXSERIES on the TPF for FO Aquarii, which is the subject of Chapter 5. This plot is used to estimate where the object was on the CCD during the observation. For FO Aquarii, it is clear from Fig. 2.5 that the star occupied the central pixels.

The next step in creating a light curve from the *Kepler* data is to create a mask using KEPMASK defined such that data inside of the mask will be used to construct a light curve, while data outside the mask can be ignored. For FO Aquarii, this was a simple task, since the star had minimal drift across the CCD during the 3 month exposure, and no source is close by to contaminate the pixels. Fig. 2.6 shows the mask defined around FO Aquarii. This mask was then passed to KEPEXTRACT which extracted the events inside of the mask and generated a 1 dimensional light curve for the entire 3 month exposure. A mask

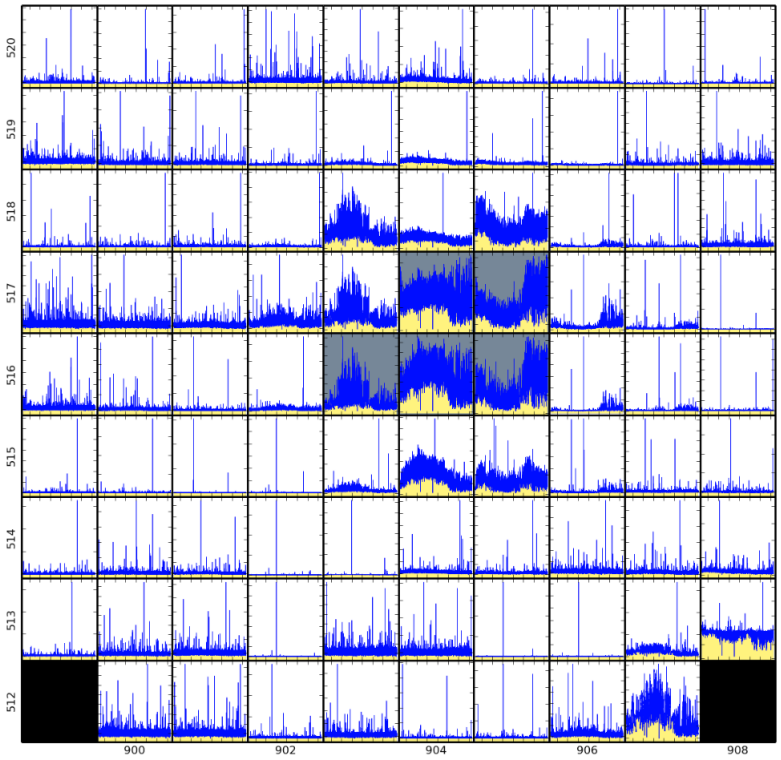

Figure 2.5: The result of running KEPPIXSERIES on the TPF from the *Kepler K2* observation of FO Aquarii. Each plot is a single pixel on the *Kepler* CCD, and each plot is a plot of the flux in that pixel over the course of the 3 month observation. The pixels with the brightest flux in the centre of the frame (x coordinate 903-906 and y coordinate 515-519) are FO Aquarii. The grey pixels are the automatical aperture chosen by the PYKE software.

was also placed over the top left of the CCD to generate a background light curve, which was subtracted from the light curve of FO Aquarii.

2.6 X-ray Data

Data from three different X-ray telescopes, *Swift*, *Chandra* and *XMM-Newton*, are presented throughout this thesis. In the following, we discuss the general steps for reducing any X-ray data. The actual reduction were carried out using CIAO 4.8.1 (Fruscione et al., 2006) and CALDB 4.7.2 for *Chandra* observations and using the SCIENCE ANALYSIS SOFTWARE (SAS v15.0.0/16.0.0; ESA: XMM-Newton SOC 2014) for *XMM-Newton* observations. Only the pipeline reduced data are used from the *Swift* observations.

The reduction of X-ray data is different to optical data reduction. Due to the low count rates from most sources, there exists a direct linear relation between

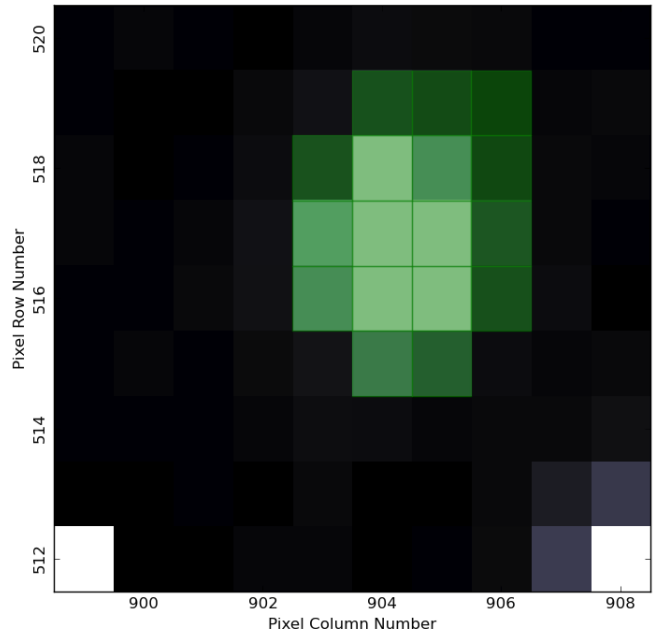

Figure 2.6: The mask defined for FO Aquarii using KEPMASK. Events recorded on the pixels highlighted green were extracted and used to make the light curve for FO Aquarii. The intensities represent the count rate per pixel over the median of 1000 exposures. FO Aqr is covered by the mask.

the number of free electrons in a pixel on the CCD and the energy of the incident photon. As long as the CCD is read out after only a single photon has hit the CCD, then the energy of the incident photon can be calculated for calibrated instruments (this differs to optical data since it is nearly always likely that mulitple photons struck a single pixel during the exposure). Situations do occur when a source is X-ray bright and there is a chance of multiple X-rays striking the CCD before the CCD can be readout. This is called pile-up, and is mitigated by inserting filters into the telescope to reduce the flux coming from the object, or by reducing the readout time of the CCD by reading out fewer pixels from the CCD (this is called windowing).

2.6.1 Event Patterns/Grades

Whenever an event is recorded on an X-ray CCD, it is given a pattern (these are called grades for events recorded by *Chandra*). The pattern is calculated by considering the pixel on which the event was recorded, along with the surrounding 3×3 or 5×5 pixel regions. Fig. 2.7 shows how the numbers assigned to the pixels in the 3×3 pixel range defined for the Advanced CCD Imaging Spectrometer (ACIS) onboard *Chandra* which are then used to

32	64	128
8	0	16
1	2	4

Figure 2.7: An example of how the 3×3 pixels surrounding an event are assigned numbers, such that a unique grade can be assigned to every event.

calculate the grade for individual events. For example, a photon which strikes and raises the threshold energy of only the centre pixel will have a grade of 0. However, if a photon comes in and strikes two pixels, raising the threshold of both above the threshold required to register an event in both pixels, then the grade will be the sum of the numbers in the two pixels triggered (for example, triggering the centre and left-centre pixels gives a grade of $0 + 8 = 8$, while triggering the centre and right-centre pixels gives a grade of $0 + 16 = 16$. Triggering 3 pixels gives a grade of the three pixels numbers summed together (e.g. $1 + 8 + 0 = 9$ would be left-bottom, left-centre and and centre pixels, while $0 + 64 + 128 = 192$ would be centre, centre-top and right-top pixels triggered).

XMM-Newton assigns patterns rather than grades, and patterns only range from 0-12. Typically, only events that have a pattern $<$4 are used in spectral analysis, as these events are registered over a maximum of 2 pixels, and their energy reconstruction is reliable.

2.6.2 Soft Proton Flaring

The first part of any X-ray data reduction is to check for times of high background. The most common cause of a high background are soft proton flares, which is when XMM-Newton passes through clouds of soft protons which are trapped in the upper parts of the Earths magnetosphere (Fioretti et al., 2016). The amount of soft proton flaring in any observation is dependant on the altitude of the satellite, the satellites position with respect to the magnetosphere, and the amount of solar activity during the observations.

The EPIC-pn instrument onboard *XMM-Newton* is particularly susceptible to times during which soft proton flares occur. These soft protons typically have energies $< 100keV$ and are funnelled towards the CCD detectors by the X-ray

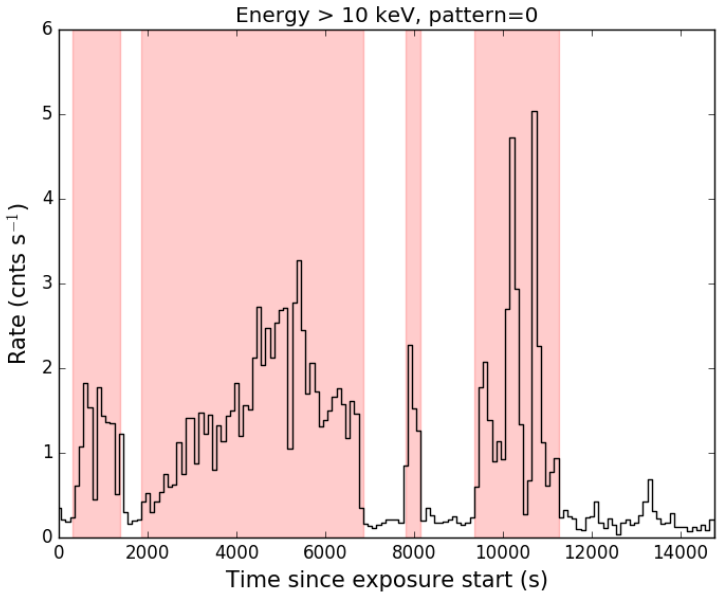

Figure 2.8: An example of the soft proton flaring that can affect the background in the EPIC-pn instrument. Times highlighted in red are times of high flaring, and must be excluded when performing spectral analysis on faint sources.

mirrors. When checking an X-ray exposure for background flaring, a light curve is made using all of the events recorded in the frame which have an energy $> 10keV$ and a pattern of 0. Fig. 2.8 shows an example of a light curve that suffers from large amounts of soft-proton flaring (a sustained period where the flux is > 0.5 counts s^{-1}). When generating any X-ray spectra using data from this observation set, if the source has a low count rate, then data recorded during these time periods must be ignored. Soft proton flaring is less important when dealing with bright sources that overpower the background. Regardless, it is good practice to always check how much flaring occurred during an observation.

2.6.3 Extraction

After periods of soft proton flaring have been removed from the data, extraction of time series and spectra can be accomplished by extracting event information from the pixels that are relevant to any object. This is done defining annuli that cover both the source region and a background region, extracting events which have (for *XMM-Newton*) a pattern $<$4 and lie within the specified energy range. Light curves are then created by subtracting the background light curve from the source light curve. Creating spectra also

requires building an Ancillary Region File (ARF) and Photon Redistribution Matrix File (RMF). Both of these files are used to calibrate the instrument reponse, making sure the count rates produced in the spectrum are accurate.

2.6.4 Pile-up

If 2 or more X-ray photons arrive at the same pixel before the CCD can be read-out, then both events can be registered as a single, higher energy event instead of 2 lower energy events. This problem, called detector pile-up, is only important for high luminosity X-ray sources, where the probability of 2 X-ray photons arriving around the same time is high. Detector pile-up can be mitigated in a few ways, all based on simulations of observations before the observations take place. Mainly, if a source is expected to be X-ray bright, then there are 3 strategies for mitigating pile-up during an observation. The first is to place a filter above the CCDs, which will reduce the photon flux at the detectors. The second is to window the read-out region of the CCD, which decreases the read-time, allowing for faster time resolution. The final solution is to take the observations in continous clocking (CC) mode. In CC mode, the image on a detector is collapsed into a 1-D strip, which allows for reading out of the CCD nearly instantaneously, but at the sacrifice of any spatial information.

In this thesis, pile-up only had to be mitigated for 2 observations, both of them of FO Aquarii. The *XMM-Newton* observations of FO Aquarii were windowed and had a medium filter inserted to both reduce the flux at the detector and reduce the read-out time, while the *Chandra* observations were performed in CC mode to mitigate pile-up.

3

The new eclipsing CV MASTER OTJ192328.22+612413.5 - a possible SW Sextantis Star

[†]**We present optical photometry and spectroscopy of the new eclipsing Cataclysmic Variable MASTER OTJ192328.22+612413.5, discovered by the MASTER team. We find the orbital period to be** $P = 0.16764612(5)$ **day /**$4.023507(1)$ **hour. The depth of the eclipse (**2.9 ± 0.1 **mag) suggests that the system is nearly edge on, and modelling of the system confirms the inclination to be between** $81.3 - 83.6°$**. The brightness outside of eclipse varies between observations, with a change of** 1.6 ± 0.1 **mag. Spectroscopy reveals double-peaked Balmer emission lines. By using spectral features matching a late M-type companion, we bound the distance to be** $d = 520 \pm 80$ **parsec if the companion is an M5 star, or** $d = 900 \pm 100$ **parsec if the companion is an M4 star.** The source displays 2 mag brightness changes on timescales of days. The amplitude of these changes, along with the spectrum at the faint state, suggest the system is possibly a dwarf nova. The lack of any high excitation HeII lines suggests this system is not magnetically dominated. The light curve in both quiescence and outburst resembles that of Lanning 386, implying MASTER OTJ192328.22+612413.5 is a possible cross between a dwarf nova and a SW Sextantis star.

[†]Published in The Astronomical Journal "The new eclipsing CV MASTER OTJ192328.22+612413.5— a possible SW Sextantis star" Kennedy, M. R., Callanan, P., Garnavich, P. M., Szkody, P., Bouanane, S., Rose, B. M., Bendjoya, P., Abe, L., Rivet, J.-P. Suarez, O., 2016, *AJ*, 152, 27

3.1 Introduction

MASTER OTJ192328.22+612413.5 (hereafter referred to as J1923), the subject of this chapter, was initially discovered by the MASTER-Tunka auto-detection system in April 2014 (Balanutsa et al., ATel 6097). The unfiltered magnitude of J1923 was observed to be 19.2 in 2010, but had brightened to an unfiltered magnitude of 17.5 on April 20, 2014 and 17.7 on April 22nd, 2014. It was classified as a CV due to its 2 magnitude difference with respect to reference images. There is also a UV counterpart to J1923, *Galex* J192328.3+612413, which has a FUV magnitude of 19.42 ± 0.15 and NUV of 19.68 ± 0.10, obtained on June 1, 2007. J1923 was also detected in the infared as WISE J192328.25+612413.1. The ALLWISE Source Catalog lists magnitudes of $W1 = 16.58 \pm 0.05$ and $W2 = 16.6 \pm 0.1$ for J192328.25+612413.1. It was also suggested that J1923 might be a magnetically dominated CV, or polar, due to its proximity to the ROSAT x-ray source 1 RXS J192333.2+612507, which has a large error circle of 14".

Lanning 386 is an eclipsing CV with a period of 3.94 hours which defies easy classification (Brady et al., 2008). The system displays recurring outbursts with an amplitude of $\Delta m \approx 2$, but is at quiescence most of the time. This would lead Lanning 386 to be classified as a dwarf nova. The spectrum of Lanning 386 in quiescence is consistent with this classification, but the spectrum in outburst tells another story. The spectrum in quiescence shows single-peaked Balmer emission lines, and in outburst displays strong He I and He II lines, and the strong excitation C IV line, consistent with a SW Sextantis star (Groot, 2000). However, in quiescence and outburst, Lanning 386 does not show the emission line radial velocity phase lag expected of the SW Sextantis stars (Brady et al., 2008). Also of interest is the recurrence time of the outbursts, which is only a few days. Other scenarios have been considered, such as Lanning 386 being a VY Scl system (which are nova-like, non-magnetic or weakly magnetic CVs that exhibit low states on a recurrence time of years; Leach et al. 1999) or even an IP, but again, Lanning 386 only shares some of the characteristic features of these classes, never all. Its true classification still remains a mystery, but is currently best described as a dwarf nova in quiescence and a SW Sextantis star in outburst.

In this chapter, we present photometry and spectroscopy of the newly discovered CV J1923, and use the data to obtain a period for the system and

classify its CV type, which is similar to Lanning 386. We also estimate the inclination of the system based on analysis of the depth of the eclipse. Finally, we present a distance estimate using constraints on the companion spectral type.

3.2 Observations

3.2.1 Photometry

Photometry of J1923 was taken in the SDSS g band using the 1.8m Vatican Advanced Technology Telescope (VATT) located at Mount Graham International Observatory over 4 consecutive nights, starting April 29 2014 (UT). Fig.řeffindingchart shows an unfiltered image of J1923. The images were taken using the VATT4K CCD with a typical exposure time of 30s. A total of 880 images were taken over these 4 nights. There were deep eclipses visible in the data from the 3rd and 4th nights of the run. On the 1st night, there was an eclipse that was not well determined due to the onset of twilight.

A single night of V band photometry was acquired at the VATT on the night of June 28 2014 (UT). A total of 518 images were taken with a typical exposure time of 15s. There was a clear eclipse visible in these data.

Data were also acquired from the dual 1m telescopes C2PU facility at the Calern Observatory (Observatoire de la Côte d'Azur, France) in the second half of August 2014. A total of two hundred and forty five 40s exposures with no filter, one hundred 60s exposures with no filter, and eighty three near-simultaneous 60s exposures using V and R filters were obtained. There were eclipses visible in all of these data sets.

All the details of the observations are given in Table. 3.1.

3.2.2 Spectroscopy

Spectroscopy of J1923 was taken using the Dual Imaging Spectrograph (DIS) on the 3.5m ARC telescope at Apache Point Observatory on the night of June 21 2014 (UT). The blue channel used the B1200 grating, which has a pixel scale of 0.62 Å/pix, while the red channel used the R1200 grating, which has a pixel scale of 0.58 Å/pix. A total of five 900s long exposures were obtained on

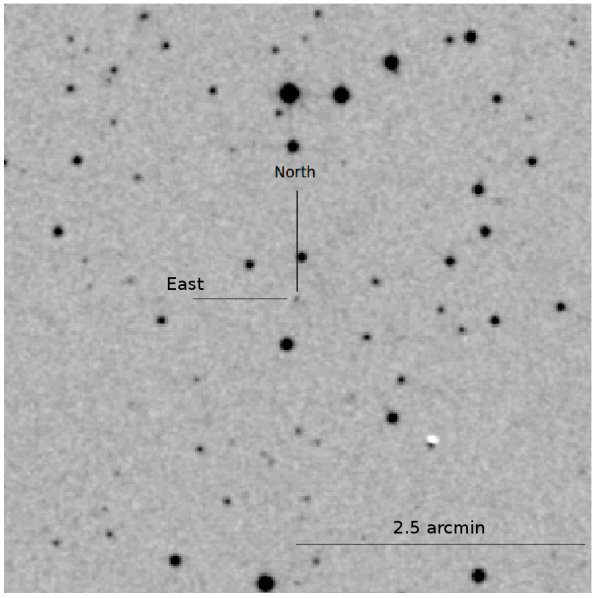

Figure 3.1: Finding chart for J1923 +6124, taken from the STScI Digitized Sky Survey. The photometry was calibrated using the bright star just to the south of J1923, which has a g band magnitude of 15.64, V band magnitude of 15.19 and R band magnitude of 15.13.

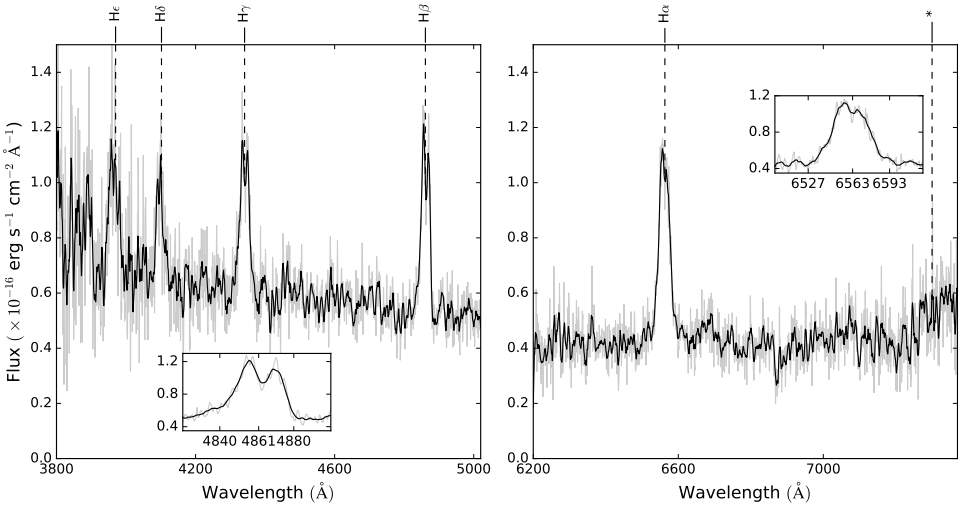

Figure 3.2: Average spectrum of J1923 in quiescence. The left panel shows the blue spectrum while the right panel shows the red spectrum. The spectra have been boxcar smoothed with a width of 6 Å. The grey spectrum is the unsmoothed data. The most prominent emission features are marked. The inset on the left shows the double-peaked Hβ line, while the right inset shows the double peaked Hα line. There is a clear rise towards the red in the spectrum on the right which is marked with a *, which matches a late M type star. Analysis of the lines can be seen in Table 3.2.

Table 3.1: Summary of Observations

Frame in Fig. 3.3	Date Observed 2014	Filter	State	Eclipse Number	Mid-eclipse Time (HJD-2,450,000.0)	Uncertainty (day)
a)	April 28th	SDSS-g	Low	-11	6776.992	0.001
b)	April 29th	SDSS-g	Low	N/A		
c)	April 30th	SDSS-g	High	0	6778.83667	0.00009
d)	May 1st	SDSS-g	High	6	6779.84257	0.00004
e)	June 27th	V	High	346	6836.84301	0.00004
f)	August 19th	Clear	High	660	6889.48331	0.00001
g)	August 25th	Clear	Low	696	6895.51890	0.00004
h)	August 27th	V/R	Low	708	6897.53010	0.00007

the blue and red channels. The first 3 spectra were obtained at an airmass greater than 1.4, while the final 2 spectra were taken later in the night, at an airmass of 1.2.

Fig. 3.2 shows the average spectrum for J1923, with variations due to the orbital motion of the system unaccounted for. The average spectrum shows distinct double-peaked emission lines, corresponding to Hα, Hβ and Hγ lines, along with a rise towards the red end of the spectrum. The flux of J1923 in the V band section of the spectrum in Fig. 3.2 is $\approx 0.45 \times 10^{-16}$ erg cm^{-2} s^{-1} Å^{-1}. This corresponds to a V band magnitude of 19.8, which is the magnitude of J1923 in the low state.

3.3 Results

The light curves for each night after standard photometric calibration can be seen in Fig. 3.3. All data reduction and photometry was done using standard IRAF* tasks. Photometry was carried out on J1923 using the PHOT command from the DIGIPHOT package, and the images were calibrated using nearby stars from the SDSS catalogue.

3.3.1 Period and Ephemeris

The period of the system was found by applying a Phase Dispersion Minimisation (PDM; Stellingwerf 1978) to the photometric data, which were first normalized to have a common non-eclipse magnitude. The period range was set to between 0.15 and 0.2 day. The resulting theta plot can be seen in

*IRAF is distributed by the National Optical Astronomy Observatory, which is operated by the Association of Universities for Research in Astronomy (AURA) under cooperative agreement with the National Science Foundation

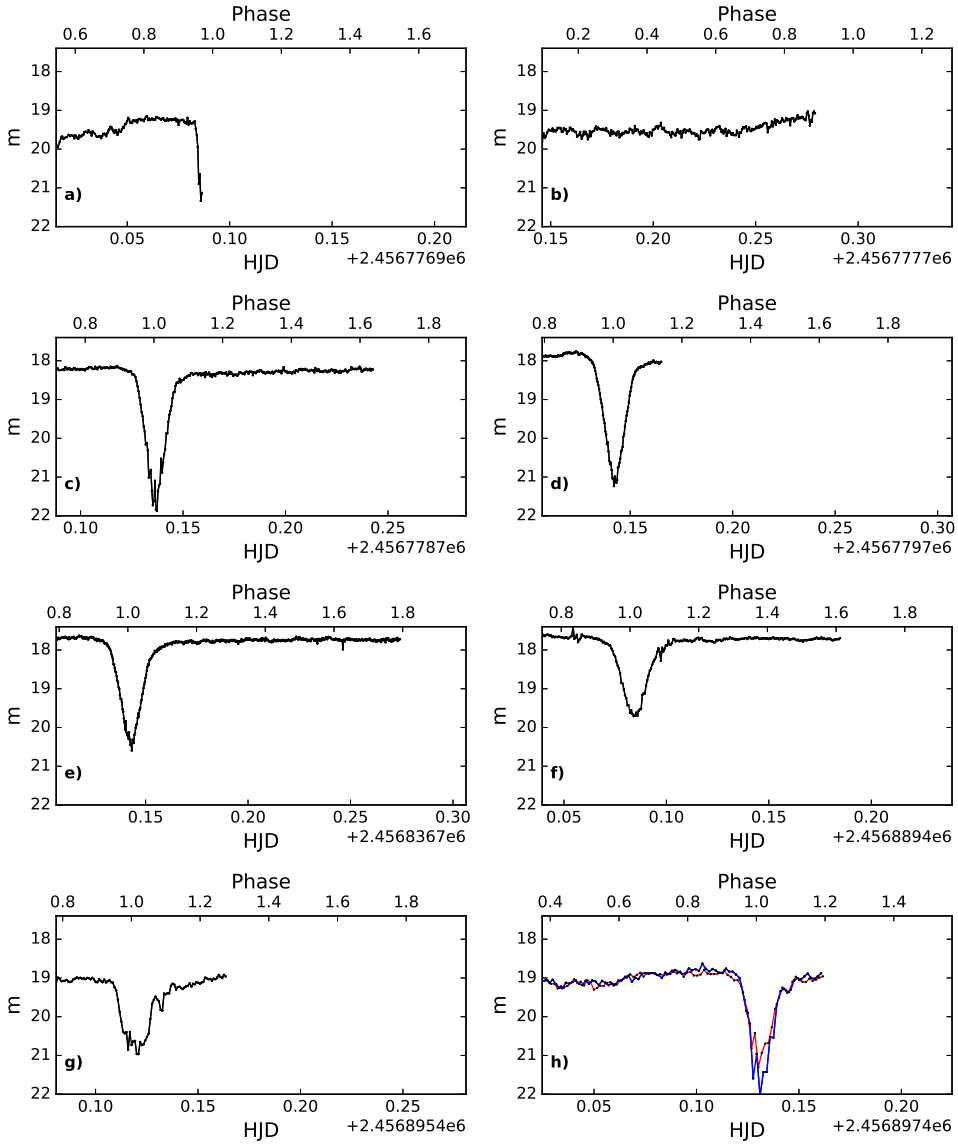

Figure 3.3: The light curve of J1923. Frames a), b), c) and d) were taken on sequential nights in the SDSS-g band. Frames a) and b) show the light curve in quiescence, with the hump from the hot (bright) spot visible in frame a) and b) and the QPOs visible in frame b). The system went into outburst between frames b) and c), with the brightness of the system again increasing between frames c) and d). Frame e) was taken 2 months later, at the end of June 2014, in the V band with a typical exposure time of 15s. Frame f) was taken 2 months later again, at the end of August 2014, without a filter, and with a typical exposure time of 40s. Frame g) was also taken in August, with no filter and a typical exposure time of 60s as the system was in quiescence. Frame h) shows the simultaneous V and R filter data taken in August, with a typical exposure time of 60s. The V band data are displayed in blue, and the R band data are in red.

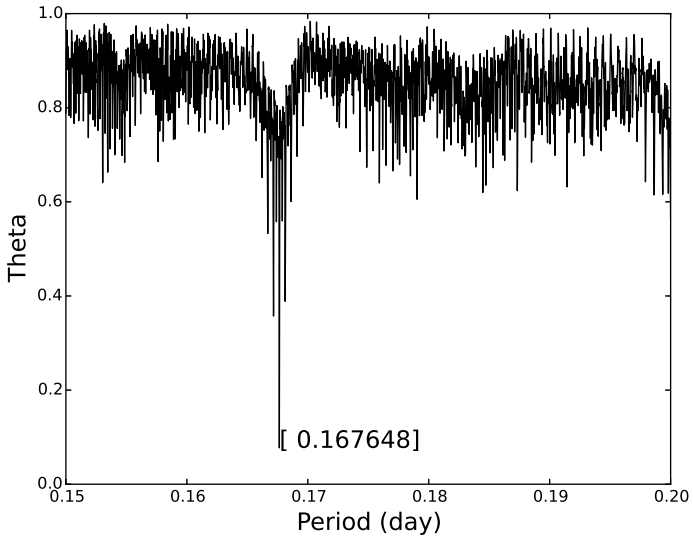

Figure 3.4: PDM of the light curve of J1923. The deepest minimum occurs at $P = 0.16765 \pm 0.00004$ day.

Fig. 3.4. The best fit period is 0.16765 ± 0.00004 day, with the error being the width of this peak. The periods on either side of the deepest trough were tested, and were found to give poor fits.

The time of the midpoint of each observed eclipse was found by fitting a Gaussian to the eclipse profiles (see Fig. 3.5 for an example) and using the centre of the Gaussian as the time of mid-eclipse, with the error in the time being the error in fitting the centre of the Gaussian. While the Gaussian does not fit the ingress and egress of the eclipse perfectly (which is related to the hot spot, WD and accretion disc contributing to the eclipse) the sides of the eclipse are fit well, suggesting this method provides an accurate value for the time of mid-eclipse.

These times and the associated eclipse numbers can be seen in Table 3.1, where the eclipse number was found by taking the 3rd night's eclipse as 0, and using the newly discovered period to find the remaining eclipse numbers relative to this night. The first nights eclipse has a much higher error than other nights as the eclipse was only partially observed. For this night, a model eclipse was constructed using a Gaussian, and the midpoint adjusted manually to see where the Gaussian matched the beginning of the eclipse.

A linear fit was applied to the data, and the resulting ephemeris was

$$T_{mid}(HJD) = 2456778.83690(3) + 0.16764612(5)E \tag{3.1}$$

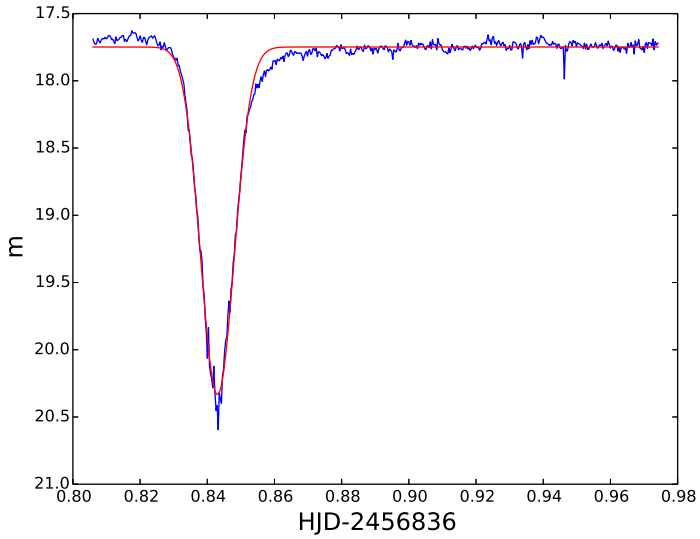

Figure 3.5: The eclipses were modelled using a gaussian function to accurately determine the time of mid-eclipse. Above is a single nights data from the VATT from June 2014, with the red line representing the best Gaussian fit.

The phased light curve using the linear ephemeris can be seen in Fig. 3.6.

3.3.2 Light curve Morphology

The first 2 nights of observations show a light curve with a pre-eclipse hump starting at phase 0.7, along with quasi-periodic oscillations (QPOs) just after the eclipse. The data were masked to remove the eclipses, and then each night of data was subjected to a Lomb-Scargle Periodogram (Lomb 1976; Scargle 1982). The power spectrum for each night were then multiplied together to reduce the power of the noise peaks while maintaining power in the peaks common to each data set. The resulting power spectrum can be seen in the lower half of Fig. 3.7. There are several strong peaks around a frequency of $\sim$3.3 hour^{-1} ($P_{QPO} \sim 20$ minute). The top panel of Fig. 3.7 shows a sine wave with a period of 21 minute plotted on top of the data from 2014 April 29, when the system was in its low state and the QPOs were most prominent. The broad power spectrum confirms these oscillations are not coherent and cannot be solely due to the spin of the central WD. Kilosecond QPOs have been seen in SW Sextantis stars before, and are thought to arise from magnetic white dwarfs that are drowned by a high accretion rate (Patterson et al., 2002).

The light curve also shows 2 distinct states. The quiescent state has a

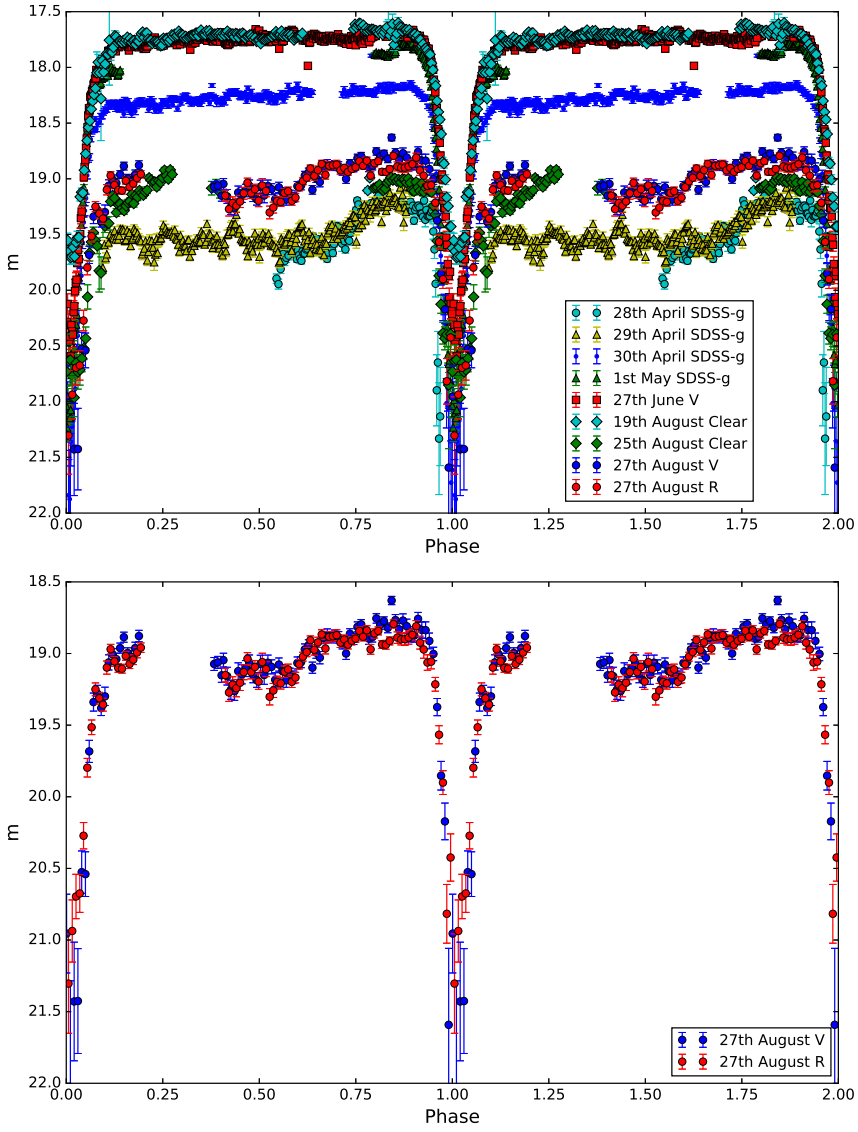

Figure 3.6: The top panel shows the phased light curve for J1923 for all 8 nights data using the linear ephemeris. The bottom panel shows just the simultaneous R and V band data taken in August, 2014

non-eclipse magnitude of 19.5 in the g band from the first 2 nights (frames a and b of Fig. 3.3), and the pre-eclipse hump and QPOs are distinct. The system had an out-of-eclipse magnitude that gradually decreased from night to night as the system went into outburst. On the first night of outburst (frame c), the average magnitude was 18.2, while on the second night of outburst, the system had brightened again to $m < 18$. The depth of the eclipse in outburst, which was well covered by observations, was $\Delta m = 3.2 \pm 0.1$ mag as seen in the g band and $\Delta m = 2.9 \pm 0.1$ in the V band.

The eclipse width was found by fitting a Gaussian to the V-band data, after

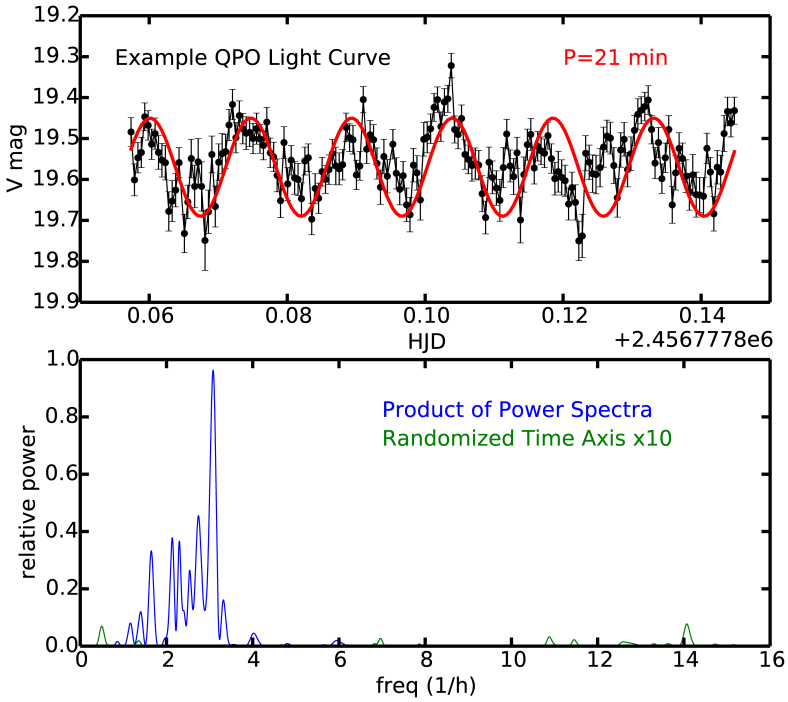

Figure 3.7: The bottom panel shows the power spectrum of the data with the eclipses masked, in order to look for the period of the QPOs. The blue shows the power spectrum of the normal data, while the green shows the power spectrum of the data after it had been randomised, to make sure the peaks in the original power spectrum were not due to noise. The top panel shows a sine wave with a frequency of 3.32 h^{-1} plotted alongside the data from 2014 April 29, when the system was in its low state and had the most prominent QPOs.

conversion from magnitude to flux. The resulting fit gave an eclipse width (FWHM) of 0.081 ± 0.001 in phase.

3.3.3 Emission Spectrum

By using the calculated ephemeris, we found the phase of each of the spectra obtained: 0.81, 0.87, 0.21, 0.29 and 0.35. The rise towards the red end of the spectrum is thought to be molecular bands visible from the companion star that match that of a late M type star, similar to the companion of Lanning 386 (Brady et al., 2008). This is further discussed in Section 3.4.2. The equivalent width (EW) of the Hα, Hβ and Hγ lines can be seen in Table 3.2, along with the Balmer decrement.

The full width at zero intensity (FWZI) of the Hα, Hβ and Hγ was measured

Table 3.2: Properties of the emission lines seen in the average spectrum of J1923. *(a)The FWZIs are given as lower limits since the ability to determine the extension of the line wings is usually set by the signal-to-noise ratio in the data. (b) Measured using a Gaussian fit.*

Feature	E.W.	Flux	FWZI[a]	FWHM[b]	Balmer Decrement
	Å	10^{-17} erg cm^{-2} s^{-1}	km s^{-1}	km s^{-1}	
Hα	47	217	> 2800	1500	1.20
Hβ	35	181	> 3000	1700	1
Hγ	24	146	> 3800	2000	0.81

within IRAF, as were the peak-to-peak separations of the Hα, Hβ and Hγ lines, found by fitting a double Lorentzian to the line region. The fits gave separations of 16Å, 16Å , and 15Å , respectively. The asymmetry between the blue and red peaks could be due to the presence of the hotspot.

3.4 Discussion

3.4.1 Inclination and Mass Ratio of J1923

The depth of the eclipse was 3.2 ± 0.1 mag in the g band on night 3 and night 4 of the data and 2.9 ± 0.1 mag in the V band on night 5. The majority of CVs with an eclipse depth close to or larger than 2.5 mag have an inclination angle greater than 85° (Ritter & Kolb, 2003). Hence, the inclination of J1923 is expected to be $> 85°$, suggesting that J1923 is a nearly edge on disc system.

The Hα peak-to-peak separation of 16 Å corresponds to a velocity separation of 800 km s^{-1}. This would normally limit the inclination of the system to be $< 30^o$ (Horne & Marsh, 1986). However, such a deep eclipse is hard to explain with such a low inclination. Instead, it is possible that this low peak-to-peak separation is due to a truncation of the accretion disc far from the surface of the primary, which might be due to the presence of a strong magnetic field on the WD, or a low velocity component (spot or wind perpendicular to the disc or magnetic curtain) could fill-in the line center (Hoard et al., 2003).

The lower bounds on the FWZI of the lines in J1923 is smaller than the FWZI of some high inclination SW Sextantis systems (Dhillon et al., 2013), which are thought to contain magnetically truncated discs (Hoard et al., 2003). This supports the idea that the accretion disc in J1923 may be truncated due to the presence of a magnetic field.

Table 3.3: The best fit models computed using a χ^2 grid search with ELC for various mass ratios (q) and inner disc temperatures (T_d).

q	T_d(K)	i°	χ^2	χ^2_R
0.5	15000	81.4-83.2	2140	4.89
	16000	81.4-83.2	2118	4.85
	17000	81.8-83.6	2097	4.80
0.4	15000	81.4-82.8	2191	5.01
	16000	81.7-83.0	2165	4.95
	17000	81.9-83.6	2147	4.91
0.33	15000	81.8-82.8	2243	5.13
	16000	82.0-83.1	2213	5.06
	17000	82.3-83.4	2187	5.00
0.285	15000	81.3-83.0	2293	5.25
	16000	81.8-83.1	2259	5.17
	17000	82.1-83.5	2230	5.10
0.25	15000	81.5-82.9	2323	5.32
	16000	81.8-83.1	2290	5.24
	17000	82.2-83.6	2260	5.17

3.4.1.1 Modelling the quiescent light curve

The light curve in quiescence was modelled using the Eclipsing Light Curve Code (ELC; Orosz & Hauschildt 2000). The basic model consisted of a WD with a temperature of 32000K (see Section 3.4.2 for more), an inner accretion disc radius in the range of 1-13R_{WD}, a temperature gradient in the disc ($T(r) = T_i \left(\frac{r_i}{r}\right)^{\xi}$) of 0.75 (which assumes a “steady-state" disc), a hotspot with angular size in the range of 2-4° centred on orbital phase 0.86, and an inclination between 72-90°. We computed best fit models based on the χ^2 statistic using ELC for mass ratios (q=$\frac{M_{sec}}{M_{WD}}$) of 0.5, 0.4, 0.33, 0.285 and 0.25 and for inner disc temperatures (T_d) of 15000 K, 16000 K and 17000 K. Table 3.3 shows the best fit inclination and χ^2 for each model. The reduced χ^2_R are far above 1 for every model, which is related to the sinusoidal variations from the QPO visible in the light curve from orbital phase 0.1-0.6 which is not reproduced by our model.

The resulting V-band fit to the data can be seen in Fig. 3.8, which shows the best and worst fits of our modelling. The best fit inclination range over all models was very narrow, between 81.3° and 83.6°. A mass ratio of q=0.5 provides the best overall fit.

The ingress of the eclipse is never well fit by any of our models, with the observed ingress always steeper than any of our models. This is a result of the simple model ELC assumes for the hotspot. ELC simply increases the temperature of the accretion disc cells which correspond to the position of the

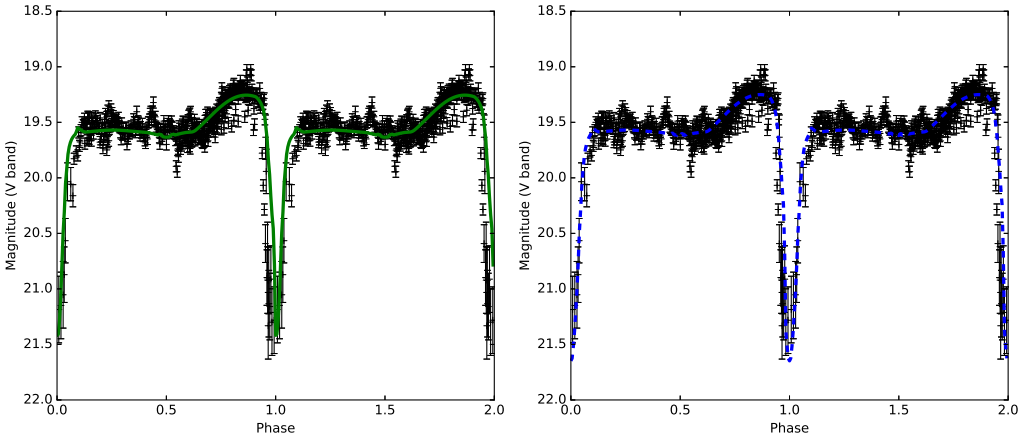

Figure 3.8: The best (blue, dashed, q=0.5, T_d=17000 K, i=83.1°, right panel) and worst (green, solid, q=0.25, T_d=15000 K, i=82.25°, left panel) model light curves generated by ELC plotted against the low state data of J1923 (black). The ingress of the eclipse is deeper in the data than in any of our models, and is possibly related to how ELC models hotspots.

hotspot, instead of making the hotspot an independent structure. As such, ELC is not able to include eclipsing of the accretion disc by a physical hotspot for high inclination systems, which, in reality, would steepen the ingress.

Fig. 3.9 shows a schematic of the system which shows the secondary star, accretion disc and accretion curtains (if the system is magnetic) for an inclination of $83°$. The truncation radius (the radius at which the magnetic field couples to the accretion disc) was taken to be $0.05a$, where a is the orbital separation of the system. This inner disc radius is based on observations of Lanning 386, which will be discussed in Chapter 4. The connection between J1923 and Lanning 386, and why their truncation radius should be similar, is made in Section 3.4.3. The small truncation radius, which leads to small accretion curtains, and high inclination may explain why the spin signal from the WD is not coherent, but only quasi-periodic. One could imagine if the edges of the disc were higher that the disc may occasionally obscure our views of the curtain, which would lead to the signal becoming quasi periodic.

3.4.2 Modelling the spectrum

We next modelled the *Galex* FUV and NUV fluxes, along with the optical spectrum, to constrain the temperature of the WD and the contribution of the secondary star. WD model atmospheres were generated using Hubeny's TLUSTY, SYNSPEC and ROTIN programs (Hubeny 1988; Hubeny & Lanz

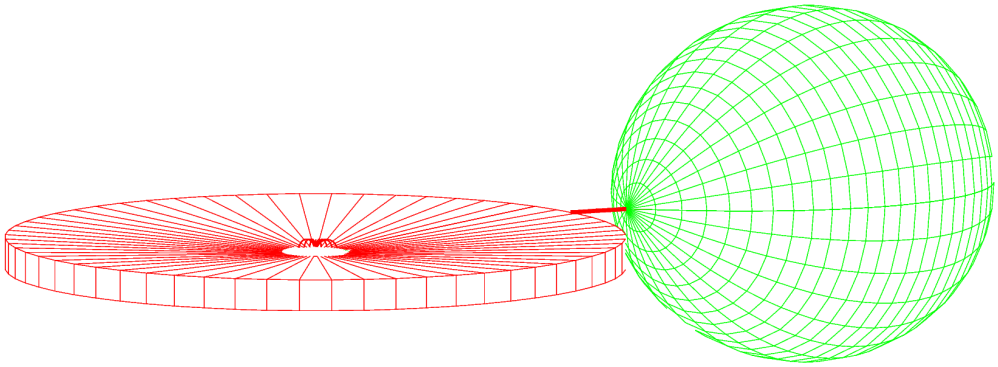

Figure 3.9: A schematic of J1923 which shows the secondary star (in green), accretion disc (in red) and accretion curtains (red lines coming out of the orbital plane close to the centre of the disc). This schematic assums J1923 is a magnetic system.

1995) for WD temperatures between 24-34000 K and with a log g of 8.

Schlafly & Finkbeiner (2011) estimated the reddening in the direction of J1923 to be $E(B-V) = 0.0471 \pm 0.0015$ mag. In the following, the spectrum has been de-reddened using this value and the Cardelli extinction function (Cardelli et al., 1989), implemented in the PYTHON module ASTROPYSICS.

Table 3.4 shows the results of our spectral fitting. The lowest temperature WD that provided an acceptable fit to the UV and the optical was a WD with a temperature of 24000 K and a minimum amount of disc contribution, along with a companion of spectral type M5V (the stellar spectrum was obtained from the MILES catalogue; Sanchez-Blazquez et al. 2006). This fit can be seen in Fig. 3.10.

The best fit model from Table 3.4 gives a WD temperature of 34000 K and an accretion disc with inner temperature of 15000 K. However, there is a degeneracy between all of our fits, which can be seen in the small change in the reduced χ^2 between all of the models. The only limit our modelling reveals is that the lowest temperature WD that fits our data is 24000 K, as cooler WDs cannot be fit with an accretion disc contribution.

The contribution of the secondary is similar throughout our models, with a flux between $(2 - 2.5) \times 10^{-16}$ erg s^{-1} cm^{-2} Å^{-1} at 5500Å.

The V-band magnitude of our M5V template is 20.7±0.3. This gives a V-W1 of 4.1±0.3, assuming that the WISE magnitudes were taken when J1923 was in

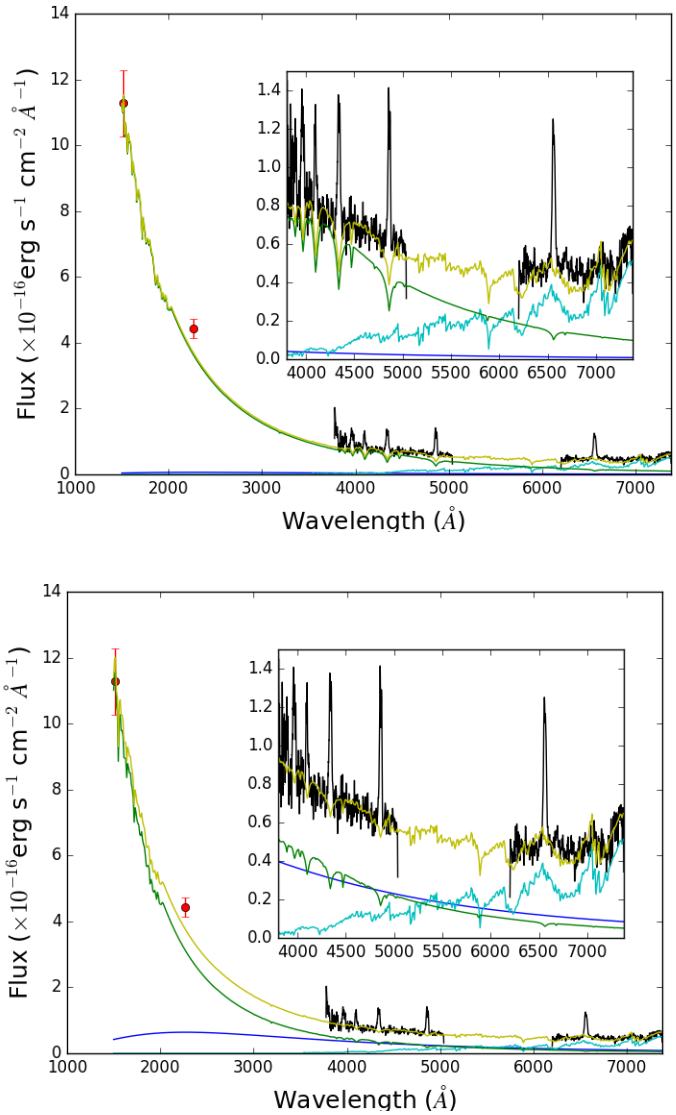

Figure 3.10: *Top:* The lowest WD temperature model spectrum fit to the *Galex* fluxes and optical spectrum. The green curve is a WD model with T=24,000 K and log g=8. The blue curve is an accretion disc with inner temperature of 15000 K and ξ=0.75. The cyan curve is the M5V spectrum from the MILES catalogue. The yellow is the sum of the three components. The inset is a zoom of the optical spectrum. *Bottom:* Requiring an equal contribution in optical flux between an accretion disc (with a maximum temperature of 15000K and a ξ=0.75, shown in blue) and a WD of temperature of T=34000 K gives a good fit to the spectrum, along with the same comparison star as in the top panel. A cooler WD allows for the WD to dominate in the optical, which is inconsistent with the results of the ELC modeling.

Table 3.4: The reduced χ^2 values for various fits to the optical spectrum and *Galex* fluxes of J1923

WD Temp (K)	T_d(K)	χ^2_R
24000	15000	1.15
	16000	1.15
	17000	1.16
26000	15000	1.13
	16000	1.14
	17000	1.14
28000	15000	1.12
	16000	1.12
	17000	1.13
30000	15000	1.10
	16000	1.11
	17000	1.12
32000	15000	1.09
	16000	1.10
	17000	1.11
34000	15000	1.09
	16000	1.10
	17000	1.10

quiescence. This is much higher than the V-W1 of 6.2 for an M5V star, but is closer to the V-W1 of 5.2 for an M4V star (Pecaut & Mamajek, 2013). Hence, we conclude the companion spectral type is M4-5. This spectral type is also in keeping with the results from Knigge et al. (2011), which shows that the expected spectral type for a CV with a period of 4 hours is a M4-M5. Furthermore, this spectral type is similar to the M5.5±0.5 companion of HS 0220+0603, another eclipsing SW Sextantis system with an orbital period between 3-4 hours (Rodríguez-Gil et al., 2015).

We use the V band magnitude of the companion in the model spectrum of 20.9±0.3, along with an absolute magnitude of 12.3 for an M5 star, to compute a distance to J1923 of $d = 520 \pm 80$ parsec. If the companion is a M4 star, then using an absolute magnitude of 11.2, the distance to J1923 is $d = 900 \pm 100$ parsec.

3.4.3 Similarity to Lanning 386

Fig. 3.11 shows a previously unpublished light curve of Lanning 386 in quiescence, taken in 2009 using the Galway Ultra Fast Imager (GUFI) on the VATT. The calibrated V-band magnitude of Lanning 386 outside of eclipse is 17.5 in quiescence. The similarities between the light curve for Lanning 386 and those presented here for J1923 are beyond coincidence. Both objects

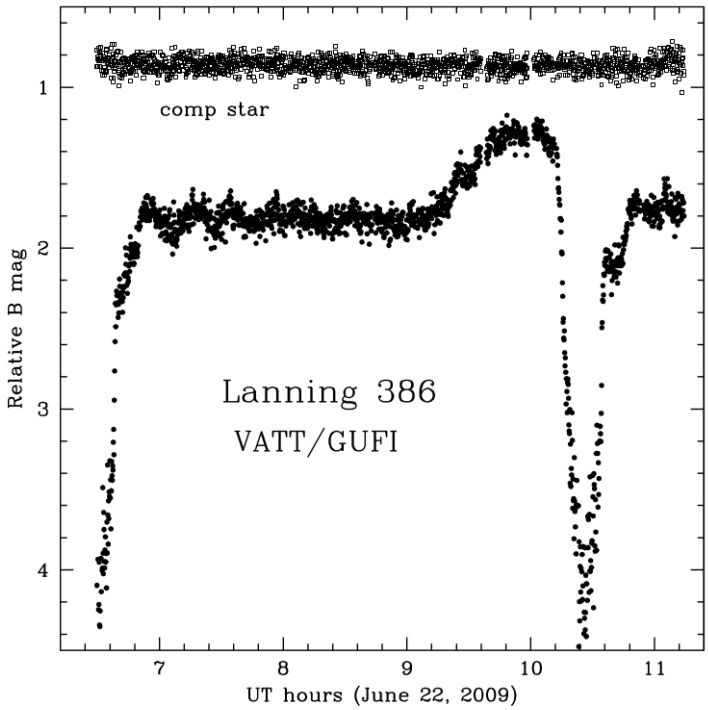

Figure 3.11: Previously unpublished VATT/GUFI light curve for Lanning 386, showing pre-eclipse hump and QPOs

show QPOs in the quiescent state, and have visible humps at phase 0.75. Both objects lose both of these features while in outburst, and brighten by similar magnitudes.

If these systems are magnetic, then they should both have strong X-ray emission associated with them. Intermediate Polars, which are moderately magnetic CVs, have X-ray luminosities between $10^{31} - 10^{32}$ erg s^{-1}, while non-magnetic CVs tend to be significantly fainter, with a luminosity $< 10^{29}$ erg s^{-1}. The X-ray behaviour of both of these objects will be considered in Chapter 4.

The spectra of both objects, taken when both were in quiescence, are also very similar. The Balmer decrements of Lanning 386 are $D_{34} = 1.15$ and $D_{54} = 0.85$ (Brady et al., 2008), which are within the measurement errors of the decrement for J1923. Both spectra also show the same M-type molecular band past 7200Å. Lanning 386 displays 2 very different spectra, depending on its state. When in quiescence, its spectrum is identical to that observed here for J1923. However, in outburst, Lanning 386 displays prominent ionized helium emission lines, along with the Bowen blend structure and C IV(5806Å). The spectrum shown in Fig. 3.2 was taken when J1923 was in the low state, which

might explain the absence of the features seen in the excited state in Lanning 386.

The peak-to-peak separation of the emission lines in J1923 is small compared to the expected value for its high inclination, and the FWZI is smaller than the value typically found in SW Sextantis stars. We propose that this is possibly due to a truncation of the accretion disc due to the WD's magnetic field.

The single-peak structure seen in SW Sex stars is thought to arise due to a strong magnetic accretion curtain (Hoard et al., 2003). A possible explanation for the slightly double-peaked emission lines in J1923 could also be that there is weaker line emission from the accretion curtain in J1923, as opposed to the strong emission line core seen from the magnetic accretion curtain in SW Sextantis stars.

3.5 Conclusions

We have found the period of J1923 to be $P = 0.16764612(5)$ day and determined a linear ephemeris for eclipses observed from April to June 2014. The best fit model to the eclipses requires a high inclination of $85.5 \pm 2^{\circ}$ and a disc that does not extend to the surface of the WD. This inclination is greater than the inclination estimated using the peak-to-peak separation of the Hα line. However, the small FWZI of the emission lines may suggest the accretion disc is truncated by the magnetic field of the WD, as proposed by Hoard et al. (2003).

J1923 shares many similarities with Lanning 386. Both show QPOs in quiescence, have similar outburst amplitudes of $\Delta m \approx 2$, have similar orbital periods and have similar Balmer line spectra in quiescence. Even though it is still debatable whether both of these systems have anything to do with the SW Sextantis stars, it is nearly certain that they are extremely similar to each other. To confirm this, more simultaneous high-resolution spectroscopy and photometry of J1923 is required to see if the He II lines become prominent when the system is in outburst. It would also be of interest to see if the C IV 5806 Å line which is visible in Lanning 386 during outburst is also present in J1923, as the C IV line is a high excitation line rarely seen in CVs, yet has been observed in SW Sex, and is also present in Wolf-Rayet stars. It would also be interesting to observe J1923 in the X-ray region, as strong X-ray emission

would suggest that J1923 may be a magnetic system. In that case, the accretion disc would be truncated before reaching the surface of the WD, which would help explain why the emission lines appear single-peaked, despite its inferred inclination. This scenario also requires a very weak emission component from a magnetic accretion curtain, as there is no evidence for a strong core in the emission lines of J1923. If this X-ray emission were also seen in Lanning 386, it would help explain why the emission lines seem single peaked, despite the systems inferred inclination.

If J1923 does exhibit the He II line at 4686 Å when in outburst, then the question still remains as to what causes this emission in both J1923 and Lanning 386. The V Sagittae stars are CVs with long periods (5<P<24 hour) that display very prominent He II 4686 Å emission (Steiner & Diaz, 1998). It is possible that the V Sagittae stars and SW Sextantis stars are related through stars similar to J1923 and Lanning 386, and that the He II 4686 Å emission is the key to linking these interesting classes together.

Acknowledgements

MRK, PC and PM acknowledge financial support from the Naughton Foundation, Science Foundation Ireland and the UCC Strategic Research Fund. PS acknowledges support from NSF grants AST-1008734 and AST-1514737. We thank the Vatican Observatory and Richard Boyle for providing us observing time on the VATT. Some of this work is based on observations obtained with the Apache Point Observatory 3.5m telescope, which is owned and operated by the Astrophysical Research Consortium. We would also like to thank the anonymous referee for constructive and useful feedback.

4

XMM-Newton Observations of the Peculiar CV Lanning 386: X-ray Evidence for a Magnetic Primary

[†]We present the first X-ray observations of the eclipsing cataclysmic variables Lanning 386 and MASTER OTJ192328.22+612413.5, possible SW Sextantis systems. The X-ray light curve of Lanning 386 shows deep eclipses, similar to the eclipses seen in the optical light curve, confirming the high inclination of the system. There is evidence of a periodicity between 17-22 min in the X-ray and optical light curves of Lanning 386, which is associated with quasi-periodic oscillations. This system also displays a hard X-ray spectrum that is well fit by a partially covered, absorbed 2 temperature plasma. The cool plasma temperature ($0.24^{+0.17}_{-0.08}$ keV) and hot plasma temperature (9^{+4}_{-2} keV) are not atypical plasma temperatures of known intermediate polar systems. Based on this model, we suggest that Lanning 386 is an intermediate polar with a high accretion rate. The hot plasma temperature limits the white dwarf mass to $>$0.5 $M_\odot$. From the optical spectrum obtained using the Large Binocular Telescope, we find that the secondary in the system is consistent with an M5V star, and refine the distance to Lanning 386 to be 160$\pm$50 pc. Finally, we use the high time resolution of the optical spectra to crudely constrain the magnetic moment of the white dwarf in Lanning 386. J1923 was not detected during the observations. However, based on the X-ray luminosity of Lanning 386 and assuming J1923 has a similar luminosity, combined with the distances to Lanning 386 and J1923, we find that we do not expect to be able to detect J1923 with the observations presented here.

[†]Published in Monthly Notices of the Royal Astronomical Society. "*XMM-Newton* Observations of the Peculiar Cataclysmic Variable Lanning 386: X-ray Evidence for a Magnetic Primary" Kennedy, M. R., Callanan, P., Garnavich, P. M., Fausnaugh, M., Zinn, J. C., 2017, MNRAS, 466(2), 2202.

4.1 Introduction

In Chapter 3, we focused on optical observations of J1923. In the following chapter we focus on X-ray observations of both Lanning 386 and J1923, which were taken after the data in Chapter 3 was published. To recap, Lanning 386 and MASTER OTJ192328.22+612413.5 (hereafter J1923) are 2 cataclysmic variables that avoid easy classification. Lanning 386 has an orbital period of 3.94 hours (Brady et al., 2008) and J1923 has an orbital period of 4.02 hours (Kennedy et al., 2016). Both systems show low amplitude, frequent outbursts with $\delta m \approx 2$, and display quasi-periodic oscillations (QPOs) in their optical light curves during quiescence, which are thought to arise in systems with magnetic primaries that are undergoing very high accretion rates (Patterson et al. 2002; Warner 2004). The light curves of Lanning 386 and J1923 show deep eclipses, and the inclinations of these systems are thought to be high (Kennedy et al., 2016). The spectra of Lanning 386 shows strong H and He I lines in quiescence and outburst. It also shows He II and C IV lines and the Bowen Blend complex in outburst. J1923 shows slightly double peaked H lines in quiescence.

It has been suggested that the primaries in these systems may be magnetic, and the accretion discs might be truncated close to the surface of the white dwarf, leading to the formation of an accretion curtain (Kennedy et al., 2016). Here, we present the first X-ray observations of Lanning 386, taken using the *XMM-Newton* telescope, in an attempt to constrain the magnetic nature of this peculiar CV. J1923 was also observed by *XMM-Newton* as part of the same program due to the similarities between Lanning 386 and J1923 in their optical light curves and spectra in quiescence. However, only upper limits on the X-ray flux for J1923 are presented here.

4.2 Observations

Lanning 386 was observed four times by *XMM-Newton*, while J1923 was observed once (see Table 4.1 for full details). The EPIC-pn (Strüder et al., 2001) and EPIC-MOS (Turner et al., 2001) instruments were operated in Large Frame mode with thin filters inserted. The RGS spectrographs (Brinkman et al. 1998; den Herder et al. 2001) were operated in their normal spectroscopy

Table 4.1: Observations of Lanning 386 and J1923 taken by *XMM-Newton*. Rev stands for the *XMM-Newton* orbit over which the data was taken, and GTI stands for "Good Time Interval", which is how much of the observations were not affected by soft proton flaring.

Object	Obs No.	Rev	Start Date (UT)	Instrument	Filter	M_V	EXP Time	Total GTI
Lanning 386	1	2816	2015-04-26	EPIC-pn	Thin		14.7 ks	13.4 ks
				EPIC-MOS	Thin		16.7 ks	
				OM	V	16.81	15.4 ks	
	2	2825	2015-05-13	EPIC-pn	Thin		20.2 ks	13 ks
				EPIC-MOS	Thin		22.2 ks	
				OM	V	16.86	18.8 ks	
	3	2828	2015-05-20	EPIC-pn	Thin		16.7 ks	8.9 ks
				EPIC-MOS	Thin		18.7 ks	
				OM	V	16.88	9.4 ks	
	4	2829	2015-05-21	EPIC-pn	Thin		14.7 ks	14.7 ks
				EPIC-MOS	Thin		16.7 ks	
				OM	V	16.85	11 ks	
J1923	5	2809	2015-04-12	EPIC-pn	Thin		26.4 ks	12.4 ks
				EPIC-MOS	Thin		26.9 ks	
				OM	V	$>$17.96	26.4 ks	

modes. The optical monitor (OM; Mason et al. 2001) was operated in fast timing mode with a V band filter inserted.

The four observations of Lanning 386 were scheduled randomly, in order to maximise the chance of observing it in outburst, as Lanning 386 spends approximately 25% of its time in outburst (Brady et al., 2008).

The data were reduced and analysed using the *XMM-Newton* Science Analysis Software (SAS v14.0.0; ESA: XMM-Newton SOC 2014). The data from the EPIC instruments were processed using the EMPROC and EPPROC tasks. The EDETECT_CHAIN command was used for source detection. The EPIC-pn and -MOS data from observations 1, 2 and 3 were affected by very high soft proton flaring. We only used events recorded during low background flaring for the spectral analysis and source identification. All events were used for timing and light curve analysis, and the task BARYCEN was run to correct all timing data to the Solar System barycentre. Figure 4.1 shows the combined EPIC-pn and -MOS images from the four observations of Lanning 386. No results are presented using the RGS instrument due to the very low signal-to-noise ratio.

Photometry of Lanning 386 was also taken using the Galway Ultra Fast Imager (GUFI; Harding et al. 2011) mounted on the 1.8m Vatican Advanced Technology Telescope (VATT*) on the nights of June 22, 2009 (UT), December 4, 2010 (UT) and December 6, 2010 (UT). There were 1620 exposures taken on June 22 with a typical cadence of 10s, 471 exposures taken on Dec 4 with a

*The VATT telescope facility is operated by the Vatican Observatory, and is part of the Mount Graham International Observatory.

typical cadence of 22s and 208 exposures on Dec 6 with a typical cadence of 42s. Reduction and analysis of these data was carried out using the typical IRAF[†] commands.

The Large Binocular Telescope (LBT) observed Lanning 386 with the Multi-Object Dual Spectrographs (MODS; Pogge et al. 2010) on 2016 June 15 (UT) in binocular mode. This means MODS1 was taking data using the SX mirror (left side) simultaneously with MODS2 on the DX (right side), although the start times of the two spectrographs were not synchronised. MODS1 and MODS2 are nearly identical and in the dual grating mode both cover a wavelength range from 320 nm to 1 μm, divided into red and blue channels separated by a dichroic at 560 nm. The exposure for each spectrum was 120 s and the time between the start of consecutive exposures averaged 183 s. A slit width of 0.8 arcsec was used and the seeing averaged slightly better than 1.0 arcsec.

Thirty spectra were obtained from each spectrograph between 10:12 UT and 11:00 UT, providing a time resolution between 30 s and 100 s when the two sets of spectra are combined. The data reduction tasks were carried out using IRAF.

4.2.1 J1923

The single *XMM-Newton* observation of the field around J1923 failed to detect any source, with an upper limit on the flux from the region of $F_X < 1.1 \times 10^{-14}$ erg cm^{-2} s^{-1} at the 2σ level. Due to the non-detection of the source, no further results on J1923 are presented, except for a comparison to Lanning 386 in Section 4.5.2.

4.3 Timing Analysis

4.3.1 Optical Light Curve

The extracted optical light curve of Lanning 386 taken with the optical monitor can be seen in the bottom panel of Figure 4.2. The V-band magnitudes

[†]IRAF is distributed by the National Optical Astronomy Observatory, which is operated by the Association of Universities for Research in Astronomy (AURA) under cooperative agreement with the National Science Foundation

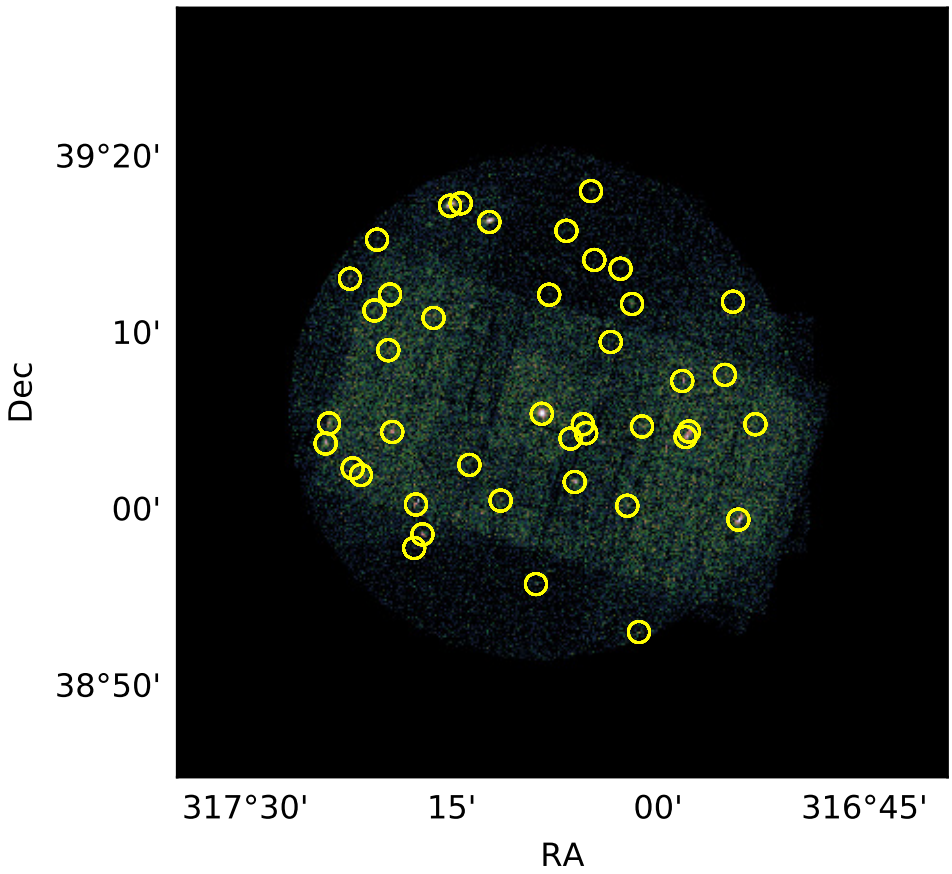

Figure 4.1: The combined images of Lanning 386 from observations 1, 2, 3 and 4 using the EPIC-pn and -MOS instruments. The yellow circles are all detected sources using EDETECT_CHAIN. Lanning 386 is in the centre of the frame.

found in Table 4.2 were calculated by taking the mean count rates of the individual observations and using the zero-point formula of

$$m = m_{zero} - 2.5 \log_{10} (cts) \tag{4.1}$$

where $m_{zero} = 17.9633$ for the V-band[‡]. The resulting magnitudes are consistent with the quiescent state of Lanning 386.

Lanning 386 was undetectable during eclipse, as its eclipse magnitude of ≈18.8 mag is below the flux sensitivity of the OM. To determine the mid-eclipse times, a Gaussian was fit to the ingress and egress of the eclipse visible in the optical observations. These mid-eclipse times were added to the

[‡]XMM OM calibration document XMM-SOC-CAL-TN-0019

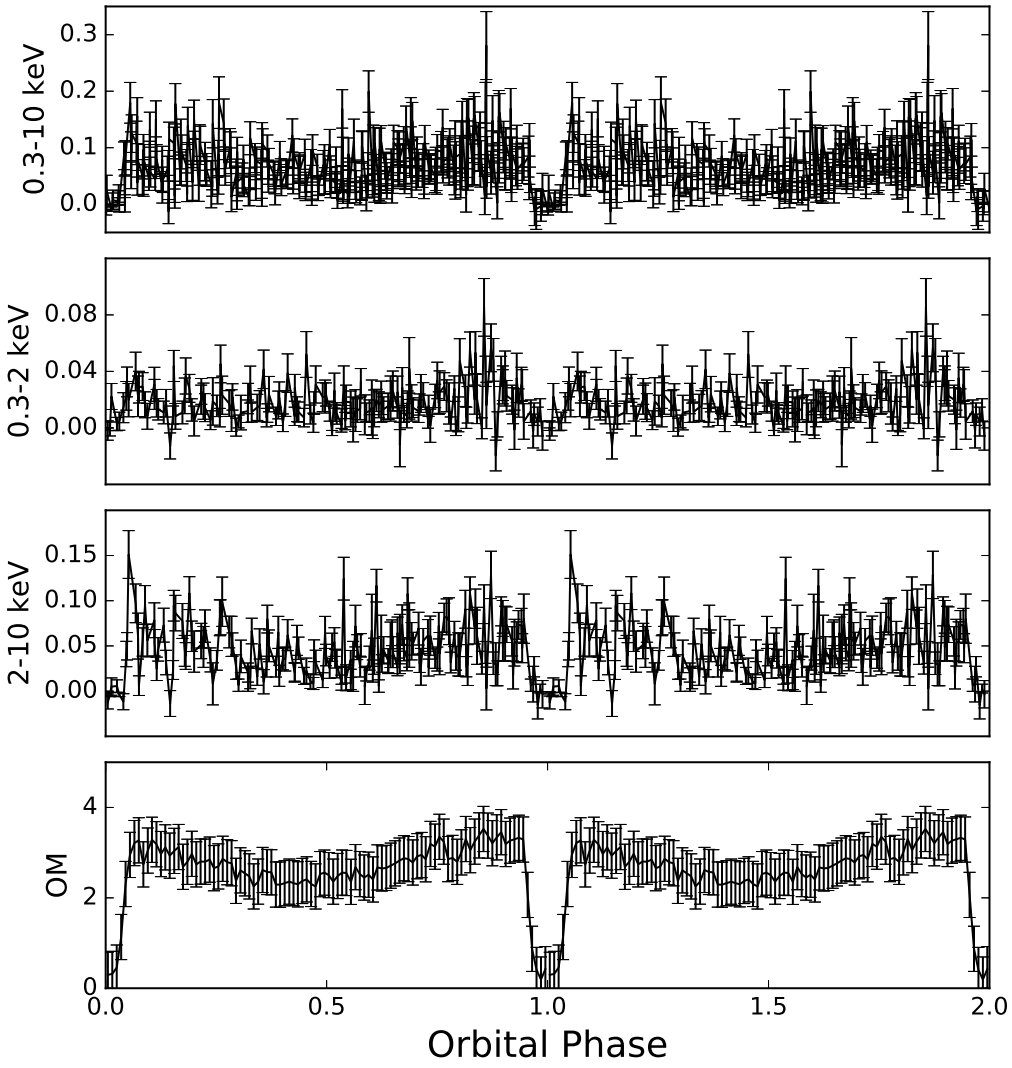

Figure 4.2: The extracted light curves of Lanning 386 from the EPIC-pn and OM data. The phase folded X-ray light curves for the full (0.3-10 keV, top panel), soft (0.3-2 keV, 2nd panel) and hard (2-10 keV, 3rd panel) spectral ranges are shown. The bottom panel is the phase folded optical data from the OM, taken in the V-band. The optical data has been binned with a bin width of 0.1 in phase. The y axis is in units of counts s^{-1}. Orbital phases have been repeated for clarity.

Table 4.2: Properties of the optical observations of Lanning 386 from *XMM-Newton* and the VATT.

Observatory	Obs No.	Mean Cnt Rate cnts s^{-1}	Mag	Mid-eclipse Time (BJD)	Cycle No.
VATT (V-band)	2009 June 22	-	16.76	2455004.937(1)	8408
VATT (V-band)	2010 Dec 04	-	15.12	2455534.6598(5)	11637
VATT (U-band)	2010 Dec 06	-	14.82	2455536.6285(5)	11649
XMM-Newton OM	1	2.88	16.81	2457138.5955(5)	21414
XMM-Newton OM	2	2.76	16.86	2457155.8218(5)	21519
XMM-Newton OM	3	2.71	16.88	2457162.7110(5)	21561
XMM-Newton OM	4	2.76	16.86	2457164.188(1)	21570

mid-eclipse times calculated from the GUFI observations presented in Section 4.2, the GUFI observations presented in Kennedy et al. (2016) and the times given in Table 5 of Brady et al. (2008) to determine a new ephemeris. The best fit linear ephemeris was

$$T(BJD) = 2453625.5876(1) + 0.16405193(2)E. \tag{4.2}$$

The O-C for these mid-eclipse timings is flat, with no detectable $\dot{P}$.

4.3.2 X-ray Light Curves

X-ray light curves of Lanning 386 and a nearby background region were extracted from the EPIC-pn data using the EVSELECT tool in SAS, and then the Lanning 386 light curves were corrected using the EPICLCCORR tool. Light curves were extracted for the full (0.3-10 keV), soft (0.3-2 keV) and hard (2-10 keV) spectral ranges, and phased using the linear ephemeris found in Section 4.3.1. The resulting light curves can be seen in the top and middle panels of Figure 4.2. The X-ray light curves have a bin width of 200s.

There is an eclipse visible at the expected phase in the full X-ray light curve, beginning at orbital phase 0.94 and lasting until orbital phase 0.05. The eclipse is the same width as the optical eclipse, suggesting that the source of the X-ray emission is eclipsed for the same duration as the dominant source of the optical emission in the system, which is thought to be the accretion disc. For the X-ray source of the system to be eclipsed, the inclination of this system must be high. The same eclipse is visible in the hard X-ray light curve (Figure 4.2, third panel), with the same eclipse width.

4.3.3 Power Spectrum

Each night of the GUFI optical data was subjected to a Lomb-Scargle periodogram (LSP, Lomb 1976; Scargle 1982) using the astroML python library (Vanderplas et al., 2012). A Lomb Scargle periodogram can be considered to be a generalised version of a fast Fourier transform (FFT). While FFT's are optimised for regularly sampled data, LSP's are optimised for irregularly sampled data. For a comprehensive review of LSPs, the conditions for using them, and advantages over other techniques see VanderPlas (2017).

The three resulting power spectra were multiplied by each other, such that common peaks between the 3 power spectra would be enhanced, while noise peaks would be diminished. The resulting normalised power spectrum can be seen in the top panel of Figure 4.3. We also applied the χ^2 period test to the GUFI data to test the validity of the periods, also shown in the top panel of Figure 4.3. The χ^2 test works by binning the data, phasing the binned data to a range of periods and calculating the χ^2 value for the binned data versus a normal distribution. When no period is present, small χ^2 values are expected, while large χ^2 values are expected when a periodic feature is present. The strongest peaks in the power spectrum were between 17-22 min, 32-43 min, and 55-65 min. The 17-22 min and 32-43 min periods are also detected in the χ^2 plot. However the 55-65 min is not as obvious in the χ^2 plot, but there is a strong peak at 75 mins. Since the LSP is a more robust way of testing for periods, we treat the peaks that are visible in both the LSP and χ^2 test as real, while the 75 min period in the χ^2 test is probably a false detection.

Phasing the data on different periods in these bands revealed a single cycle was present when the data was phased with a period in 17-22 min range, similar to that of J1923. The origin of these QPOs could be an obsured view of the accretion curtains as shwon for J1923 in Fig. 3.9, assuming the system is magnetic. The strong peaks seen in the power spectra at 32-43 min and 55-65 min are likely harmonics of the 17-22 min period.

We also subjected the *XMM-Newton* OM and 0.3-10 keV X-ray light curves to a LSP. The resulting power spectra can be seen in Figure 4.4. The periodogram was bootstrap re-sampled (Suveges, 2012) 2000 times to determine the 1σ, 2σ and 3σ levels.

The optical power spectra shows 2 broad peaks with periods centred on 18.5 and 22.5 minutes which are detected at the 3σ level.

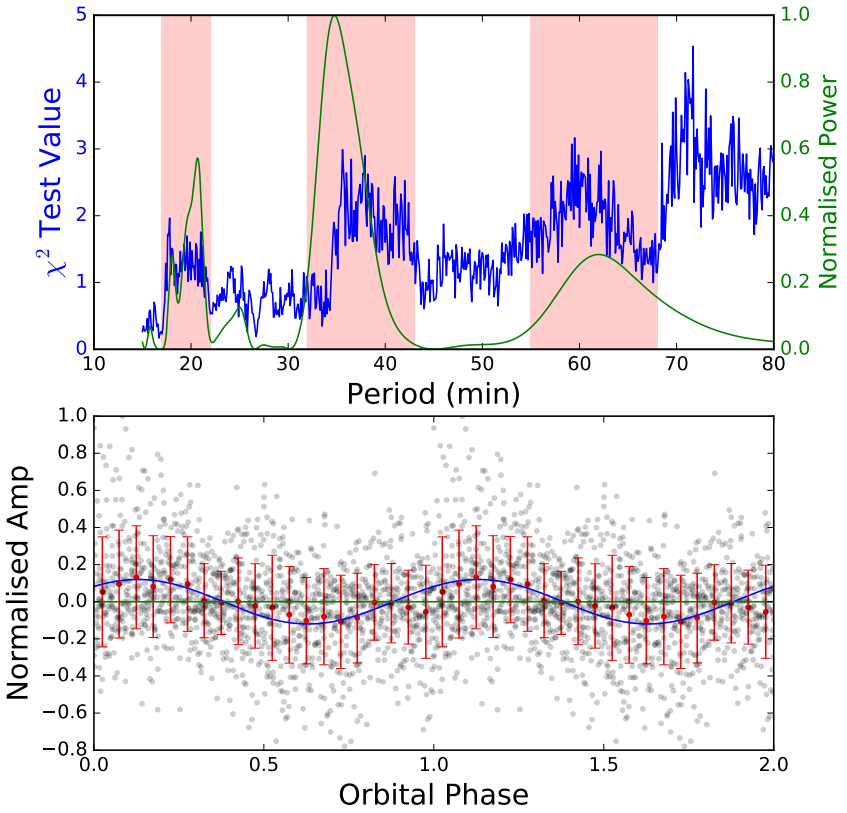

Figure 4.3: *Top:* The χ^2 test values (blue) and normalised Lomb Scargle power (green) of the Lanning 386 GUFI data. In both the χ^2 test and power spectrum, there are strong periods detected between 17-22 min, 32-43 min (these regions are highlighted in red) while the power spectrum shows another signal at 55-65 mins. The noise level of the χ^2 test increases for longer periods. *Bottom:* The GUFI data phased on a period of 17.8 minutes (grey), and the data binned with a bin width of 0.05 in phase (red). The data shows a single cycle when phased on the 17.8 min period, and two cycles when phased on a 35 min period, suggesting the shorter period is the period of the QPO. An example sine curve is plotted (blue) for comparison.

There is a sharp peak in the X-ray power spectrum at 18.7 minutes which was detected above the 3σ level.This X-ray peak is as wide as the optical QPO peak at 18.5 minutes. Due to the position and shape of this peak, we consider it to be real and probably related to the optical QPOs.

The GUFI, OM and X-ray data all exhibit a similar QPO, with a periodicity of around 18.5 minutes. These peaks occur at the same periods as the QPOs seen in the similar object J1923, where the QPOs have a period of $\approx$ 20 minutes (Kennedy et al., 2016). Based on this, we attribute the periods in the optical

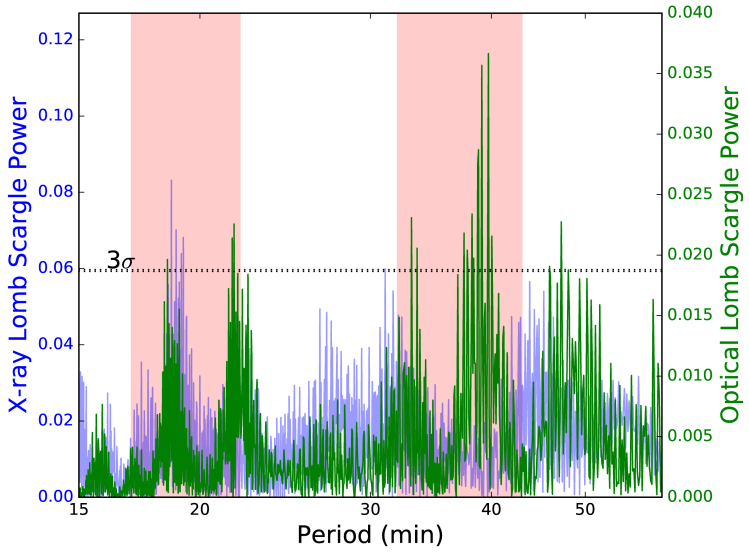

Figure 4.4: The optical (green) and X-ray (blue) power spectra of Lanning 386. There are two strong peaks at 18.7 min and 21.5 min in the optical spectrum, which are detected the 3 σ level. There is one peak that is also present in the X-ray power spectrum at 18.7 min. The red shaded areas correspond to the same shaded areas as in Figure 4.3.

and X-ray power spectrum to be a result of the QPOs present in this system.

4.4 Spectral Analysis

4.4.1 Optical

The series of spectra obtained by the LBT begin at phase 0.80 and end at mid-eclipse (phase 1.00). Figure 4.5 shows the average spectrum out of eclipse and the spectrum close to maximum eclipse. The ultraviolet and blue continua are seen to fade by a factor of 30 in brightness. The Balmer and HeI lines remain visible during eclipse and fade only by a factor of six in total flux. The spectral features of an M5-type secondary star become more prominent in eclipse. Using the MILES stellar library[§], we find the M5V star HD173740 (Cenarro et al., 2007) is a good fit to the secondary star spectrum and that the spectral type of the companion in Lanning 386 is likely in the M4-M5V range. This is slightly later than the M3.5e star suggested by Brady et al. (2008).

The acquisition images and calibrated flux out of eclipse indicate that

[§]http://www.iac.es/proyecto/miles/

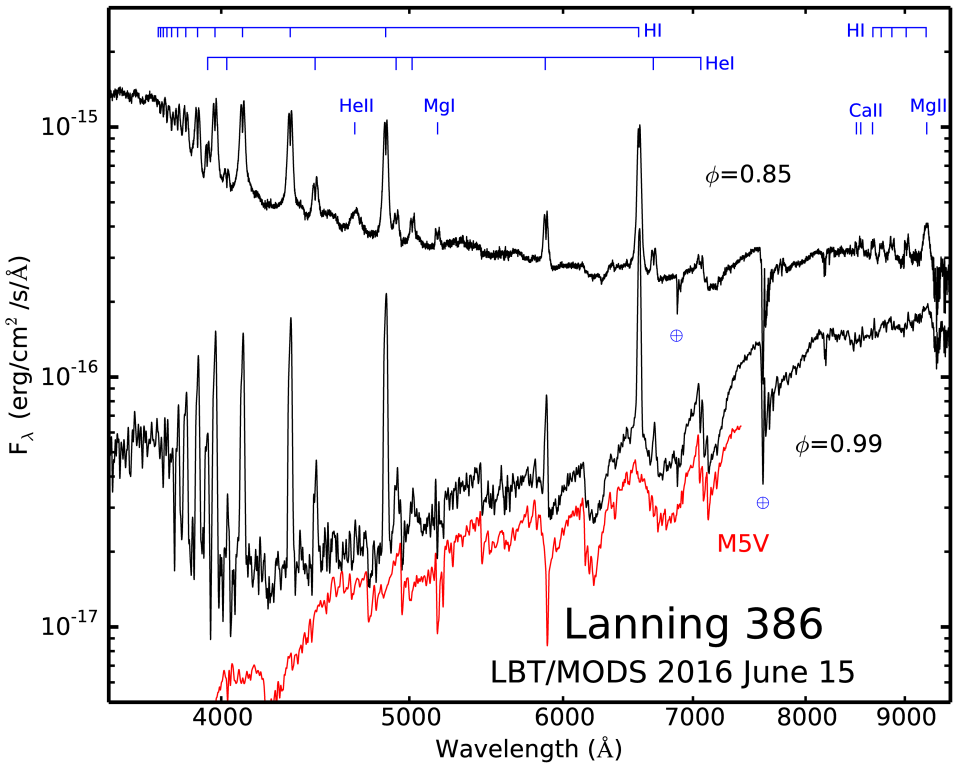

Figure 4.5: The spectrum of Lanning 386 taken at 2 different orbital phases using the MODS spectrographs on the 8.4 m LBT. The spectrum, taken during quiescence, shows strong H and He I emission lines. The lines are double peaked outside of eclipse, and there is a weak He II component visible. The red line is a template M5V, which shows that most of the light in the continuum beyond 5000Å is coming from the late-type secondary.

Lanning 386 was fainter than $V > 17.3$ at the time of the LBT spectra and therefore in the quiescent state (as were the X-ray observations). Outside of eclipse, the Balmer and HeI lines are double peaked which can be due to the accretion disc or absorption by an accretion curtain if the system is magnetic.

During outburst, Lanning 386 shows a very strong He II plus Bowen blend emission feature but He II is significantly weaker in quiescence according to Brady et al. (2008). Our spectra clearly shows a weak but broad HeII line out of eclipse and no detection at mid-eclipse. The velocity width of He II is 3400 km s^{-1} (FWHM) compared with 1800 km s^{-1} for the Hβ emission.

With 30 optical spectra taken over a phase range of 0.2, the typical temporal resolution is 2 minutes (0.008 in phase). Figure 4.6 shows the trailed spectra

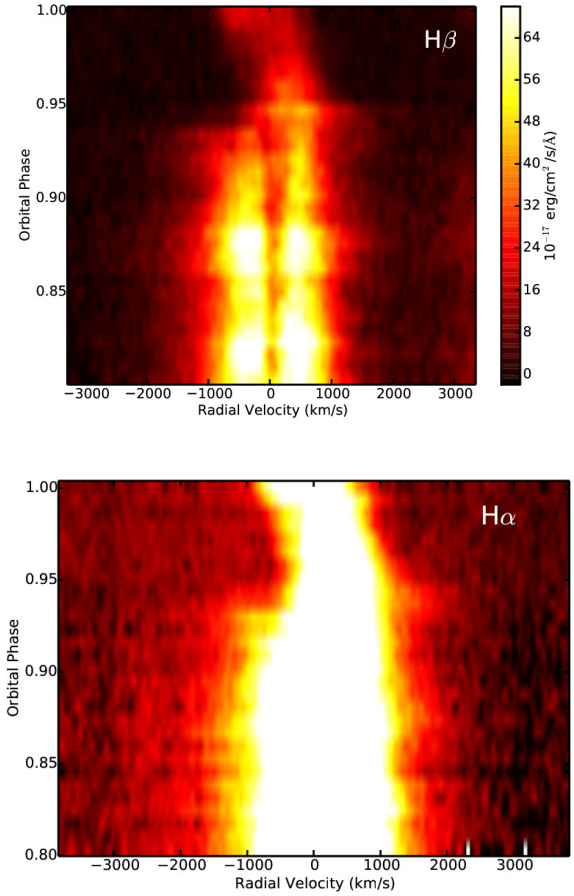

Figure 4.6: *Top:* The trailed spectrum of Hβ for Lanning 386 shows the lines are clearly double peaked outside of eclipse and during quiescence. As the system enters eclipse, the blue wing of the emission line is eclipsed first. *Bottom:* The high contrast trailed spectrum of Hα shows how quickly the blue wing of the Hα line is eclipsed, with all blue emission eclipsed by phase 0.95. The red wing starts a shift towards 0 km s^{-1} as the secondary begins to eclipse the red-shifted part of the accretion disc.

of the Hα and Hβ lines after the continuum has been subtracted. Some variability in the line flux is seen out of eclipse that may be due to a QPO seen in the X-ray and optical light curves. The double-peaked profile in Hβ is clear and there is an obvious asymmetry between the red and blue shifted high-velocity tails. The blue emission is seen to extend beyond -2000 km s^{-1} while the red side falls off more quickly. The scaling of Hα has been set to clearly show the highest velocity emission.

As expected, the blue side of the emission line is the first to be eclipsed at phase 0.934, but its disappearance is particularly fast, blinking out in less than 0.01 in phase. A large fraction of the redshifted component is eclipsed at

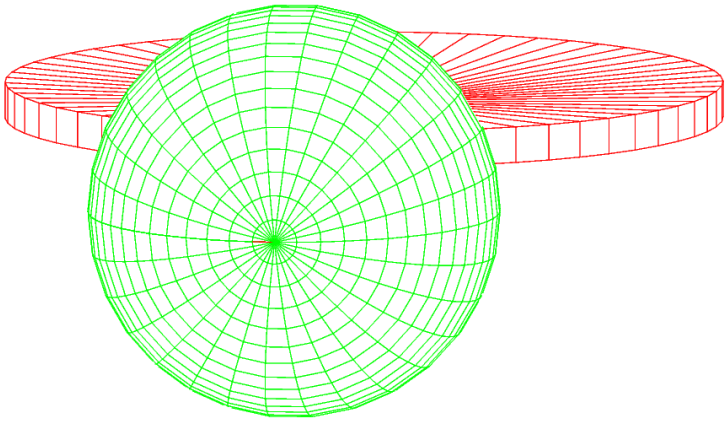

Figure 4.7: A schematic of Lanning 386 which shows the secondary star (in green) and accretion disc (in red) at orbital phase 0.98 for an inclination of 78°. There is still a large amount of the red shifted side of the accretion disc visible at this orbital phase, which might explain the residual emission in the trailed spectra of H.

phase 0.948. A low-velocity redshifted component survives, transforming to a slightly blueshifted emission at mid-eclipse. The phase at which the blue side of the emission line is eclipsed also matches the phase at which the X-ray light curve beings to eclipse.

The fast disappearance of the blue side of the emission suggests that it comes from a very small region. The secondary motion of 0.05 radians means the size of the emission region is less than 6% of the separation between the two stars. The time between the blue and red sides being eclipsed means they are separated by 9% of the orbital radius. After the eclipse there remains a weak Balmer emission moving from red to blue, but it is not clear from where this light is originating. Fig. 4.7 shows a schematic for Lanning 386 at orbital phase 0.98. During this part of the orbit, the WD and inner parts of the accretion disc are eclipsed, but there remains an appreciable amount of slow moving material visible in the red side of the accretion disc. This may be the cause of the excess emission during eclipse as, as the secondary moves further in front of the disc, more of the red side of the disc will be eclipse while the blue side is revealed. This would lead to the red wing of the emission moving through 0 km s^{-1} and then out to the blue wing of the line. Unfortunately, observations stopped just after orbital phase 0, which is when the line should have started moving towards the blue if this were the cause of the emission.

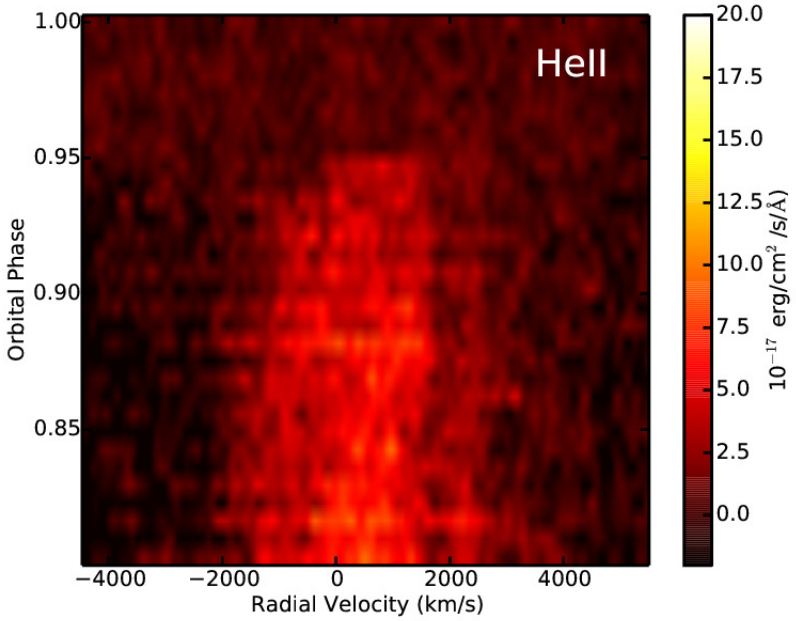

Figure 4.8: The trailed spectrum of He II 4686Å shows that weak He II emission is present in the system even in quiescence, and becomes fully eclipsed around the same time as the Hβ emission. As with the Hα line, the He II is eclipsed very quickly, only taking $\sim$0.01 phase for the line to become undetectable. There is an absorption feature present at 2000 km s^{-1}, which is consistent with an absorption feature from an M type star.

Figure 4.8 shows the trailed spectrum for He II. It shows a similar rapid eclipse of the blue side (phase 0.936) and then red side (phase 0.948). There are no further emission components beyond phase 0.948 and we conclude the eclipse is total for the He II line.

4.4.2 X-ray

X-ray spectra were extracted for the energy range 0.3-10 keV for all 4 observations of Lanning 386 using the EPIC-pn and EPIC-MOS instruments. The average X-ray spectrum from both instruments is shown in Figure 4.9. The spectra have been rebinned to have 25 counts per spectral bin.

The data were analysed using the HEASARC software package XSPEC (version 12.9.0; Arnaud 1996). Analysis was limited to the EPIC-pn spectrum, as the -MOS spectrum had a low signal-to-noise ratio.

Initially, the data were fit using an absorbed power law model (TBABS*POWERLAW). The resulting fit showed a hard spectrum with a spectral

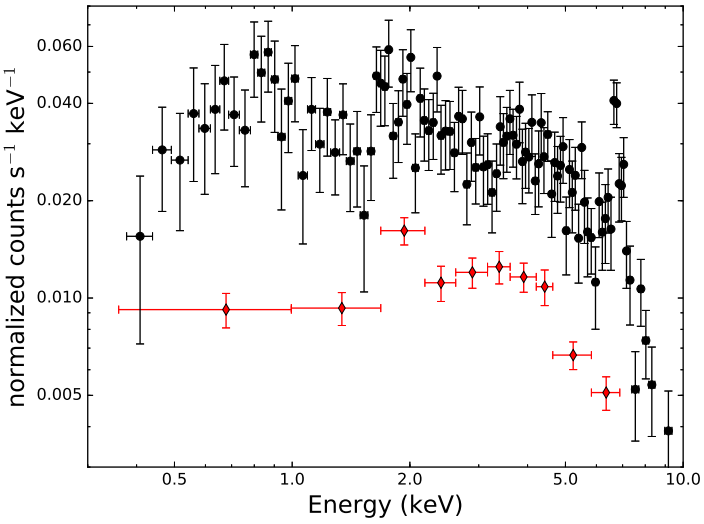

Figure 4.9: The average X-ray spectrum of Lanning 386. The black circles are the EPIC-pn spectrum, while the red diamonds are the EPIC-MOS data. There are 2 blended strong emission lines in the EPIC-pn spectrum at 6.7 keV and 6.9 keV, which match the energies of Fe XXV and Fe XXVI.

index $\Gamma = 0.32 \pm 0.05$ and a column density of $N_H = 0.05 \pm 0.03 \times 10^{22}$ cm^{-2}, but the fit was poor, with a $\chi^2_R = 2.00$. We next added 2 GAUSSIAN components to try and fit the 6.701 keV Fe XXV and 6.97 keV Fe XXVI line. The resulting fit had a $\chi^2_R = 1.66$ and is listed as Model 1 in Table 4.3.

The most common model used to describe the X-ray emission of a cataclysmic variable is a single temperature thin thermal plasma (MEKAL in XSPEC). Fitting an absorbed MEKAL model to the data gave a $\chi^2_R = 2.75$ and a high $N_H = 1.7 \pm 0.1 \times 10^{22}$ cm^{-2}. However, there were large, systematic residuals below 2 keV for this fit. This suggests a single temperature model with simple absorption is insufficient to model this source. We next attempted to fit a multi temperature model by adding a second MEKAL component to fit the spectrum below 2 keV. The result was slightly poorer than the simpler model, with a $\chi^2_R = 2.81$ and a similar column density of $N_H = 1.7 \pm 0.1 \times 10^{22}$ cm^{-2}.

IPs are often modelled using a single MEKAL component along with a complex absorption model (Staude et al., 2008). Following this approach, we next fit Lanning 386 using the relatively complex model of TBABS*(PARTCOV*TBABS)*(MEKAL). Here, the first TBABS component accounts for interstellar absorption, (PARTCOV*TBABS) models the circumstellar absorption and MEKAL is as before. As in Nasiroglu et al. (2012), our first fit could not constrain the plasma temperature, but provided a lower

limit of > 8 keV at the 3σ level. The resulting fit did not model the 6.7 keV Fe XXV line well, and had a $\chi^2_R = 1.04$. Finally, we allowed the metal abundance of the MEKAL component to vary, such that the model fit around the 6.7 keV Fe XXV line might be improved. The final fit had a $\chi^2_R = 0.84$ and can be seen in Figure 4.10. The best fit parameters are listed under Model 2 in Table 4.3.

Eracleous et al. (2002) used the strength of the λ4430 diffuse interstellar band (DIB) to estimate an $A_V = 1.5 \pm 0.2$ in the direction of Lanning 386. Using the linear relation between column density and A_V given by Güver & Özel (2009), this equates to a column density of $N_H = 3.3 \pm 0.4 \times 10^{21}$ cm^{-2}. This is higher than the column density of $N_H = 2.54 \times 10^{21}$ cm^{-2} from the Leiden/Argentine/Bonn (LAB) Survey of Galactic HI (Kalberla et al., 2005)[¶].

The column density of the interstellar absorber in Model 2 ($N_H = (0.8^{+1.0}_{-0.7}) \times 10^{21}$ cm^{-2}) is far below the values from Eracleous et al. (2002) and the LAB survey. Motivated by this descrepancy, the column density was fixed to 3.3×10^{21} cm^{-2}, and the X-ray spectrum refit using Model 2. This model had large errors in the soft X-rays, and a $\chi^2_R = 1.2$. As such, we added a second MEKAL component with a low plasma temperature. The resulting model, TBABS*(PARTCOV*TBABS)*(MEKAL+MEKAL) is listed under Model 3 in Table 4.3, and shown in Figure 4.10. The best fit had a $\chi^2_R = 0.82$, and did not require a variable metallicity. In the following Sections, the MEKAL model with the lower plasma temperature of $0.24^{+0.17}_{-0.08}$ keV is referred to as the "cool" plasma component, and the MEKAL model with the higher plasma temperature of 9^{+4}_{-2} keV is the "hot" plasma component

The unabsorbed flux in the 2-10 keV X-ray spectral range, $F_{X(2-10)}$, was found to be $(5.7 \pm 0.8) \times 10^{-13}$ erg cm^{-2} s^{-1} by multiplying the MEKAL components by the CFLUX model in XSPEC, which estimates the flux of a given component over a given energy range.

4.4.2.1 Equivalent Widths and intensities of the Fe lines

We measured the equivalent widths of the 6.7 keV Fe XXV and 6.97 keV Fe XXVI lines using the EQWIDTH command in XSPEC after fitting a GAUSSIAN model to both of the lines. The equivalent width of the 6.7 keV line was 420$\pm$50 eV, and the equivalent width of the 6.97 keV line was 200$\pm$50 eV. The intensity of both

[¶]Calculated using the online N_H tool available at `https://heasarc.gsfc.nasa.gov/cgi-bin/Tools/w3nh/w3nh.pl`

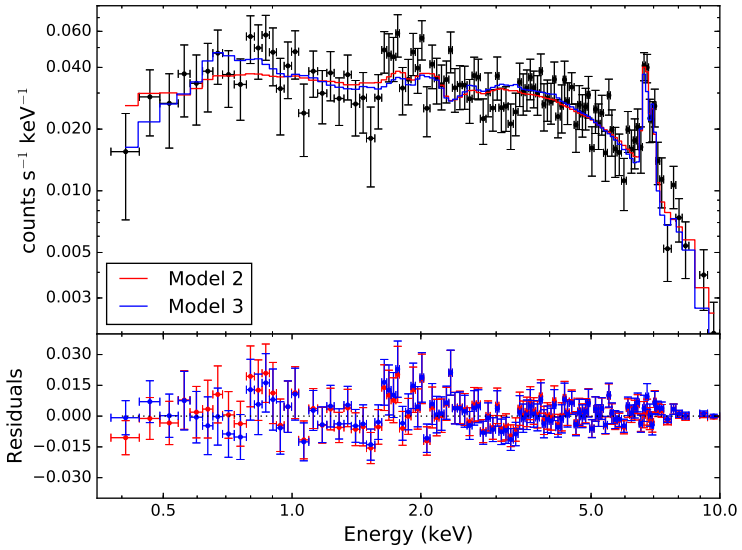

Figure 4.10: The 2 best fit models to the EPIC-pn spectrum. Model 2 (red) is a single temperature model with a lower than expected interstellar column density. Model 3 (blue) has a column density fixed at the interstellar value found by Eracleous et al. (2002), but requires two different plasma temperatures (a hot and cold component) to fit the spectrum. The details of both model can be seen in Table 4.3.

of these lines was also estimated by wrapping the GAUSSIAN models in the CFLUX model in XSPEC. The intensities were measured to be $I_{6.7} = 2.4 \pm 0.7 \times 10^{-14}$ erg cm^{-2} s^{-1} and $I_{6.97} = 1.3 \pm 0.5 \times 10^{-14}$ erg cm^{-2} s^{-1}.

To determine an upper limit on the flux from the 6.4 keV Fe LINE, a GAUSSIAN and POWERLAW model was fit to the region around 6.4 keV. The resulting upper limit on the 6.4 keV line was $I_{6.4} < 3.2 \times 10^{-15}$ erg cm^{-2} at the 3σ level. The upper limit on the equivalent width of the 6.4 keV Fe LINE was < 50 eV.

4.4.3 An updated distance measurement

Brady et al. (2008) estimated the distance to Lanning 386 to be $\sim$ 500 pc using a spectral type of M3.3 for the secondary and assuming a reddening of $E(B-V) < 0.2$ ($A_V = 0.62$ mag). The new best matching spectral type of M5V gave an absolute magnitude for the companion in the system of $M_V = 13.2 \pm 0.3$, using the relation between spectral type and surface brightness from Beuermann (2006). Combined with a visual extinction of $A_V = 1.5$ (Eracleous et al., 2002), the distance to Lanning 386 was determined to be 160$\pm$50 pc. This is much larger than the previous value reported by

Table 4.3: Parameters obtained for various models in XSPEC using the Lanning 386 data. *(a) parameter frozen at this value for the fit*

Component	Parameter	Model 1	Model 2	Model 3
TBABS (INTERSTELLAR)	N_H (10^{22} cm^{-2})	0.06(3)	$0.08^{+0.10}_{-0.07}$	0.33^a
TBABS (STELLAR)	N_H (10^{22} cm^{-2})	-	$4.0^{+1.7}_{-1.1}$	$4.8^{+2.0}_{-1.4}$
PARTCOV	cvf	-	$0.86^{+0.05}_{-0.07}$	$0.88^{+0.04}_{-0.06}$
POWERLAW	Γ	0.37(6)	-	-
	norm ($\times 10^{-5}$)	1.13(9)	-	-
MEKAL	kT (keV)	-	9^{+5}_{-2}	9^{+4}_{-2}
	Abundance	-	$1.2^{+0.96}_{-0.60}$	1.0^a
	norm ($\times 10^{-3}$)	-	0.35(2)	0.35(2)
MEKAL	kT (keV)	-	-	$0.24^{+0.17}_{-0.08}$
	Abundance	-	-	1.0^a
	norm ($\times 10^{-3}$)	-	-	0.2(1)
GAUSSIAN1	Line Centre (keV)	6.70^a	-	-
	Sigma (keV)	0.1(1)	-	-
GAUSSIAN2	Line Centre (keV)	6.97^a	-	-
	Sigma (keV)	0.1(1)	-	-
	χ^2_R	1.66	0.84	0.82

Brady et al. (2008), and is a result of our use of a later spectral type for the secondary and a higher interstellar extinction.

Using this distance we derive an (unabsorbed) X-ray luminosity of $L_{X(2-10)} = \left(1.6^{+2.0}_{-0.9}\right) \times 10^{30}$ erg s^{-1}.

4.5 Discussion

4.5.1 Is Lanning 386 magnetic?

Lanning 386 is thought to be an SW Sextantis type star, which are suspected to be magnetic CVs with very high accretion rates. The light curve of Lanning 386, which shows frequent outbursts and QPOs, suggests such a high accretion rate.

From the X-ray modeling of Lanning 386, we favour Model 3 over Model 2, as this model, by design, had an interstellar absorber equal to that measured by Eracleous et al. (2002). This model also had the added bonus of not requiring a variable metallicity. In the following, we limit our discussion to Model 3 with a brief mention of Model 2 later on.

The X-ray spectrum of Lanning 386 was very hard, and is typical of IPs, but also of nova-like CVs, which are non-magnetic CVs undergoing high mass transfer rates (Balman et al., 2014). The hot plasma temperature of $kT = 9^{+4}_{-2}$ keV is not atypical of the plasma temperature found in IPs, arising from the interaction between the accretion curtain and the white dwarf (Kuulkers et al., 2006). However, we do note that this plasma temperature is lower than the majority of IPs. The soft MEKAL component, with a plasma temperature of $kT = 0.24^{+0.17}_{-0.08}$ keV, has also been seen in other IPs. Additionally, the requirement of a partial covering absorption component is common for an IP (Evans & Hellier 2007; Bernardini et al. 2012; Bernardini et al. 2015). Table 4.4 shows the partially covered, absorbed Bremsstrahlung/mekal fits to a range of IPs from the literature. We note that Lanning 386 and FO Aqr have the highest partial covering fraction of all of the IPs listed in Table 4.4. If Model 2 had been chosen as the appropriate model for the system, it would not alter these conclusions much. Model 2 required the same partial covering absorber as Model 3 and had the same hot plasma temperature, suggestive of an IP. However, it lacked the requirement of a cooler plasma to fit the soft X-rays, which would make it less comparable to other IPs. Given this, we would still argue for a probable IP classification using Model 2.

There was a weak signal detected between 17-22 min in the X-ray light curve of Lanning 386. This period was also detected in the optical monitor data and the archival GUFI data. Patterson et al. (2002) and Warner (2004) have proposed that the cause of QPOs is the spin period of the WD but instead of obtaining a clean signal at a single period, the spin period is smeared out into a QPO by reprocessing of the rotating beam by a varying period QPO source. Hence, in the case of Lanning 386, this weak optical QPO may be a manifestation of the spin period of the WD. The low significance detection of the signal in the X-ray data could be due to the systems inferred high inclination, which might be blocking most of the spin signal from the WD. For IPs, it is common for the spin period to be detected in the X-rays and for the beat period

Table 4.4: Model fits to different IPs, showing the partial covering fraction, circumstellar column density and plasma temperature

Name	Partial Covering		kT_{cold}	kT_{max}	Reference
	n_H (10^{23}cm^{-2})	CvrFract	keV	keV	
RXS J070407.9+262501	$1.2^{+1.2}_{-0.6}$	$0.54^{+0.07}_{-0.09}$	0.088±0.005	11^{+13}_{-3}	Anzolin et al. (2008)
RXS J180340.0+401214	5^{+5}_{-2}	$0.5^{+0.3}_{-0.2}$	0.10±0.02	12^{+27}_{-3}	Anzolin et al. (2008)
MU Camelopardalis	0.79±0.06	0.61±0.02	0.059±0.07	35±10	Staude et al. (2008)
IGRJ04571+4527	0.54±0.01	0.32±0.03	$6.8^{+1.7}_{-1.2}$	63^{+8}_{-19}	Bernardini et al. (2015)
Swift J0525.6+2416 3.2.1	0.18±0.02	0.45±0.02	0.19±0.01	40^{+9}_{-5}	Bernardini et al. (2015)
IGR J08390-4833	0.68±0.08	0.60±0.02	0.69±0.05	54±9	Bernardini et al. (2012)
IGR J18308-1232	1.5±0.2	0.60±0.03	0.16±0.01	40±20	Bernardini et al. (2012)
IGR J16500-3307	1.1±0.1	0.62±0.01	0.18±0.01	59±8	Bernardini et al. (2012)
IGR J17195-4100	0.63±0.03	0.43±0.01	0.159±0.005	30±2	Bernardini et al. (2012)
V2069 Cyg	0.8±0.1	0.64±0.02	0.070±0.004	32±4	Bernardini et al. (2012)
RX J0636+3535	1.1±0.1	0.57±0.03	0.079±0.002	36±5	Bernardini et al. (2012)
IGR J15094-6649	0.66±0.06	0.54±0.01	0.12±0.01	34±3	Bernardini et al. (2012)
RXS J073237.6−133113	-	-	-	37±7	Butters et al. (2007)
V405 Aur	$0.61^{+0.06}_{-0.05}$	0.54±0.03	$0.168^{+0.008}_{-0.003}$	9±1	Evans & Hellier (2004)
UU Columbae	$0.83^{+0.52}_{-0.32}$	$0.43^{+0.15}_{-0.17}$	0.18±0.01	$27^{+\infty}_{-17}$	de Martino et al. (2006)
FO Aqr	$1.9^{+0.12}_{-0.09}$	$0.86^{+0.02}_{-0.03}$	0.176±0.002	14^{+7}_{-3}	Evans et al. (2004)
WX Pyx	-	-	-	18^{+24}_{-6}	Schlegel (2005)
EX Hya	0.001-0.086	0.22-0.35	0.66±0.01	30-60	Pekön & Balman (2011)
Lanning 386	$0.48^{+0.20}_{-0.14}$	$0.88^{+0.04}_{-0.06}$	$0.24^{+0.17}_{-0.08}$	9^{+4}_{-2}	

$$P_{beat} = \frac{1}{\frac{1}{P_{spin}} - \frac{1}{P_{orb}}} \tag{4.3}$$

to be detected in the optical. If we take the spin period of the WD to be 17.8 min, the beat period would be 19.25 mins, which is within the period range detected in the GUFI and OM data. This suggests that the spin period and beat period are indistinguishable in our data. If the 17.8 min signal is the spin period of the white dwarf, then $P_{spin} = 0.08\ P_{orb}$, which is close to the $\frac{P_{spin}}{P_{orb}} = 0.1$ value around which IPs seem to cluster (Scaringi et al., 2010).

IPs typically have an observed $L_{X(2-10)}$ in the range 10^{32}-10^{33} erg s^{-1} (e.g. Xu et al. 2016). This is two orders of magnitude higher than our calculated luminosity of $L_{X(2-10)} = \left(1.6^{+2.0}_{-0.9}\right) \times 10^{30}$ erg s^{-1}, suggesting Lanning 386 is very under-luminous in the 2-10 keV X-ray range.

A smaller discrepancy has been seen in IPs previously, and can be seen in DQ Her itself (Patterson, 1994) and also in EX Hya, which is an IP (Vogt et al., 1980) that displays some SX Sextantis properties (Hellier et al. 2000; Hoard et al. 2003 [||]) and has an estimated $L_{X(2-10)} = 4.13 \pm 0.13 \times 10^{31}$ erg s^{-1}. However, Lanning 386 is still between 10-15 times fainter than this. There are several factors which could be affecting the X-ray luminosity. The first, and

[||] See D. W. Hoard's Big List of SW Sextantis Stars at `http://www.dwhoard.com/biglist` (Hoard et al., 2003).

most important, is the high inclination of this system, which may be leading us to underestimate the X-ray luminosity of the source. It also could be due to Lanning 386 having a much lower magnetic moment in comparison to other IPs. We will return to this point in Section 4.5.1.2.

If Lanning 386 is magnetic, then a lower bound on the white dwarf mass can be made using the higher plasma temperature from the MEKAL model in Model 3. The MEKAL component of our model can be replaced with the IPOLAR model of Suleimanov et al. (2016), where the only input parameters are the white dwarf mass and the magnetospheric radius of the white dwarf. (Formerly, this was the IPM model of Suleimanov et al. (2005), but was recently updated to include the magnetospheric boundary in the system). This model relies on the assumption that the maximum shock temperature in the accretion curtain of an IP is related solely to the white dwarf mass and magnetospheric boundary. Replacing the MEKAL component with IPOLAR gives a white dwarf mass > 0.5 $M_{\odot}$, and does not constrain the magnetospheric boundary.

4.5.1.1 Fe line comparisons

Next, we compare our X-ray emission-line measurements to those in the recent compilation of Xu et al. (2016). The low upper limit on the 6.4 keV equivalent width (EW), combined with the 6.7 keV/6.97 keV EW ratio, suggest a quiescent dwarf nova (DN) classification, consistent with the relatively low L_X we measure for Lanning 386. On the other hand, the 6.97 keV/6.7 keV line intensity ratio of 0.6 ± 0.3 for Lanning 386 is comparable to values measured for both DNs as a class and IPs as a class (Xu et al., 2016). Indeed, the most comparable source in the list of measurements of Xu et al. (2016) is EX Hya (closest in EWs, intensity ratios and Lx), the previously mentioned IP with a possible SW Sex association.

Hence, we conclude that whilst the X-ray emission-line and continuum characteristics of Lanning 386 are difficult to reconcile with the average values of any particular CV sub-type, they are most consistent with those of the IP EX Hya.

4.5.1.2 An upper limit of the magnetic moment of Lanning 386

Based on the separation of blue and red emitting regions of the accretion disc of approximately 9% of the orbital separation, the inner radius of the accretion disc is approximately 0.05a, where a is the orbital separation. Patterson et al. (2002) estimated that, for an upper limit on inner disc radius of $R_d \leq 0.3a$, the magnetic moment is related to the period of the system and the mass accretion rate by

$$\mu_{33} \leq 0.2\dot{M}_{16}^{1/2} P_{hr}^{7/6} \tag{4.4}$$

where μ_{33} is the magnetic moment in units of 10^{33} gauss cm^3, $\dot{M}_{16}^{1/2}$ is the mass-transfer rate in units of 10^{16} g s^{-1} and P_{hr} is the orbital period in hours. This equation assumes a weak dependence on the total mass of the system, M, and the mass of the white dwarf, M_1 (for more, see Patterson et al. 2002).

By changing the limit on the inner disc radius to $R_d \leq 0.05a$, Equation 4.4 becomes

$$\mu_{33} \leq 0.008\dot{M}_{16}^{1/2} P_{hr}^{7/6} \tag{4.5}$$

Assuming a mass-transfer rate of 2×10^{17} g s^{-1} (a typical value for IPs; Patterson 1994; Ballouz & Sion 2009) and using the orbital period of 3.94 hours gives an upper limit on the magnetic moment of $\mu \leq 1.2 \times 10^{32}$ gauss cm^3 for the WD in Lanning 386. This upper limit on μ, when compared to Figure 16 of Patterson et al. (2002), is below the μ of polars, but within the limits of the predicted μ for IPs. This is also shown in Fig. 4.11, which shows the limits on μ for polars, IPs and non-magnetic CVs, as discussed in Patterson et al. (2002). Patterson et al. (2002) show that IPs can have magnetic moments as high as 10^{34} gauss cm^3, suggesting the magnetic moment of Lanning 386 is on the low side for IPs. This, coupled with the low X-ray luminosity found in Section 4.5.1, suggests Lanning 386 is very weakly magnetic, even for an IP. This is probably why the system has not been identified as an IP previously.

4.5.2 The X-ray flux limit for J1923

Kennedy et al. (2016) proposed that J1923 and Lanning 386 belong to the same CV class. Assuming comparable X-ray luminosities for J1923 and Lanning 386 (based off of their similar orbital periods and the similarities in their optical spectra and light curves), and using distances of 750$\pm$250pc (Kennedy et al., 2016) and 160$\pm$50 pc respectively, the observed X-ray flux of

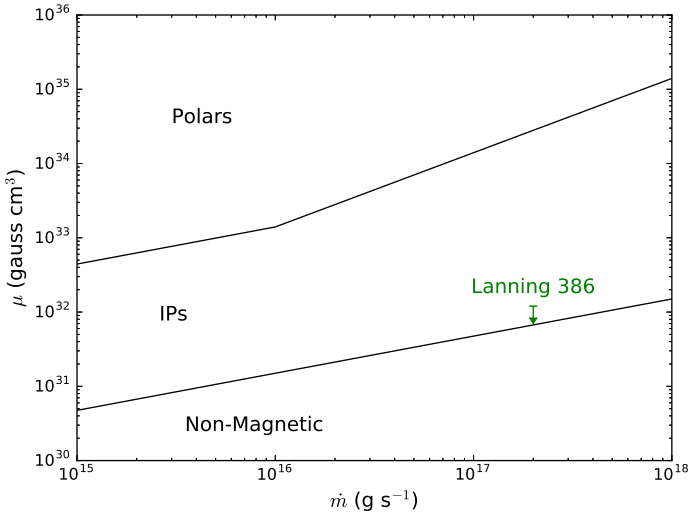

Figure 4.11: The magnetic moment versus mass accretion rate for CVs. The upper limit on Lanning 386 is plotted in green, and is just above the lower limit for IPs. The upper black line denotes the expected lower bound on μ for polars, where the inner disc radius/magnetospheric radius is equal to the orbital separation. The lower black line shows the expected lower bound on μ for polars, where $R_{mag} \sim 3R_{WD}$, as done in Patterson et al. (2002).

Lanning 386 suggests that J1923 should be detected at a flux of $\sim 5^{+5}_{-4}\times10^{-14}$ erg cm^{-2} s^{-1}. However, we do not detect J1923, to a limiting flux of 1.1×10^{-14} erg cm^{-2} s^{-1} at the 2σ level. This is barely within the range of expected fluxes, and has 3 possible explanations. The first is that J1923 is at the far end of the distance limit. The second is that, due to the higher inclination in J1923 when compared to Lanning 386, the accretion disc in J1923 is blocking a significant proportion of the X-rays, lowering the flux. The third is that J1923 is intrinsically even less luminous in the X-rays than Lanning 386.

4.6 Conclusion

The requirement of a complex absorption model in the X-ray modelling of Lanning 386 favours a magnetic primary in the system, with the partial covering fraction and lower limit on the plasma temperature comparable to other IPs. The EW and fluxes from the Fe lines in Lanning 386 remain a bit of a mystery, as they do not match the expected values for a conventional IP. However, Lanning 386 best resembles the well studied IP/SW Sex system EX Hya. Additionally, the QPOs are possibly consistent with a magnetic primary.

The limit on the magnetic moment of $\mu \leq 1.2 \times 10^{32}$ gauss cm^3, the low X-ray luminosity of $L_{X(2-10)} = \left(1.6^{+2.0}_{-0.9}\right) \times 10^{30}$ erg s^{-1} and the low "hot" plasma temperature of $kT = 9^{+4}_{-2}$ keV suggest the magnetic field is very low when compared to other IPs.

However, there are still many questions surrounding systems like Lanning 386 and J1923. Lanning 386 lacks the strong persistent He II lines associated with magnetic accretion, as the He II are only strong when the system is in outburst. When in quiescence, as the system was for these observations, the He II lines are faint. There has also only been a tenuous detection of a periodicity in the X-ray light curve. Further X-ray observations are encouraged to test whether the 18.7 min period is real and coherent. It is also important to obtain an X-ray spectrum of Lanning 386 when in outburst as the dramatic differences seen between the outburst and quiescent optical spectrum may be reflected in the shape of X-ray spectrum or in the strength of its emission lines.

Finally, we did not detect J1923 with an upper limit on the X-ray flux of 1.1×10^{-14} erg cm^{-2} s^{-1} at the 2σ level. This is still in line with J1923 and Lanning 385 having similar X-ray luminosities and further X-ray observations of J1923 to try and detect it are encouraged.

Acknowledgements

Mark R Kennedy, Paul Callanan and Peter M Garnavich acknowledge financial support from the Naughton Foundation, Science Foundation Ireland and the UCC Strategic Research Fund. Mark R Kennedy and Peter M Garnavich acknowledge support for program number 13427 which was provided by NASA through a grant from the Space Telescope Science Institute, which is operated by the Association of Universities for Research in Astronomy, Inc., under NASA contract NAS5-26555. We thank the Vatican Observatory and Richard Boyle for providing us observing time on the VATT. This chapter used data obtained with the MODS spectrographs built with funding from NSF grant AST-9987045 and the NSF Telescope System Instrumentation Program (TSIP), with additional funds from the Ohio Board of Regents and the Ohio State University Office of Research. The LBT is an international collaboration among institutions in the United States, Italy and Germany. The LBT Corporation partners are: The University of Arizona on behalf of the Arizona university system; Istituto Nazionale di Astrofisica, Italy; LBT

Beteiligungsgesellschaft, Germany, representing the Max Planck Society, the Astrophysical Institute Potsdam, and Heidelberg University; The Ohio State University; The Research Corporation, on behalf of The University of Notre Dame, University of Minnesota and University of Virginia. APO is a 3.5m telescope owned and operated by the Astrophysical Research Consortium. This research made use of Astropy, a community-developed core Python package for Astronomy (Astropy Collaboration et al., 2013).

5

Kepler K2 Observations of the Intermediate Polar FO Aquarii

[†]We present photometry of the intermediate polar FO Aquarii obtained as part of the *K2* mission using the *Kepler* space telescope. The amplitude spectrum of the data confirms the orbital period of 4.8508(4) h, and the shape of the light curve is consistent with the outer edge of the accretion disc being eclipsed when folded on this period. The average flux of FO Aquarii changed during the observations, suggesting a change in the mass accretion rate. There is no evidence in the amplitude spectrum of a longer period that would suggest disc precession. The amplitude spectrum also shows the white dwarf spin period of 1254.3401(4) s, the beat period of 1351.329(2) s, and 31 other spin and orbital harmonics. The detected period is longer than the last reported period of 1254.284(16) s, suggesting that FO Aqr is now spinning down, and has a positive $\dot{P}$. There is no detectable variation in the spin period over the course of the *K2* observations, but the phase of the spin cycle is correlated with the system brightness. We also find the amplitude of the beat signal is correlated with the system brightness.

[†]Published in Monthly Notices of the Royal Astronomical Society. "*Kepler K2* Observations of the Intermediate Polar FO Aquarii" Kennedy, M. R., Garnavich, P., Breedt, E., Marsh, T. R., Gänsicke, B. T., Steeghs, D., Szkody, P., Dai, Z. , 2016, *Mon. Not. R. Astron. Soc*, 459,3622

5.1 Introduction

FO Aquarii (FO Aqr) is a binary system containing a magnetic white dwarf (WD) which accretes material from a near-main sequence companion. It was initially discovered as the X-ray source H2215-086 (Marshall et al., 1979) and classified as a cataclysmic variable upon discovery of an optical counterpart by Patterson & Steiner (1983). It is considered the King of the intermediate polar class of cataclysmic variables mainly due to the large amplitude (0.2 mag) of its spin signal (Patterson & Steiner, 1983).

Understanding accretion in binary systems is not only important for CVs, but also for neutron star binaries, where the neutron star primary is spun up to have a period of milliseconds by accretion of matter (Wijnands & van der Klis, 1998) and where the accretion disc can also be truncated by the strong magnetic moment of the neutron star. It is also important for understanding accretion in young stellar objects, low mass black hole binaries and active galactic nuclei, where the primary accretor is a supermassive black hole (Scaringi et al., 2015). Recent work has shown that, despite the differences in the primary star and the energy of these systems, there is a possible common link in their accretion physics. The rms-flux relation, which shows a linear relationship between the flux and amount of "flickering" in a system, seems to hold true for all of these systems (Scaringi et al. 2015 and references therein). It is best seen as a break in the amplitude spectrum of an accreting system, and for CVs, this break occurs at $\sim 10^{-3}$ Hz (Scaringi et al. 2012; Scaringi et al. 2015).

The spin period of the white dwarf primary in FO Aqr was found to be 1254 s (Shafter & Targan 1982; Patterson & Steiner 1983) while optical modulations of the light curve revealed periods of 4.03 h (Shafter & Targan 1982; Patterson & Steiner 1983) and 4.85 h (Patterson & Steiner, 1983). The 4.85 h signal was later confirmed as the orbital period $(2\pi/\Omega)$ of the system by Osborne & Mukai (1989). Modulations at these wavelengths have also been seen in the X-ray and infrared. The beat period ($P_B = 2\pi/\omega - 2\pi/\Omega$) of 1350 s has also been seen in the optical and X-ray. 4 other harmonics of the spin frequency (2ω to 5ω) and various sideband periods have been seen in the X-ray (Beardmore et al., 1998).

The spin period in FO Aqr has fluctuated significantly since it was discovered. In 1982, Shafter & Targan (1982) found it to be 1254.44(1) s, while during

the 1980's the spin period was refined to 1254.4514(3) s and had a positive $\dot{P}$ (Shafter & Macry, 1987), meaning the WD was spinning down. However, observations reported by Steiman-Cameron et al. (1989) from 1987 showed the period to be 1254.4511(4) s with a $\dot{P} \approx 0$. In 1993, Kruszewski & Semeniuk (1993) found the spin period to be 1254.4518(2) s. This period had decreased to 1254.4446(2) s by 1998 (Patterson et al. 1998; Kruszewski & Semeniuk 1998) with a negative $\dot{P}$ reported, suggesting the WD was now spinning up. The period had further decreased to 1254.4441(1) s by 2003 (Williams, 2003), and to 1254.284(16) s by 2004 (Andronov et al., 2005).

There is strong evidence for disc-overflow accretion in FO Aqr. The strength of the spin frequency signal seen in the X-ray and optical amplitude spectrum supports the disc-fed model, while the strength of the beat frequency in the amplitude spectrum supports the stream-fed model. The combination of both of these suggest that FO Aqr accretes via the disc-overflow model (Norton et al. 1992; Hellier 1993).

Here, we present photometry taken of FO Aqr as part of the *K2* mission (Howell et al., 2014), spanning a range of 69 days with a cadence of 1 minute. We analyse the amplitude spectrum, and track the changing amplitudes of the various components that make up the spin modulation, and relate these changes to the changing accretion rate and modes in the system.

5.2 Observations

Observations of FO Aqr were taken by the *Kepler* space telescope as part of the *K2* mission observing campaign field 3 between 2014 Nov 14 and 2015 Feb 3 (MJD 56977-57046). The data are stored under the Ecliptic Plane Input Catalogue (EPIC) identification number EPIC206292760. The 1 min cadence data were extracted using PyKE (Still & Barclay, 2012). *Kepler* fires its thrusters every 48 h, and as such, the target flux of FO Aqr decreased to zero while the spacecraft readjusted. Data taken during the thruster firing had `QUALITY` tags in the *Kepler* FITS file data structure greater than 0, and were removed from the light curve.

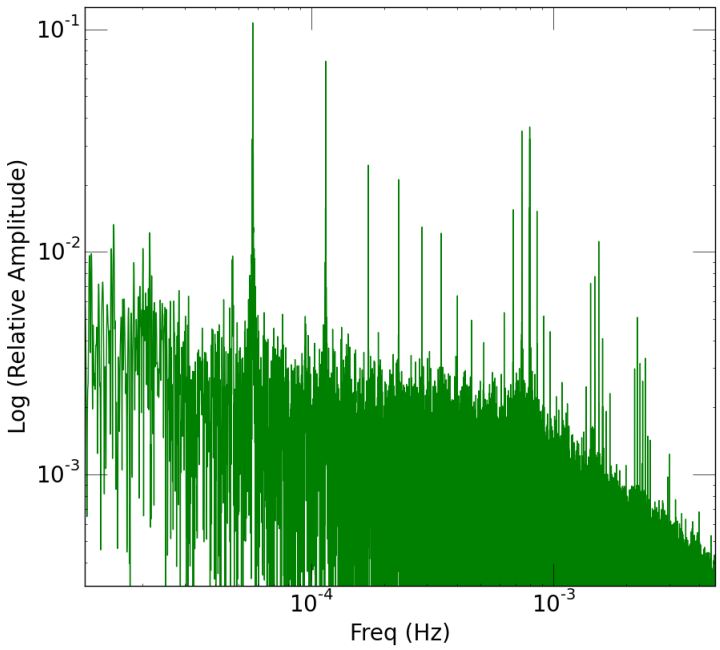

Figure 5.1: The amplitude spectrum of FQ Aqr. The break in the amplitude spectrum of FO Aqr occurs just before 10^{-3} Hz, similar to the break seen in other CVs such as MV Lyrae (Scaringi et al., 2012). The strongest signals are identified in Table 5.1 and shown in greater detail in Figure 5.2.

5.3 Light Curve Analysis

5.3.1 Full Light Curve

The 1 min cadence data were subjected to a Lomb-Scargle Periodogram (Lomb 1976; Scargle 1982) using the astroML python library (Vanderplas et al., 2012) to search for the spin period of the WD and the orbital period. A small section of the amplitude spectrum, around the main/strongest signal in the light curve, can be seen in Figure 5.1 and Figure 5.2. The top left panel of Figure 5.2 shows the orbital frequency of 0.57265×10^{-4} Hz and 9 higher harmonics. The top right panel of Figure 5.2 has a strong frequency peak at $7.972319(2)\times10^{-4}$ Hz (P = 1254.3401(4) s)*. Also visible is the beat frequency of $7.40015(1)\times10^{-4}$ Hz (P_b= 1351.329(2) s). Table 5.1 shows the

*After the publication of the paper which this chapter is based on, we found that the period presented here is inflated from considering the entire dataset in our power spectra. Section 6.3.1.1 of Chapter 6 discusses this, and presents a corrected spin period of 1254.3342(8). We have left this chapter as it was published for consistency, but it should also be noted that the period found in Chapter 6 does not affect the rest of the results of this chapter.

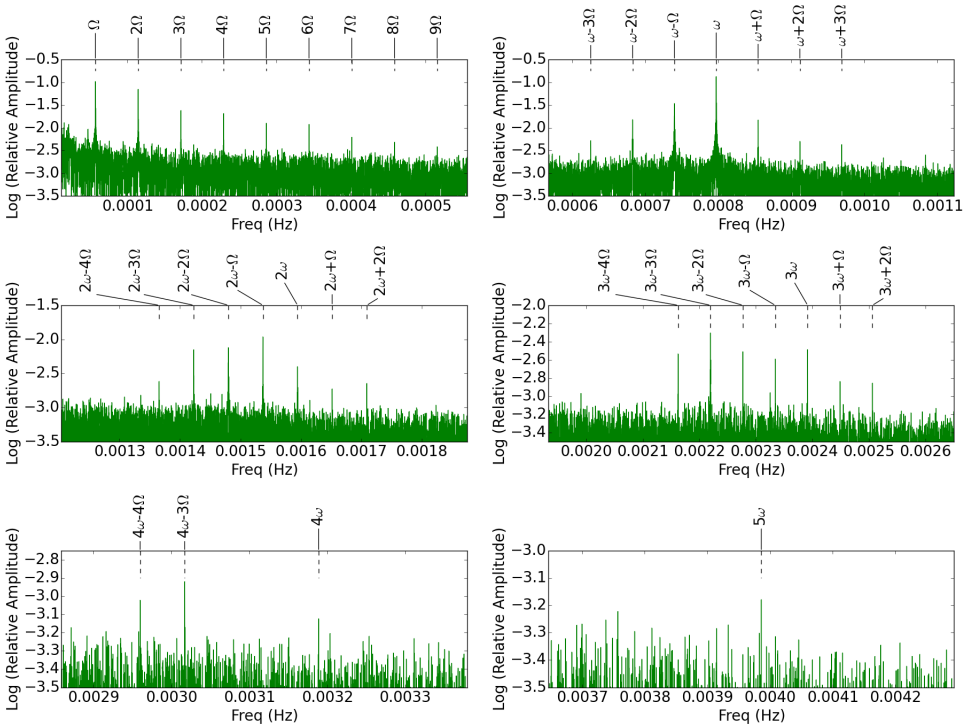

Figure 5.2: Several cuts of the amplitude spectrum, around the main/strongest signals in the light curve. The strongest signals are the orbital frequency Ω at 0.57265×10^{-4} Hz and the spin frequency ω at $7.972319(2)\times10^{-4}$ Hz. A large number of sideband frequencies are also clearly detected and are identified as labelled.

frequency of all detected peaks, along with their amplitudes.

The amplitude spectrum of FO Aqr in Figure 5.1 shows a break at $\sim 10^{-3}$ Hz, where the slope of the continuum in the amplitude spectrum changes. This matches the break seen in other CVs such as MV Lyrae (Scaringi et al., 2012), V1504 Cyg, KIC 8751494 (Van de Sande et al., 2015), BZ Cam, CM Del, KR Aur, RW Tri, UU Aqr, and V345 Pav (Scaringi et al., 2015), and is associated with the rms-flux relation. The high frequency flickering associated with the rms-flux relation is thought to originate from the inner parts of the accretion disc close to the surface of the WD (Scaringi et al., 2012). If this is true, then it is surprising that the frequency break in FO Aqr matches the frequency break in systems such as MV Lyrae, since the inner radius of the accretion disc in FO Aqr, which is truncated by the magnetic field, is much larger than in these non-magnetic systems.

Table 5.1: Frequency peaks seen in Figure 5.2.

	Frequency Hz ($\times 10^{-4}$)	Period h	Relative Amplitude
Ω	0.57265(4)	4.8508(4)	0.101(4)
2Ω	1.1456(8)	2.425(3)	0.071(3)
3Ω	1.7185(8)	1.6164(8)	0.0240(3)
4Ω	2.2912(8)	1.2123(4)	0.0208(3)
5Ω	2.8639(9)	0.9699(3)	0.0126(3)
6Ω	3.4369(8)	0.8082(2)	0.0118(2)
7Ω	4.007(1)	0.6928(2)	0.0061(2)
8Ω	4.5825(8)	0.6062(1)	0.0048(1)
9Ω	5.1547(9)	0.5389(1)	0.0038(1)
		s	
ω	7.972319(2)	1254.3401(4)	0.1367(4)
ω-Ω	7.40015(1)	1351.329(2)	0.0282(4)
ω+Ω	8.54509(1)	1170.262(2)	0.0205(4)
ω-2Ω	6.82652(1)	1464.876(2)	0.0222(4)
ω+2Ω	9.1179(8)	1096.74(6)	0.0050(3)
ω-3Ω	6.2541(8)	1599.0(2)	0.0052(3)
ω+3Ω	9.6907(8)	1031.94(6)	0.0042(2)
2ω	15.9443(8)	627.18(3)	0.0040(2)
2ω-Ω	15.3721(9)	650.53(4)	0.0107(3)
2ω+Ω	16.5177(9)	605.41(4)	0.00185(3)
2ω-2Ω	14.7993(9)	675.71(4)	0.0075(3)
2ω+2Ω	17.090(1)	585.12(4)	0.0023(2)
2ω-3Ω	14.2267(8)	702.91(4)	0.0071(3)
2ω-4Ω	13.6539(8)	732.39(4)	0.0024(2)
3ω	23.9171(9)	418.11(2)	0.0032(2)
3ω-Ω	23.3443(9)	428.37(2)	0.0025(2)
3ω+Ω	24.490(1)	408.34(2)	0.0014(1)
3ω-2Ω	22.7714(8)	439.15(2)	0.0030(2)
3ω+2Ω	25.0628(8)	399.00(1)	0.0013(1)
3ω-3Ω	22.1991(8)	450.47(2)	0.0048(4)
3ω-4Ω	21.6258(8)	462.71(2)	0.0029(2)
4ω	31.8880(9)	313.58(1)	0.00075(1)
4ω-3Ω	30.1714(9)	331.44(1)	0.00120(3)
4ω-4Ω	29.5987(8)	337.85(1)	0.00095(3)
5ω	39.862(1)	250.87 (1)	0.00065(1)

5.3.2 Phased light curve

Hellier et al. (1989) proposed that the companion in FO Aqr eclipses the near side of the accretion disc and suggested an inclination between 65° and 75° , based on the recurring minimum present in the light curve when phased to the orbital period. We now consider if this minimum is present for the 69 days of observations.

We initially phased the light curve using the orbital period from Table 5.1. Then, the phased light curve was binned, and the minimum of the light curve was set to ϕ=0 (T_0(BJD)=2,456,982.2278(6)). Figure 5.3 shows this phased

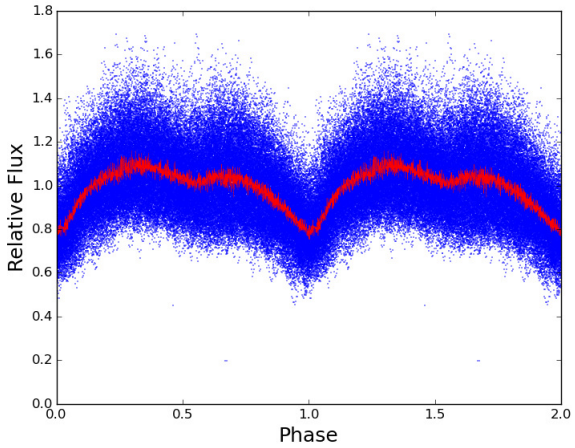

Figure 5.3: The phased light curve of FO Aqr using the orbital period. The 0 phase corresponds to the eclipse of the outer accretion disc as proposed by Hellier et al. (1989). The red light curve uses a bin width of 60 points. The minimum rms of the light curve occurred at ϕ=0

light curve. The eclipse of the outer accretion disc as proposed by Hellier et al. (1989) is clearly visible at ϕ=0. The minimum rms of each bin in Figure 5.3 occured at ϕ=0, which is when the outer part of the accretion disc is being eclipsed. The double-peaked nature of this phased light curve will be discussed in Section 5.4.2.

5.4 Variability of the Spin Signal

Long-term monitoring of IPs usually reveals either a spin up or spin down of the WD, as the magnetic connection between the inner edge of the disc and a magnetic primary star exerts accretion torques on the magnetic primary (Ghosh & Lamb 1978; Ghosh & Lamb 1979). As mentioned previously, FO Aqr has a history of switching from spin up to spin down (Patterson et al., 1998). We now investigate whether we can detect variations in the spin signal of FO Aqr from the *K2* data, and establish how the period has changed since the last reported value of 1254.284(16) s (Andronov et al., 2005).

T_0 for calculating the spin period was set to the maximum of one of the spin cycles located in the middle of the data set, at T_0(BJD)=2,457,012.4554(1).

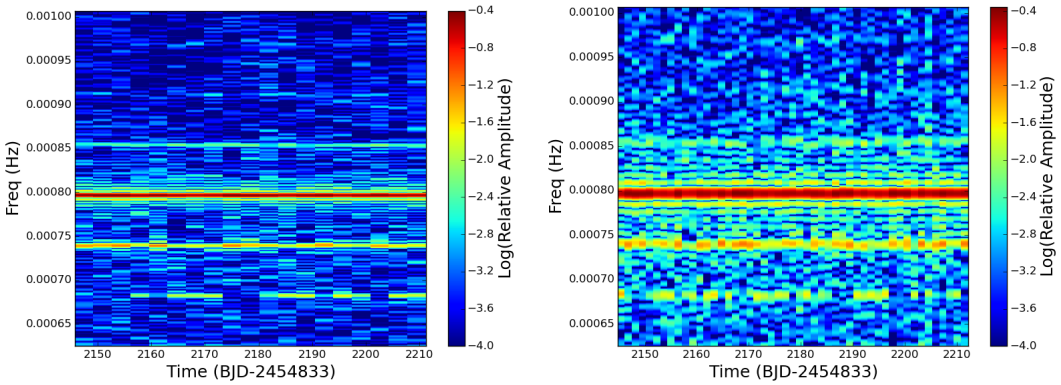

Figure 5.4: *Left Panel*: Running LS Periodogram for 5000 min bins. *Right Panel*: Same, but for 2000 min bins.

5.4.1 Variability of Spin Period

In order to look for variations in the WD spin frequency, the light curve was split into segments and each segment was subjected to a Lomb Scargle Periodogram. The results of 2 different segment sizes (5000 points (3.5 days) per segment and 2000 points (1.4 days) per segment) are shown in Figure 5.4. The WD spin frequency is stable for both segment sizes, as is the beat frequency. The stability of the spin frequency would normally be associated with a stable mass transfer rate over the observations. However, as we will show in Section 5.4.2, the observations were not sensitive to large variations in $\dot{m}$.

The power of the $\omega - 2\Omega$ peak seems to vary with time, but the detectability of this peak is strongly dependent on the size of the data segment used to estimate the amplitude. Hence we attribute this to poor signal-to-noise, as opposed to a physical mechanism within the system. To better see this, consider the segments before T(BJD-2454833)=2190 in both the left and right plots. Using the 5000 point per bin data (left plot), the $\omega - 2\Omega$ peak is clearly visible with strong power. However, using the 2000 point per bin data, this peak is lost in noise. This is also visible in reverse in the bins just after T(BJD-2454833)=2190, where $\omega - 2\Omega$ is lost in noise in the 5000 point per bin data, while it is well detected in the 2000 point per bin data.

The spin period detected by *K2* was 1254.3401(4) s. This period is shorter than the previously recorded periods of 1254.4446(2) s (Patterson et al. 1998; Kruszewski & Semeniuk 1998) and 1254.4441(1) s (Williams, 2003), but longer than the period from 2004 of 1254.284(16) s (Andronov et al., 2005).

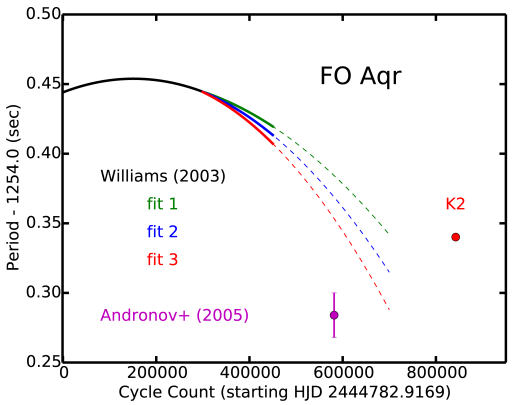

Figure 5.5: The observed spin period changes in FO Aqr (solid line), adopted from Williams (2003) based on 20 years of data. The dashed lines show three possible 4th order extrapolations from Williams (2003) caused by an uncertainty in the cycle count. The period measure by K2 is shown at the right and the errorbars in both period and cycle count are smaller than the size of the point. Andronov et al. (2005) measure a spin period that is shorter than that seen by K2 suggesting that some time between 2005 and 2014, FO Aqr ceased spinning up, and began to spin down.

Figure 5.5 shows three 4th order fits to the data in Williams (2003), along with the period from Andronov et al. (2005) and our *K2* period. This suggests that between 2005 and the beginning of the *K2* observations, FO Aqr ceased spinning up, and began to spin down. Taking the period from the *K2* observations and the period from Andronov et al. (2005) gives an estimate of the current $\dot{P} = 2.0(5) \times 10^{-10}$ s s^{-1}. Williams (2003) estimated $\dot{P}$ to be -4.1×10^{-10} s s^{-1} by 2015 based on their 3rd order ephemeris. However, the large cycle-count ambiguity between the *K2* observations and the observations in Patterson et al. (1998), Kruszewski & Semeniuk (1998) and Williams (2003) prevents a direct linking of these datasets. Williams (2003) also show that relating the observed $\dot{P}$ to the mass accretion rate $\dot{m}$ is non trivial, and requires estimates for the magnetic field of the WD, truncation radius of the accretion disc, equilibrium period of the WD and amount of interaction between the magnetic field of the WD and the secondary. They find that mass accretion rate between $(5 - 8) \times 10^{16}$ g s^{-1} would give the observed $\dot{P}$ in FO Aqr, which is the typical accretion rate assumed for IPs.

5.4.2 Variability of Spin Phase

There is no evidence of a significant $\dot{P}$ from our data alone in Section 5.4.1, so we now look for changes in the phase of the spin signal, which is a more sensitive technique than Section 5.4.1, to confirm the lack of a $\dot{P}$ in the Kepler data.

In order to investigate whether the spin signal of the WD varies over the orbital period, the light curve was phased using the orbital and spin periods. The orbital and spin phase was calculated for each data point in the light curve and then, to align the spin phases, the zero phase of the spin period closest to the zero phase of the orbital period was shifted so that the two zero phases overlapped. As there are several cycles of the spin signal within an orbital period of the binary, we can measure the zero phase of spin signal accurately and align it with the zero phase of the orbital period. This shows the variation due to the spin signal of the white dwarf within a single binary period. We now investigate whether there is a change in the spin phase over the length of the light curve, which will indicate a spin up or spin down of the white dwarf. The resulting phased light curve can be seen in the left panel of Figure 5.6, which shows how the amplitude and phase of the spin signal changes over the course of the orbital period. This is better seen in the 3-D plot in the right panel of Figure 5.6, which show that the amplitude of the spin signal is strongest at the orbital phase of 0.75 and 0.25, and also that the arrival time of the spin signal depends on the orbital phase. At orbital phase 0, the spin signal arrives when expected, but at orbital phase 0.5, the spin signal arrives earlier than expected. This means the phase of the spin signal changes over the orbital period.

The left panel of Figure 5.6 also helps explain the orbital variation seen in Figure 5.3. The two maxima seen per orbit coincide with when the spin signal is strongest in the system. This suggests that around orbital phase 0.25 and 0.75, a maximum of the surface area of the accretion curtains can be seen during the spin pulses, and at other times during the orbital period, components of the system (the secondary, accretion disc, stream) are reducing the amount of light visible from the curtains.

To investigate the change of the spin signal over the entire observation window, the data were split up into sections consisting of 1000 points each

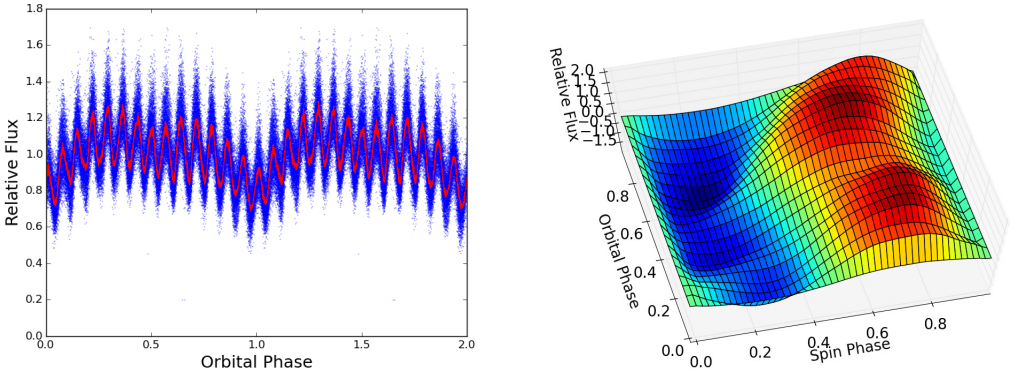

Figure 5.6: *Left Panel*: The phased light curve of FO Aqr, where the spin phase for each successive orbit has been shifted so that 0 spin phase of each orbit corresponds to 0 orbital phase. *Right Panel*: A 3-D representation of the spin signal as a function of the orbital phase. The peak of the spin signal arrives earliest near orbital phase 0.7 and latest just before eclipse.

(~ 50 spin periods per section). A multi-sine function of the form

$$F(t) = \sum_{n=1}^{4} A_n \sin\left(2\pi\left(f_n t + \phi_n\right)\right) \tag{5.1}$$

was fit to the white dwarf spin signal, after the orbital variation in the light curve had been removed. The values for f_1, f_2, f_3 and f_4, which are the spin frequency and the 3 strongest side band frequencies, were set at 7.972319×10^{-4} Hz, 7.40015×10^{-4} Hz, 8.54509×10^{-4} Hz and 6.82652×10^{-4} Hz, respectively, using the values from Table 5.1, and each A_n and ϕ_n was allowed to vary. Figure 5.7 shows $\Delta\phi_1$, the change in phase of the spin signal versus time along with the change in flux from FO Aqr.

Figure 5.7 shows that $\Delta\phi_1$, the change in phase of the spin signal, correlates well with the observed change in flux from FO Aqr. If this change in phase of the spin signal is due to the torque between the accretion disc and the WD, then the radius at which the accretion disc is truncated by the magnetic field can be estimated.

First, assume the instantaneous accretion rate $\dot{m}$ results in a spin up of the WD

$$I\frac{d\omega}{dt} = \dot{m}R_K^2\Omega_K - \alpha \tag{5.2}$$

where I is the moment of inertia of the WD, R_K is the radius at the coupling point where the material connects to the magnetic field and $\Omega_K = \sqrt{GM/R_K^3}$

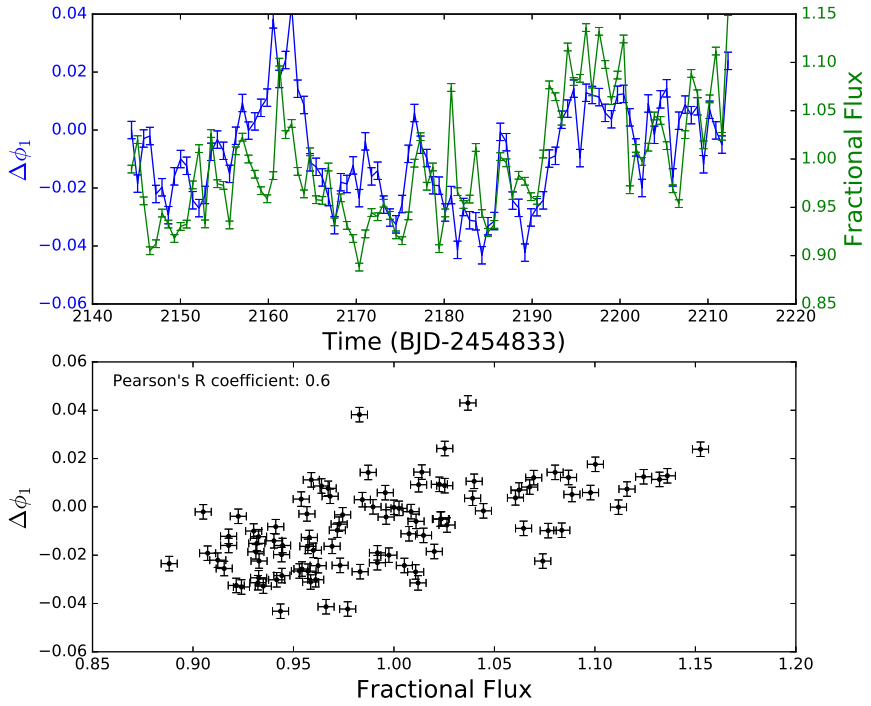

Figure 5.7: The change in phase of the spin signal (blue) and the change in flux relative to the 69 day average (green) versus time. The change in the phase of the spin signal is thought to be related to either the torque exerted on the WD or a change in the mass accretion rate. *Bottom:* A plot of $\delta\phi_1$ versus the change in flux, along with the Pearson's R coefficient for correlation of 0.6.

is the corresponding Keplerian angular velocity. α represents a constant drag on the magnetic field by the disc material. Assuming that the mean accretion rate, $\langle\dot{m}\rangle$, results in no net spin up or down of the WD, α can be expressed as $\alpha = \langle\dot{m}\rangle\sqrt{GMR_K}$, so that

$$I\frac{d\omega}{dt} = \sqrt{GMR_K}\left(\dot{m} - \langle\dot{m}\rangle\right). \tag{5.3}$$

The change in accretion rate above its mean value also results in an increase of the observed flux f. Let β be a constant scaling factor, then $\dot{m} - \langle\dot{m}\rangle = \beta\Delta f$. In this, we have assumed that the relationship between a change in the accretion rate and a change in the observed flux from the system is linear, and the constant relating the two is β. Finally, writing the spin frequency in terms of the phase change $\omega = \dot{\phi}$ and integrating twice, we find,

$$\phi(t) = \phi(0) + \dot{\phi}(0)t + \beta\frac{\sqrt{GMR_K}}{I}\int_0^t\int_0^{t'}\Delta f(t'')dt''dt' \tag{5.4}$$

Δf here is the fractional flux shown in Figure 5.7. We numerically integrated equation 5.4 to determine R_K, i.e. the disc truncation radius required if the observed phase change was due to a spin-up torque. Using a canonical value for the WD mass in a CV ($M \sim 0.87 M_\odot$; Littlefair et al. 2008; Zorotovic et al. 2011) and the average accretion rate for FO Aqr of $\langle \dot{m} \rangle \sim 1 \times 10^{-9} M_\odot$ yr^{-1} calculated by Williams (2003), then we find that $R_K \approx 10^7$ R$_\odot$. The binary separation in a $P_{\rm orb} = 4.85$ h binary such as FO Aqr is ≈1.5 R$_\odot$, so the required R_K is orders of magnitude larger than the binary separation of the system. As such, we attribute the change in the phase of the spin signal to a possible change in either the mass accretion rate or the accretion geometry, as opposed to a genuine variation in the spin phase of the WD.

5.4.3 Modulation of the Spin and Beat Frequencies

Figure 5.8 shows the amplitudes of the various components for each section of data, found in the same way that $\Delta\phi$ was found in the previous section, along with the change in flux relative to the 69 day average for each section of data from the uncorrected *Kepler* light curve.

The amplitude variations seen in the spin and beat signals strongly correlate with the change in flux from the system, as seen in Figure 5.8. This suggests the mass accretion rate in this system is not stable over a timescale of ~ 50 spin periods. However, this is due to the increased sensitivity of this method of fitting sine waves with a fixed period (vs a running periodogram) to small changes in the mass accretion rate.

For the first 50 days of observations, the amplitudes of the $\omega - \Omega$ and the $\omega + \Omega$ signals were similar, and the flux in the system increased and decreased in line with the changing amplitude of the spin signal. The easiest way to have equal power in both of these sideband frequencies was if the accretion geometry was a simple disc, without accretion disc overflow, as proposed by Norton et al. (1992). After day 2192 (BJD-245833), the amplitude of the $\omega - \Omega$ peak began to increase, while the amplitude of $\omega + \Omega$ remained stable. This suggests an increase in the accretion rate in the system at this time, which caused more optical light to be reflected by the source of the beat signal in the system (either the hot spot or the heated side of the companion).The increased accretion rate is supported by the sustained increase in the amplitude in the spin frequency and the overall flux.

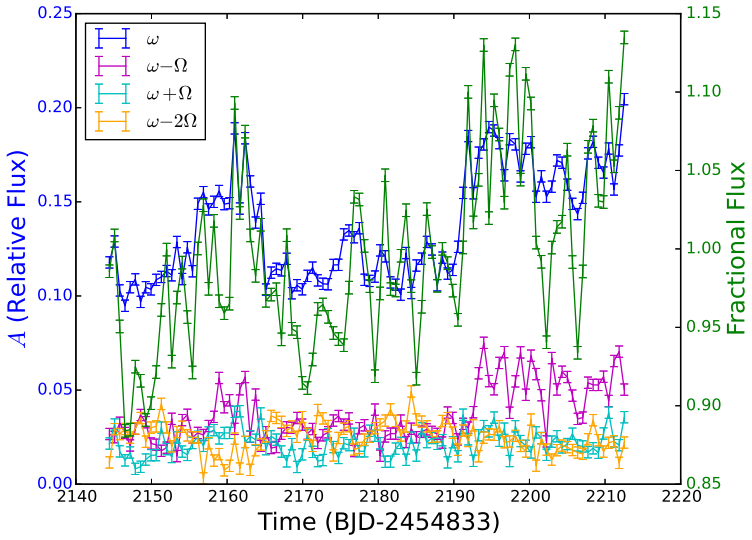

Figure 5.8: The change in amplitudes, measured in relative flux, for the spin signal (blue) and its strongest sidebands (magenta, cyan and orange) for the multi sine curve fit to the spin signal and the change in flux relative to the 69 day average (green) versus time. The change in the amplitude of the $\omega - \Omega$ peak (magenta) is thought to be related to a change in the accretion rate in the system, as it is correlated with the increased flux and increased amplitude of the spin signal.

5.5 Conclusion

The 69 day light curve of FO Aqr taken by the *Kepler K2* mission displays the power of observing an IP continuously for long periods of time. The *K2* data gave an accurate spin period of the WD and determined the varying power in the sidebands of the amplitude spectrum over 69 days of continuous observation. It provided comparable accuracy to ground based observations which took place over decades. This is a true testament to the power of *K2* in studying the time varying mechanisms that are present in magnetically accreting objects.

The eclipse of the outer accretion disc proposed by Hellier et al. (1989) is consistently seen throughout the 69 day light curve. The minimum of the rms is seen at orbital phase zero also, in line with the outer part of the accretion disc being eclipsed. There is no evidence for a precessing disc in the system, which would have shown up as a period longer than the orbital period in the amplitude spectrum.

The spin period has increased to 1254.3401(4) s since the last reported value

from 2005, when FO Aqr was shown to be spinning up. It appears this spin up has ceased, and further short observations over the coming year should be carried out to confirm that FO Aqr is now in a state of spinning down, and to allow for an accurate value of $\dot{P}$ to be determined using our T_0 and spin period.

The *K2* observations will help to establish an unambiguous cycle count for future observations of FO Aqr, which will be important in determining if the current spin down in FO Aqr continues. Future *K2* observations of other IPs may help us to probe changes in their spin frequencies on time scales as short as $\sim$2.5 months.

Acknowledgments

The theory for Section 5.4.2 relating the fractional flux change and the truncation radius of the disc was devloped by Tom Marsh. Elme Breedt and Tom Marsh also heavily contributed in writing this section. This work made use of PyKE (Still & Barclay, 2012), a software package for the reduction and analysis of *Kepler* data. This open source software project is developed and distributed by the NASA *Kepler* Guest Observer Office. Paula Szkody acknowledges support from NSF grant AST-1514737. Mark R Kennedy and Peter Garnavich acknowledge support from the Naughton Foundation and the UCC Strategic Research Fund. Elme Breedt, Tom Marsh and Danny Steeghs are supported by the STFC under grant ST/L000733. Boris Gansicke is supported by the ERC Advanced Grant n. 320964 (WDTracer). Zhibin Dai is supported by CAS “Light of West China” Program.”

6

X-ray observations of FO Aquraii during and after the 2016 low state

We present the first ever X-ray data taken of an intermediate polar, FO Aqr, when in a low accretion state and during the subsequent recovery. The *Swift* and *Chandra* X-ray data taken during the low accretion state in July 2016 both show a softer spectrum when compared to archival data taken when FO Aqr was in a high state. The X-ray spectrum in the low state shows a significant increase in the ratio of the soft X-ray flux to the hard X-ray flux due to a change in the partial covering fraction of the white dwarf from $> 85\%$ to $70^{+5}_{-8}\%$ and a change in the hydrogen column density within the disc from $\mathbf{19}^{+1.2}_{-0.9} \times 10^{22}$ cm^{-2} to $\mathbf{1.3}^{+0.6}_{-0.3} \times 10^{22}$ cm^{-2}. *XMM-Newton* observations of FO Aqr during the subsequent recovery suggest that the system had not yet returned to its typical high state by November 2016, with the hydrogen column density within the disc found to be $\mathbf{15}^{+3.0}_{-2.0} \times 10^{22}$ cm^{-2}. The partial covering fraction varies in the recovery state between 85% and 95%. The spin period of the white dwarf in 2014 and 2015 is refined to 1254.3342(8) s. Finally, we find an apparent phase difference between the high state X-ray pulse and recovery X-ray pulse of 0.17, which may be related to a restructuring of the X-ray emitting regions within the system.

6.1 Introduction

Variability in the optical and X-ray light curves of IPs is often used to characterise which accretion mechanism in the system dominates. The spin period of the WD manifests itself as a pulse in the optical and X-ray light curves. In power spectra of IPs, the strongest signals occur at the spin frequency, ω, the orbital frequency Ω, and the beat frequency $\omega - \Omega$ (which can arise due to either accretion via the "stream-fed" model or the reprocessing of X-rays by a fixed structure in the systems rest frame). Wynn & King (1992) and Ferrario & Wickramasinghe (1999) showed how the strength of these peaks can be used to determine the dominant accretion mechanism in the system. For disc accretion (and assuming a perfect up-down symmetry to the magnetic field), the strongest signals are at ω in both the X-ray and optical power spectra, with additional power at the beat frequency in the optical power spectrum also expected due to reprocessing of the X-ray pulses to an optical signal by fixed structures in the system. For stream accretion, the picture is more complicated. The X-ray power spectrum should show strong power at ω, $\omega - \Omega$, $2\omega - \Omega$ and, depending on the inclination of the system, 2ω. The optical power spectrum should show dominant power at ω for high inclination systems (~ 60 or higher) or at $2(\omega - \Omega)$ for lower inclination systems.

Some IPs, such as AO Psc and V1223 Sgr, have been observed to display low states, where the optical magnitude of the IP can decrease by 1-1.5 mag (Garnavich & Szkody, 1988). The cause of these low states is currently suspected to be star spots passing over the L1 point on the surface of the companion star, temporarily halting mass transfer (Livio & Pringle, 1994). This effect has been explored in detail in the system AE Aqr. Hessman et al. (2000) modelled the surface of the secondary star in AE Aqr and found that nearly 50% of the surface of the secondary is covered by star spots, while (Watson et al., 2006), (Watson et al., 2007), (Hill et al., 2014), and (Hill et al., 2016) found observational evidence for a trail of star spots on the secondary star that led down to the L1 point, which supports the modelling done by Hessman et al. (2000) and suggests a high amount of magnetic activity in the secondary stars. This fits with the idea that starspots may often pass infront of the L1 points in these systems. Before May 2016, FO Aqr, the "King of the Intermediate Polars" which was the name given to FO Aqr by Patterson & Steiner (1983) due to the large optical modulations in the light curve which

are associated with the spin of the WD, had never been observed in a low state, with observations dating back as far as 1923 (Garnavich & Szkody, 1988).

Previous X-ray observations of FO Aqr using the *XMM-Newton* space telescope revealed a complex X-ray spectrum. Evans et al. (2004) observed FO Aqr during its typical high state in 2001, and found a multi-temperature plasma model combined with partial absorbers that had covering fractions as high as 0.94 could describe the spectrum well. They also noted that the ratio of soft to hard X-rays varied over the 4.8508 hour orbital period, suggesting material within the accretion disc or the stream-disc impact region periodically obscured the WD. Parker et al. (2005) performed a study of IPs, and found an orbital modulation in the X-rays is common among IPs. The cause of the orbital modulation is thought to be due to photoelectric absorption by material in the impact region between the ballistic stream and the accretion disc. Pekön & Balman (2012) also noted this behaviour in FO Aqr, and showed how the X-ray spectrum varied over the orbital period.

In April of 2016, FO Aqr was found to be at a V-band magnitude of 15.7 (Littlefield et al., 2016a), compared to its normal V-band magnitude of 13.6. Detailed analysis of the optical photometry taken in this low state revealed that the strongest signal in the power spectrum of FO Aqr was no longer the spin period of 20.9 min, but rather both the spin signal and a signal with a period of 11.26 mins, which is half the beat period of the system (Littlefield et al., 2016b), had equal power. Analysis of this power spectrum led Littlefield et al. (2016) to conclude that the accretion geometry in FO Aqr had transitioned from a disc-fed geometry to a "disc-overflow" geometry, where the disc-fed accretion was generating the spin signal while the stream-fed accretion was generating the half beat signal. This is not the first time that the "disc-overflow" geometry has been applied to FO Aqr (Hellier 1993; Norton et al. 1996). Evidence for "disc-overflow" accretion has also been seen in previous X-ray observations of FO Aqr and the X-ray pulse has been seen to change shape depending on the accretion geometry (Beardmore et al., 1998).

The photometry presented in Littlefield et al. (2016) also revealed that, during the low state, the dominant power in the power spectrum was orbital dependant, with a 22.54 minute period dominating from orbital phase $0.9 < \phi < 1.4$ and the 11.26 minute period dominating from $0.4 < \phi < 0.9$. Phasing the light curves on the known orbital period of the system also revealed the presence of the eclipse around orbital phase 0. This eclipse has

Table 6.1: Details of the various X-ray observations of FO Aqr in 2016. The average count rate of the X-ray observations from *Swift* and *XMM-Newton* are in the 0.3-10 keV band and the *Chandra* count rate is in the 0.3-7 keV band.

Date (YYYY-MM-DD)	Telescope	Average Flux	Duration	Phase Coverage
X-ray		counts s^{-1}	ks	
$2016-07-10$	*Swift*	0.4±3	1.545	0.11-0.15
$2016-07-11$	*Swift*	0.27±0.08	1.19	0.77-0.80
$2016-07-12$	*Swift*	0.24±0.12	1.5	0.06-0.09
$2016-07-13$	*Swift*	0.25±0.08	0.075	0.61-0.61
$2016-07-14$	*Swift*	0.28±0.10	0.73	0.95-0.99
$2016-07-16$	*Swift*	0.46±0.13	1.48	0.28-0.32
$2016-07-26$	*Chandra*	1.3±0.9	18.02	0.00-1.00
$2016-11-13$	*XMM-Newton*	2.6±1.6	45.6	0.00-1.00

been seen previously in FO Aqr during its high state, and is thought to be a grazing eclipse of the outer accretion disc (Hellier et al., 1989). The appearance of this eclipse in the photometry presented by Littlefield et al. (2016) suggests the accretion disc was still present during the low state.

Here, we present X-ray observations of FO Aqr in its first confirmed low state and during its subsequent recovery.

6.2 Observations

6.2.1 *Swift*

Target of Opportunity (ToO) observations of FO Aqr were carried out using the *Swift* Gamma-Ray Burst Telescope for a total of 6.5 ks over several observations as detailed in Table 6.1. The observations were taken using the X-ray Telescope (XRT; Burrows et al. 2000; Hill et al. 2000) instrument operated in photon counting (PC) mode. The data were obtained from the *Swift*-XRT data products generator*. The average flux from FO Aqr in the 0.3-10 keV energy range was 0.3-0.4 counts s^{-1} for the 2006 observations during the high state. The low state had a similar count rate in the *Swift* data of 0.2-0.4 counts s^{-1}. The average V-band magnitude of FO Aqr during these observations was 14.9±0.2.

*http://www.swift.ac.uk/user_objects/

6.2.2 *Chandra*

X-ray observations of FO Aqr were carried out for a total of 18.02 ks starting 2016 Jul 26 7:26AM (UT) (ObsID #18889) using the ACIS-S instrument (Garmire et al., 2003). To mitigate pileup, ACIS-S was run in continuous clocking (CC) mode. CC mode allows for higher time resolution for observations, at the cost of a spatial dimension in the data (rather than the typical 1024×1024 pixel image from a *Chandra* observation, the resultant image from the CC-mode observation was 1024×1 pixel, since one of the spatial dimensions had been collapsed). Source and background regions were extracted from the 1024×1 pixel image. Data reprocessing was carried out using CIAO 4.8.1 (Fruscione et al., 2006) and CALDB 4.7.2. Again, the average V-band magnitude of FO Aqr during these observations was 14.9±0.2.

6.2.3 XMM Newton

FO Aqr was observed by *XMM-Newton* on 2016 Nov 13 20:00 (UT) for a total of 45.6 ks. The EPIC-pn (Strüder et al., 2001) and EPIC-MOS (Turner et al., 2001) instruments were operated in Small Window mode with medium filters inserted. The RGS spectrographs (Brinkman et al. 1998; den Herder et al. 2001) were operated in their normal spectroscopy modes. The optical monitor (OM; Mason et al. 2001) was operated in fast timing mode with the UVW1 filter (effective wavelength= 291 nm, width= 83nm) inserted for the first half of the observations, and the UVM2 filter (effective wavelength= 231 nm, width= 48nm) inserted for the second half of the observation. The data were reduced and analysed using the *XMM-Newton* SCIENCE ANALYSIS SOFTWARE (SAS v15.0.0; ESA: XMM-Newton SOC 2014). The data from the EPIC instruments were processed using the EMPROC and EPPROC tasks. The files used for generating light curves were corrected to Barycentric Julian Date (BJD) using the command BARYCEN. All events were used for generating light curves, while only events that were recorded during good time intervals (GTI) were used for generating spectra. The average V-band magnitude of FO Aqr during the 2016 $XMM-Newton$ observations was 13.7±0.2, which is 0.2 magnitudes fainter than FO Aqr would have been during the archive 2001 *XMM-Newton* observations (Evans et al., 2004) and a magnitude brighter than during the *Chandra* observations.

6.2.3.1 Ground-based Photometry

Simultaneous ground-based optical photometry observations of FO Aqr during the 2016 *XMM-Newton* observations were also obtained. FO Aqr was observed in the V-band using the Sutherland High-Speed Optical Camera (SHOC) on the South African Astronomical Observatory (SAAO) 1m telescope.. A total of 11355 images were taken with a cadence of 1s between 18:15 UTC and 21:25 UTC with the Johnson V-band filter inserted. FO Aqr was also observed using the 80 cm Sarah L. Krizmanich Telescope (SLKT) at the University of Notre Dame. 2724 images were taken with no filter inserted, with a typical cadence of 6s. Finally, a total of 1927 images of FO Aqr were taken with a mean cadence of 21s by various members of the American Association of Variable Star Observers (AAVSO) during the *XMM-Newton* observations. 704 of these images were taken in the Johnson V-band, and the rest were taken without a filter inserted.

6.3 Analysis

6.3.1 Timing Analysis

6.3.1.1 The Spin Period of FO Aqr

The spin ephemeris used by Littlefield et al. (2016) is defined such that maximum optical light from the spin pulse should occur at spin phase 1.0. However, when this ephemeris was used to phase the optical data presented here, the phase of maximum light in the spin-phased optical light curve occurred at phase 0.75. Littlefield et al. (2016) encountered this same issue, and tentatively suggested that the arrival phase of maximum light seemed to be related to the overall brightness of the system (Fig 5 of their paper). Based on their proposal, we would expect the phase of maximum light to be around spin phase 0.95, given FO Aqr's optical magnitude of 13.7 during the *XMM-Newton* observations. Since the predicted and observed phases do not agree, an alternate explanation is necessary.

Our re-analysis suggests that the spin period in the ephemeris used by Littlefield et al. (2016), which was taken from an analysis of the *K2* photometry by Kennedy et al. (2016), was too large. As Kennedy et al. pointed

out, the pulse arrival times during the high state were closely correlated with the system's brightness; thus, when the system brightened for the final third of the *K2* observations, the spin pulse moved to a later phase. To measure how this impacts the measured spin period, we split the *K2* data into two bins based on FO Aqr's brightness, and the measured spin period in each bin (1254.3355 sec) is shorter than the global period (1254.3401 sec), implying that the phase shift of the spin pulse introduced a small error into the measured period.

As an additional test of this result, we simulated the *K2* light curve with a piecewise light curve consisting of four consecutive, non-overlapping sinusoids. All four sinusoids had the same true period (1254.3355 sec), but the second and fourth segments had a phase offset of 0.02 with respect to the first and third segments. The length of each segment and its phase shift were approximated from the *K2* data, and we matched the sampling rate to the median *K2* sampling rate. Power spectra of the simulated bright data (the second and fourth segments) and of the simulated faint data (the first and third segments) both successfully recovered the true input period. However, a power spectrum of the full simulated dataset showed an inflated period of 1254.3407 sec. Thus, our simulations validate our re-analysis of the *K2* spin period, demonstrating that even a relatively small phase shift can interfere with an accurate determination of the spin period. Simple power spectral analysis of a lengthy dataset is not a reliable method of measuring FO Aqr's true spin period; the brightness of the system must be taken into account.

We have calculated a new ephemeris that combines the *K2* data with spin timings from Bonnardeau (2016). We divide up the *K2* data into 85 sections each containing 50 spin cycles and fit a linear ephemeris to each group. The phase shift that correlates with the brightness variations is easily seen in this binned data and results in a root-mean-squared (RMS) variation of 0.25 minutes over the 85 independent measurements. This can be considered the uncertainty floor on any spin timing unless there is a correction for the brightness/phase correlation. We increase the 2014 and 2015 Bonnardeau (2016) error estimates to 0.25 minutes and find a new ephemeris of

$$T(BJD) = 2456977.1057(8) + E * 0.014517757(9) \tag{6.1}$$

which is a period of 1254.3342(8) seconds. This is consistent with the *K2* spin period found by splitting the measurements by brightness. We show in Fig. 6.1

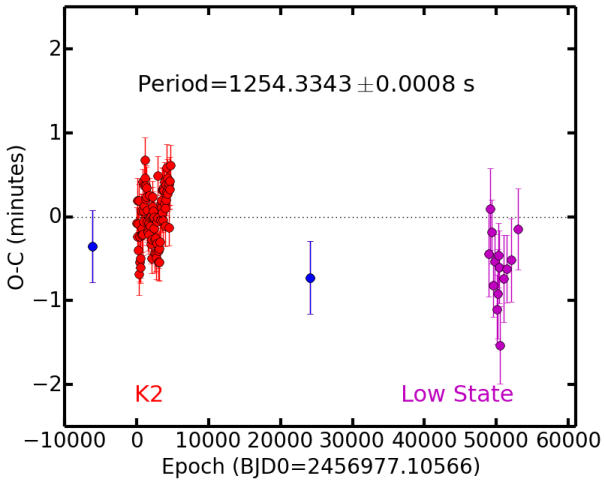

Figure 6.1: The residuals to the new ephemeris. The *K2* measurements (red) show a coherent variation that correlates with brightness changes. The blue points are Bonnardeau (2016) measurements for 2014 and 2015. The timing measurements at the end of the low state were not used to calculate the new ephemeris, but are clearly consistent with an extrapolation into 2016.

the residuals to the ephemeris. We include spin timing measurements obtained toward the end of the faint state, when individual spin pulses were sufficiently strong to be easily identifiable in optical light curves. These spin timings are consistent with this new ephemeris and suggests no major phase shift occurred across the low state. Taken in isolation, the spin timing residuals shown in Fig. 6.1 imply an even shorter period would be a better fit to the 2014 to 2016 data. However, the long-term period changes seen in FO Aqr require high-order polynomial solutions that are beyond the scope of the current data.

When propagated across the two-year span between the *K2* observations and the low state, the error accumulates into a large phase shift ($\sim$0.2 in phase) of the spin pulse towards earlier phases, similar to the one observed in Littlefield et al. (2016). There might have been a true phase shift during the low state, but the one reported in that paper was not physical in origin.

6.3.1.2 X-ray

The X-ray light curves of FO Aqr taken by *Chandra* in 2016 (Fig. 6.2), *XMM-Newton* in 2001 (Fig. 6.3) and *XMM-Newton* in 2016 (Fig. 6.4) show very different behaviours. An X-ray pulse was visible in the full, soft (0.3-2 keV) and hard (2-7 keV) light curves from the *Chandra* observations of FO Aqr

when the system was in the low state, with most hard X-ray pulses having a soft X-ray counterpart. The archived *XMM-Newton* data from 2001 show a very different behaviour, with the X-ray pulses only visible in the hard X-rays, with little obvious variability in the soft X-rays. The 2016 *XMM-Newton* light curves, taken when the system was returning to the high state (which for the rest of this chapter is referred to as the "recovery" state), showed variability somewhere in between the low and high states, with some hard X-ray pulses having a soft X-ray counterpart, while other hard X-ray pulses had no detectable counterparts. The orbital phases of the *Chandra* and 2016 *XMM-Newton* data were calculated using the ephemeris of

$$T(HJD) = 2456982.2278 + 0.20205976(E) \tag{6.2}$$

which is a combination of the mid-eclipse time taken from (Kennedy et al., 2016) and the orbital period from (Marsh & Duck, 1996), while the orbital phases of the 2001 *XMM-Newton* data were calculated using the ephemeris of

$$T(HJD) = 2452041.806 + 0.20205976(E) \tag{6.3}$$

which is a combination of the time of minimum light taken from Evans et al. (2004) and the orbital period from Marsh & Duck (1996).

To understand how the variability in the soft and hard X-rays has changed, a Lomb-Scargle periodiogram (LSP; Lomb 1976; Scargle 1982) was applied to the light curves to search for the strongest frequencies in each energy band and observation set. The LSP of the *Chandra* and XMM observations is shown in Fig. 6.5, and highlights the dramatic change in the variability of the soft X-rays coming from FO Aqr.

6.3.2 Spectral Analysis

6.3.2.1 Low State

The full X-ray spectrum from 0.3-7.0 keV was extracted from the *Chandra* ACIS-CC data using the CIAO analysis software, and analysed using the HEASARC software package XSPEC (version 12.9.0). Fig. 6.6 shows the X-ray spectrum from the full exposure.

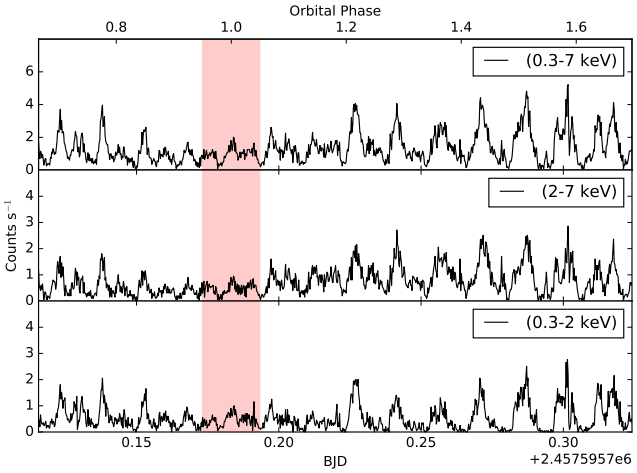

Figure 6.2: The full, hard (2-7 keV) and soft (0.3-2 keV) light curves taken by *Chandra* of FO Aqr in the low state in July 2016. The count rate in the soft and hard X-rays is comparable, and both components contribute nearly equally to the variability. This behaviour is very different to the X-ray light curves taken by *XMM-Newton* in 2001, when FO Aqr was in its high state. The highlighted region shows the data taken between orbital phase 0.95 and 0.05, which is when the grazing eclipse of the system has been observed previously. The orbital phase was calculated as described in the text.

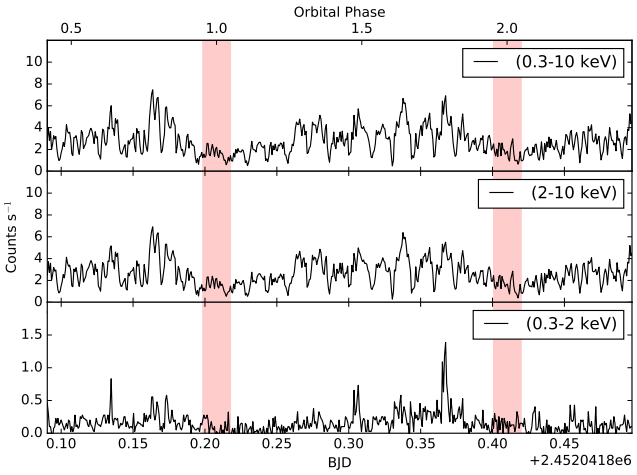

Figure 6.3: The full, hard (2-10 keV) and soft (0.3-2 keV) light curves from 2001, taken using the EPIC-pn instrument onboard *XMM-Newton* when the system was in the high state. The count rate in the soft X-rays is much lower than in the hard, and the variability of the source is only weakly detected in the soft X-rays.

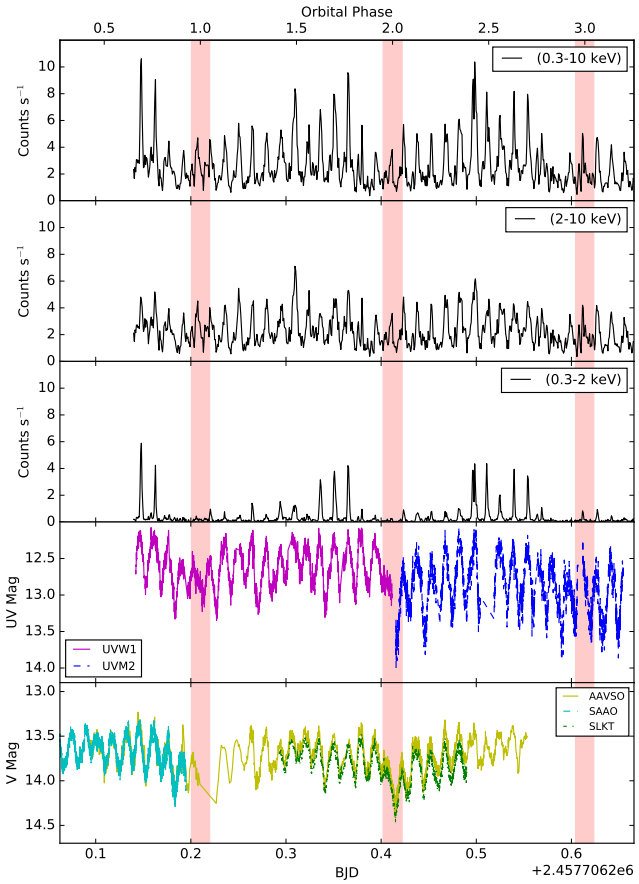

Figure 6.4: The full (1st panel), hard (2-10 keV; 2nd panel) and soft (0.3-2 keV; 3rd panel) X-ray light curves from 2016, taken using the EPIC-pn instrument onboard *XMM-Newton* when the system was returning to the high state along with the UV light curve from the OM (4th panel), the ground based V-band data taken by AAVSO observers (5th panel, yellow), the SAA0 1m telescope (5th panel, magenta) and the SLKT (5th panel, green). The variability in the soft X-rays lies somewhere between the high variability seen in the low state *Chandra* data and the constant flux seen in the 2001 *XMM-Newton* data. The optical and UV pulses arrived at the same phase as the X-ray pulses. The highlighted region again shows data taken between orbital phase 0.95 and 0.05.

Evans et al. (2004) previously fit the *XMM-Newton* PN and MOS X-ray spectrum using the complex model of an interstellar absorber, two partial absorbers (one representing absorption by the accretion curtains and one representing absorption by the accretion disc) and three single temperature thin thermal plasma (MEKAL) components, alongside various GAUSSIAN components to model emission lines. The resulting fit, shown in Fig. 3 and described in Table 1 of Evans et al. (2004), models the spectrum very well, with a $\chi^2_R = 1.03$.

Initially, the complex model of Evans et al. (2004) was fit to the low state

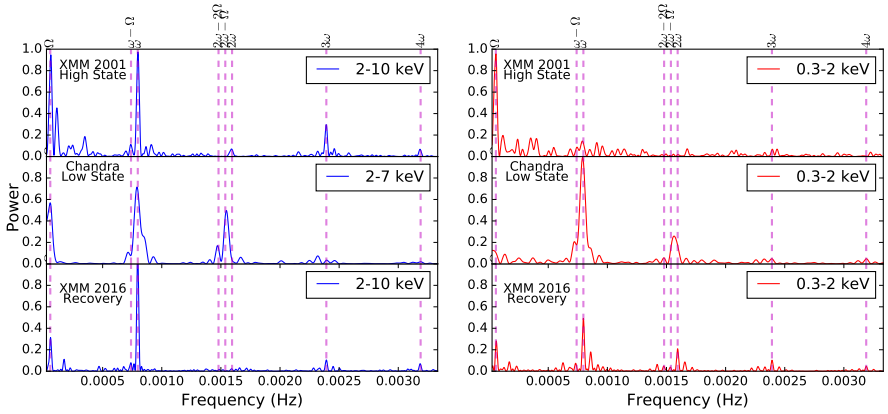

Figure 6.5: A Lomb Scargle periodogram (LSP) of the archive *XMM-Newton* (top), *Chandra* (middle) and 2016 *XMM-Newton* (bottom) light curves. The spin frequency (ω) shows significant power in all three data sets in the 2-10 keV band. However, hard (left plots) and soft (right plots) X-ray contributions to the various peaks in the LSP vary significantly between the high, low and recovery states. To make direct comparison easier between the three data sets, the power of each spectrum has been normalised such that the strongest peak in power spectrum of the combined soft and hard data had a power of 1.

X-ray spectrum (XSWABS*XSPCFABS*XSPCFABS*(XSMEKAL+XSMEKAL+XSMEKAL) in XSPEC). While this model fit the spectrum well, with a $\chi^2_R = 0.788$, many of the fit parameters were very poorly constrained, and significantly different to Evans et al. (2004). Most notable were the lower absorption columns in both of the partial absorber components, alongside the unbounded covering fractions, and also the lack of a constraint on the highest temperature MEKAL component.

The *Chandra* spectrum was next fit using a very basic model common to many IPs: a simple interstellar absorber (TBABS), partial absorber (PARTCOV*TBABS) and a single temperature thin thermal plasma (MEKAL). The resulting fit, given in Table. 6.2 and shown in Fig. 6.6, described the low state X-ray spectrum well.

Fig. 6.7 shows the average spectrum from the 2006 and 2016 observations of FO Aqr using the XRT instrument on the *Swift* spacecraft. Despite the similar X-ray count rates detected by *Swift* between 2006 and 2016, it is immediately obvious that the energy distribution has changed, with the low state spectrum appearing softer than the high state.

The 2016 spectrum was modelled using a similar model to that used for the *Chandra* data, and the resulting best fit is shown in Fig. 6.6, with the best fit parameters listed in Table 6.2. The parameters from both the *Chandra* and

Table 6.2: The best fit models to the 2016 *Chandra*, *Swift* and *XMM-Newton* data, and the 2006 *Swift* data. Errors quoted are at the 3σ level. The plasma temperature for the *Swift* 2006 modelling of FO Aqr was fixed at 29.7 keV based on IBIS observations (Landi et al., 2009).

		Chandra	*Swift*		XMM
Component	Parameter	2016	2016	2006	2016
TBABS (INTERSTELLAR)	N_H (10^{22} cm^{-2})	$0.02^{+0.08}_{-0.02}$	$0.05^{+0.2}_{-0.05}$	$0.78^{+0.19}_{0.18}$	$0.09^{+0.06}_{-0.04}$
TBABS (CIRCUMSTELLAR 1)	N_H (10^{22} cm^{-2})	$1.3^{+0.6}_{-0.3}$	$1.5^{+2.7}_{-0.7}$	$7.2^{+1.2}_{0.9}$	$15^{+3.0}_{-2.0}$
PARTCOV 1	cvf	$0.70^{+0.05}_{-0.08}$	$0.70^{+0.15}_{-0.26}$	$0.82^{+0.04}_{-0.03}$	$0.71^{+0.04}_{-0.05}$
TBABS (CIRCUMSTELLAR 2)	N_H (10^{22} cm^{-2})	-	-	-	$3.6^{+0.6}_{-0.5}$
PARTCOV 2	cvf	-	-	-	0.89±0.02
MEKAL	kT (keV)	>15	>7	-	>28
	Abundance	1.0	1.0	-	$0.5^{+0.3}_{-0.2}$
	norm	$0.160^{+0.365}_{-0.094}$	$0.83^{+1.5}_{-?}$	-	$0.037^{+0.002}_{-0.002}$
MEKAL	kT (keV)	-	-	-	$0.11^{+0.03}_{-0.02}$
	Abundance	-	-	-	$0.5^{+0.3}_{-0.2}$
	norm	-	-	-	$0.025^{+0.05}_{-0.02}$
BBODY	kT (keV)	-	-	61^{+8}_{-6}	-
BREMSS	kt (keV)	-	-	[29.7]	-
GAUSSIAN	Centre	-	-	-	$6.49^{+0.04}_{-0.02}$
	Sigma	-	-	-	$0.17^{+0.04}_{-0.05}$
	norm ($\times 10^{-4}$)	-	-	-	$1.3^{+0.3}_{-0.3}$
	χ^2_R	1.14	1.01	0.92	1.36

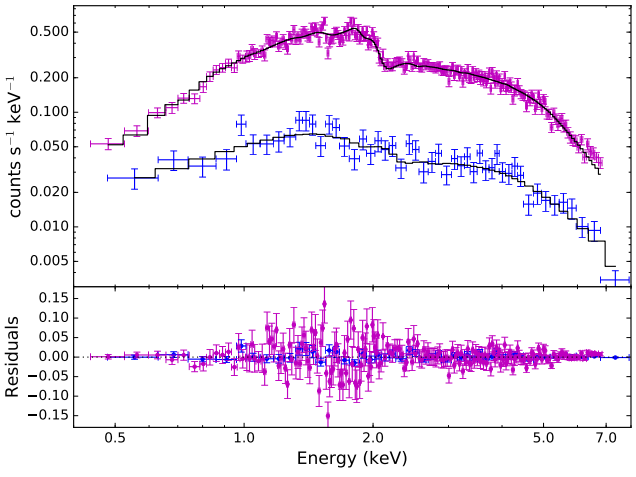

Figure 6.6: The observed X-ray spectrum of FO Aqr during its low state taken with the ACIS instrument onboard the *Chandra* spacecraft (magenta, top) and using the XRT instrument on *Swift* (blue, bottom). The black histogram shows the best fit models as described in Table 6.2.

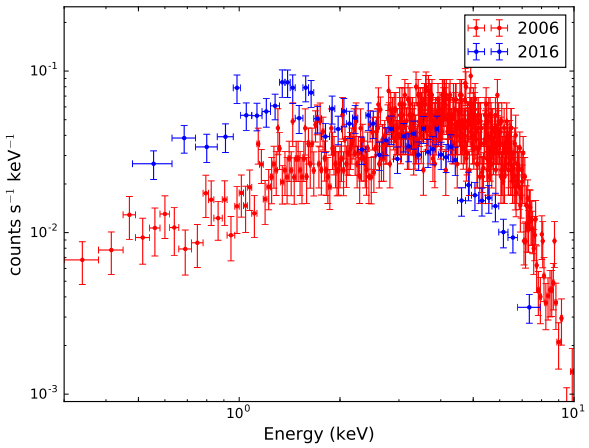

Figure 6.7: The average X-ray spectrum of FO Aqr taken using the *Swift* XRT during the 2 different states. The 2006 data (red) were taken during the high state, while the 2016 data were taken during the low state. Both sets of data are consistent with emission from a hot plasma with a temperature $> 7keV$. The differences in the spectra arise due to a change in the circumstellar absorbers, which is discussed in detail in Section 6.4.2.

Swift modelling are consistent with each other. The unabsorbed flux in the 0.3-10 keV band was estimated from the models in XSPEC to be $(3.1 \pm 0.2) \times 10^{-11}$ erg cm^{-2} s^{-1} for the *Chandra* data and $(2.6 \pm 0.4) \times 10^{-11}$ erg cm^{-2} s^{-1} for the *Swift* data.

The high state spectrum of FO Aqr taken by *Swift* in 2006 was previously modelled using an absorbed, partially covered Bremsstrahlung and black body model (Landi et al., 2009). The best fit parameters from this model are listed in Table 6.2.

6.3.2.2 Recovery State

The full X-ray spectrum from 0.3-10.0 keV was extracted from the *XMM-Newton* EPIC-pn, -MOS1 and MOS2 instruments and analysed using the HEASARC software package XSPEC (version 12.9.0). Fig. 6.8 shows the X-ray spectrum extracted using events recorded during good time intervals only.

As with the low state data, the recovery spectrum was initially fit using the model of Evans et al. (2004). The spectra from the EPIC-pn, -MOS1 and -MOS2 spectra were fit simultaneously, allowing for a constant calibration factor between the instruments.

Again, the best fit failed to constrain many of the parameters. A simplified

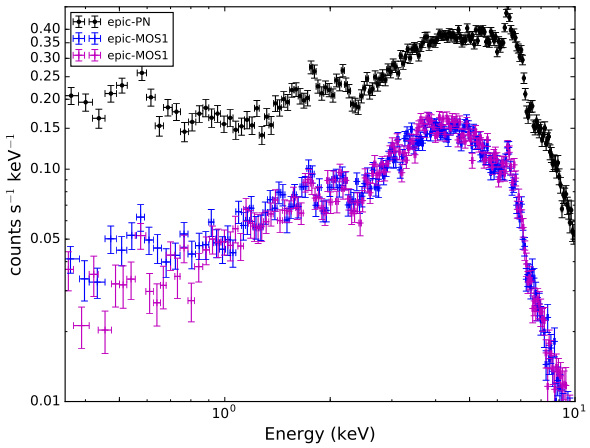

Figure 6.8: The observed X-ray spectrum of FO Aqr during its recovery state taken with the EPIC-pn, -MOS1 and -MOS2 instruments onboard the *XMM-Newton* spacecraft.

version of the model used by Evans et al. (2004) was next used: a two MEKAL model with a interstellar absorber and two circumstellar absorbers (TBABS*(TBABS*PARTCOV)*(TBABS*PARTCOV)*(XSMEKAL+XSMEKAL)). While the initial fit was good, there were large residuals around the 6.4 keV Fe line. A GAUSSIAN component was added to the model to account for these residuals, as was also done by Evans et al. (2004). This model fit the three spectra with a $\chi^2_R = 1.33$, and can be seen for the EPIC-pn spectrum in Fig. 6.9. The best fit parameters are given in the last column of Table 6.2. The unabsorbed flux in the 0.3-10 keV band for the recovery state model was $(7.2 \pm 0.6) \times 10^{-11}$ erg cm^{-2} s^{-1}.

6.4 Discussion

6.4.1 Long Term Recovery

Fig. 6.10 shows the unabsorbed 0.3-10 keV X-ray flux from the low state observations taken by *Swift* and *Chandra* and from the recovery state observations taken by *XMM-Newton*, alongside the unabsorbed flux of $(19.7 \pm 0.2) \times 10^{-11}$ erg cm^{-2} s^{-1} from the 2001 *XMM-Newton* observations. It is clear from this plot that by November 2016, FO Aqr had still not fully recovered from the low state. This is unsurprising as Littlefield et al. (2016) estimated the e-folding time (which is the time taken for the flux to change by

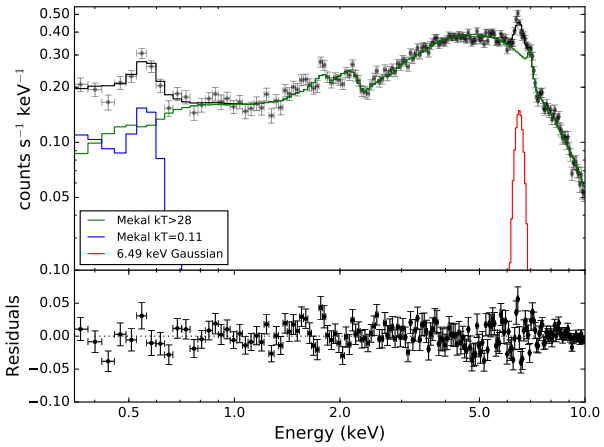

Figure 6.9: The X-ray model (black histogram) as described in the text for the EPIC-pn data, taken in 2016 when FO Aqr was in the recovery state. The individual components of the model are also shown.

a factor of e) for the optical light in FO Aqr to be 115±7 days. Based on a scaled fit of the same model used by Littlefield et al. (2016) to the X-ray fluxes shown in Fig. 6.10, we find that the e-folding time for the X-ray recovery is 124±10 days, which is in agreement with the optical recovery time from Littlefield et al. (2016). This fit also suggests that if FO Aqr continues recovery uninterrupted, then it should return to its typical high state flux by March 2017.

Based on our spectral modelling and assuming the unabsorbed 0.3-10 keV X-ray flux is proportional to the mass accretion rate, the change in X-ray flux between the high state and the low state suggests that the mass accretion rate in the system decreased by a factor of 7 at the start of the low state.

6.4.2 The softened X-ray spectrum

The power spectrum of the *Chandra* X-ray light curves and the energy spectrum of the *Chandra* and 2016 *Swift* data show a significant change when compared to the high state *XMM-Newton* and *Swift* data, and also when compared to the recovery state *XMM-Newton* data. The power spectrum of the *Chandra* data shows a near-equal distribution in power between the soft and hard X-rays at the spin frequency of the WD. There is also evidence of a strong signal at the beat period, which was not detected in the 2001 *XMM-Newton* observations. Additionally, the $2\omega - 2\Omega$ and $2\omega - \Omega$ peaks show strong power

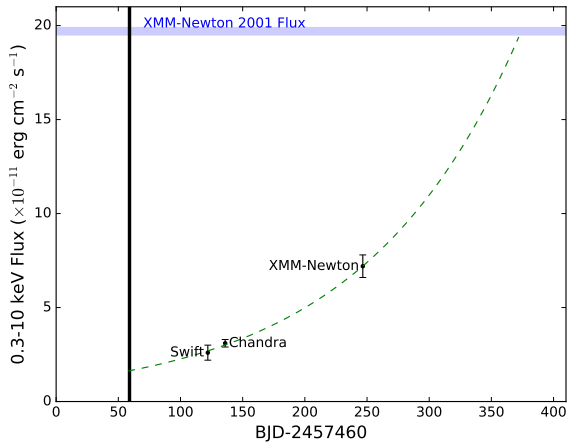

Figure 6.10: The long term X-ray recovery of FO Aqr. The blue shaded region shows the unabsorbed X-ray flux from the modelling of the 2001 *XMM-Newton* data, when FO Aqr was in its high state. The black line shows the approximate time when FO Aqr was at its faintest. The green-dashed line shows the exponential fit from Littlefield et al. (2016) rescaled to fit the X-ray data, and is extended to show what the X-ray flux of FO Aqr should have been during faintest light, and when the X-ray flux should return to its normal high state. While a low order polynomial would also fit this data, we fit an exponential in line with the model used in Littlefield et al. (2016).

in the hard X-rays and the 2ω peak shows strong power in the soft X-rays in 2016, compared to the 2001 data, when only the 2ω was detected, and only in the hard X-rays.

The interpretation of the change in the power spectrum is not an easy task. Based on the power spectra of optical data taken in the low state, Littlefield et al. (2016) suggested that FO Aqr had possibly transitioned into a "disc-overflow" accretion geometry. Following the analysis in both Wynn & King (1992) and Ferrario & Wickramasinghe (1999), the strong power at ω in 2001 is indicative of disc-fed accretion, while the strong power at $2\omega - \Omega$ and the power visible at $\omega - \Omega$ and Ω in the 2016 *Chandra* supports the claim by Littlefield et al. (2016) that accretion had switched primarily to the stream-fed geometry.

X-rays with an energy > 5 keV in IPs are thought to be generated at the top of the accretion column and are rarely absorbed by circumstellar material, while lower energy X-rays come from the accretion flow close to the surface of the WD and are subject to absorption through the accretion flow itself (this is called the self-absorption accretion curtain model; Rosen et al. 1988). The drop in hard X-ray flux visible in the 2016 *Swift* spectrum when compared to

the 2006 spectrum suggests less hard X-rays were being produced, leading to the conclusion that the mass accretion rate had decreased. The increase in the soft X-ray flux suggests there was less material in the curtains and whatever remains of the accretion disc to absorb soft X-rays. This is supported by the modelling of the various datasets, which shows a much lower circumstellar absorption density ($N_H = 1.3^{+0.6}_{-0.3} \times 10^{22}$ cm^{-2}) in 2016 than in 2006 ($N_H = 7.2^{+1.2}_{-0.9} \times 10^{22}$ cm^{-2}; *Swift*) and in 2001 ($19.0^{+1.2}_{-0.9} \times 10^{22}$ cm^{-2}; *XMM-Newton*).

6.4.3 The Recovery State

Comparing the power spectrum of the *XMM-Newton* data taken during the recovery state with the low state *Chandra* data and the high state *XMM-Newton* data suggests that FO Aqr had not fully returned to its typical high state by November 2016. The signal at $2\omega - \Omega$ visible in the *Chandra* data during the low state had disappeared by the time the *XMM-Newton* data were taken, and in the hard X-rays, the power spectrum of the recovery state resembled the power spectrum of the high state data from 2001. However, the power spectrum of the soft X-rays from the recovery state still showed significant power at the ω peak, which was not visible in the high state.

The implications of the recovery state power spectrum on the accretion geometry are important. The orbital modulation, Ω, was detectable in both the hard and soft X-ray power spectra. However, the power of the orbital signal was much lower than during the high state observations in 2001. The weaker orbital modulation in the recovery state data is consistent with the photoelectric absorption model of Parker et al. (2005). In this model, cool material around the impact region between the stream and the accretion disc responsible for absorbing X-rays and leads to a orbital modulation in X-ray light curves. In the low state, due to the lower accretion rate, this impact region should be less dense, leading to less photoelectric absorption, which would weaken the orbital modulation.

The loss of power at the $2\omega - \Omega$ and $\omega - \Omega$ peaks suggest that FO Aqr had switched back to a disc-fed accretion system when the 2016 *XMM-Newton* observations were taken. The signal at ω in the soft X-ray power spectrum also implies that the system had still not fully recovered. A comparison of the soft X-ray light curves from 2001 (Fig. 6.3) and 2016 (Fig. 6.4) shows that, during

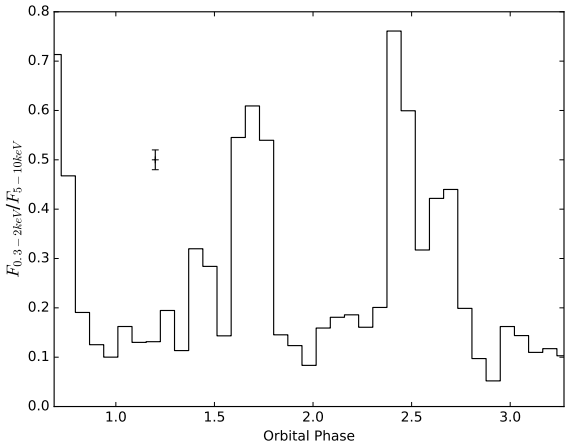

Figure 6.11: The softness ratio, defined as the flux in the 0.3-2 keV band divided by the flux in the 5-10 keV band, versus the orbital phase for the *XMM-Newton* observations taken during the recovery state in 2016. The softness ratio displays a minimum around orbital phase 0, and show maxima when soft X-ray pulses were visible in the 0.3-2 keV light curve. The data have not been folded on orbital phase.

the high state, no soft X-ray pulses are visible, but in the recovery state, an occasional soft X-ray pulse is detected. However, in the recovery state, strong soft X-ray pulses were never detected around orbital phase $\phi = 0$, suggesting an orbital phase dependence of the material which is absorbing the soft X-rays.

To better see this, light curves were extracted from the EPIC-pn instrument in the 0.3-2.0 keV and the 5.0-10.0 keV bands, and the ratio of these bands calculated for the duration of the *XMM-Newton* observation. Fig. 6.11 shows this softness ratio versus the unfolded orbital period. The light curve was binned to 1254.3343 s, the spin period of the WD, to remove effects of the spin pulse on this plot.

From Fig. 6.11, it is clear that the softness ratio in FO Aqr varies over the orbital period, but does not vary by the same amount during each orbit. For example, during the first full orbit observed by *XMM-Newton*, the softness ratio peaks with a value of 0.60 ± 0.02 at orbital phase 0.7, while in the next full orbit, the softness ratio peaks with a value of 0.76 ± 0.3 at orbital phase 0.4. However, for all 3 orbits observed, the softness ratio reaches a minimum around or just before orbital phase 0.0.

To better quantify the changes in the spectrum between periods when soft X-ray pulses are and are not visible, the EPIC-pn, -MOS1 and -MOS2 data were split up. A spectrum was constructed out of events which arrived when soft

Table 6.3: The parameters for modelling the two spectra shown in Fig. 6.12. The two models have nearly identical components, with the exception of the covering fractions for the partial absorbers. The change in the partial absorbers is thought to be the reason for the appearance of the occasional soft X-ray pulse in the 0.3-2 keV band of the recovery state data.

Component	Parameter	Soft pulses	No Soft pulses
TBABS (INTERSTELLAR)	N_H (10^{22} cm^{-2})	0.10±0.07	$0.07^{+0.09}_{-0.06}$
TBABS (CIRCUMSTELLAR 1)	N_H (10^{22} cm^{-2})	$13^{+6.0}_{-4.0}$	$15^{+3.0}_{-2.0}$
PARTCOV 1	cvf	$0.65^{+0.09}_{-0.11}$	0.74±0.05
TBABS (CIRCUMSTELLAR 2)	N_H (10^{22} cm^{-2})	2.9±1.0	$3.9^{+0.7}_{-0.6}$
PARTCOV 2	cvf	$0.81^{+0.04}_{-0.07}$	0.95±0.01
MEKAL	kT (keV)	>20	> 29
	Abundance	$0.3^{+0.5}_{-0.25}$	$0.5^{+0.4}_{-0.3}$
	norm	$0.036^{+0.005}_{-0.003}$	0.037±0.002
MEKAL	kT (keV)	<0.13	$0.12^{+0.05}_{-0.03}$
	Abundance	$0.3^{+0.5}_{-0.25}$	$0.5^{+0.4}_{-0.3}$
	norm	$0.05^{+0.2}_{-0.04}$	$0.02^{+0.05}_{-0.01}$
GAUSSIAN	Centre	$6.49^{+0.07}_{-0.05}$	$6.05^{+0.05}_{-0.04}$
	Sigma	$0.17^{+0.10}_{-0.07}$	$0.18^{+0.08}_{-0.05}$
	norm ($\times 10^{-4}$)	$1.3^{+0.5}_{-0.4}$	1.3±0.3
	χ^2_R	1.23	1.38

X-ray pulses were visible in the recovery state light curve (see the highlighted regions in the top panel of Fig. 6.12). Another spectrum was constructed out of events which arrived at all other times (during the good time interval). Both of the EPIC-pn spectra are visible in the middle panel of Fig. 6.12, and show that the spectrum of FO Aqr when these soft X-ray pulses are visible has a significantly stronger soft component compared with when there are no soft X-ray pulses. The same model that was fit to the spectrum in Section 6.3.2.2 was fit to the -pn, -MOS1 and -MOS2 spectra for these separate time intervals. The results of the fitting can be seen in Table 6.3.

The two models in Table 6.3 are nearly identical - the interstellar absorber, MEKAL values and GAUSSIAN values all lie within 3σ of each other in both fits. However, there is a significant difference in the partial covering fraction of the second circumstellar absorber between the two models. When the soft X-ray pulses are present, the partial covering fraction is $0.81^{+0.04}_{-0.07}$, while when no soft X-ray pulses are present, this covering fraction is 0.95±0.01 (the errors here are quoted at the 3σ level). This suggests that for part of the orbit, the region

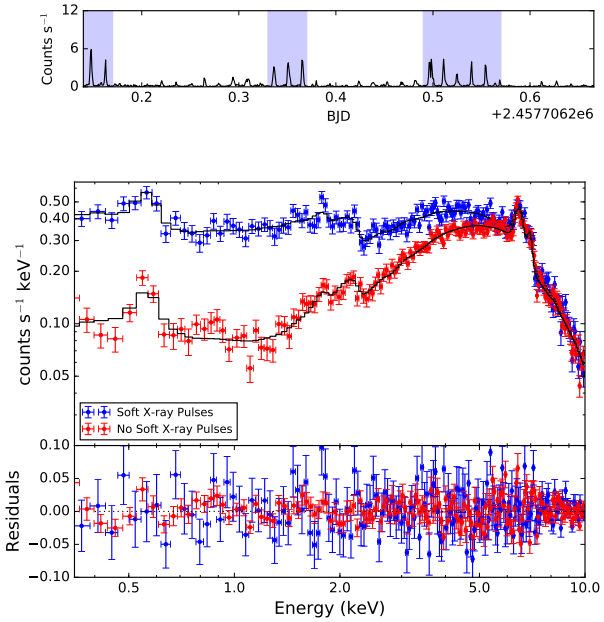

Figure 6.12: The top panel shows the 0.3-2 keV light curve from *XMM-Newton*. The middle panel shows the spectrum extracted from the highlighted times in the top panel (upper curve, blue) and the spectrum extracted when all other events are used (bottom curve, red). The blue spectrum has a significantly softer component than the red spectrum, which is characterised by lower partial-covering fraction in the partial absorbers (see Table 6.3).

which is producing the soft X-ray component is obscured by an optically thick region.

6.4.4 X-ray and Optical Pulse

6.4.4.1 Low State

Fig. 6.13 shows the X-ray light curve for the 0.3-2 keV, 2-4 keV, 4-6 keV and 6-7 keV energy bands phased using Equation 6.1. The X-ray pulse is most obvious in the 0.3-2 keV band, and has a decaying amplitude at increasing energies. The shape of the pulse is also quite peculiar - the pulse has a very fast, sharp rise starting around spin phase 0.92. and ending around phase 1.00, while the decay is gradual and slow, lasting from spin phase 1.00 until the rise starts again. This suggests the region producing the soft X-rays comes into view very quickly, and then is gradually eclipsed by material of increasing optical depth.

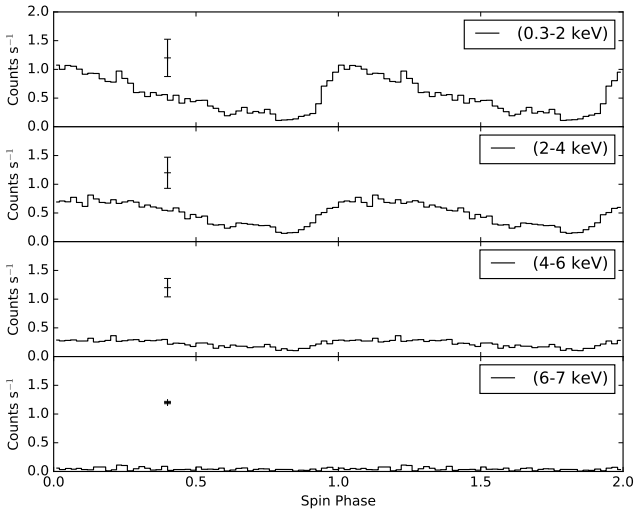

Figure 6.13: Various X-ray light curves taken by *Chandra* in July 2016. There is a clear X-ray pulse visible in the 0.3-2 and 2-4 keV bands. The rise time of the pulse is faster than the decay time, suggesting the X-ray producing region is extended in the azimuth direction close to the WD.

6.4.4.2 Recovery State

The arrival times of the optical and X-ray pulses seen in the 2016 *XMM-Newton* data are similar, suggesting the origin of the optical and X-ray pulses are very close. Hellier et al. (1990) calculated the *V/R* ratio for the optical emission lines (which is simply the ratio of the equivalent widths on either side of the line rest wavelength) and found that at spin maximum, the *V/R* ratio also has a maximum, which suggests that whatever material is producing the emission must be streaming towards the observer at this phase. To explain the similar arrival of the pulses in the optical and X-rays, along with the observed *V/R* for the emission lines at the phase maximum, Hellier et al. (1990) proposed that the optical and X-ray modulations in FO Aqr are caused by “self-absorption” by the optically thick accretion curtain. In this scenario, the maxima of the optical and X-ray pulse are seen when the magnetic pole closest in orientation to us is pointed away from the Earth, allowing us to see a maximum area of the part of the accretion curtain which is producing the optical and soft X-rays, while the minima of the pulse is seen when this pole is pointed towards us, but through the accretion curtain which is now absorbing a majority of the produced radiation. This scenario has also been employed to explain the simultaneous arrival of the optical and X-ray pulses in EX Hya (Hellier et al. 1987; Rosen et al. 1988; Rosen et al. 1991). For the rest of this chapter, we refer to this pole as the “top" magnetic pole, while the magnetic pole which is orientated

furthest from Earth is the "bottom" pole. For a diagram of this geometry, see Fig 2 of Wynn & King (1992) or the introduction to this thesis.

To check if this scenario still applies to FO Aqr, the X-ray light curve was split up into several energy bands (0.3-2 keV, 2-4 keV, 4-6 keV, 6-8 keV and 8-10 keV) and phased on the spin period. The resulting light curves are shown in Fig. 6.14, and show that the X-ray pulsations are strongest in the 2-4 keV band, and undetectable in the 8-10 keV band, confirming that the "self-absorption" model invoked by Hellier et al. (1990) applies to this new high state.

The constant flux from the 8-10 keV band suggests that the accretion region which is producing the hard X-rays around the top magnetic pole is always visible from Earth, or that when this location is hidden from Earth, the accretion region around the bottom magnetic pole becomes visible, which helps maintain the hard X-ray flux.

The shape of the X-ray pulse in the recovery state is very different to the pulse seen in the low state. The rise of the X-ray pulse is slower than in the low state, starting at spin phase 0.92 and reaching a maximum at 0.05, but the decay is much faster, reaching a constant flux level by spin phase 0.3. This suggests the material absorbing the X-ray pulses is more symmetric in the recovery state than in the low state.

Fig. 6.15 shows the spin-phased light curves from the recovery data and the high state data. The high state X-ray observations from Evans et al. (2004) were phased using their spin ephemeris, since the spin ephemeris here would have had a large error associated with it if propagated back to 2001. It is important to note that both X-ray light curves are phased based off of ephemerides derived from the optical pulsations.

The X-ray pulse in the recovery state seems to share many of the features seen in the high state pulse, except they are reduced and phase shifted. The 3 main features identified by Evans et al. (2004) in the high state X-ray pulse were the minimum at spin phase $\phi \sim 0.67 - 0.87$, the 'notch' at spin phase $\phi \sim 0.99 - 1.11$ and the maximum at spin phase $\phi \sim 0.12 - 0.36$. The minimum and maximum are both apparent in the recovery state spin pulse, but are at spin phases $\phi \sim 0.51 - 0.68$ and $\phi \sim 0.0 - 0.14$ respectively. This corresponds to a phase shift of 0.17 between the high and recovery state pulse. The 'notch' is also present in the recovery spin pulse. However, it is much weaker, which is most likely related to the lower count rate right before the notch in the

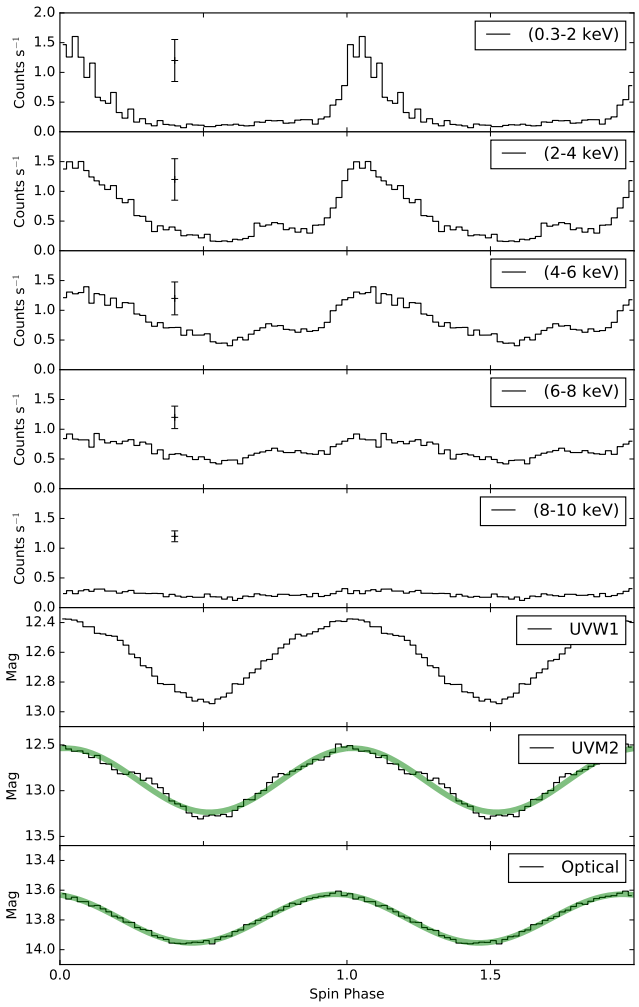

Figure 6.14: Various X-ray light curves taken by *XMM-Newton* in November 2016. The X-rays with energies 2 keV<E<8 keV are pulsed, while hard X-rays with energy $>$ 8 keV are not. The pulsed X-rays are in phase with the optical pulses, suggesting the "self-absorption" model of accretion curtains is leading to the pulsed emission in FO Aqr. The pulses in the 0.3-2 keV band are not always present, but are orbital phase dependant, as shown in Fig. 6.4. The green line in the bottom two plots shows the sine curve fit to the UV and optical pulses.

recovery state at spin phase $\phi \sim 0.67 - 0.78$, and also phase shifted to $\phi \sim 0.80 - 0.90$. The apparent phase shift in the X-ray pulse is striking, since the UV pulses observed during both the high and recovery state data arrive at $\phi \sim 0.0$. This means that during the high state, the phase difference between the arrival of the maximum of the UV pulse and the maximum of the X-ray pulse was $\sim 0.12 - 0.36$, while the phase difference during the recovery state was much less, closer to $\sim 0.0 - 0.14$.

Evans et al. (2004) suggested that the magnetic field lines in FO Aqr may be

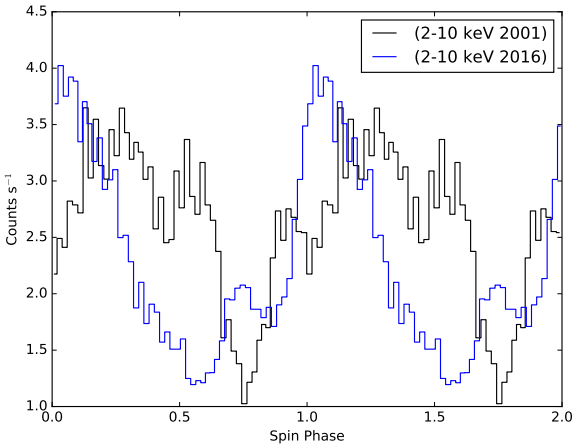

Figure 6.15: The spin-phased 2-10 keV X-ray pulses observed during the high (black) and recovery (blue) observations. The X-ray pulses show three distinct features (a minimum, maximum and notch) in both light curves, but with the recovery features phase shifted relative to the high state features.

twisted such that the infalling material is trailing the accreting magnetic pole. In their interpretation of the X-ray pulse, the 'notch' is caused by the brief disappearance of part of the X-ray emitting region, and that the minimum is caused by absorption of the X-ray flux coming from the lower magnetic pole by the upper curtain. For a symmetric magnetic field, it would then be expected that the phase difference between the 'notch' and the minimum is ~ 0.5. However, Evans et al. (2004) noted that the spin phase difference between the 'notch' and the minimum was closer to ~ 0.77 in the high state, which was their evidence for the twisted magnetic field lines. During the time of the high state observations, FO Aqr was spinning up (the spin period was decreasing; Williams 2003). Another object of interest is PQ Gem, which is an IP that is spinning down (spin period is increasing; Mason 1997; Evans et al. 2006) and whose magnetic field lines are also twisted, but in the opposite direction such that the infalling material is leading the accreting magnetic pole (Evans et al., 2006).

Hellier (2014) suggested that the trailing and leading of infalling material may be related to the spin up and spin down of these systems, based on FO Aqr and PQ Gem. While this hypothesis has not been fully tested, it does provide an explanation for the observed phase difference in the X-ray observations of FO Aqr between the high and recovery state. As Kennedy et al. (2016) showed, FO Aqr is no longer spinning up, but has transitioned to spinning down. It may be that the observed X-ray phase change is related to the flip in the sign of $\dot{P}$,

and is indicative of a change in the twist in the magnetic field lines. We do note that the phase separation of $\phi \sim 0.8$ between the notch at $\phi \sim 0.80 - 0.90$ and the minimum at $\phi \sim 0.51 - 0.68$, which is what Evans et al. (2004) used to suggest the magnetic field lines were twisted, in the recovery spin pulse is the same as the phase separation in the high state. This suggests the twist in the magnetic field may not have changed at all. However, since the spin pulse in the recovery state has a slightly different shape (the high state pulse was significantly broader, as shown in Fig. 6.15) and the notch in particular was less obvious our ability to measure this phase difference accurately is limited. One thing for certain is that further X-ray observations of FO Aqr must be carried out to identify the long term nature of this apparent X-ray phase shift.

The UV and optical pulses shown in the bottom two panels of Fig. 6.14 are out of phase with each other. This phase lag was measured to be 0.062$\pm$0.001 in spin phase units by modelling the optical and UV pulses as sine functions (these models are also shown in Fig. 6.14). Since the optical and UV pulse comes from the pre-shock accretion flow, it is likely that this lag is associated with a twist in the accretion curtains, as proposed by Evans et al. (2004).

6.5 Conclusions

We have presented the first-ever X-ray observations of an IP during a low state, along with X-ray observations during the subsequent recovery. In the low state, the X-ray spectrum suggests the accretion rate within FO Aqr dropped significantly, leading to a lower production of hard X-rays. Additionally, the lower accretion rate led to a lower density within the accretion structures, allowing more soft X-rays to be transmitted out of the system, increasing the observed soft X-ray flux. The power spectrum of the X-ray data suggests that the majority of the accretion occurring in FO Aqr was happening via an accretion stream.

The recovery spectra suggest that, as of November 2016, FO Aqr still had not fully returned to its typical high state. While the power spectrum of the hard X-rays in the recovery state resembled the power spectrum of the archival data, implying the accretion geometry had returned to a disc-fed scenario, the 0.3-2 keV light curve showed occasional pulses, which are absent in the archive X-ray data from 2001. Detailed analysis of the X-ray spectrum suggests that the densities within the accretion disc and curtains had increased since

the low state observations in July. The appearance of the occasional soft X-ray pulse between orbital phases 0.3-0.8 suggests there are still areas of low density within the accretion structure, which is allowing occasional glimpses into the soft X-ray emitting regions of the system.

When compared with the X-ray pulse observed in the high state, the recovery X-ray pulse shows many similar features, albeit with a phase shift. This suggests a possible change in the structure of the accretion flow which is generating the soft X-rays. However, whether this phase shift is now a permanent feature of FO Aqr, or was only visible in the recovery state remains to be seen.

Further X-ray observations of FO Aqr are encouraged to establish whether the recovery state is stable or if FO Aqr will eventually return to the high state seen in 2001, when no soft X-ray pulses were visible.

Acknowledgements

We thank Neil Gehrels for granting target of opportunity observations with the *Swift* satellite. Sadly Dr. Gehrels passed away before this research was complete. We acknowledge his tremendous contribution to many fields of astrophysics. We would like to thank Belinda Wilkes, director of the *Chandra* X-ray Center, for granting us Director Discretionary Time on the *Chandra* X-ray Telescope and Norbert Schartel and the *XMM-Newton* OTAC for granting us TOO observations of FO Aqr. MRK, PC and PMG acknowledge financial support from the Naughton Foundation, Science Foundation Ireland and the UCC Strategic Research Fund. MRK and PMG acknowledge support for program number 13427 which was provided by NASA through a grant from the Space Telescope Science Institute, which is operated by the Association of Universities for Research in Astronomy, Inc., under NASA contract NAS5-26555. STSDAS and PyRAF are products of the Space Telescope Science Institute, which is operated by AURA for NASA. We would also like to thank the AAVSO for support observations during the *XMM-Newton* observations. In particluar, we would like to thank Teofilo Arranz, Michelle Dadighat, Emery Erdelyi, James Foster, Nathan Krumm, David Lane, Damien Lemay, Diego Rodriguez Perez, Geoffrey Stone and Brad Vietje. This research made use of Astropy, a community-developed core Python package for Astronomy (Astropy Collaboration et al., 2013).

7

The Evolved Main-Sequence Channel: HST and LBT observations of CSS120422:111127+571239

[†]The "evolved main-sequence" channel is thought to contribute significantly to the population of AM CVn type systems in the Galaxy, and also to the number of cataclysmic variables detected below the period minimum for hydrogen rich systems. CSS120422:J111127+571239 was discovered by the Catalina Sky Survey in April 2012. Its period was found to be 56 minutes, well below the minimum, and the optical spectrum is clearly depleted in hydrogen relative to helium, but still has two orders of magnitude more hydrogen than AM CVn stars. Doppler tomography of the Hα line hinted at a spiral structure existing in the disc. Here we present spectroscopy of CSS120422:J111127+571239 using the COS FUV instrument on the Hubble Space Telescope and using the MODS spectrograph on the Large Binocular Telescope. The UV spectrum shows Si IV, N V and He II, but no detectable C IV. The anomalous nitrogen/carbon ratio is seen in a small number of other CVs and confirms a unique binary evolution. We also present and compare the optical spectrum of V418 Ser and advocate that it is also an evolved main-sequence system.

[†]Published in the Astrophysical Journal. "The Evolved Main-Sequence Channel: HST and LBT Observations OF CSS 120422: 111127+ 571239" Kennedy, M., Garnavich, P., Callanan, P., Szkody, P., Littlefield, C., Pogge, R., 2015, ApJ, 815, 131.

7.1 Introduction

The period distribution of CVs shows very few systems with a period below $P \approx 78$ min, which is the period minimum for systems that have a main sequence (MS) companion (Kolb, 2002). In short period binaries, angular momentum loss is caused by the emission of gravitational radiation, which shortens the orbital period of the system. However, when the thermal time scale of the donor star becomes comparable to the angular momentum loss time scale, the period can increase, resulting in a period minimum (Paczynski 1981; Paczynski & Sienkiewicz 1981). There are close binary systems that have periods below this minimum, suggesting that there are ways to avoid the minimum.

There are currently 3 different channels to create systems that have a period below the period minimum: 1) The system is double degenerate. That is, both objects are white dwarfs (WD), with the more massive WD accreting material from the less massive WD (Tutukov & Yungelson 1979; Nather et al. 1981). 2) The companion is a helium burning star, which means the system has a much shorter minimum period (Savonije et al. 1986; Iben & Tutukov 1991) as the secondary becomes degenerate once the system is much smaller when compared to a system with a hydrogen burning star. 3) The companion evolved off of the main sequence (MS) just as mass transfer began. This last channel is known as the evolved main sequence (EMS) channel (Podsiadlowski et al., 2003), which was initially proposed by Tutukov et al. (1985) and Nelson et al. (1986). An evolved main sequence star is a star which has a helium core surrounded by a hydrogen burning shell, but the helium core is not undergoing fusion.

Early work on generating populations of CVs with periods below the minimum found that the first 2 of these channels were important, and that the EMS channel did not contribute to the overall population (Nelemans et al., 2001). Since then, more in-depth modelling has found that the choice of efficiency in ejecting material during the common-envelope stage, which is when the primary star initially evolved off of the main sequence and engulfed the secondary star, has a dramatic effect on which channels are important, and that for inefficient common-envelope ejection, the EMS channel contributes significantly to systems with short periods (Podsiadlowski et al., 2003).

The mechanism for forming an ultracompact system by the EMS channel

requires a very particular set of starting conditions. First, the mass of the companion must initially be greater than that of the white dwarf primary i.e. $q > 1$. If this condition is satisfied, then after the common envelope stage, the system can undergo thermal timescale mass transfer (TTMT), as the Roche lobe radius (R_L) shrinks faster or at the same rate as its thermal equilibrium radius (R_{th}) (Tutukov & Yungelson, 1979). Once enough mass has been lost by the secondary and q has become small enough, R_L shrinks slower than R_{th}, and the system detaches when R_{th} drops below R_L.

Second, the companion star must have just finished hydrogen burning when the system becomes semi-detached directly after the common envelope stage. If this is true, then as the system evolves, the star becomes fully convective after it has lost more mass than if it had been a main sequence star. Thus magnetic braking becomes ineffective at smaller periods and the period of detachment (known as the period gap) is much shorter than in conventional CVs (Podsiadlowski et al., 2003). It follows that the system undergoes high rates of mass transfer for longer times than conventional CVs. The period minimum is also affected by having an evolved companion. The modelling done by Podsiadlowski et al. (2003) shows that if the secondary is evolved and has a helium core surrounded by a hydrogen envelope, then the period minimum can drop down to $P_{min} \approx 11$ minutes for a helium core mass of $0.063\ M_{\odot}$.

Identification of a short period CV formed by the EMS channel should be easy. First, as opposed to double degenerate or helium star channels, EMS channel systems should have detectable hydrogen in their spectrum, even when the system is below the period minimum for main sequence companions. In most of the evolutionary tracks simulated by Podsiadlowski et al. (2003), they found that the efficiency of magnetic braking, and by proxy, the evolutionary state of the companion, affects the value of the period minimum. For most of the tracks, when the period minimum is $>$ 11 min, the EMS systems still have detectable H after reaching the period minimum. However, for the most extreme case of magnetic braking efficiency, where the period minimum is $\approx$ 11 min, the hydrogen is exhausted from the companion at the period minimum, and the EMS systems that evolve along this path become similar to the systems formed by the first 2 channels, which is supported by the abundance ratios calculated by Nelemans et al. (2010). Second, these systems are predicted to have very high N/C ratios, as the CNO (Carbon-Nitrogen-Oxygen) processed material in the hydrogen shell should be

at the surface of the secondary. This is due to the high rates of accretion that these systems undergo, which strips away the layers above the CNO (Carbon-Nitrogen-Oxygen) processed material which is normally hidden in stars (Marks & Sarna 1998; Podsiadlowski et al. 2003; Harrison et al. 2005; Nelemans et al. 2010).

The first observed inverted N/C ratio system was BY Cam (Bonnet-Bidaud & Mouchet, 1987), and was thought to be due to anomalous abundances from either a nova outburst or an evolved main sequence star. Since then more CV systems have displayed this anomaly in the ultraviolet (UV) (Gänsicke et al. 2003; Sanad 2011) and it has also been proposed that this anomaly can be detected in the infrared (IR) (Hamilton et al., 2011). There is a bottleneck in the carbon-nitrogen cycle, which sees the majority of ^{12}C close to the core of MS stars processed into ^{14}N, resulting in the a inverted N/C ratio close to the core of MS stars. Typically, this layer is not observable. However, in the EMS channel, the outer hydrogen layer is stripped away during the period of TTMT. This exposes the inner hydrogen layer above the helium core, which has been nitrogen enriched via this process, leading to the inverted N/C ratio (Schenker et al. 2002; Gänsicke et al. 2003). Out of the sample observed by Gänsicke et al. (2003), only 2 objects had a period below the period minimum - EI Psc (RXJ2329.8+0628) with $P = 64.176$ min (Thorstensen et al., 2002) and CE 315 with $P = 65.1$ min (Ruiz et al., 2001). CE 315 has been confirmed to be a double degenerate system, but EI Psc shows hydrogen emission lines alongside strong He lines, suggesting that EI Psc is a CV following the EMS channel.

CSS120422:J111127+571239, also known as SBSS 1108+574 and SDSS J111126.84+571238.6 and hereby referred to as CSS1111, is a CV system discovered by the Catalina Sky Survey when it went into outburst in April 2012. It was observed to have superhumps with an ultrashort period of 0.038449(6) days (Kato et al., 2013). Carter et al. (2013) reported a spectroscopic period of 55.3 ± 0.8 min using radial velocity measurements, and found evidence of a possible eclipse of the accretion disc based on observations of the He II 4686Å line. The orbital period was confirmed to be 55.36 minutes using photometry obtained in 2012 while the optical spectrum of the object showed hydrogen emission lines alongside the strong helium lines expected in an AM CVn system (Carter et al. 2013; Littlefield et al. 2013). Due to the high N/C ratio expected from EMS systems, the most important part of the spectrum in classifying CSS1111 is the UV, due to the presence of the N V 1238Å and C IV 1550Å lines. The Cosmic Origins Spectrograph on the Hubble

Space Telescope is the perfect instrument for observing these far UV lines.

V418 Ser is a faint (m>20) cataclysmic variable that was discovered by the ROTSE-III telescope in 2004 after going into outburst and reaching a magnitude of 15.4 (Rykoff et al., 2004). The CRTS observed V418 Ser to be in outburst again in May 2014, and extensive photometry found a photometric period of 64.2(5) minutes, which has been attributed to the superhump period of the system (Littlefield, VSNET alert 17321; de Miguel, VSNET alert 17322). The orbital period should lie within a few $\%$ of the superhump period.

Here, we present the first UV data, as well as new optical spectroscopy taken after an extended period of quiescence, to investigate whether CSS1111 is indeed a product of the EMS channel. We compare our data to previous observations, search for possible eclipses in the UV continuum or emission lines and determine whether the spiral structure in the disc at the 2:1 resonance as found by Littlefield et al. (2013) was still present in 2014. We also present optical spectroscopy of V418 Ser, and confirm that it is also a product of the EMS channel. Finally, we discuss the relationship between EMS channel systems and Type Ia supernovae.

7.2 Observations and Analysis

Observations of CSS1111 were obtained using the Hubble Space Telescope (HST), the Large Binocular Telescope (LBT), the Vatican Advanced Technology Telescope (VATT) and Apache Point Observatory (APO) as detailed in the sections below. Table 7.1 shows a summary of the observations.

7.2.1 HST Observations

Observations of CSS1111 were taken during six HST orbits on 2014 May 16 using the Cosmic Origins Spectrograph (COS). A total of 10 spectra were obtained in TIME-TAG mode using the G140L grating. The G140L grating has a dispersion of 80 mÅ pixel^{-1}, with a resolving power of $R = 1500 - 4000$ in the bandpass $950 - 2150$Å. The grating was in the standard position for the first 3 orbits, covering the range 1130Å to 2000Å. For the last 3 orbits, the grating was shifted such that the spectral range went from 900Å to 1200Å and 1275Å to 2000Å. The phase coverage of each observation can be seen in

Table 7.1: Details of Observations of CSS1111 and V418 Ser

Date (UT)	Object	Obs	Filter	Exp(s)	UT Time	Phase
24 April 2014	CSS1111	LBT	MODS1	200	05:52:49	0.21
24 April 2014	CSS1111	LBT	MODS1	200	05:57:52	0.30
24 April 2014	CSS1111	LBT	MODS1	200	06:02:55	0.39
24 April 2014	CSS1111	LBT	MODS1	200	06:13:04	0.57
24 April 2014	CSS1111	LBT	MODS1	200	06:18:06	0.66
24 April 2014	CSS1111	LBT	MODS1	200	06:23:09	0.75
24 April 2014	CSS1111	LBT	MODS1	200	06:28:12	0.85
24 April 2014	CSS1111	LBT	MODS1	200	06:33:14	0.94
24 April 2014	CSS1111	LBT	MODS1	200	06:38:17	0.03
24 April 2014	CSS1111	LBT	MODS1	200	06:43:23	0.12
24 April 2014	CSS1111	LBT	MODS1	200	06:48:25	0.21
24 April 2014	CSS1111	LBT	MODS1	200	06:53:28	0.30
24 April 2014	CSS1111	LBT	MODS1	200	06:58:30	0.39
24 April 2014	CSS1111	LBT	MODS1	200	07:03:32	0.48
24 April 2014	CSS1111	LBT	MODS1	200	07:08:35	0.57
29 April 2014	CSS1111	VATT	sdss-g	265 Images		
01 May 2014	CSS1111	VATT	sdss-g	198 Images		
02 May 2014	CSS1111	VATT	sdss-g	322 Images		
16 May 2014	CSS1111	HST	G140L Standard	2754	06:30:41	0.09-0.92
16 May 2014	CSS1111	HST	G140L Standard	2000	07:53:09	0.59-0.18
16 May 2014	CSS1111	HST	G140L Standard	1081	08:28:33	0.22-0.54
16 May 2014	CSS1111	HST	G140L Standard	1000	09:29:06	0.31-0.61
16 May 2014	CSS1111	HST	G140L Standard	2090	09:47:41	0.64-0.27
16 May 2014	CSS1111	HST	G140L Shifted	3205	11:05:03	0.04-0.00
16 May 2014	CSS1111	HST	G140L Shifted	2000	12:40:58	0.77-0.38
16 May 2014	CSS1111	HST	G140L Shifted	1084	13:16:22	0.41-0.74
16 May 2014	CSS1111	HST	G140L Shifted	1000	14:16:52	0.51-0.81
16 May 2014	CSS1111	HST	G140L Shifted	2090	14:35:27	0.84-0.47
30 June 2014	V418 Ser	LBT	MODS1	300	05:08:49	
30 June 2014	V418 Ser	LBT	MODS1	300	05:15:30	
30 June 2014	V418 Ser	LBT	MODS1	300	05:22:12	
30 June 2014	V418 Ser	LBT	MODS1	300	05:28:53	
30 June 2014	V418 Ser	LBT	MODS1	300	05:35:35	

Table 1, and is based on the ephemeris calculated later in this chapter.

The spectra and TIME-TAG data were analysed using a combination of PYRAF routines from the STSDAS package HSTCOS (version 3.17) and basic PYTHON procedures. Light curves were made for various parts of the UV spectrum to look for an eclipse of the accretion disc, which had possibly been seen in the He II 4686Å line during outburst (Carter et al., 2013). Since the count rate for the system changed when the grating was shifted, the light curves were normalised, and the variations in the light curve are expressed as a fraction of the median number of counts.

If CSS1111 had been in outburst (which happens approximately once per year, see Section 7.5 for more information) during the HST observations, the flux would have been too bright for the COS instrument. As such, the American

Association of Variable Star Observers (AAVSO) provided observations leading up to and during the HST observations to confirm that CSS1111 was in quiescence.

7.2.2 LBT Observations

Fifteen optical spectra of CSS1111 were obtained using the MODS spectrograph (Pogge et al., 2010) on the Large Binocular Telescope (LBT) on 2014 April 23, 23 days before the HST observations. The MODS spectrograph has 2 gratings, one blue grating covering the wavelength range $3200 - 5800$Å with a dispersion of 0.5 Å pixel^{-1} and one red grating covering the wavelength range $5800 - 10000$Å with a dispersion of 0.8 Å pixel^{-1}. Both gratings provide a resolution of $R \approx 2000$. The 1.2-arcsec segmented long-slit was used to obtain spectra, each with an exposure time of 200s. The spectra were flat fielded, debiased and wavelength and flux calibrated using calibration data from the same run. The wavelength calibration is based on observations of Argon, Krypton and Xenon lamps for the blue arm, Neon and Argon lamps for the red and standard LBT line lists. The data reduction tasks were carried out using PYRAF and IRAF.

Archive observations of CSS1111 taken with the LBT in 2012, as detailed in Littlefield et al. (2013), were also reduced and analysed, so that a direct comparison between the spectrum in 2014 and 2012 could be made.

Five optical spectra of V418 Ser were obtained using the MODS spectrograph on 2014 June 30, each with an exposure time of 300s. The spectra were reduced in the same manner as the CSS1111 spectra.

7.2.3 VATT Observations

Photometry of CSS1111 was taken in the SDSS *g* band using the 1.8m Vatican Advanced Technology Telescope (VATT) located at Mount Graham International Observatory on 3 separate nights - 2014 April 29, May 1 and May 2. The images were taken using the VATT4K CCD with a typical exposure time of 30s. A total of 785 images were taken over these 4 nights.

7.2.4 APO Observations

Nine optical spectra of CSS1111 were obtained on 2014 May 4 and 6, 12 and 10 days prior to the HST observations, using the Dual Imaging Spectrograph (DIS) on the 3.5m ARC telescope at Apache Point Observatory. The blue channel used the B1200 grating, which has a pixel scale of 0.62 Å/pix, while the red channel used the R1200 grating, which has a pixel scale of 0.58 Å/pix. While these spectra will not be discussed in detail as the S/N is poorer than the LBT spectra, they do confirm the quiescent state of the system and have similar properties to the LBT data.

7.3 Results

7.3.1 Optical Spectrum

The average optical spectrum taken with the LBT in both 2012 and 2014 can be seen in Figure 7.1. The strongest emission lines have been marked, which include the Balmer series, He I and He II, Si II, N I and Mg I and Mg II. The N I and Mg I and Mg II lines were identified by comparison with the spectrum of the disc in GP Comae (Marsh et al., 1991). The lab wavelengths of the N I lines are 8200Å and 9050Å versus the observed wavelengths of 8206Å and 9037Å. Like Marsh et al. (1991), our identification of N I is not exact, but may be due to the large line width and complexity of the spectrum in these regions, making accurate measurements difficult. There have been significant changes in the spectrum since 2012. Every emission line has a higher flux and higher equivalent width (see Table 7.2). Also, as shown in the inset of Figure 7.1, the emission features have become more prominently double peaked with wider emission wings. The peak-to-peak separation of the Hα line is unchanged at 27Å.

Table 7.2: Equivalent width and fluxes of some of the most prominent emission lines in the optical spectrum for both CSS1111 and V418 Ser. *(a)Flux measured in* 10^{-15} *erg* cm^{-2} s^{-1} *(b) E.W. measured in Å*

	Hα (E.W.)Flux[a,b]	Hβ (E.W.)Flux[a,b]	He I (5876 Å) (E.W.)Flux[a,b]	He II (4686 Å) (E.W.)Flux[a,b]	Si II (6347 Å) (E.W.)Flux[a,b]
CSS1111(2012,LBT)	(-57 ± 3) 1.75 ± 0.05	(-24 ± 2) 1.35 ± 0.05	(-28 ± 2) 1.24 ± 0.07	(-5 ± 1) 0.3 ± 0.1	(-5 ± 1) 0.17 ± 0.03
CSS1111(2014, APO)	(-80 ± 3) 1.65 ± 0.05	(-35 ± 3) 1.6 ± 0.1	-	(-11 ± 1) 0.6 ± 0.1	$(< -6) < 0.1$
CSS1111(2014,LBT)	(-87 ± 3) 2.47 ± 0.02	(-34 ± 2) 2.05 ± 0.05	(-56 ± 2) 1.95 ± 0.05	(-11 ± 1) 0.65 ± 0.05	(-10 ± 3) 0.28 ± 0.05
V418 Ser	(-44 ± 3) 0.65 ± 0.05	(-15 ± 3) 0.44 ± 0.06	(-33 ± 3) 0.53 ± 0.04	(-4 ± 1) 0.13 ± 0.03	$(< -5) < 0.08$

Figure 7.2 shows the trailed spectra of the Hα, He I 5876Å and He II 4686Å lines in both 2012 and 2014. The continuum around each line was fit with a second order polynomial and then subtracted off each spectrum to increase the contrast, and the spectra were Gaussian smoothed to help identify features. The He II 4686Å also lies very close to the He I 4713Å line. In an attempt to remove contamination of the He II line by He I, a model He I line was constructed using the He I 5876Å line. This model was then shifted to 4713Å and subtracted off. The remaining signal was taken to be the He II 4686Å line, and can be seen in the bottom row of Figure 7.2.

Littlefield et al. (2013) used the Shafter method (Shafter, 1983) on the Hα emission line to estimate the orbital period, semi-amplitude velocity of the emission lines and systematic velocity of the system. The Shafter method works by fitting the wings of the emission lines, and since the lines appeared broader in 2014 than in 2012, we expected different results from the fitting. We set the period of the system to be 55.36 minutes, which is the photometric period found by Littlefield et al. (2013) and Kato et al. (2013), and chose the K_1 and γ which provided the best χ^2 to construct a radial velocity curve using the Hα emission line. The results of the Shafter method can be seen in Figure 7.3, while the RV curve for the 2014 and 2012 data can be seen in Figure 7.4. We also used the results of the Shafter method to compute the ephemeris of both data sets, such that the zero phase corresponds to inferior conjunction of the companion.

The ephemeris for each data set was found to be:

$$T = 2456771.7776(4) + 0.03845(2)E \ \ (2014) \tag{7.1}$$

$$T = 2456094.6784(4) + 0.03845(2)E \ \ (2012) \tag{7.2}$$

We also constructed Doppler tomograms (Marsh & Horne, 1988) using the code described in Spruit (1998) and implemented by Kotze et al. (2015).

Doppler Tomography

Doppler tomography is a technique used to locate areas of strong emission inside accretion discs. The intuitive way to think about Doppler tomography is that each point inside of an accretion disc can be assigned a velocity, (V_x, V_y). As the disc rotates, each point follows a nearly perfect sinusoidal curve in

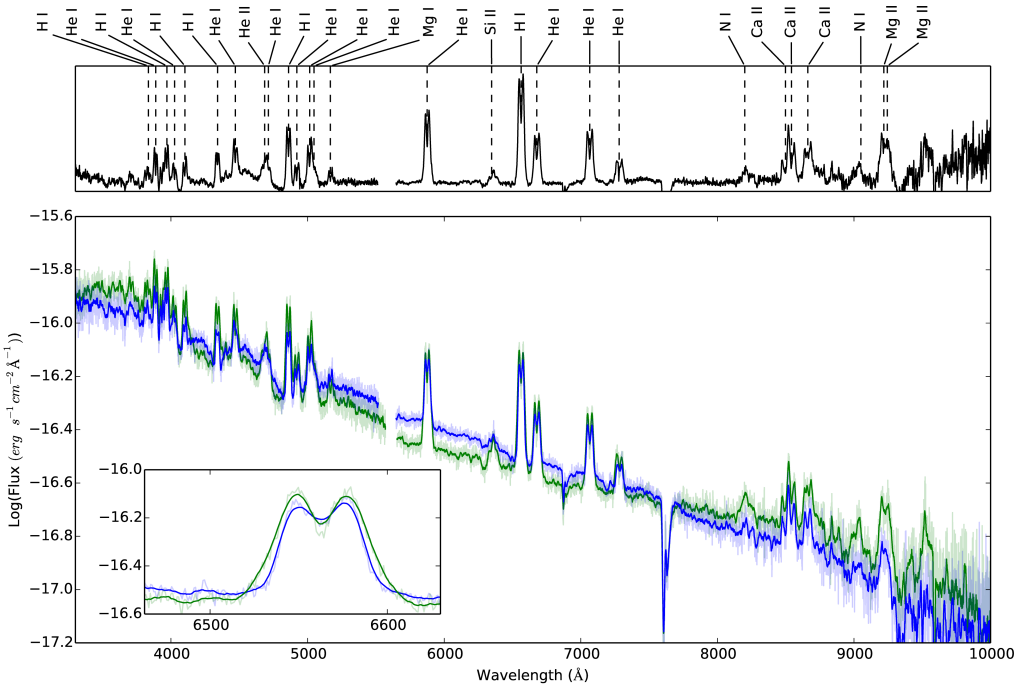

Figure 7.1: Average spectrum of CSS1111 using the MODS1 spectrograph on the LBT. The blue line is the data taken in 2012, and the green line is from 2014. The inset compares the spectral differences between 2012 and 2014 for Hα, most notably the wider wings of the lines, suggesting changes in the accretion disc. The transparent green and blue lines represent the unsmoothed averaged spectrum. The top panel shows the 2014 and 2012 data averaged together and normalised, to make line identification easier.

velocity space (assuming over a single orbit that the radial motion of any particle is negligible). The trailed emission line spectrum observed from such a system should then just be a summation of the sinusoidal curves generated by each point. Doppler tomography works by taking these trailed spectra and inverting them, looking for a solution which would generate the observed line profile. The resulting tomograms are given in velocity space. There are two main techniques for creating tomograms. The first is the filtered back-projection method (Rowland, 1979). The second is maximum entropy inversion (see Chapter 1 of (Boffin et al., 2001)). The method used in this thesis is the maximum entropy inversion.

There are many caveats to deal with when generating tomograms. First, the technique assumes that all points generated in a tomogram are equally visible at all times. Second, the flux from any point which is fixed in the rotating frame of the binary is constant. Third, all motion is parallel to the orbital plane. Fourth, all velocity vectors rotate with the binary star. Fifth, the intrinsic width of the profile from any point is negligible. What this physically

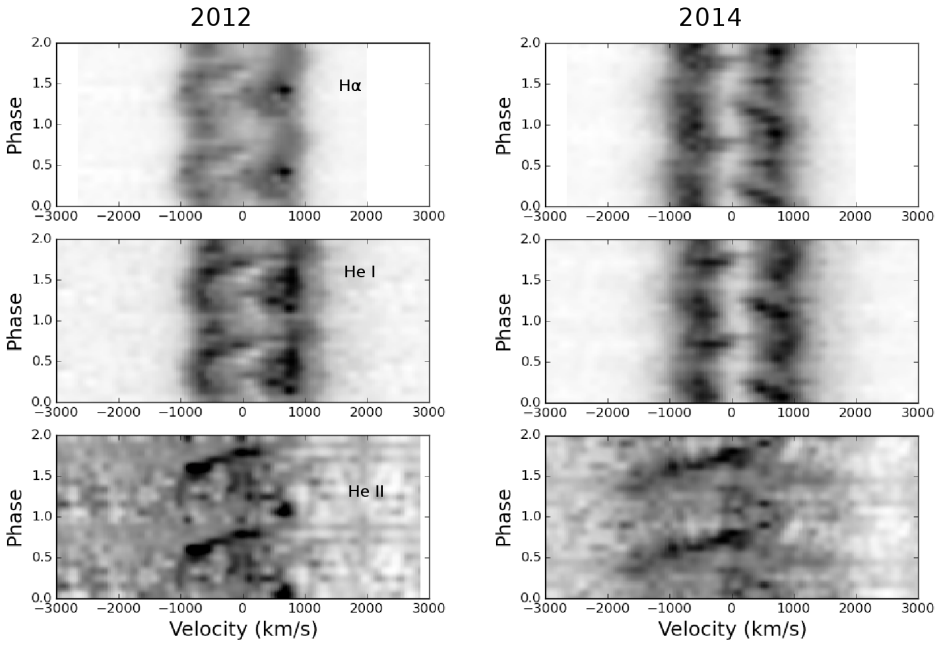

Figure 7.2: The left column shows, in descending order, the Hα, He I 5876Å and the He II 4686Å lines in 2012, while the right column shows the same for the 2014 data. Both the Hα and He I 5876Å lines display a complex structure in both years of data, which we interpret as the intertwining of 2 S-wave patterns from different regions of emission within the disc, while the He II line seems to only appear from phase 0.5 to 0.85 in 2012, and from 0.3 to 0.85 in 2014. The line appears in the blue and trails towards the red as the phase increases, suggesting a strong phase dependence in this line. This dependence is possibly what caused the apparent eclipse seen in Carter et al. (2013).

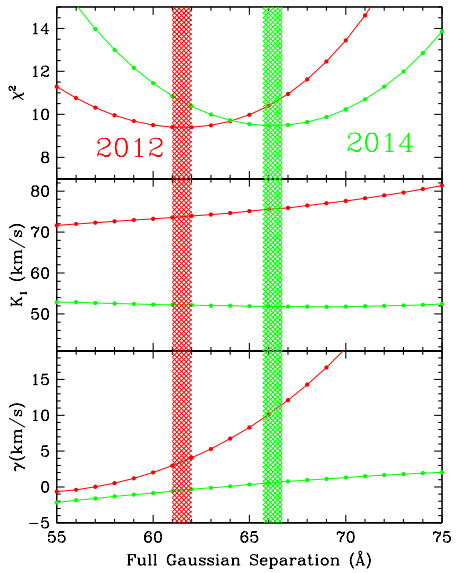

Figure 7.3: Shafter method applied to Hα for both the data from 2012 and 2014. The orbital period was fixed to the photometric orbital period of 55.36 minutes. The hatched lines represent the 1σ errors for both data sets.

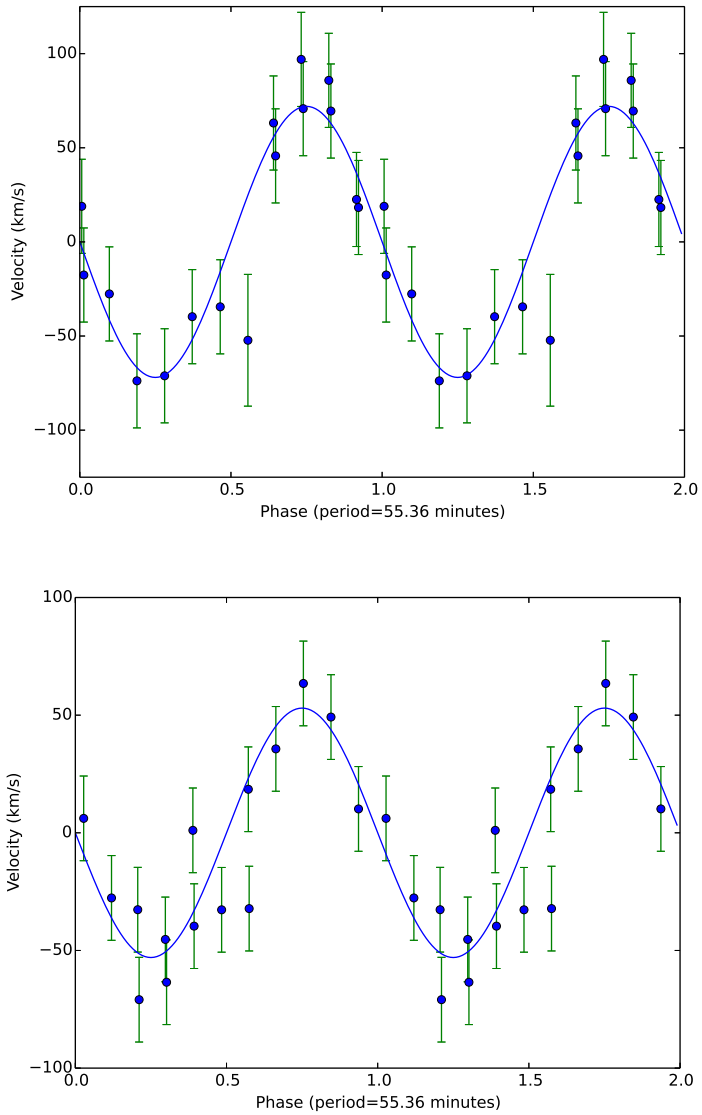

Figure 7.4: The top graph shows the RV curve for the Hα line from 2012, which has a $K_1 = 72\,km\,s^{-1}$. The bottom graph shows the RV curve for the 2014 data, which has a $K_1 = 53\,km\,s^{-1}$.

means for any given system is this: tomograms work best for systems which show shallow or no eclipses (as any eclipses would violate the first axiom. The systems are also assumed to have constant fluxes - that is, no flares (or else the second axiom would be broken). All motion is parallel to the orbital plane confines tomography to systems where the discs do not have significant radial drifts (viscosity is low). For a thorough introduction to Doppler tomography, see Boffin et al. (2001). Since the inclination of CSS111 is relatively low (given that the light curve only shows a grazing eclipse) and the disc undergoes dwarf nova outbursts, suggesting that between outbursts it is in a

low state, then the axioms are reasonable for this system.

The tomograms of Hα were used to see if the structures present in 2012 were still evident in 2014 and those of He II 4686Å were used to check for the phase dependence of the He II emission. The Doppler maps can be seen in Figure 7.5. The He II emission is coming from a single point seen in both 2012 and 2014, and is slightly offset from the area of Hα emission in the lower left quadrant. It is obvious from direct comparison of the Hα Doppler maps that the disc in 2014 extended in to higher velocities. The two areas of enhanced emission proposed by Littlefield et al. (2013), thought to be the accretion stream and a spiral shock located at the 2:1 resonance (Lin & Papaloizou, 1979) were still present in the 2014 map. However, the phasing between our 2012 tomogram and the tomogram presented by Littlefield et al. (2013) is different. Littlefield et al. (2013) used the maximum of the optical light curve, which also corresponds to the maximum of the radial velocity curve, to define phase 0, while here, the 0 point of the radial velocity is used, corresponding to a phase shift of 0.25 between the tomogram presented in Littlefield et al. (2013) and the tomograms presented here. This difference in the definition of the 0 phase leads to different interpretations of the Doppler tomograms.

Littlefield et al. (2013) interpreted one of the areas of emission in the 2012 tomograms as being the traditional hot spot, as it appeared at the expected phase in the tomogram (the (-V_x,+V_y) quadrant), and the other emission region as being a single spiral arm. However, using our 0 phase, which is well defined by the radial velocity curves as inferior conjunction of the companion, we find that neither of the emission regions lies close to the expected phase of the hot spot in 2012 or 2014. Instead, it is likely that both emission regions are spiral arms, and that there is no strong emission coming from the intersection of the accretion stream with the disc. Littlefield et al. (2013) also suggested that the emission feature in their tomogram not associated with their hot spot could be due to accretion stream overflow, where material striking the disc at the hot spot overflows and strikes the disc closer to the WD (Armitage & Livio 1996; Armitage & Livio 1998). The velocity of this second hot spot should be higher than the original hotspot, as the overflow material is accelerated to higher velocities by the WDs strong gravitational field (Armitage & Livio, 1998). Since both emission regions in our tomograms are orbiting with very similar velocities, we find this scenario very unlikely, supporting the tidally induced spiral shock proposed by Littlefield et al. (2013).

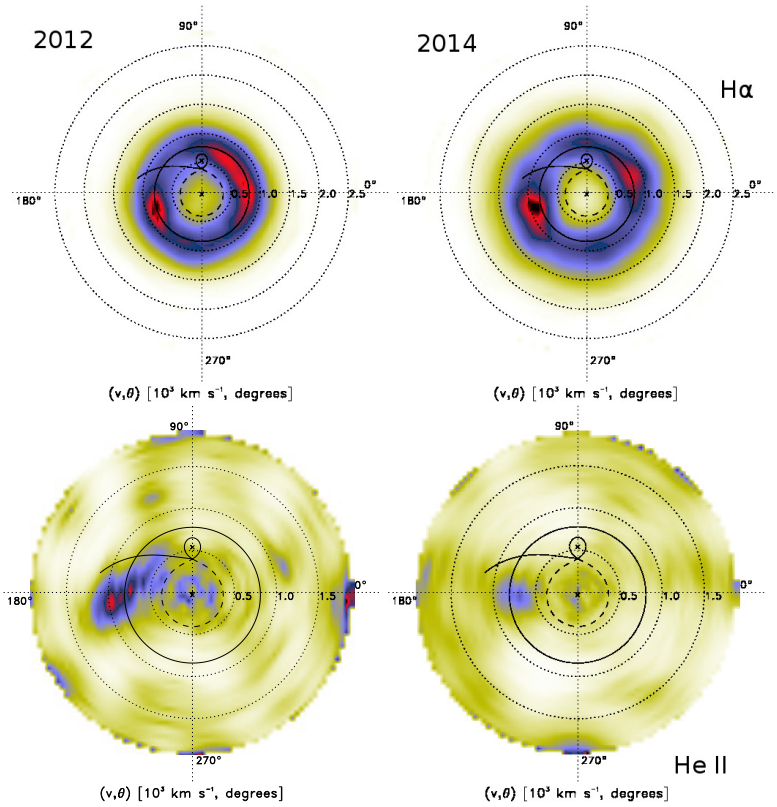

Figure 7.5: The left column shows the doppler maps generated from the 2012 LBT spectra, while the right column shows the map from the 2014 spectra. The top row are the Hα maps, and the bottom are the He II 4686Å maps. In the Hα maps, the main features remain distinct between the maps: the area of enhanced emission in the lower left quadrant and the upper right quadrant, which are associated with a tidally induced spiral shock (Littlefield et al., 2013). The solid circle represents the 2:1 orbital resonance velocity of 750 km s^{-1}. In the He II maps, emission is only seen coming from a single point, located at an angle of 180° which corresponds to an orbital phase of 0.75, and is slightly offset from the main region of emission in the lower left quadrant seen in the Hα maps. We adopted a white dwarf mass of 0.83 M$_\odot$, in line with Littlefield et al. (2013).

7.3.2 UV Spectrum

7.3.2.1 Average Spectrum

The average UV spectrum for both grating positions taken using the COS instrument can be seen in Figure 7.6. The most readily identifiable lines in the spectrum are N V 1240Å, Si IV 1400Å and He II 1640Å. Both the Si IV and N V lines are doublets, and the blending of these doublets is attributed to the triple peaked appearance of these lines. This is more readily seen in Figure 7.7, which shows how the Si IV doublet is split and makes a triple peaked feature.

Table 7.3: Fluxes of some of the most prominent emission lines in the UV spectrum

Line	Flux 10^{-15} erg cm^{-2} s^{-1}
N V	16±3
Si IV	12±2
C IV	<5
He II	6±3

The peak-to-peak separation of the lines in the doublet was found to be 8.8 ± 0.6 Å , which gives a velocity of 950 ± 60 km s^{-1}, which suggests the Si IV emission is coming from an inner, high excitation region of the disc. The details of these three lines can be seen in Table 7.3, along with an upper limit on the C IV line. It is important to note the distinct lack of carbon emission in this spectrum, which will be addressed in Section 7.6. There also is no clear evidence for the O VI 1032Å line. However, it is probable that this is due to poor signal-to-noise in this region of the spectrum, as shown by the unbinned spectrum. The O I 1300Å line is air glow, and is not attributed to CSS1111.

7.3.2.2 TIME-TAG Light Curves

The TIME-TAG spectroscopic data from HST was used to make light curves for three different wavelength ranges to look for variability of the continuum or emission lines. The three ranges selected were: 1327-1379 Å and 1412-1610 Å for the continuum, $1226\text{Å} - 1255\text{Å}$ for the N V emission feature and $1379\text{Å} - 1412\text{Å}$ for the Si IV emission feature. The light curves show no obvious periodic features other than the orbit, and no eclipse is visible. The background subtracted light curves, binned up to 10s temporal resolution, can be seen in the middle column of Figure 7.8. However, Carter et al. (2013) noted that the grazing eclipse seen in the He II 4686Å line may only occur during outburst, when the disc radius is greater than during quiescence. Since our observations were taken when the system was in quiescence, the non-detection of an eclipse does not rule out the eclipse seen by Carter et al. (2013).

The data were subjected to a Lomb Scargle periodogram (Lomb 1976; Scargle 1982) using the ASTROML PYTHON library (Vanderplas et al., 2012). The power spectrum for each of the 3 light curves can be seen in the right column of Figure 7.8, where the confidence levels were obtained by using the Lomb

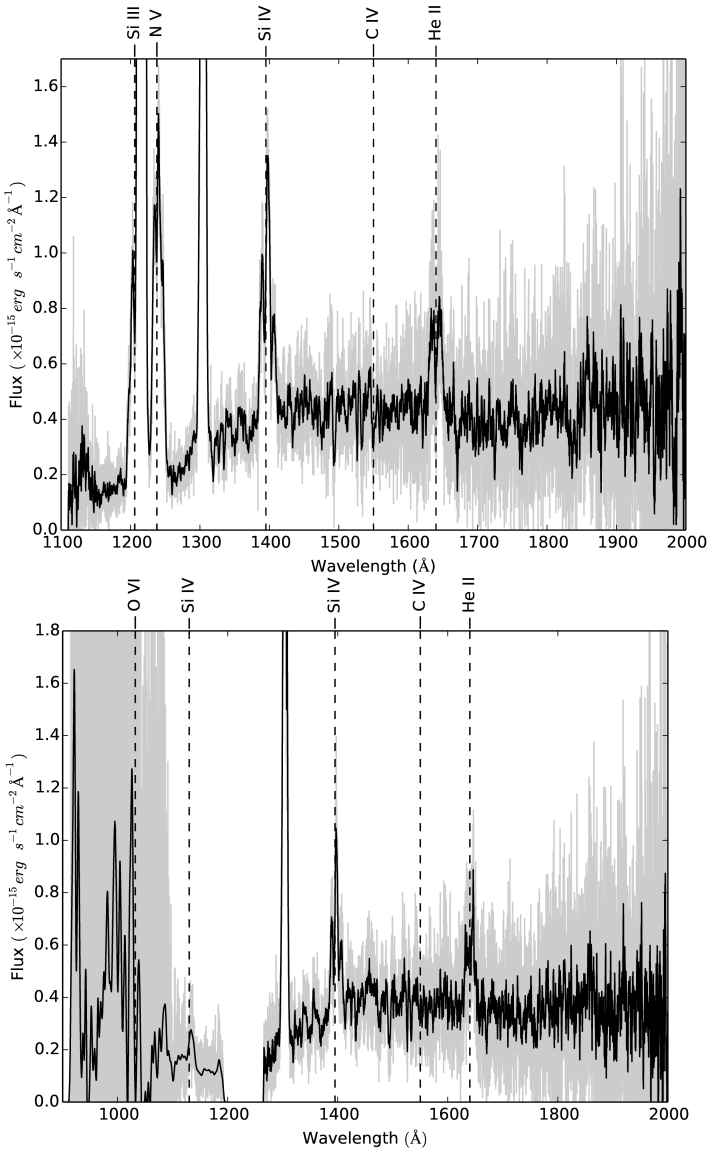

Figure 7.6: The average UV spectrum from the COS instrument aboard the HST. The spectra show that there is no detection of C IV while there is a very strong N V line. This N/C anamoly suggests CSS1111 is a product of the EMS channel. The top panel shows the average spectrum using the G140L grating in the 1105Å setting. The spectrum has been boxcar smoothed with a boxcar smoothing width of 1.2Å . The bottom panel shows the spectrum using the G140L grating in the offset position. The blue part of the spectrum was smoothed by convolution with a Gaussian with $\sigma = 0.8$Å in an attempt to clean up the noise. The red part of the spectrum was boxcar smoothed in the same way as with the top figure. The grey in each figure shows the unsmoothed averaged spectrum.

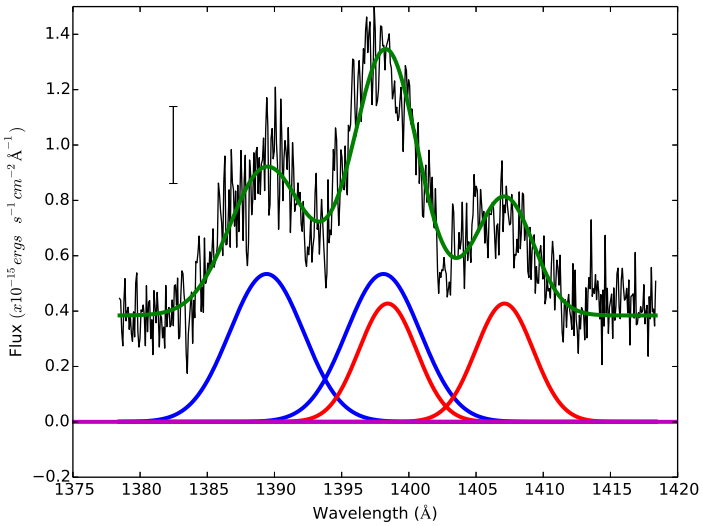

Figure 7.7: An example of how we explain the triple peaked features in the UV spectrum. Si IV has a doublet at 1393Å and 1402Å . Each doublet is doppler shifted due to the source of the emission being the accretion disc. We modelled each doublet as a pair of Gaussians, and the resulting total structure looks triple peaked. The single bar shows the typical size of an error bar in the spectrum

Scargle bootstrap routine over 1000 iterations. The continuum returned a strong peak at 25 ± 1 cycles/day, (57 ± 3 min), while the Si IV range returned a strong peak at 25 ± 2 cycles/day (57 ± 5 min). The N V wavelength range, which was only visible for 3 orbits due to the shift in the grating, has a peak at 22 ± 4 (65^{+15}_{-10} min).

7.4 White Dwarf Temperature

In order to obtain an estimate for the temperature of the WD, we used Hubeny's TLUSTY, SYNSPEC and ROTIN programs (Hubeny 1988; Hubeny & Lanz 1995) to generate synthetic spectra of white dwarfs with various temperatures and log g. To account for contribution from the accretion disc in the UV, we adopt a power law of the form

$$f_\lambda = f_\lambda(1200\text{Å}) \times \left(\frac{\lambda}{1200\text{Å}}\right)^{\alpha-2} \tag{7.3}$$

as done in Long et al. (2009). Here, $f_\lambda(1200\text{Å})$ is the disc contribution to the overall flux at 1200 Å , which was taken to be 10% of the continuum around

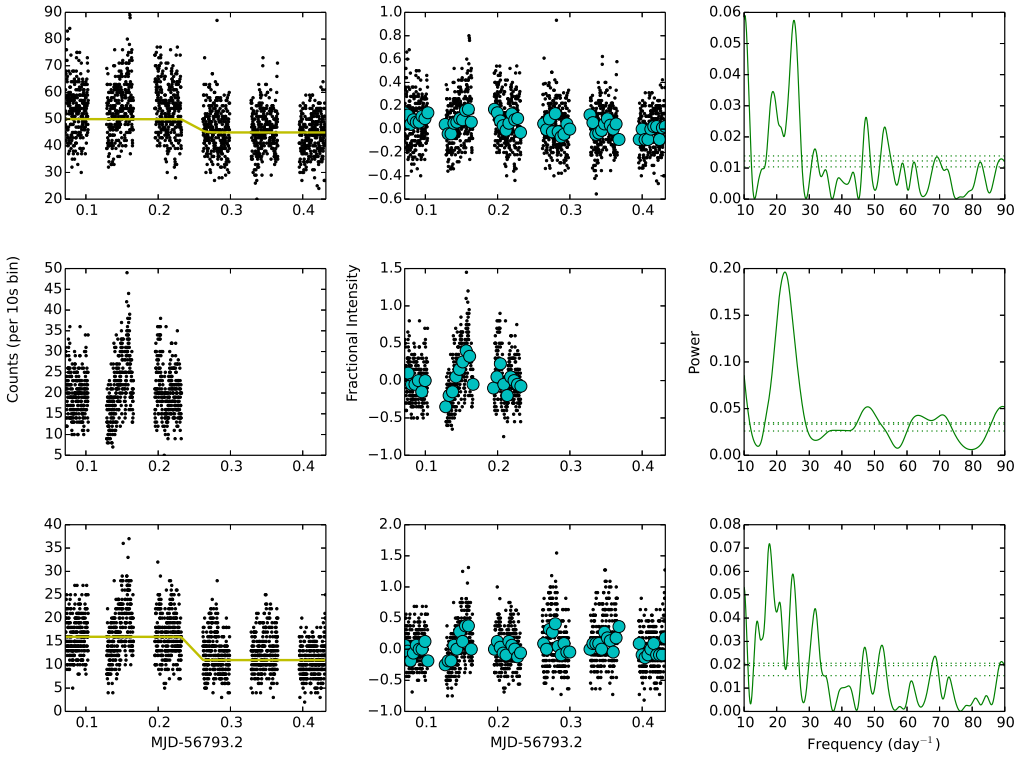

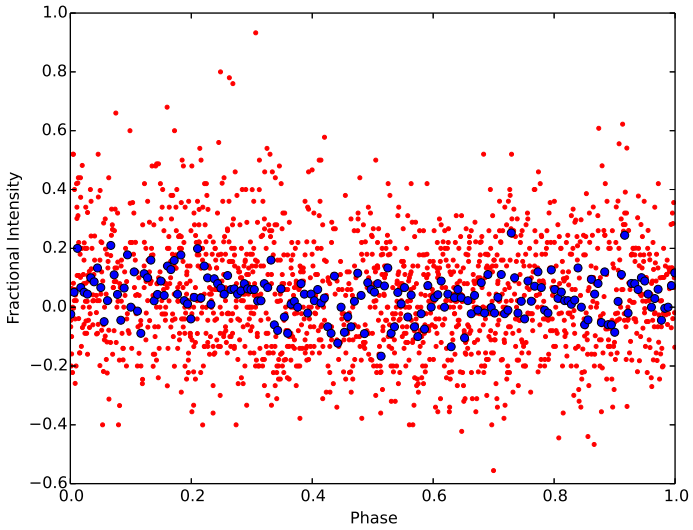

Figure 7.8: The time tag data extracted from the HST COS data. 3 different wavelength segments were analysed: 1327-1379 Å and 1412-1610 Å as a sample of the continuum (top row); 1226-1255 Å to look at the N V feature (middle row); 1379-1412 Å to look at the Si IV feature (bottom row). The left column shows the background subtracted counts for each segment, while the yellow line in the continuum and Si IV plots show the long term trend due to shifting the G140L grating, which was then subtracted. The middle column shows the fractional variation after the background had been subtracted from the counts and the light curve had been normalised by the long term trend. The right column shows the results of the Lomb Scargle periodogram. The lines represent the 95%, 99% and 99.5% confidence levels, found by using a bootstrap Lomb Scargle periodogram routine with 1000 iterations. The bottom graph shows the continuum light curve phased to the 57 minutes period, using the ephemeris in equation 7.1. The red points are the corrected, normalised counts, while the blue points are a binned light curve with a bin width of 10 data points.

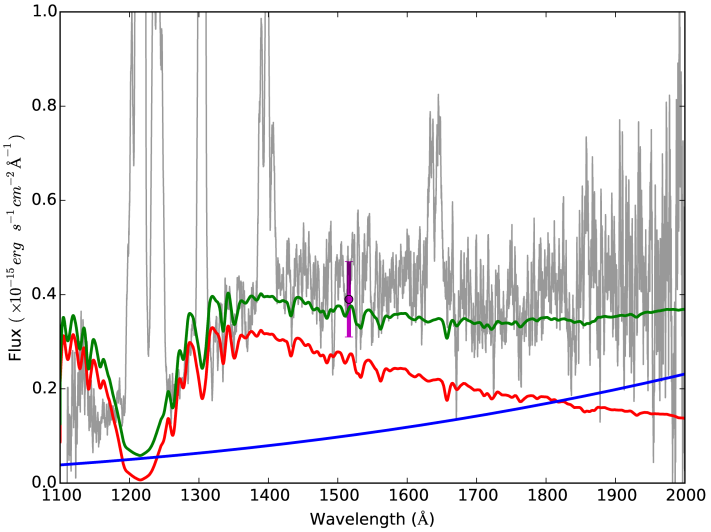

Figure 7.9: The best fit model to the UV spectrum (shown in grey) using TLUSTY and a power law contribution from an accretion disc. The red line represents the WD model for $T = 16000$ K and log $g = 8$, while the blue line shows the power law contribution from the disc with $\alpha = 5$. The green line is the combination of both these models. The purple point is the *GALEX* FUV (effective wavelength = 1516 Å) flux of 0.39±0.08 erg s^{-1} cm^{-2} Å^{-1}.

this point. It is important to note that when fitting a white dwarf and power law model to a spectrum, there is a strong covariance between the temperature of the WD model and the α of the power law. In this case, the shape of the spectrum at low wavelengths (<1400 Å) reveals important information about the WD spectrum due to the weak contribution of the disc, and the strength of the Lyman α absorption by the WD can also help give important constraints on the temperature of the WD. Taking into account the shape of the spectrum, the width of the Lyman α absorption and the unusual structure of this disc, our best fit model can be seen in Figure 7.9. The WD temperature was found to be $T = 16000 \pm 2000$ K, with $\alpha = 5 \pm 1$.

Carter et al. (2013) found the WD temperature in CSS1111 to be 12000±1000 K by modelling the optical spectrum along with the GALEX FUV and NUV fluxes of 30.74±5.92 μJy and 48.25±1.34 μJy respectively. However, they did not include any UV contribution from the accretion disc when modelling the system. Since the GALEX fluxes are broadband, it is difficult to get an accurate SED to to fit for the temperature. Our model is consistent with the GALEX FUV measurement, as shown in Figure 7.9. Extrapolating our UV WD temperature to the optical yields a flux from the WD below the observed optical flux, which

is expected as the accretion disc should be dominant in the optical.

7.5 An evolving disc

The two Doppler maps in Figure 7.5 and the averaged spectra in Figure 7.1 show a significant change has occurred in the 2 year gap between LBT observations. In 2014, there was significant emission in the disc for velocities above 1300 km s^{-1}, while in 2012 there was very little. Also, the equivalent width of the optical emission lines increased.

It is possible that this is due to an increase in mass in the inner disc at the time of the 2014 observations compared to the 2012 observations. The observations in 2012 were taken only 2 months after the system had gone into outburst. In fact, the system was still above its quiescent magnitude 2 weeks prior to the LBT observations, as the outbursts have a duration of 25 days, as seen in Figure 46 of Kato et al. (2013). Following the theory that disc instabilities cause dwarf nova outbursts, it would be expected that the disc would have a lower mass density in observations taken around the time directly after an outburst (Osaki, 1996). Figure 7.10 shows the long term light curve of CSS1111 from the Catalina Real-Time Transient Survey (CRTS) Data Release 2 (Drake et al., 2009). The light curve shows the outburst in 2012, along with another outburst in March 2013.

Since March 2013, no outburst has been conclusively detected. This includes a gap in observations between April 2013 and January 2014. However, as seen in Figure 7.10, the system seemed to be brighter than its quiescent magnitude on 2014 March 11, 43 days before the LBT observations and 66 days before the HST observations. Since there were no observations of the system by the CRTS for 28 days preceding observations, and the outburst in 2012 lasted 25 days, then it is likely that the system was in outburst during this time, and the CRTS caught the system as it was returning to quiescence. This means that in 2012, the system only had 14 days to recover before the LBT observations, compared to the 43 days or more it had in 2014. This extended period of time, and the possible high rate of mass accretion in this system, should be enough to explain the differences seen in the optical spectra, as the accretion disc had longer to recover in 2014.

The AAVSO (Figure 7.11) and CRTS (Figure 7.10) light curves show the

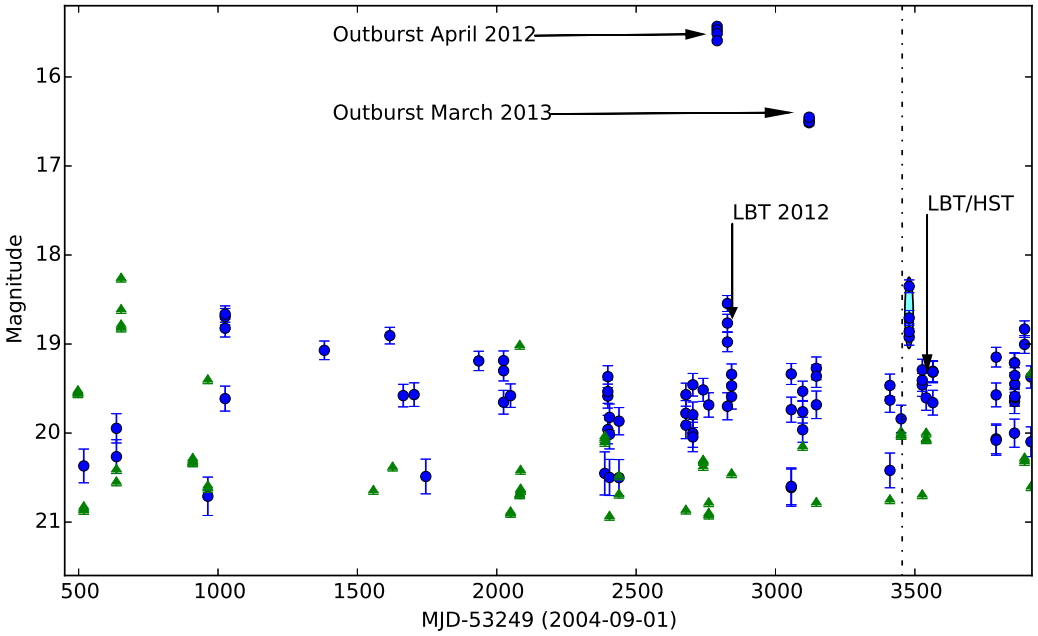

Figure 7.10: The longterm light curve from the Catalina Surveys Data Release 2 (blue for detections, green arrows for lower limits). The data starts in 2006, shows 2 outbursts, one in April 2012 and one in March 2013, and then ends in April 2015. It looks like there was no outburst between March 2013 and our LBT and HST observations in April 2014. However the gap in observations from April 2013 to January 2014 makes this difficult to confirm. There is a possible outburst seen by the CRTS during March 2014. The data taken on 2014-03-11 have a magnitude of 18.5-19, which is thought to be the end of an outburst and is highlighted, while the quiescent magnitude of CSS1111 is 19.5. The dashed black line here represents when an outburst, which lasts for 25 days (Kato et al., 2013), would have had to occur for the system to be at 18.5 on 2014-03-11. Since the CRTS only samples a region of the sky every 28 days, it could have missed the system at its brightest and caught only the tail end of the outburst. The light curve also shows periods of non detection, where the source seems to be fainter than 20.5 mag, which is outside the 0.2 mag orbital variation. This leads us to believe CSS1111 might exhibit a very faint quiescent state.

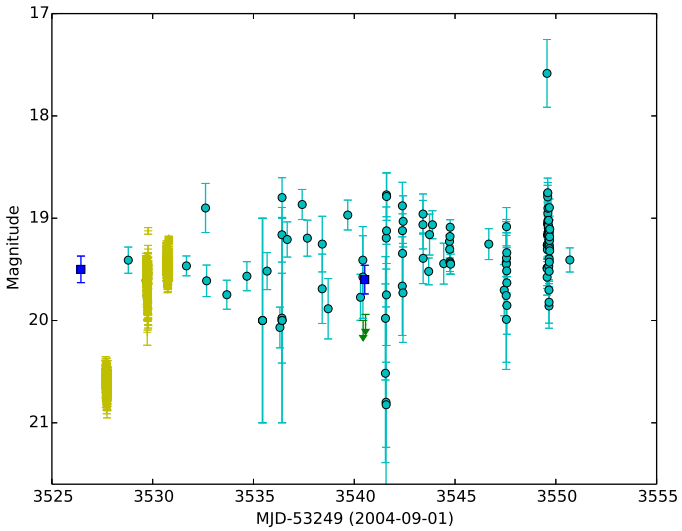

Figure 7.11: The AAVSO observations (cyan), combined with the observations taken from the Catalina Surveys Data Release 2 (same as Figure 7.10), around the HST observations. CSS1111 has a variation of 0.2 magnitudes during its orbital period, which accounts for the fluctuations seen in the AAVSO light curve, but not for the very low non detections ($>$ 20.5 magnitudes) seen in the CRTS light curve. The yellow shows the data obtained with the VATT as detailed in Section 7.2.3.

photometric variability of CSS1111. While the AAVSO light curve finds CSS1111 with a mean magnitude of 19.5, with error bars larger than the expected orbital modulation of 0.2 magnitudes (Littlefield et al., 2013), the CRTS light curve shows very different behaviour - CSS1111 is not detected for periods of time with a limiting magnitude of 20.5 at stages, and often even down to 21 magnitude. The light curve of CSS1111 has been seen to vary by 0.6 magnitudes over a single night (see Figure 1 of Littlefield et al. 2013), and combining this single night of observations with the CRTS light curve leads us to believe CSS1111 might exhibit a hitherto unknown deeper quiescent state, where the magnitude of the object drops to below 20.5. This is further confirmed by the VATT observations shown in Figure 7.11, where CSS1111 had magnitude > 20.5 during the first night of VATT data.

Littlefield et al. (2013) proposed that the region of enhanced emission in the Doppler tomograms not associated with the hot spot is possibly due to a spiral shock in the accretion disc. Typically, spiral shocks are not seen in CVs, as the radius at which the 2:1 orbital resonance ($R_{2:1}$) occurs is beyond the maximum radius of the accretion disc. However, for systems with a small mass ratio, $q < 0.1$, $R_{2:1}$ lies within the accretion disc, allowing spiral shocks to

form. The estimated mass ratio of CSS1111 is 0.06 (Kato et al., 2013), and as such, $R_{2:1}$ in velocity space lies at 750 km s^{-1}. This radius is plotted on both Doppler tomograms, and shows that the emission region on the right hand side of the tomograms lies along this radius. Even with a disruption to the disc, the spiral shock should be stable up to the 3:1 orbital resonance, which lies at a velocity 850 km s^{-1}, and the emission region lies within this radius.

The trailed spectra in Figure 7.2 confirm similar structure in the disc between the observations in 2012 and in 2014. The double S-wave shapes of two emission areas intertwined seen in the 2012 Hα and He I lines is still visible in the 2014 data. Also, the weak He II 4686Å line, which is partially blended with the 4713 line, is only visible for part of the orbit in both 2012 and 2014. The shape of the He II line is an arc that starts with a velocity of < -1000 km s^{-1} at phase 0.5 and moves towards 0 km s^{-1} at phase 1.0.

This shape follows the arcs which move from < -750 km s^{-1} to 0 km s^{-1} in the Hα and He I lines very well. We attribute the origin of the He II emission to the same area which produces these arcs, which is the emission area seen in the lower left quadrant of the Doppler tomograms. This is re-enforced by the Doppler tomograms depicted in Figure 7.5, which show the He II emission coming from a similar area to one of the regions of enhanced emission in Hα.

7.6 The Evolved Main Sequence Channel

Figure 7.12 shows our HST line ratio data combined with the line ratios of other CVs from Mauche et al. (1997) taken by the *International Ultraviolet Explorer* (IUE), and the lines ratios of EY Cyg, BZ UMa and EI Psc (RXJ 2329+0628) from Gänsicke et al. (2003) using the Space Telescope Imaging Spectrograph (STIS) on the HST. The data show that CSS1111 lies far away from the region of normal CVs, closer to the anomalous ones identified by Gänsicke et al. (2003) to within our ability to measure C IV emission from the system.

The N/C anomaly suggests that the material coming from the companion star has undergone significant nitrogen enrichment by the carbon-nitrogen process. For this material to be available for accretion, CSS1111 must have undergone TTMT to remove the outer hydrogen layers and expose the hydrogen burning layer above the core. These 2 spectral signatures, the N/C anomaly and the

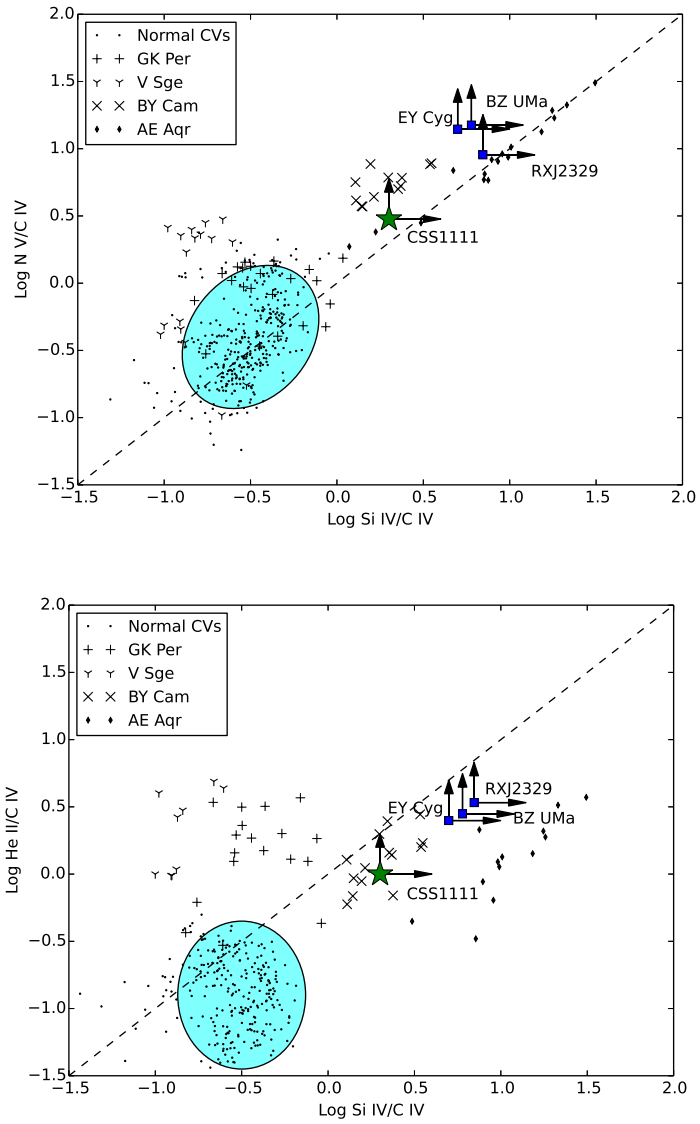

Figure 7.12: The line ratios obtained using our COS HST data for CSS1111. It is clear that CSS1111 (green star) lies far away from the normal CV line ratio in both plots (highlighted circle), closer to the anomalous N V/ C IV inverted systems BY Cam, EY Cyg, BZ UMa, RXJ2329 (EI Psc) and AE Aqr. This suggests that the companion in this system is evolved, and the white dwarf is accreting from a hydrogen shell which has been enriched in nitrogen and depleted in carbon by the CNO process. The GK PER, V Sge, BY Cam, AE Aqr and normal CV data were kindly supplied by C. Mauche, while the data for EY Cyg, BZ Uma and RX J2329 were taken from Gänsicke et al. (2003).

presence of hydrogen alongside the strong helium lines in the optical spectrum, confirm CSS1111 is an ultracompact binary produced by the EMS channel.

There are clear Si and Mg lines visible in the optical spectrum, along with the strong Si IV line visible in the HST spectrum. While the appearance of these lines is unusual, further modelling is required to quantify the abundances of these elements in CSS1111.

The Si II 6347Å/6371Å doublet has been seen in other CVs before, most notably CP Eri (Groot et al., 2001), which is an AM CVn system with an orbital period of 29 minutes (Howell et al., 1991). Previous modelling of accretion discs suggests that, for progenitor stars with solar metallicity and optically thin He discs, the strongest metal lines in the optical should be Si II (Marsh et al., 1991). However, since CSS1111 still has substantial hydrogen visible in its spectrum when compared to AM CVn systems, the modelling done for the AM CVn systems would need to be modified to include hydrogen before being applied to this source to confirm the origin of the Si II line.

Another explanation for the appearance of these rarely seen lines could be due to the He novae that are predicted to happen in this system. For He novae where the He shell has a small mass ($< 10^{-1} M_{\odot}$) and is polluted by C and N, the primary nuclear products of the detonation are ^{28}Si and ^{40}Ca (Shen & Moore, 2014). In an attempt to explain the observed N/C anomaly in the photospheres of some WDs, as opposed to in their accretion discs, Sion & Sparks (2014) proposed that when a nova occurs in a binary system, some of the processed material ejected from the WD ($\approx 2\% - 4\%$) is captured by the surface of the secondary star, and is then recycled through the accretion disc back to the surface of the WD. It is possible that a similar process is occurring in CSS1111 and other EMS channel CVs, where a He nova produces Si and other metals, which are then captured by the secondary and appear in the accretion disc.

7.6.1 V418 Ser

We obtained 5 optical spectra of V418 Ser using the LBT on 2014 June 24 after it returned to quiescence (Garnavich et al., 2014). The average continuum-normalised spectrum of V418 Ser can be seen in Figure 7.14, alongside the spectrum of CSS1111. The main features of these spectra are

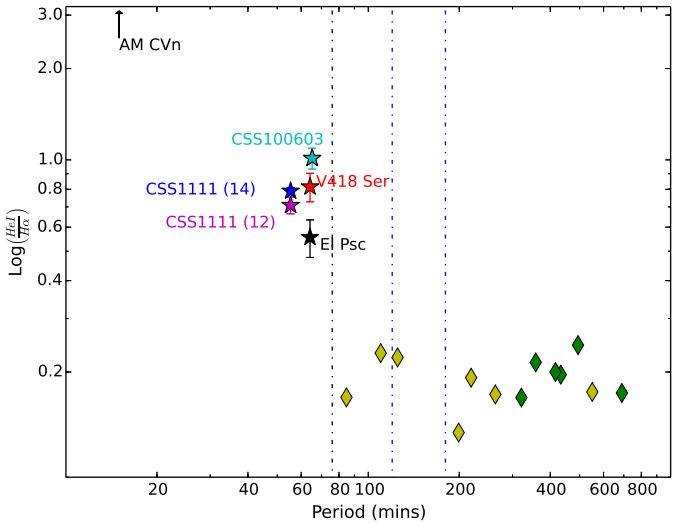

Figure 7.13: The flux ratio of He I 5876Å over Hα versus orbital period for different systems. CSS1111, V418 Ser and CSS 100603 have ratios between 0.7-1. We have taken the superhump period of 64.2 min to be the orbital period of V418 Ser, since the orbital period should lie close to this period. The yellow diamonds represent several long period novae and dwarf novae systems, where the ratios were taken from Williams & Ferguson (1982) and the periods were taken from Ritter & Kolb (2003). The green diamonds show the ratio for 5 CVs with periods above 5 hours, taken from Thorstensen et al. (2004). The black dashed line shows the period minimum of 76 mins, and the 2 blue dashed lines show the period gap between 2 and 3 hours.

nearly identical - He I is unusually strong compared to Balmer emission, there is some He II emission and also detectable SiII 6347Å. The fluxes and EW of several lines can be seen in Table 7.2. Figure 7.13 shows the flux of He I 5876Å over the flux of Hα emission versus orbital period for CSS1111, V418 Ser and CSS 100603, another possible EMS channel CV (Breedt et al., 2012). It is clear that the He I/Hα ratio is very different for the EMS CVs (0.7-1.0) compared to typical CVs (0.2-0.3). Because the orbital period is shorter than the hydrogen period minimum, and the spectrum is near-identical to that of CSS1111, we classify V418 Ser as a product of the EMS channel.

7.6.2 EMS Channel and Type Ia Supernovae

Type Ia supernovae (SNIa) are thought to be detonations of carbon/oxygen (C/O) WDs as they approach the Chandrasekhar mass limit (Chandrasekhar, 1931). Despite their use as important cosmological probes (e.g. Riess et al.

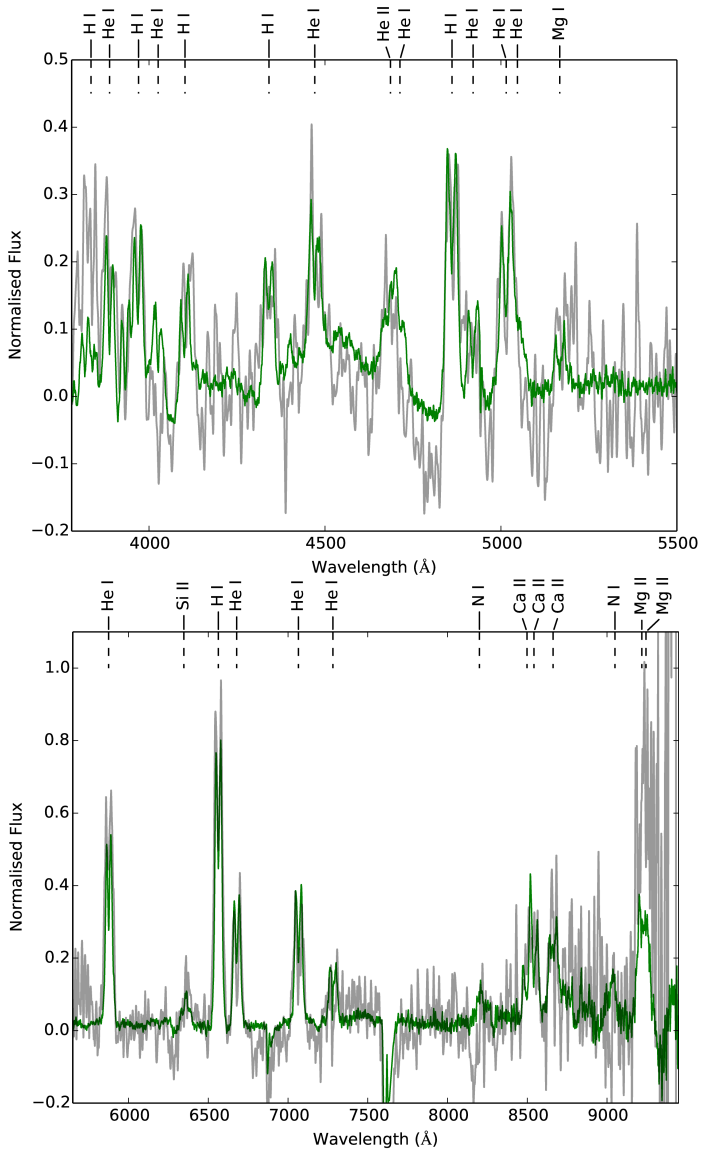

Figure 7.14: The average spectrum obtained of V418 Ser using the LBT is shown in grey. The green line shows a scaled version of the spectrum from CSS1111 to help compare the features common to both spectra. From the similar ratios of equivalent width of He I 5876 Å to Hα and the appearance of the SiII 6347 Å lines, it is nearly beyond doubt that V418 Ser is a product of the evolved main sequence channel.

1998; Perlmutter et al. 1999), the progenitors of SNIa remain a mystery. Two mechanisms for increasing the mass of a white dwarf have long been debated without a clear resolution. Mass transfer through a "single degenerate" channel (SD) where the donor is a non-degenerate stellar companion (Whelan & Iben, 1973) was the model of choice for several decades. However, slow transfer of hydrogen to the WD results in nova outbursts that appear to erode the WD mass, while the number of binaries with continuous hydrogen burning appear too low to explain the SNIa rate. Alternatively, the recent revival of the "double degenerate" channel, where two white dwarfs combine to reach or exceed the Chandrasekhar limit, has its own shortcomings. These include the lack of WD binaries with sufficient total mass and short orbital periods, as well as the difficulty in disrupting a WD without fusing the C/O before detonation can be achieved (see the review by Maoz et al. 2014).

The SNIa progenitor problem has led to a re-examination of older models, in particular, the possibility that sub-Chandrasekhar mass WDs are the source of some SNIa. This has received support from the analysis of supernova light curves by Scalzo et al. (2014) that suggests SNIa with fast decaying light curves eject less than 1.4 $M_\odot$ of material in their explosions. The trick is to get runaway fusion in the C/O core when the WD is not close to the Chandrasekhar mass. This can be done through a "double detonation" where the detonation of surface helium drives a shock toward the center that can trigger the C/O detonation (Taam 1980; Shen & Moore 2014).

Early calculations required a helium shell more massive than 0.1 $M_\odot$ to achieve a detonation and the resulting explosion had a large amount of iron-group elements at high velocities so the results did not look like a SNIa (Höflich & Khokhlov 1996; Nugent et al. 1997). Recent models suggest significantly lower mass helium shells polluted with carbon and nitrogen can detonate (Shen & Bildsten 2009; Fink et al. 2010) and little sign of the He shell would be present in the SNIa spectra (Shen & Moore, 2014). Shen & Moore (2014) also place an upper limit on the accretion rate in these systems of $\dot{M}_c < 10^{-6} M_\odot$ yr^{-1}, such that stable helium burning does not occur on the surface of the WD.

If a low-mass helium shell double detonation mechanism works to make SNIa, then the products of the EMS channel are progenitors of some SNIa events. The EMS systems discussed here are transferring a larger and larger fraction of helium over time. The accretion rates in these systems are expected to be much less than $\dot{M}_c$, as the accretion rate for CVs with a period of ≈ 55 mins is

$10^{-9} M_{\odot}$ yr^{-1} (Podsiadlowski et al., 2003). The helium sinks in the WD atmosphere and survives hydrogen nova events. The over-abundance of silicon and calcium in the accretion disc may be signs that helium nova explosions have polluted the secondary, as suggested at the end of Section 6, and these eruptions are precursors to a helium detonation that could ignite the C/O in the core.

7.7 Conclusions

CSS1111 shows a high N/C ratio, along with hydrogen and strong helium lines in the optical. These two spectral features are most likely caused by the companion in this system having just evolved off the main sequence just as mass transfer began. The main result of having an evolved main sequence star is that this system has evolved below the hydrogen period minimum, while still having hydrogen in its spectrum, unlike ultra compact systems produced by the double degenerate and helium burning channels. It is thought that as CSS1111 continues evolving, the hydrogen abundance in the system will drop as hydrogen is lost due to mass exchange. Depending on the efficiency of magnetic braking in these systems, it is possible that both CSS1111 and V418 Ser will reach a period minimum of 11 min. At this point, the hydrogen abundance in the system will be low enough that it will likely become undetectable in the optical spectrum, and the system will look like an AM CVn system formed by the double degenerate channel.

V418 Ser shows the same optical signatures as CSS1111, and has a period below the period minimum. Due to its similarity to CSS1111, we classify V418 Ser as an EMS ultra compact binary, which along with EI Psc and CSS 100603, brings the total number of CVs with strong cases for evolving by the EMS channel up to 4.

Acknowledgements

The authors would like to thank the financial support from the Naughton Foundation, the Strategic Research Fund in University College Cork, and from the University of Notre Dame. We would also like to thank Science Foundation Ireland for financial support. We acknowledge C. Mauche for kindly supplying

us with the IUE line ratio data shown in Figure 7.12. We would like to thank the AAVSO members for observing CSS1111 before and during HST observations, in particular Emery Erdelyi, James Foster, Franklin Guenther, Radu Gherase, Gordon Myers, Eddy Muyllaert, Velimir Popov, Roger Pickard, Richard Stanton, Daniel Taylor, Bradley Walter and Gary Walker. We would also like to thank David Lathan and Allyson Bieryla for observations made with KeplerCAM at the FLWO the night before the HST visit, and finally Henk Spruit for his Doppler mapping software. Support for program number 13427 was provided by NASA through a grant from the Space Telescope Science Institute, which is operated by the Association of Universities for Research in Astronomy, Inc., under NASA contract NAS5-26555. The CSS survey is funded by the National Aeronautics and Space Administration under Grant No. NNG05GF22G issued through the Science Mission Directorate Near-Earth Objects Observations Program. The CRTS survey is supported by the U.S. National Science Foundation under grants AST-0909182 and AST-1313422. This chapter used data obtained with the MODS spectrographs built with funding from NSF grant AST-9987045 and the NSF Telescope System Instrumentation Program (TSIP), with additional funds from the Ohio Board of Regents and the Ohio State University Office of Research. The LBT is an international collaboration among institutions in the United States, Italy and Germany. The LBT Corporation partners are: The University of Arizona on behalf of the Arizona university system; Istituto Nazionale di Astrofisica, Italy; LBT Beteiligungsgesellschaft, Germany, representing the Max Planck Society, the Astrophysical Institute Potsdam, and Heidelberg University; The Ohio State University; The Research Corporation, on behalf of The University of Notre Dame, University of Minnesota and University of Virginia. APO is a 3.5m telescope owned and operated by the Astrophysical Research Consortium.

8

Do X-ray bursts dream of optical reprocessing? - The optical bursts in UW CrB

UW Coronae Borealis is a low mass X-ray binary that shows both Type 1 X-ray and optical bursts which typically last for 30 s. The system has a binary period of close to 2 hours and is thought to have a relatively high inclination due to the presence of an eclipse in the optical light curve. There is also evidence that an asymmetric disk is present in the system, which precesses every 5.5 days based on changes in the depth of the eclipse. In this chapter, we present optical photometry and spectroscopy of UW Coronae Borealis taken over 2 years. We update the orbital ephemeris using observed optical eclipses and refine the orbital period to 110.97680(1) min. A total of 17 optical bursts are presented, with 10 of these bursts being resolved temporally. The average e-folding time of 19 ± 3s for the bursts is consistent with the previously found value. Optical bursts are observed during a previously identified gap in orbital phase centred on $\phi = 0.967$, meaning the reprocessing site is not eclipsed as previously thought. Finally, we find that the apparent P-Cygni profiles present in some of the atomic lines in the optical spectra are due to transient absorption, which suggests the origin of the absorption is not a wind from the neutron star.

8.1 Introduction

UW Coronae Borealis (UW CrB), also known as MS 1603.6+2600, was discovered by the *Einstein Observatory* Extended Medium Sensitivity Survey and classified as an unusual binary system with an orbital period between 1-2 hours (Morris et al., 1990). It was considered unusual as it did not match the properties of any known CV and a Low Mass X-ray Binary (LMXB) classification was proposed to be an LMXB but, at the time, no other LMXB had been discovered which had an orbital period in the 1-2 hour range (Morris et al., 1990). The optical spectrum of the source showed a strong blue continuum, along with Balmer, He I and He II emission lines alongside the Bowen blend emission feature at 4640Å, and the orbital period was estimated to be close to 2 hours based on variations in the optical light curve (Morris et al., 1990). However, these variations were found to vary from night to night. Hakala et al. (1998) confirmed the variations in the optical light curve, and also ruled out a non-magnetic CV classification for UW CrB, and again proposed that UW CrB could be a LMXB. Mukai et al. (2001) finally confirmed UW CrB as a LMXB after the discovery of a Type 1 X-ray burst in the X-ray light curve obtained using *ASCA*. These X-ray bursts are typically short in duration, and have a sharp rise lasting between $1 - 10$s and slow decay lasting between 10 s up to a few minutes. Type 1 X-ray bursts are indicative of a neutron star (NS) primary as they are thought to arise during brief periods of thermonuclear runwaway on the surface of the NS. For a review on our current understanding of Type 1 X-ray bursts, see Parikh et al. (2013).

However, it is not these X-ray bursts that make UW Crb an interesting system. Hynes et al. (2004) and Muhli et al. (2004) discovered that UW CrB also produces optical bursts that last between 15-30 s and have an optical brightness between 2-3 times that of the system. They proposed that these optical bursts are counterparts to the X-ray bursts, and are produced by reprocessing of the X-ray bursts by material in the system. These type 1 optical bursts are not unique to UW CrB, and have been seen in a handful of other systems (MXB 1735-44, Grindlay et al. 1978; V801 Arae and UY Volantis, Schoembs & Zoeschinger 1990; Aquila X-1, Robinson & Young 1997; GS 1826-24, Homer et al. 1998; and others).

Since 2004, multiple optical observations of UW CrB have revealed more about the structure of the system. Mason et al. (2008) refined the orbital

period to 110.97671(1) min, and discovered that the nightly variations in the shape and width of the eclipse varied periodically with a 5.5 day period, and could be explained by an asymmetric accretion disc in the system which precesses around the NS once every 5.5 days. Hakala et al. (2009) confirmed the super-orbital period of 5.5 days, and also analysed 11 more optical bursts, finding a similar duration to Hynes et al. (2004). Finally, Mason et al. (2012) presented analysis of another 9 optical bursts, and combined the optical bursts from their work with the bursts presented in Hynes et al. (2004) and Hakala et al. (2009). They found that no optical bursts have been observed during an orbital phase gap centred on orbital phase 0.967 and with a width of $\delta\phi = 0.210$, and suggested that this was due to an eclipse of the reprocessing site.

Here, we present new optical photometry taken with the intent to extend the optical ephemeris from Mason et al. (2012), and also to observe more optical bursts. We also present optical spectroscopy of UW CrB, the first taken in 20 years.

8.2 Observations

8.2.1 Photometry

Optical observations of UW CrB were carried out over 10 nights between 2014-2016. Table 8.1 shows the full details of individual observations. The Vatican Advanced Technology Telescope (VATT) 2014 observations were taken using the VATT4K CCD. The Large Binocular Telescope (LBT) 2014 observations were taken using the Large Binocular Camera (LBC) mounted on the DX (right side) of the telescope. The VATT 2015 and 2016 observations were taken using the Galway Ultrafast Imager (GUFI). The data were processed in the usual way sing IRAF. Fig. 8.1 shows the light curve from each individual observation run.

8.2.2 Spectroscopy

While LBC on the DX mirror of the LBT was taking photometry of UW CrB, the Multi-Object Dual Spectrographs (MODS1; Pogge et al. 2010) on the SX

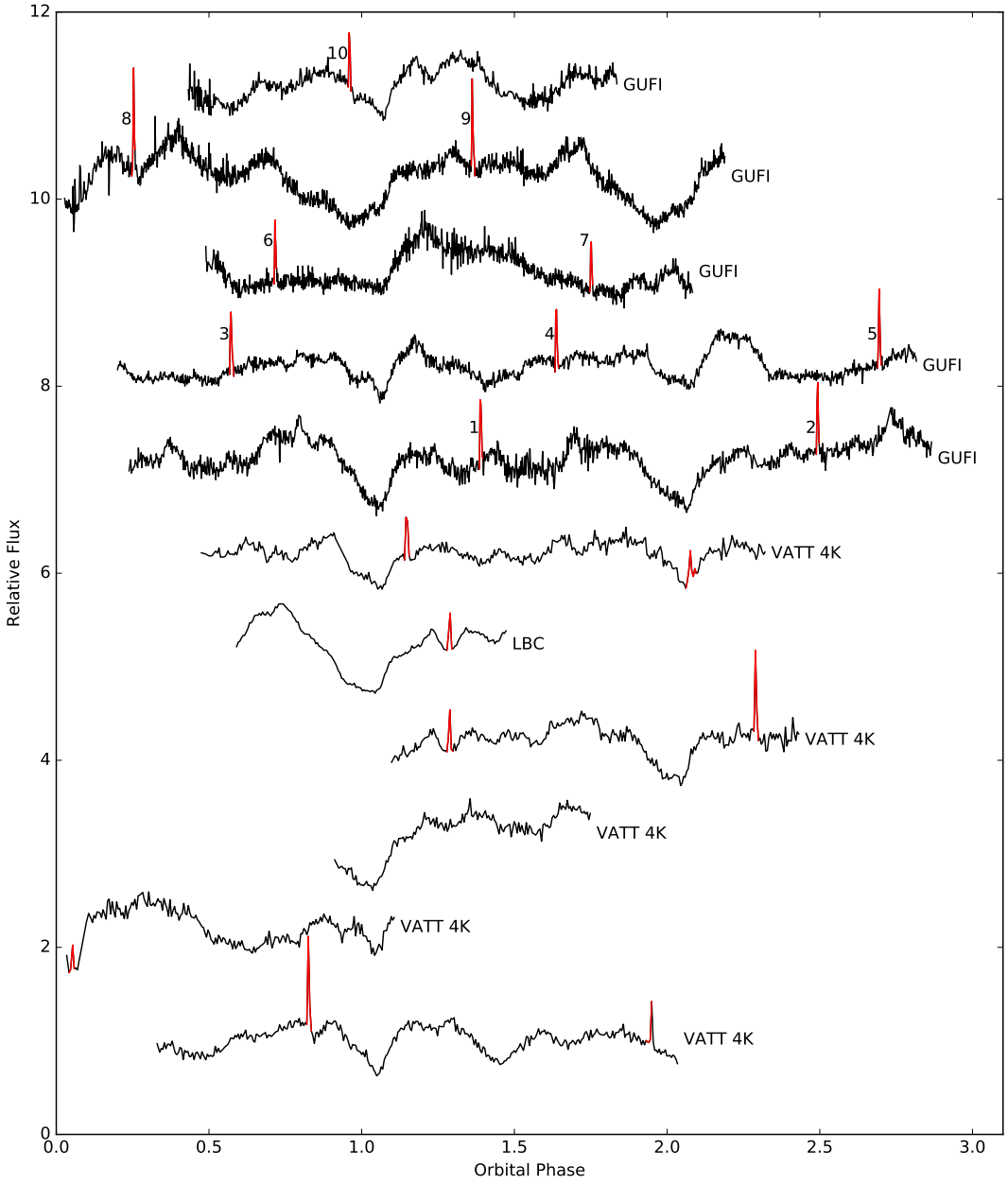

Figure 8.1: The individual light curves for each observation listed in Table 8.1. The light curves have been offset from each other by a constant factor, and are plotted in ascending order, with the bottom light curve taken on $2014-04-29$ and the top light curve taken on $2016-06-07$. The data plotted in red are optical flares whose identification is described in the text. The 10 flares taken using the GUFI instrument, which are numbered 1-10, are analysed in depth later in this chapter. Note that the data taken on $2014-06-30$ from the VATT and LBT overlap, and cover the same flare.

Table 8.1: Details of the various optical observations of UW CrB between 2014 and 2016.

Date (UT) (YYYY-MM-DD)	Telescope	Instrument	Cadence (s)	No. of Frames	Phase Coverage
$2014-04-29$	VATT	VATT4K	34	335	0.3-2.3
$2014-04-30$	VATT	VATT4K	34	212	0.3-1.1
$2014-04-02$	VATT	VATT4K	34	166	0.9-1.7
$2014-06-30$	VATT	VATT4K	34	270	0.1-1.4
$2014-06-30$	LBT	LBC	34	169	0.6-1.5
$2014-07-01$	VATT	VATT4K	34	366	0.5-2.3
$2015-04-10$	VATT	GUFI	15	1130	0.2-2.9
$2015-04-11$	VATT	GUFI	15	1151	0.2-2.8
$2016-06-03$	VATT	GUFI	10	1020	0.5-2.1
$2016-06-04$	VATT	GUFI	10	1387	0.0-2.2
$2016-06-07$	VATT	GUFI	17	583	0.4-1.8

mirror (left side) was taking simultaneous spectroscopy of UW CrB. MODS1 in the dual grating mode covers a wavelength range from 320 nm to 1 μm, divided into red and blue channels separated by a dichroic at 560 nm. The exposure for each spectrum was 60 s and the time between the start of consecutive exposures averaged 120 s.

Fifty spectra were obtained from each spectrograph between 06:18 UT and 7:54 UT. The data reduction tasks were carried out using IRAF. The brightest spectra were corrected for variable seeing. However, during the observing run some spectra were taken when an eclipse of UW CrB was occurring. Since the flux levels of the continuum were so low during these exposures, no such correction was applied.

8.3 Orbital Ephemeris

There were 13 total and 3 partial eclipses observed between 2014 and 2016. Table. 8.2 lists the mid times of these eclipses (estimated by fitting a quadratic to the bottom of the eclipse) and the eclipse numbers calculated using the orbital ephemeris presented in Mason et al. (2012). These eclipse times were added to the 32 mid-eclipse times from Mason et al. (2012) and the 24 mid-eclipse times from Mason et al. (2008), and all 72 mid-eclipse times were fit to determine an accurate ephemeris. The resulting linear ephemeris was

Table 8.2: Mid-eclipse times for the 16 eclipses in the new data.

Eclipse No.	Mid-eclipse Time (HJD)	Error day
47465	2456776.8384	0.0007
47477	2456777.764	0.001
47505	2456779.9180	0.0007
48269	2456838.7972	0.0007
48270	2456838.8746	0.0007
48282	2456839.8008	0.0007
48283	2456839.880	0.001
51955	2457122.8696	0.0007
51956	2457122.9465	0.0007
51968	2457123.8728	0.0007
51969	2457123.9481	0.0007
57403	2457542.728	0.001
57415	2457543.655	0.001
57416	2457543.7286	0.0007
57417	2457543.8042	0.0007
57455	2457546.7397	0.0007

$$T_{mid}(HJD) = 2453118.8390(4) + 0.077067223(9)E. \quad (8.1)$$

The O-C curve for this linear ephemeris is shown in Fig. 8.2, and this ephemeris was used for calculating the orbital phases shown in Fig. 8.1. A quadratic fit was also applied to the data, which gave a quadratic ephemeris of

$$T_{mid}(HJD) = 2453118.8377(4) + 0.077067235(9)E + (8(2) \times 10^{-13})E^2. \quad (8.2)$$

However, this quadratic ephemeris was not a significant improvement on the linear ephemeris. The scatter of the points in Fig. 8.2 is related to the dependance of the mid-eclipse time on the phase of the 5.5 day disc precession.

8.4 Optical Spectrum

The average optical spectrum is shown in Fig. 8.3. The most prominent emission and absorption lines are marked, which correspond to Hα, Hβ, a

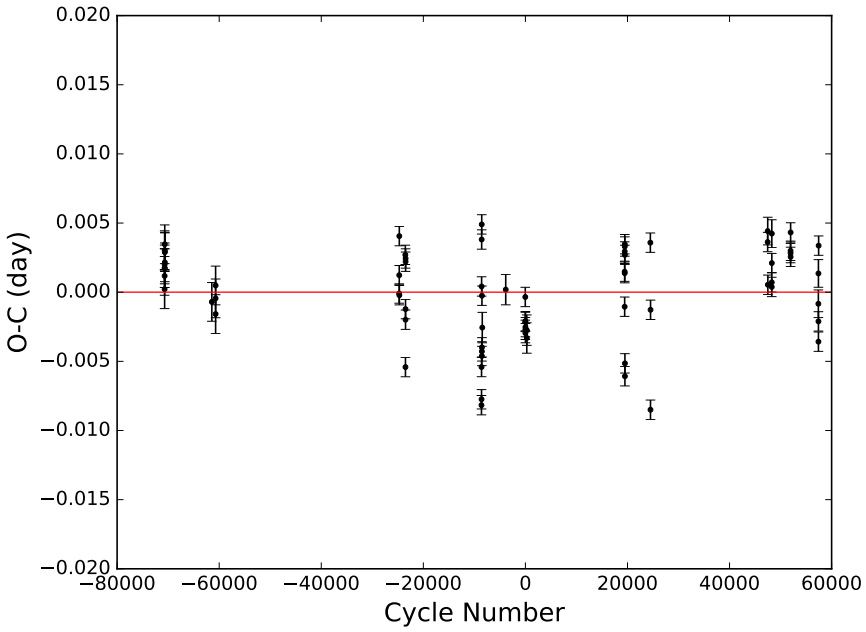

Figure 8.2: The observed-calculated times of mid-eclipse for UW CrB. The cycle number was calculated using Equation 8.1.

series of He I and He II lines and the Bowen blend structure (C III and N III) at 4640Å. The most interesting features of the optical spectrum are the absorption dips seen around He I lines and Hβ. Fig. 8.4 shows the time averaged line profile of He I 5875Å alongside Hβ (here the wavelength has been converted to velocity around the line centres). The average line profiles are characterised by wide blue-shifted absorption dips, with a red-shifted emission component. While these average line profiles resemble the traditional P Cygni line profile, where the emission feature comes from the disc or heated secondary, and the blue-shifted absorption feature is associated with a wind coming from the primary or form an expanding shell of gas around the system, the time resolved spectra suggest a different origin.

Fig. 8.5 shows the light curves constructed from the LBT spectra when different wavelength ranges are chosen. Here, we have chosen 3500-4000Å, 4000-4800Å, 4800-5600Å, and 5800-7500Å as approximations for the U, B, V, and R filters. The trailed plots also show that Hα maintains most of its strength throughout the eclipse, which suggests that the source of the Hα emission is not fully eclipsed by the secondary.

Fig. 8.6 shows the trailed spectrum around He I 5875Å. It is immediately obvious from this trailed spectrum that the line profile of He I is not that of a

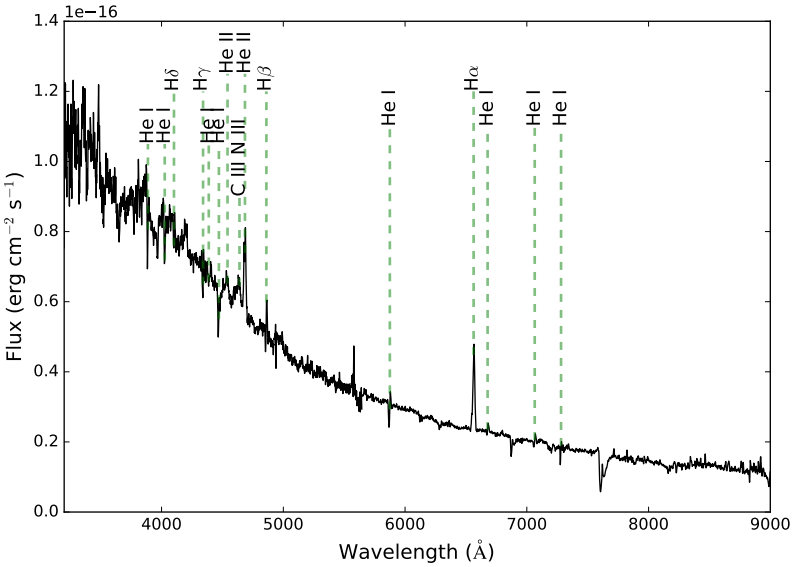

Figure 8.3: The average spectrum of UW CrB taken using the MODS instrument. The most prominant emission lines are marked.

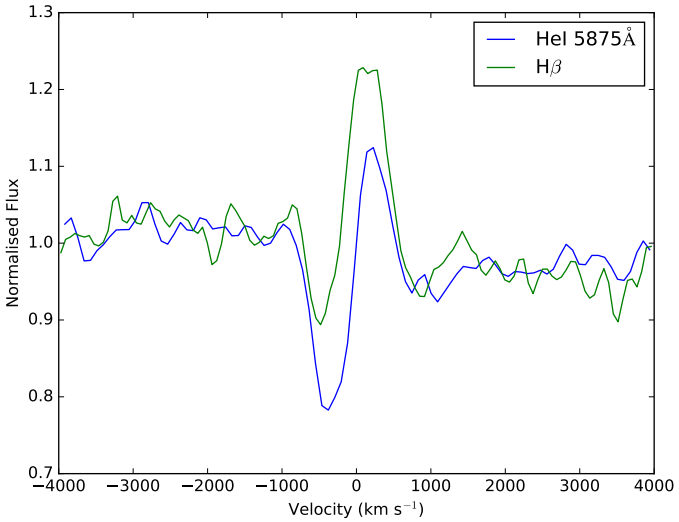

Figure 8.4: Average line profiles of Hβ (green) and He I 5875Å (blue).

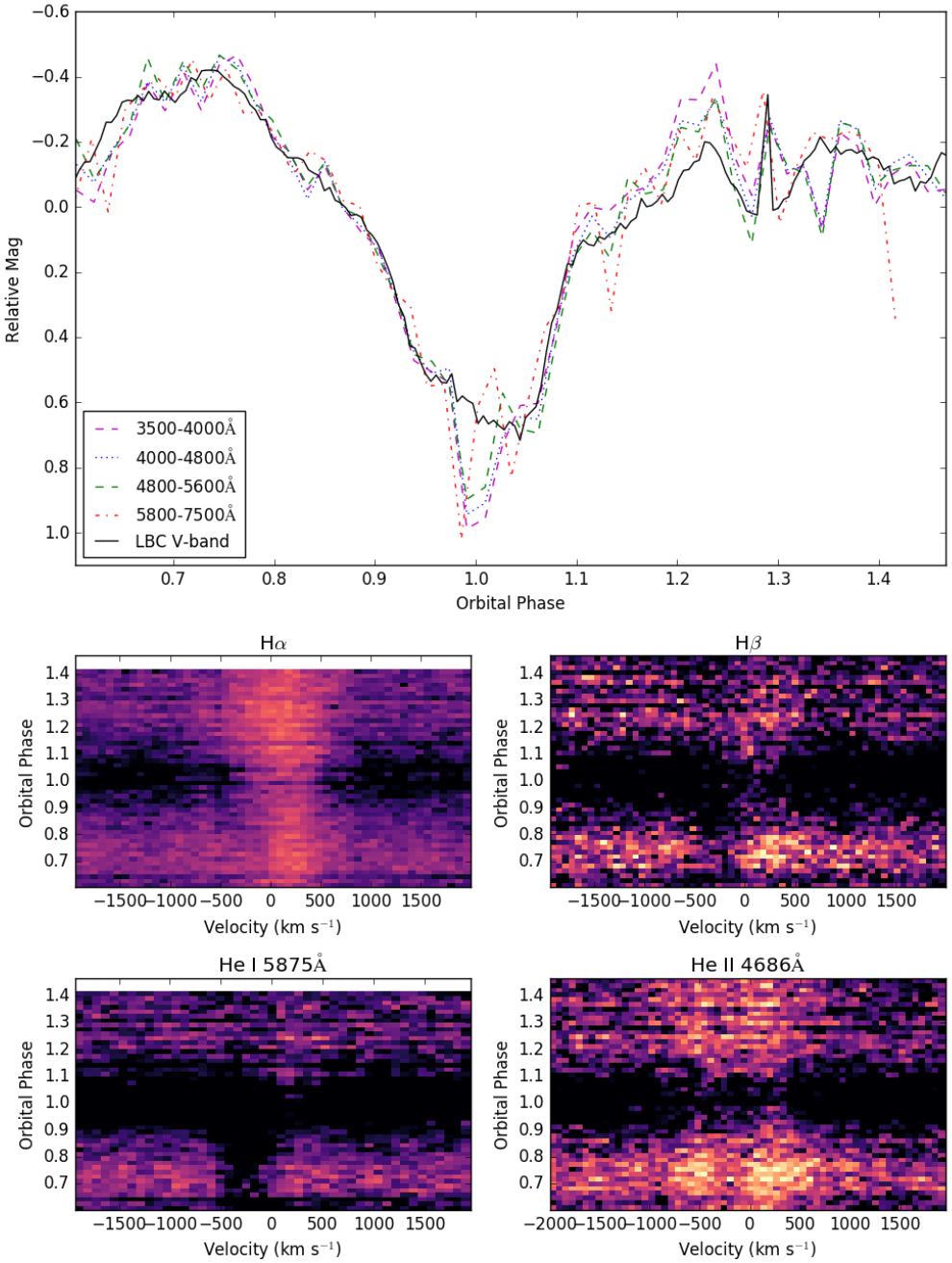

Figure 8.5: The top panel shows the light curves generated by considering different parts of the spectrum along with the LBC light curve. This shows that the eclipse depth and width are consistent across the blue and red wavelengths. The bottom 4 plots show the trailed spectra of Hα, Hβ, He I and He II. These trailed spectra show how the intensity (represented by the colour) of the lines varies over the orbital phase. In particular, all the lines experience a drop in intensity during eclipse. He II shows a strong double peaked nature throughout the binary orbit, while He I shows transient absorption.

conventional P Cygni line. In typical P Cygni lines, the blue-shifted absorption component arises due to either an expanding shell of high velocity gas around the system (typically the remnant of a Nova shell in a CV) or from a strong stellar wind that either originates from the primary or from a high mass companion (which could not be the case for UW CrB since the secondary is thought to be low mass). In any case, all of these scenarios should lead to a blue shifted absorption component that is visible throughout the orbital period.

This is not the case for UW CrB, where the absorption component is visible without any emission counterpart for orbital phase $0.6 - 0.93$. Then, around the time of optical eclipse, the line undergoes a reversal, with the absorption feature becoming weaker, and a strong, red-shifted emission component develops in the line profile. Finally, at orbital phase 0.16, both features disappear (or, at the very least, become significantly weaker, as shown by the top average spectrum shown in Fig. 8.6). The strong emission seen around orbital phase 0 is probably due to a weakening of the continuum as the accretion disc is eclipsed, allowing for the line to become detectable, as opposed to an actual strengthening of the emission line itself. This suggests that the emission feature is not present for the whole orbit. Rather, it is just drowned out by the continuum, and only becomes detectable during eclipse. Thus, we only treat the absorption feature as transient.

8.4.1 Optical Burst Spectrum

The top panel of Fig. 8.7 shows the LBC light curve around the time of the optical burst seen in the LBT data. Fortunately, both sides of the spectrograph were exposed for the burst, albeit probably not for the full duration of the burst. The observed optical burst spectrum shown in the main panel of Fig. 8.7 has a stronger continuum than the spectra taken either side of the burst. However, no changes in any of the emission lines is detectable, with Hα best resolved. The residual spectrum (burst spectrum - average spectrum) is consistent with being flat. This means we cannot get any temperature constraints from the optical spectrum. The detection of the burst is promising, and suggests a larger telescope will be able to obtain higher signal-to-noise burst spectra which will help constrain the site of the optical reprocessing. The physical origin of the feature around 7700Å is unknown, but is visible in several spectra throughout the orbit, suggesting it is not related to the burst.

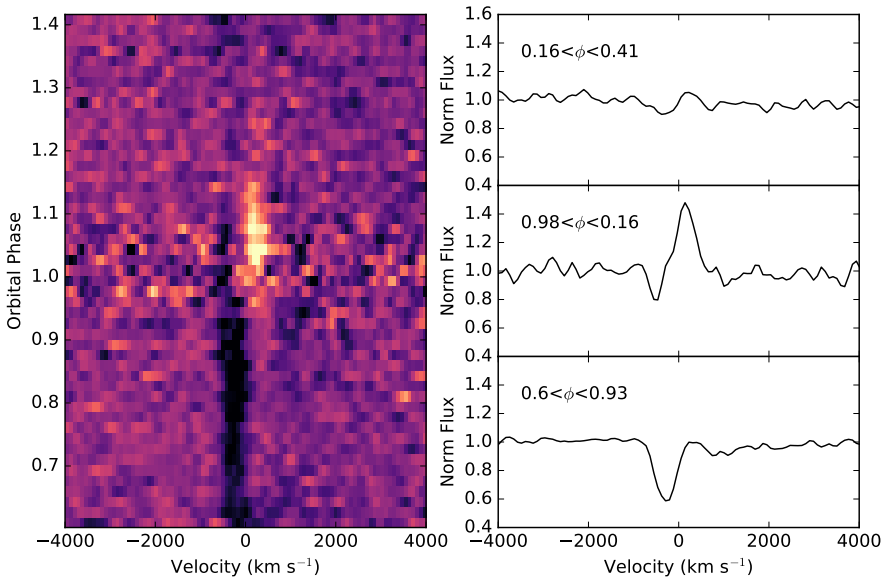

Figure 8.6: The left panel shows the trailed spectrum around He I 5875Å. The right panels show the average spectrum for selected orbital phases, highlighting when the line displayed strong absorption, strong emission and just continuum. The spectra here have been smoothed by convolving the spectrum with a gaussian with a $\sigma = 0.9$Å.

8.5 Optical Bursts

A total of 17 optical bursts were detected in all of the observations taken of UW CrB. These bursts were identified in the observed light curves by looking for points which were more than 3σ away from the median of the surrounding 40 points, where σ is the standard deviation of the 40 points. These bursts were then inspected by eye to ensure they were bursts. Seven (one of which was also detected in the LBC observations) of these bursts were detected using the VATT4K instrument with a temporal resolution of 35s. Since the optical bursts have been observed to have an $e-$folding time of 20s, this means the VATT4K observations were unable to resolve bursts. However, even though these bursts cannot be modelled, the orbital phases at which they were detected is important, and will be discussed in Section 8.5.2.

8.5.1 Modeling the Optical Bursts

There were ten bursts detected using the GUFI instrument with a temporal resolution of 15s or better. These bursts were modeled using an instantaneous

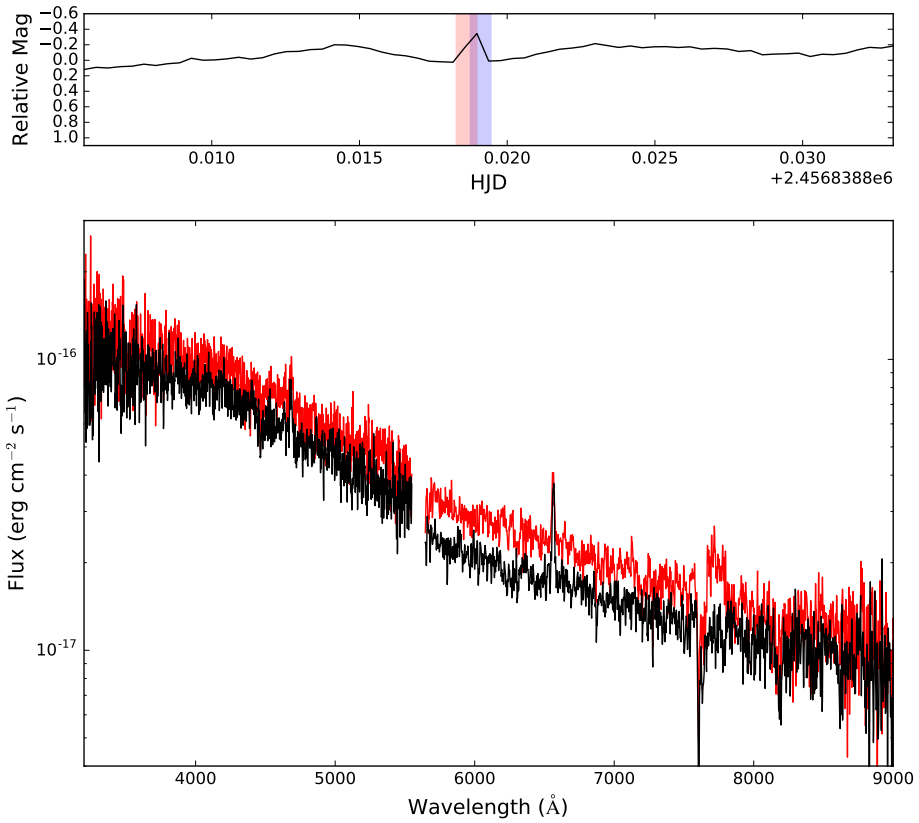

Figure 8.7: The top panel shows the LBC light curve, focused on the time around the optical burst. The transparent red region highlights the time when the red spectrograph of MODS1 was exposed, while the transparent blue region highlights the time when the blue spectrograph was exposed. The main panel shows the entire optical spectrum observed during the burst (red) versus the average of the spectra taken directly before and after the burst (black).

rise and exponential decay model, as done previously by Hynes et al. (2004) and Hakala et al. (2009). This model has the form,

$$F(t) = A\, e^{\left(\frac{t-t0}{\tau}\right)}, \tag{8.3}$$

where $t0$ is the start time of the burst and τ is the $e-$folding time of the bursts. The model fit to each of the 10 bursts observed using GUFI can be seen in Fig. 8.8, along with the τ for each burst. The average τ from all 10 bursts was 19 ± 3s. This is longer than the model $e-$folding time of $10-15$s found by Hynes et al. (2004) , but closer to their observed $e-$folding time of $15-28$s and in good agreement with the $e-$folding time $15-27$s found by Hakala et al. (2009).

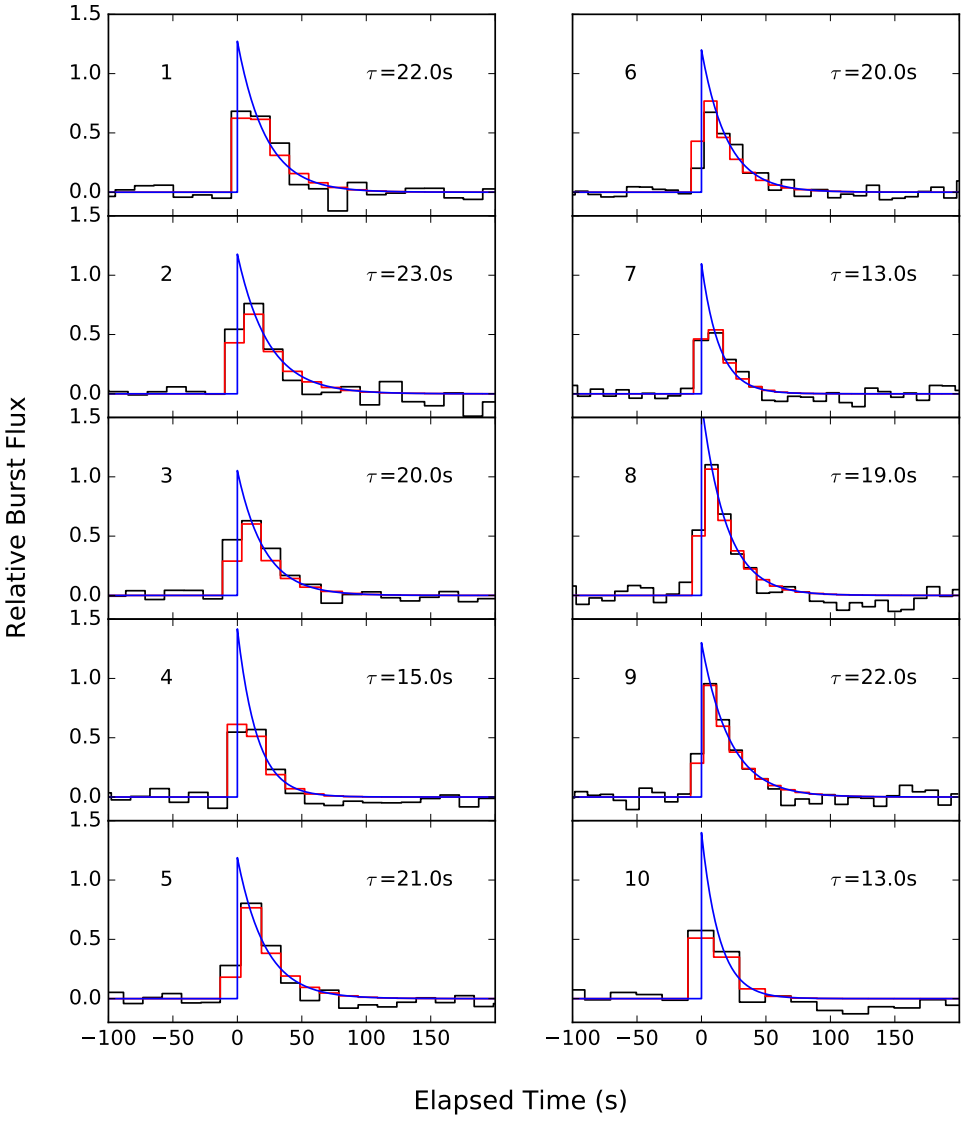

Figure 8.8: The 10 optical bursts observed with the GUFI instrument (in black) along with the resulting model from fitting Equation 8.3 (blue). The red line shows the model rebinned to match the data sampling rate. The resulting $e-$folding time is shown in each panel.

8.5.2 Orbital phases of the bursts

The relative fluence of all 17 optical bursts and the phases at which they occurred were added to the 33 optical bursts listed in Mason et al. (2012). Fig. 8.9 shows a polar plot of the bursts, with the angle of the burst representing the orbital phase at which the burst occurred, and the radial extent of the burst representing the relative fluence of the burst. The gap in observed bursts noted by Mason et al. (2012) now has 2 bursts present (these are the second burst in the first VATT4K light curve, and the burst marked 10 in the last GUFI light curve). Mason et al. (2012) initially proposed that the apparent gap centred around orbital phase 0.967 was due to an eclipse of the reprocessing region, masking the optical bursts from view. However, the detection of these two bursts rules out this theory. In particular, the two bursts had a relative fluence which was comparable to the average relative fluence of the bursts, suggesting the reprocessing sight is not eclipsed.

8.6 Conclusions

Two optical bursts have now been observed during the orbital phase gap proposed by Mason et al. (2012), suggesting the site of reprocessing is not eclipsed as previously thought. However, it remains to be seen whether the orbital phase gap is dependant on the phase of the 5.5 day precessing accretion disc. Since it is possible that the reprocessing site is located within the disc, it is also possible that during certain parts of the 5.5 day precession of the disc, this site does become eclipsed during the orbital phases proposed by Mason et al. (2012) (logically, this would be when the site lies in between the NS and the secondary), and that during the other phases of the precessing disc, this site is not eclipsed (logically, this would be when the site lies on the far side of the NS, furthest from the companion). This argument is fully dependant on whether the reprocessing site is in the disc, which is yet to be confirmed. One thing is for certain - further optical monitoring of UW CrB, preferably over the 5.5 day disc period, should be performed to see if the appearance of the bursts is dependant on the phase of the disc.

The optical spectra presented here raise more questions than they answer. Previously, the P Cygni profiles seen in He I and Hβ were thought to arise due to a wind from the NS. However, our time resolved spectra show that the blue

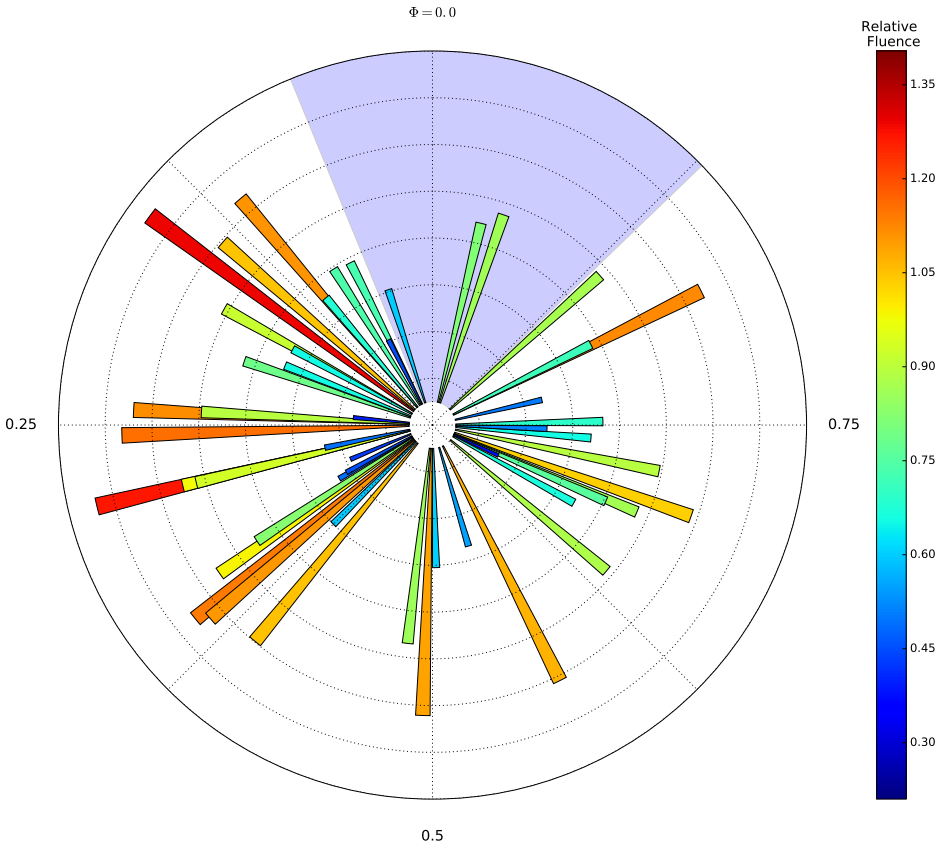

Figure 8.9: The fluences and orbital phases of every optical burst seen in UW CrB. This combines the 17 bursts presented in this work and the 33 optical bursts listed in Mason et al. (2012). The blue shaded region shows the gap identified by Mason et al. (2012). There are now 2 detected bursts in this region.

absorption wing of these lines is transient, which is not expected for a wind component. It may be that our viewing angle of the accretion structures changes through the orbit, which leads to different amounts of absorption in the lines (this may also be related to the 5.5 day disk precession period). Furthermore, the brightest emission line (Hα) is not fully eclipsed, and is only slightly reduced in flux during the eclipse. This suggests the site of Hα emission is not fully eclipsed by the secondary, and could mean that some emission is generated above the plane of the disc. Finally, we have seen evidence of the Bowen blend emission in the averaged spectrum. Further optical spectra with a high time resolution should be obtained to fully characterise the transient nature of the absorption in different spectral lines, and to track the Bowen blend emission over a full orbital period in order to

constrain the mass of the NS.

9 Summary & Future Work

In this work, we have presented optical and X-ray properties of new and old binary systems containing a compact object. We have focused on the photometric, spectroscopic and X-ray behaviour of these systems, which has allowed us to investigate:

1. the magnetic properties of newly discovered cataclysmic variables, which possibly contribute to the low X-ray luminosity CV population.
2. the first recorded X-ray observations of an intermediate polar during a low state, and establish a time line for recovery.
3. the cause of hydrogen emission in CVs below the period minimum, and a method to identify new evolved main sequence candidates through optical spectroscopy.
4. the cause, duration and timing of the type 1 optical bursts seen in the low mass X-ray binary UW CrB, and possibly the first optical spectrum of one of these bursts.

Below, we summarise the conclusions of each of the chapters, and future work for each system.

9.1 Lanning 386 & J1923

We have presented results which suggest both J1923 and Lanning 386 harbour magnetic WDs as their primary stars, based on a QPO visible in the light curves of both objects with a periodicity of 20 min. We have constrained the inclination on J1923 to $81.3 - 83.6°$, indicating it is a nearly edge on system. We also presented X-ray results on Lanning 386, along with an upper limit on the X-ray flux from J1923. The X-ray spectrum of Lanning 386 suggests the X-rays produced in the system are subject to a high circumstellar absorber, and the visibility of a clear X-ray eclipse confirms the high inclination of this source. Finally, we presented a method to put an upper limit on the magnetic moment of the WD in Lanning 386 based on high time resolution optical spectroscopy.

9.1.1 Future Work

There are still many questions surrounding J1923 and Lanning 386. Mainly, what is causing the frequent high and low states in these systems, and why is

the X-ray luminosity of Lanning 386 so low for a probably magnetic system?

Future plans to further investigate the magnetic nature of Lanning 386 is to perform radio observations of the system. Several IPs and a few novalike CVs have been detected at radio wavelengths (Mason & Gray 2007; Coppejans et al. 2015). Given Lanning 386's relatively close proximity to Earth (160$\pm$50 pc) when compared to these detected sources, it may be possible to detect Lanning 386 using new technology radio telescopes. We are also considering applying to use Ultracam or HiPERCAm, which are 2 instruments capable of high time resolution photometry, to monitor the behaviour of the QPOs in Lanning 386 as the system enters eclipse, as the orbital phase at which the QPOs are eclipsed can be used to identify where the QPOs are being generated in the system. This will likely require the use of a medium size (> 4 m) telescope and will have to cover severeal eclipses of the system.

Furthermore, given our success at limiting the magnetic moment in Lanning 386, the method of using high time resolution spectroscopy to estimate the time taken for the inner radius of the accretion disc to be eclipsed should be applied to other objects that display deep optical eclipses. We have begun searching the Ritter & Kolb catalogue for candidates. This would be particularly useful for studying SW Sextantis systems, as it can constrain the magnetic nature of these systems.

9.2 FO Aqr

In this work, we have demonstrated the value of having long time scale, short cadence observations of an intermediate polar. Based on the *K2* observations, we have refined the spin period of the WD to be 1254.3342(8) s, and found a correlation between the brightness of the system and the phase of the spin pulse. We also discovered that during the *K2* observations, the WD in FO Aqr had switched from spinning up to spinning down. When following up on this work in April 2016, we also noticed that FO Aqr had gone into its first ever recorded low state. Analysis of the subsequent X-ray data led us to conclude that the accretion rate in FO Aqr had dropped significantly, and that the hydrogen density within the accretion structure had decreased. Our analysis suggested that FO Aqr should have fully recovered by March 2017.

9.2.1 Future Work

The mechanism for triggering a low state in an IP is still not fully understood, even though it is probably related to the clustering of star spots at the L1 point on the companion star (Livio & Pringle 1994; Hessman et al. 2000). Observing more IPs as they descend into and recover from their low states is key to confirming this scenario. Also, future X-ray observations of any IP in a low state will be essential in confirming the change in accretion mechanisms which we have proposed to have occurred in FO Aqr during its low state. We also have obtained optical spectroscopy of FO Aqr, both during the low state in July 2016 and during the recovery in November 2016. Analysis of these spectra is on going, and should help constrain the structural changes in the accretion disc. We have also successfully proposed for X-ray observations of FO Aqr to be taken in the coming *XMM-Newton* observation window in May 2017 to confirm the system's full recovery.

Additionally, 2 other IPs have been observed by *Kepler* during the *K2* mission - V4743 Sgr (Zemko et al., 2016) and 1RXS J180431.1-273932 (Nucita et al. 2007; Masetti et al. 2012). The short cadence data of both of these CVs will be analysed in the same way that we analysed the data on FO Aqr. This is especially important for 1RXS J180431.1-273932 since its classification as an IP is still tenuous at best.

9.3 CSS1111

We have identified and characterised a likely Evolved Main Sequence Cataclysmic Variable, CSS1111. We have analysed UV spectra of CSS1111 and found that anomalous nitrogen/carbon ratio seen in the UV suggetss the companion in this system is not a main sequence star, but had begun its evolution towards the red giant branch before contact between the Roche lobe and the secondary began. We have also confirmed the previously suggested spiral structure in the accretion disc, and identified another likely EMS candidate, V418 Ser, through its optical spectra.

9.3.1 Future Work

As the number of EMS candidates increases, a better understanding of the evolution of CVs and the underlying population of stars which generate compact binaries will become apparent. Efforts should be made to characterise more CVs that have hydrogen in their optical spectra, but are below the period minimum.

In relation to CSS1111, we predicted (based on long term optical monitoring) that CSS1111 should go into outburst around March/April of each year. Since the work on CSS1111 was published (Nov 2015), the system has had a recorded outburst in March 2016 and a superoutburst in December 2016. Long term monitoring of this object is required to characterise the outbursts, and see if the super outburst has affected the structure of the spiral arms in the accretion disc, or the rate of outbursts in the system.

9.4 UW CrB

We have shown that the optical bursts present in the light curve of UW CrB do not have a preferential orbital phase at which they occur, suggesting the source of optical reprocessing is not eclipsed by the secondary. We also presented analysis of 10 optical bursts taken with high time resolution, confirming the expected burst duration of 20-30 s.

The optical spectra, obtained during orbital phases $0.6 - 0.5$ present a mystery - the cause of the transient absorption seen in He I is not known, but could be related to the orbital phase of the system - it may be that during orbital phases $0.6 - 0.93$, we are viewing the system through an extended region of high optical depth (likely the hotspot at the edge of the disc).

9.4.1 Future Work

It has still not been established whether every X-ray burst produces an optical counterpart. The only way to definitively answer this question is by obtaining simultaneous ground-based optical photometry alongside X-ray observations. This is a difficult ask, and one which X-ray missions are hesitant to commit to since the production of optical bursts does not have a constant rate. However,

an attempt should still be made, for seeing an X-ray burst without an optical counter part would require an obscuration of the reprocessing site, which is counter to what we have proposed here.

We also intend to obtain spectra of UW CrB with longer exposure times and using both mirriors on the LBT in an attempt to resolve any orbital variability in the Bowen Blend emission. If variability is observed, this would lead to an estimate on the radial velocity of the secondary star, and would allow us to put a mass constraint on the NS primary.

A List of Publications

A.1 Peer-reviewed Publications

- "Roche lobe underfilling of the secondary star in PSR J102347.6+003841?" , McConnell,O., Callanan, P. J., Kennedy, M., Hurley, D., Garnavich, P., Menzies, J., 2015, *Mon. Not. R. Astron. Soc*, **451**, 3468
- "The evolved main-sequence channel: HST and LBT observations of CSS 120422: 111127+571239", Kennedy, M., Garnavich, P., Callanan, P., Szkody, P., Littlefield, C., Pogge, R., 2015, *The Astrophysical Journal*, **815**, 131
- "Cataclysmic Variables observed during K2 campaigns 0 and 1", Dai, Z., Szkody, P., Garnavich, P., Kennedy, M., 2016, *The Astronomical Journal*, **152**,5
- "Kepler K2 Observations of the Intermediate Polar FO Aquarii", Kennedy, M. R., Garnavich, P., Callanan,P., Breedt, E., Marsh, T. R., Gänsicke, B. T., Steeghs, D., Szkody, P., Dai, Z. , 2016, *Mon. Not. R. Astron. Soc*, **459**,3622
- "The new eclipsing CV MASTER OTJ192328.22+612413.5 - a possible SW Sextantis Star", Kennedy, M. R., Callanan, P., Garnavich, P., Szkody, P., Bounane, S., Rose, B. M., Bendjoya, P., Abe, L., Rivet, J. P., Suarez, O., 2016, *The Astronomical Journal*, **152**, 27
- "Return of the King: Time-Series Photometry of FO Aquarii's Initial Recovery from its Unprecedented 2016 Low State", Littlefield, C.,

Garnavich, P., Kennedy, M. R., Aadland, E., Terndrup, D. M., Calhoun, G. V., Callanan, P., Abe, L., Bendjoya, P., Rivet, J.P., Vernet, D., Devogele, M., Shappee, B., Holoien, T., Heras, T. A., Bonnardeau, M., Cook, M., Coulter, D., Debackere, A., Dvorak, S., Foster, J. R., Goff, W., Hambsch, F.J., Harris, B., Myers, G., Nelson, P., Popov, V., Solomon, R., Stein, W.L., Stone, G., Vietje, B., 2016, *The Astrophysical Journal*, **833**, 93

- "XMM-Newton Observations of the Peculiar Cataclysmic Variable Lanning 386: X-ray evidence for a Magnetic Primary", Kennedy, M. R., Callanan, P., Garnavich, P. M., Fausnaugh, M., Zinn, J. C., 2017, *Mon. Not. R. Astron. Soc.*, **466(2)**, 2202
- "X-ray observations of FO Aqr during the 2016 low state", Kennedy, M. R., Garnavich, P. M., Littlefield, C., Callanan, P., Mukai, K., Aadland, E., Kotze, M. M., Kotze, E. J., 2017, *Mon. Not. R. Astron. Soc.*, in print, arXiv ID:1704.01909

A.2 Oral Presentations

- "Optical observations of the transiently accreting radio pulsar binary PSR J1023+ 0038", June 2014, The X-ray Universe 2014, Trinity College Dublin, Ireland
- "CSS120422 J111127+571239: Diving Below the Period Minimum with HST and LBT spectra", August 2015, Irish National Astronomy Meeting, Queens University Belfast, United Kingdom
- "XMM-Newton Observations of the Peculiar Cataclysmic Variable Lanning 386: Hot, Sexy, and Magnetic?", September 2016, Irish National Astronomy Meeting, University College Dublin, Ireland

A.3 Conference Poster Presentations

- "Optical and Spectroscopic Observations of J192328.22+612413.5: A high inclination Catclysmic Varible", August 2014, Irish National Astronomy Meeting, Trinity College Dublin, Ireland
- "CSS120422 J111127+571239: Diving Below the Period Minimum with

HST and LBT spectra", January 2015, American Astronomical Society 225th Meeting, Seattle, U.S.A

- "A Look Inside a Star: The Evolved Main-Sequence Channel and Hydrogen Depleted Ultracompact Binaries", March 2015, Meeting of the Joint Institute for Nuclear Astrophysics, University of Michigan, Lansing MI, U.S.A
- "Do x-ray bursts dream of optical reprocessing? The optical bursts in UW CrB", November 2015, Instituto de Astrofísica de Canarias Winter School 2015 on High Time Resolution Astrophysics, Tenerife, Spain
- "*Kepler K2* Observations of the Intermediate Polar FO Aquarii", March 2016, Institute of Physics in Ireland Spring Meeting 2016, Belfast, United Kingdom

Built on the shoulders of

Abbott, B. P., Abbott, R., Abbott, T. D., et al. 2016, Physical Review Letters, 116, 061102

Andronov, I. L. 1987, Astrophysics and Space Science, 131, 557

Andronov, I. L., Ostrova, N. I., & Burwitz, V. 2005, ASP Conference Series, 335, 229

Andronov, N., Pinsonneault, M., & Sills, A. 2003, The Astrophysical Journal, 582, 358

Anupama, G. C. 2013, in IAU Symposium, Vol. 281, Binary Paths to Type Ia Supernovae Explosions, ed. R. Di Stefano, M. Orio, & M. Moe, 154–161

Anzolin, G., de Martino, D., Bonnet-Bidaud, J.-M., et al. 2008, Astronomy & Astrophysics, 489, 1243

Armitage, P. J., & Livio, M. 1996, The Astrophysical Journal, 470, 1024

—. 1998, The Astrophysical Journal, 493, 898

Arnaud, K. A. 1996, in Astronomical Society of the Pacific Conference Series, Vol. 101, Astronomical Data Analysis Software and Systems V, ed. G. H. Jacoby & J. Barnes, 17

Astropy Collaboration, Robitaille, T. P., Tollerud, E. J., et al. 2013, Astronomy & Astrophysics, 558, A33

Avara, M. J., McKinney, J. C., & Reynolds, C. S. 2016, Monthly Notices of the Royal Astronomical Society, 462, 636

Balbus, S. A., & Hawley, J. F. 1991, The Astrophysical Journal, 376, 214

Ballouz, R.-L., & Sion, E. M. 2009, The Astrophysical Journal, 697, 1717

Balman, Ş., Godon, P., & Sion, E. M. 2014, The Astrophysical Journal, 794, 84

Beardmore, A. P., Mukai, K., Norton, A. J., Osborne, J. P., & Hellier, C. 1998, Monthly Notices of the Royal Astronomical Society, 297, 337

Beltrán, M. T., & de Wit, W. J. 2016, The Astronomy and Astrophysics Review, 24, 6

Bernardini, F., de Martino, D., Falanga, M., et al. 2012, Astronomy & Astrophysics, 542, A22

Bernardini, F., de Martino, D., Mukai, K., et al. 2015, Monthly Notices of the Royal Astronomical Society, 453, 3100

Beuermann, K. 2006, Astronomy & Astrophysics, 460, 783

Beuermann, K., Stasiewski, U., & Schwope, A. D. 1992, Astronomy & Astrophysics, 256, 433

Bode, M. F., & Evans, A. 2008, Classical Novae

Boffin, H. M. J., Steeghs, D., & Cuypers, J., eds. 2001, Lecture Notes in Physics, Berlin Springer Verlag, Vol. 573, Astrotomography

Bonnardeau, M. 2016, Information Bulletin on Variable Stars, 6181, arXiv:1609.01844

Bonnet-Bidaud, J. M., & Mouchet, M. 1987, Astronomy & Astrophysics, 188, 89

Brady, S., Thorstensen, J., Koppelman, M., et al. 2008, Publications of the Astronomical Society of the Pacific, 120, 301

Breedt, E., Gänsicke, B. T., Marsh, T. R., et al. 2012, Monthly Notices of the Royal Astronomical Society, 425, 2548

Brinkman, A., Aarts, H., den Boggende, A., et al. 1998, in Science with XMM

Buat-Ménard, V., Hameury, J.-M., & Lasota, J.-P. 2001a, Astronomy & Astrophysics, 366, 612

—. 2001b, Astronomy & Astrophysics, 369, 925

Burrows, D. N., Hill, J. E., Nousek, J. A., et al. 2000, in Proceedings of SPIE,

Vol. 4140, X-Ray and Gamma-Ray Instrumentation for Astronomy XI, ed. K. A. Flanagan & O. H. Siegmund, 64–75

Butters, O. W., Barlow, E. J., Norton, A. J., & Mukai, K. 2007, Astronomy & Astrophysics, 475, L29

Cannizzo, J. K. 1993, The Astrophysical Journal, 419, 318

Cardelli, J. a., Clayton, G. C., & Mathis, J. S. 1989, The Astrophysical Journal, 345, 245

Carroll, B. W., & Ostlie, D. A. 2006, An Introduction to Modern Astrophysics and Cosmology (Addison-Wesley)

Carter, P. J., Steeghs, D., de Miguel, E., et al. 2013, Monthly Notices of the Royal Astronomical Society, 431, 372

Cenarro, A. J., Peletier, R. F., Sánchez-Blázquez, P., et al. 2007, Monthly Notices of the Royal Astronomical Society, 374, 664

Chabrier, G., Baraffe, I., Leconte, J., Gallardo, J., & Barman, T. 2009, in American Institute of Physics Conference Series, Vol. 1094, 15th Cambridge Workshop on Cool Stars, Stellar Systems, and the Sun, ed. E. Stempels, 102–111

Chandrasekhar, S. 1931, The Astrophysical Journal, 74, 81

Coppejans, D. L., Körding, E. G., Miller-Jones, J. C. A., et al. 2015, Monthly Notices of the Royal Astronomical Society, 451, 3801

Cropper, M. 1990, Space Science Reviews, 54, 195

de Martino, D., Matt, G., Mukai, K., et al. 2006, Astronomy & Astrophysics, 454, 287

den Herder, J. W., Brinkman, A. C., Kahn, S. M., et al. 2001, Astronomy & Astrophysics, 365, L7

Dhillon, V. S. 1996, in Astrophysics and Space Science Library, Vol. 208, IAU Colloq. 158: Cataclysmic Variables and Related Objects, ed. A. Evans & J. H. Wood, 3

Dhillon, V. S., Smith, D. A., & Marsh, T. R. 2013, Monthly Notices of the Royal Astronomical Society, 428, 3559

Drake, A. J., Djorgovski, S. G., Mahabal, A., et al. 2009, The Astrophysical Journal, 696, 870

Dunford, A., Watson, C. A., & Smith, R. C. 2012, Monthly Notices of the Royal Astronomical Society, 422, 3444

Eracleous, M., Wade, R. A., Mateen, M., & Lanning, H. H. 2002, Publications of the Astronomical Society of the Pacific, 114, 207

ESA: XMM-Newton SOC, . 2014, Users Guide to the XMM-Newton Science Analysis System, Issue 11.0

Evans, P. A., & Hellier, C. 2004, Monthly Notices of the Royal Astronomical Society, 353, 447

—. 2007, The Astrophysical Journal, 663, 1277

Evans, P. A., Hellier, C., & Ramsay, G. 2006, Monthly Notices of the Royal Astronomical Society, 369, 1229

Evans, P. A., Hellier, C., Ramsay, G., & Cropper, M. 2004, Monthly Notices of the Royal Astronomical Society, 349, 715

Ferguson, D. H., Green, R. F., & Liebert, J. 1984, The Astrophysical Journal, 287, 320

Ferrario, L., & Wickramasinghe, D. T. 1999, Monthly Notices of the Royal Astronomical Society, 309, 517

Fink, M., Roepke, F. K., Hillebrandt, W., et al. 2010, Astronomy & Astrophysics, 514, A53

Fioretti, V., Bulgarelli, A., Malaguti, G., Spiga, D., & Tiengo, A. 2016, in Proceedings of the SPIE, Vol. 9905, Space Telescopes and Instrumentation 2016: Ultraviolet to Gamma Ray, 99056W

Flannery, B. P. 1975, Monthly Notices of the Royal Astronomical Society, 170, 325

Fox, A. J., & et al. 2015, COS Data Handbook v. 3.0

Frank, J., King, A., & Raine, D. J. 2002, Accretion Power in Astrophysics: Third Edition, 398

Fruscione, A., McDowell, J. C., Allen, G. E., et al. 2006, in Proceedings of SPIE,

Vol. 6270, Society of Photo-Optical Instrumentation Engineers (SPIE) Conference Series, 62701V

Gänsicke, B., Szkody, P., De Martino, D., et al. 2003, The Astrophysical Journal, 594, 443

Gänsicke, B. T. 2000, in Reviews in Modern Astronomy, Vol. 13, Reviews in Modern Astronomy, ed. R. E. Schielicke, 151

Garmire, G. P., Bautz, M. W., Ford, P. G., Nousek, J. A., & Ricker, Jr., G. R. 2003, in Proceedings of SPIE, Vol. 4851, X-Ray and Gamma-Ray Telescopes and Instruments for Astronomy., ed. J. E. Truemper & H. D. Tananbaum, 28–44

Garnavich, P., Littlefield, C., Terndrup, D., & Adams, S. 2014, The Astronomer's Telegram, 6287, 1

Garnavich, P. M., & Szkody, P. 1988, Publications of the Astronomical Society of the Pacific, 100, 1522

Gehrz, R. D., Truran, J. W., Williams, R. E., & Starrfield, S. 1998, Publications of the Astronomical Society of the Pacific, 110, 3

Ghosh, P., & Lamb, F. K. 1978, Astrophysical Journal, 223, L83

—. 1979, The Astrophysical Journal, 232, 259

Giacconi, R., Gursky, H., Kellogg, E., Schreier, E., & Tananbaum, H. 1971, The Astrophysical Journal, 167, L67

Green, J. C., Froning, C. S., Osterman, S., et al. 2012, The Astrophysical Journal, 744, 60

Grimm, H.-J., Gilfanov, M., & Sunyaev, R. 2002, Astronomy & Astrophysics, 391, 923

Grindlay, J., Gursky, H., Schnopper, H., et al. 1976, The Astrophysical Journal, 205, L127

Grindlay, J. E., McClintock, J. E., Canizares, C. R., et al. 1978, Nature, 274, 567

Groot, P. J. 2000, New Astronomy Reviews, 44, 137

Groot, P. J., Nelemans, G., Steeghs, D., & Marsh, T. R. 2001, The Astrophysical Journal, 558, L123

Güver, T., & Özel, F. 2009, Monthly Notices of the Royal Astronomical Society, 400, 2050

Hakala, P., Hjalmarsdotter, L., Hannikainen, D. C., & Muhli, P. 2009, Monthly Notices of the Royal Astronomical Society, 394, 892

Hakala, P. J., Chaytor, D. H., Vilhu, O., et al. 1998, Astronomy & Astrophysics, 333, 540

Hameury, J. M., King, A. R., & Lasota, J. P. 1986, Monthly Notices of the Royal Astronomical Society, 218, 695

Hamilton, R. T., Harrison, T. E., Tappert, C., & Howell, S. B. 2011, The Astrophysical Journal, 728, 16

Harding, L. K., Hallinan, G., Boyle, R. P., et al. 2011, in Astronomical Society of the Pacific Conference Series, Vol. 448, 16th Cambridge Workshop on Cool Stars, Stellar Systems, and the Sun, ed. C. Johns-Krull, M. K. Browning, & A. A. West, 219

Harrison, T. E., Osborne, H. L., & Howell, S. B. 2005, The Astronomical Journal, 129, 2400

Hellier, C. 1993, Monthly Notices of the Royal Astronomical Society, 265, L35

Hellier, C. 2014, in European Physical Journal Web of Conferences, Vol. 64, European Physical Journal Web of Conferences, 07001

Hellier, C., Cropper, M., & Mason, K. O. 1991, Monthly Notices of the Royal Astronomical Society, 248, 233

Hellier, C., Kemp, J., Naylor, T., et al. 2000, Monthly Notices of the Royal Astronomical Society, 313, 703

Hellier, C., Mason, K., & Cropper, M. 1989, Monthly Notices of the Royal Astronomical Society, 237, 39

Hellier, C., Mason, K. O., & Cropper, M. 1990, Monthly Notices of the Royal Astronomical Society, 242, 250

Hellier, C., Mason, K. O., Rosen, S. R., & Cordova, F. A. 1987, Monthly Notices of the Royal Astronomical Society, 228, 463

Hessman, F. V., Gänsicke, B. T., & Mattei, J. A. 2000, Astronomy & Astrophysics, 361, 952

Hewish, A., Bell, S. J., Pilkington, J. D. H., Scott, P. F., & Collins, R. A. 1968, Nature, 217, 709

Hill, C., Watson, C. A., Steeghs, D., Dhillon, V. S., & Shahbaz, T. 2016, Monthly Notices of the Royal Astronomical Society, 459, 1858

Hill, C. A., Watson, C. A., Shahbaz, T., Steeghs, D., & Dhillon, V. S. 2014, Monthly Notices of the Royal Astronomical Society, 444, 192

Hill, J. E., Zugger, M. E., Shoemaker, J., et al. 2000, in Proceedings of SPIE, Vol. 4140, X-Ray and Gamma-Ray Instrumentation for Astronomy XI, ed. K. A. Flanagan & O. H. Siegmund, 87–98

Hoard, D. W., Szkody, P., Froning, C. S., Long, K. S., & Knigge, C. 2003, The Astronomical Journal, 126, 2473

Hoard, D. W., Szkody, P., Froning, C. S., Long, K. S., & Knigge, C. 2003, The Astronomical Journal, 126, 2473

Höflich, P., & Khokhlov, A. 1996, The Astrophysical Journal, 457, 500

Homer, L., Charles, P. A., & O'Donoghue, D. 1998, Monthly Notices of the Royal Astronomical Society, 298, 497

Horne, K., & Marsh, T. 1986, Monthly Notices of the Royal Astronomical Society, 218, 761

Howell, S. B., Dobrzycka, D., Szkody, P., & Kreidl, T. J. 1991, Publications of the Astronomical Society of the Pacific, 103, 300

Howell, S. B., Sobeck, C., Haas, M., et al. 2014, Publications of the Astronomical Society of the Pacific, 126, 398

Hubeny, I. 1988, Computer Physics Communications, 52, 103

Hubeny, I., & Lanz, T. 1995, The Astrophysical Journal, 439, 875

Hulse, R. A., & Taylor, J. H. 1975, The Astrophysical Journal, 195, L51

Hussain, G. A. J. 2011, in Astronomical Society of the Pacific Conference Series, Vol. 447, Evolution of Compact Binaries, ed. L. Schmidtobreick, M. R. Schreiber, & C. Tappert, 143

Hynes, R. I., Robinson, E. L., & Jeffery, E. 2004, The Astrophysical Journal, 608, L101

Iben, Jr, I., & Tutukov, A. V. 1991, The Astrophysical Journal, 370, 615

Joss, P. C., Rappaport, S. A., & Katz, J. I. 1979, The Astrophysical Journal, 230, 176

Kalberla, P. M. W., Burton, W. B., Hartmann, D., et al. 2005, Astronomy & Astrophysics, 440, 775

Kato, T., Hambsch, F. J., Maehara, H., et al. 2013, Publications of the Astronomical Society of Japan, 65, 23

Kennedy, M. R., Garnavich, P., Breedt, E., et al. 2016, Monthly Notices of the Royal Astronomical Society, 459, 3622

Kennedy, M. R., Callanan, P., Garnavich, P. M., et al. 2016, The Astronomical Journal, 152, 27

Kepler, J. 1618, Epitome astronomiae copernicanae usitata forma quaestionum & responsionum conscripta, inque VII. libros digesta, doi:10.3931/e-rara-3122

King, A. R. 1988, Quarterly Journal of the Royal Astronomical Society, 29, 1

Knigge, C., Baraffe, I., & Patterson, J. 2011, The Astrophysical Journal Supplement Series, 194, 28

Koch, D. G., Borucki, W., Dunham, E., et al. 2004, in Proceedings of SPIE, Vol. 5487, Optical, Infrared, and Millimeter Space Telescopes, ed. J. C. Mather, 1491–1500

Kolb, U. 2002, in The Physics of Cataclysmic Variables and Related Objects, ed. B. Gaensicke, K. Beuermann, & K. Reinsch (ASP Conf. Series 261), 180

Kotze, E. J., Potter, S. B., & McBride, V. A. 2015, Astronomy & Astrophysics, 579, A77

Kruszewski, A., & Semeniuk, I. 1993, Acta Astronomica, 43, 127

—. 1998, Acta Astronomica, 48, 757

Kuulkers, E., Norton, A., Schwope, A., & Warner, B. 2006, in Compact stellar X-ray sources, ed. W. H. G. Lewin & M. van der Klis, 421–460

Lamb, F. K., Aly, J.-J., Cook, M. C., & Lamb, D. Q. 1983, The Astrophysical Journal, 274, L71

Landi, R., Bassani, L., Dean, a. J., et al. 2009, Monthly Notices of the Royal Astronomical Society, 392, 630

Lasota, J.-P. 2001, New Astronomy Reviews, 45, 449

Leach, R., Hessman, F. V., King, A. R., Stehle, R., & Mattei, J. 1999, Monthly Notices of the Royal Astronomical Society, 305, 225

Lin, D. N. C., & Papaloizou, J. 1979, Monthly Notices of the Royal Astronomical Society, 186, 799

Littlefair, S. P., Dhillon, V. S., Marsh, T. R., et al. 2008, Monthly Notices of the Royal Astronomical Society, 388, 1582

Littlefield, C., Aadland, E., Garnavich, P., & Kennedy, M. 2016a, The Astronomer's Telegram, 9216, 1

—. 2016b, The Astronomer's Telegram, 9225, 1

Littlefield, C., Garnavich, P., Applegate, a., et al. 2013, The Astronomical Journal, 145, 145

Littlefield, C., Garnavich, P., Kennedy, M. R., et al. 2016, The Astrophysical Journal, 833, 93

Livio, M., & Pringle, J. E. 1994, The Astrophysical Journal, 427, 956

Lomb, N. R. 1976, Astrophysics & Space Science, 39, 447

Long, K. S., Gaensicke, B. T., Knigge, C., Froning, C. S., & Monard, B. 2009, The Astrophysical Journal, 697, 1512

Lubow, S. H. 1989, The Astronomical Journal, 340, 1064

MacDonald, J. 1984, The Astrophysical Journal, 283, 241

Maoz, D., Mannucci, F., & Nelemans, G. 2014, Annual Review of Astronomy and Astrophysics, 52, 107

Marks, P. B., & Sarna, M. J. 1998, Monthly Notices of the Royal Astronomical Society, 301, 699

Marsh, T. R., & Duck, S. R. 1996, New Astronomy, 1, 97

Marsh, T. R., & Horne, K. 1988, Monthly Notices of the Royal Astronomical Society, 235, 269

Marsh, T. R., Horne, K., & Rosen, S. 1991, The Astrophysical Journal, 366, 535

Marshall, F. E., Boldt, E., Holt, S. S., et al. 1979, The Astrophysical Journal Supplement Series, 40, 657

Masetti, N., Nucita, A. A., & Parisi, P. 2012, Astronomy & Astrophysics, 544, A114

Mason, K. O. 1997, Monthly Notices of the Royal Astronomical Society, 285, 493

Mason, K. O., Breeveld, A., Much, R., et al. 2001, Astronomy & Astrophysics, 365, L36

Mason, P. A., & Gray, C. L. 2007, The Astrophysical Journal, 660, 662

Mason, P. A., Robinson, E. L., Bayless, A. J., & Hakala, P. J. 2012, The Astronomical Journal, 144, 108

Mason, P. A., Robinson, E. L., Gray, C. L., & Hynes, R. I. 2008, The Astrophysical Journal, 685, 428

Mauche, C. W., Lee, Y. P., & Kallman, T. R. 1997, The Astrophysical Journal, 477, 832

McClintock, J. E., & Remillard, R. A. 1986, The Astrophysical Journal, 308, 110

McConnell, O., Callanan, P. J., Kennedy, M., et al. 2015, Monthly Notices of the Royal Astronomical Society, 451, 3468

Mitsuda, K., Inoue, H., Koyama, K., et al. 1984, Publicatiosn of the Astronomical Society of Japan, 36, 741

Morris, S. L., Liebert, J., Stocke, J. T., et al. 1990, The Astrophysical Journal, 365, 686

Muhli, P., Hakala, P. J., Hjalmarsdotter, L., Hannikainen, D. C., & Schultz, J. 2004, in Revista Mexicana de Astronomia y Astrofisica Conference Series, Vol. 20, Revista Mexicana de Astronomia y Astrofisica Conference Series, ed. G. Tovmassian & E. Sion, 211–211

Mukai, K. 1988, Monthly Notices of the Royal Astronomical Society, 232, 175

—. 2015, Acta Polytechnica CTU Proceedings, 2, 246

Mukai, K., Smale, A. P., Stahle, C. K., Schlegel, E. M., & Wijnands, R. 2001, The Astrophysical Journal, 561, 938

Nasiroglu, I., Słowikowska, A., Kanbach, G., & Haberl, F. 2012, Monthly Notices of the Royal Astronomical Society, 420, 3350

Nather, R. E., Robinson, E. L., & Stover, R. J. 1981, The Astrophysical Journal, 244, 269

Nelemans, G., Portegies Zwart, S. F., Verbunt, F., & Yungelson, L. R. 2001, Astronomy and Astrophysics, 368, 939

Nelemans, G., Yungelson, L. R., Sluys, M. V. V. D., & Tout, C. a. 2010, Monthly Notices of the Royal Astronomical Society, 401, 1347

Nelson, L. A., Rappaport, S. A., & Joss, P. C. 1986, The Astrophysical Journal, 304, 231

Norton, A. J. 1993, Monthly Notices of the Royal Astronomical Society, 265, 316

Norton, A. J., Beardmore, A. P., & Taylor, P. 1996, Monthly Notices of the Royal Astronomical Society, 280, 937

Norton, A. J., & Watson, M. G. 1989, Monthly Notices of the Royal Astronomical Society, 237, 715

Norton, A. J., Watson, M. G., King, A. R., Lehto, H. J., & McHardy, I. M. 1992, Monthly Notices of the Royal Astronomical Society, 254, 705

Nucita, A. A., Carpano, S., & Guainazzi, M. 2007, Astronomy & Astrophysics, 474, L1

Nugent, P., Baron, E., Branchm, D., Fisher, A., & Hauschildt, P. H. 1997, The Astrophysical Journal, 485, 812

Orosz, J. a., & Hauschildt, P. H. 2000, Astronomy and Astrophysics, 364, 265

Osaki, Y. 1974, Publications of the Astronomical Society of Japan, 26, 429

—. 1989, Publications of the Astronomical Society of Japan, 41, 1005

Osaki, Y. 1996, Publications of the Astronomical Society of the Pacific, 108, 39

Osaki, Y., & Kato, T. 2014, Publications of the Astronomical Society of Japan, 66, 15

Osborne, J., & Mukai, K. 1989, Monthly Notices of the Royal Astronomical Society, 238, 1233

Paczyński, B. 1967, Acta Astronomica, 17, 287

Paczynski, B. 1981, Acta Astronomica, 31, 1

Paczynski, B., & Sienkiewicz, R. 1981, The Astrophysical Journal, 248, 27

Paczynski, B., & Sienkiewicz, R. 1983, The Astrophysical Journal, 268, 825

Parikh, A., José, J., Sala, G., & Iliadis, C. 2013, Progress in Particle and Nuclear Physics, 69, 225

Parker, T. L., Norton, A. J., & Mukai, K. 2005, Astronomy & Astrophysics, 439, 213

Patterson, J. 1994, Publications of the Astronomical Society of the Pacific, 106, 209

Patterson, J., & Richman, H. 1991, Publications of the Astronomical Society of the Pacific, 103, 735

Patterson, J., & Steiner, J. E. 1983, The Astrophysical Journal, 264, L61

Patterson, J., Kemp, J., Richman, H. R., et al. 1998, Publications of the Astronomical Society of the Pacific, 110, 415

Patterson, J., Fenton, W. H., Thorstensen, J. R., et al. 2002, Publications of the Astronomical Society of the Pacific, 114, 1364

Pecaut, M. J., & Mamajek, E. E. 2013, The Astrophysical Journal Supplement Series, 208, 9

Pekön, Y., & Balman, S. 2011, Monthly Notices of the Royal Astronomical Society, 411, 1177

Pekön, Y., & Balman, Ş. 2012, The Astronomical Journal, 144, 53

Pence, W. D., Chiappetti, L., Page, C. G., Shaw, R. A., & Stobie, E. 2010, Astronomy & Astrophysics, 524, A42

Penna, R. F., McKinney, J. C., Narayan, R., et al. 2010, Monthly Notices of the Royal Astronomical Society, 408, 752

Perlmutter, S., Aldering, G., Goldhaber, G., et al. 1999, The Astrophysical Journal, 517, 565

Podsiadlowski, P., Han, Z., & Rappaport, S. 2003, Monthly Notices of the Royal Astronomical Society, 340, 1214

Pogge, R. W., Atwood, B., Brewer, D. F., et al. 2010, in Society of Photo-Optical Instrumentation Engineers (SPIE) Conference Series, Vol. 7735, 77350A

Prialnik, D., & Kovetz, A. 1995, The Astrophysical Journal, 445, 789

Pringle, J. E. 1981, Annual Review of Astronomy and Astrophysics, 19, 137

Rappaport, S., Verbunt, F., & Joss, P. C. 1983, The Astrophysical Journal, 275, 713

Reis, R. C., Wheatley, P. J., Gänsicke, B. T., & Osborne, J. P. 2013, Monthly Notices of the Royal Astronomical Society, 430, 1994

Revnivtsev, M., Postnov, K., Kuranov, A., & Ritter, H. 2011, Astronomy & Astrophysics, 526, A94

Riess, A. G., Filippenko, A. V., Challis, P., et al. 1998, The Astronomical Journal, 116, 1009

Ritter, H., & Kolb, U. 2003, Astronomy and Astrophysics, 404, 301

Robinson, E. L., & Young, P. 1997, The Astrophysical Journal, 491, L89

Rodríguez-Gil, P., Casares, J., Martínez-Pais, I. G., Hakala, P., & Steeghs, D. 2001, The Astrophysical Journal, 548, L49

Rodríguez-Gil, P., Gansicke, B. T., Hagen, H.-J., et al. 2007, Monthly Notices of the Royal Astronomical Society, 377, 1747

Rodríguez-Gil, P., Shahbaz, T., Marsh, T. R., et al. 2015, Mon. Not. R. Astron. Soc, 452, 146

Rosen, S. R., Mason, K. O., & Cordova, F. A. 1988, Monthly Notices of the Royal Astronomical Society, 231, 549

Rosen, S. R., Mason, K. O., & Córdova, F. A. 1988, Monthly Notices of the Royal Astronomical Society, 231, 549

Rosen, S. R., Mason, K. O., Mukai, K., & Williams, O. R. 1991, Monthly Notices of the Royal Astronomical Society, 249, 417

Rowland, S. W. 1979, Computer implementation of image reconstruction formulas, ed. G. T. Herman, 9

Ruiz, M. T., Rojo, P. M., Garay, G., & Maza, J. 2001, The Astrophysical Journal, 552, 679

Rykoff, E., Akerlof, C., Ashley, M., et al. 2004, Information Bulletin on Variable Stars, 5559, 1

Sanad, M. R. 2011, New Astronomy, 16, 19

Sanchez-Blazquez, P., Peletier, R. F., Jimenez-Vicente, J., et al. 2006, Monthly Notices of the Royal Astronomical Society, 371, 703

Savonije, G. J., de Kool, M., & Van Den Heuvel, E. P. J. 1986, Astronomy and Astrophysics, 155, 51

Scalzo, R. a., Ruiter, A. J., & Sim, S. A. 2014, Monthly Notices of the Royal Astronomical Society, 445, 2535

Scargle, J. 1982, The Astrophysical Journal, 263, 835

Scaringi, S., Kording, E., Uttley, P., et al. 2012, Monthly Notices of the Royal Astronomical Society, 421, 2854

Scaringi, S., Bird, A. J., Norton, A. J., et al. 2010, Mon. Not. R. Astron. Soc, 401, 2207

Scaringi, S., Maccarone, T. J., Kording, E., et al. 2015, Science Advances, 1, e1500686

Schaefer, B. E. 2010, The Astrophysical Journal Supplement Series, 187, 275

Schatzman, E. 1962, Annales d'Astrophysique, 25, 18

Schenker, K., King, A., Kolb, U., Wynn, G. A., & Zhang, Z. 2002, Monthly Notices of the Royal Astronomical Society, 337, 1105

Schlafly, E. F., & Finkbeiner, D. P. 2011, The Astrophysical Journal, 737, 103

Schlegel, E. M. 2005, Astronomy & Astrophysics, 433, 635

Schoembs, R., & Zoeschinger, G. 1990, Astronomy & Astrophysics, 227, 105

Shafter, A. W. 1983, The Astrophysical Journal, 267, 222

Shafter, A. W., & Macry, J. D. 1987, Monthly Notices of the Royal Astronomical Society, 228, 193

Shafter, A. W., & Targan, D. M. 1982, The Astronomical Journal, 87, 655

Shen, K. J., & Bildsten, L. 2009, The Astrophysical Journal, 699, 1365

Shen, K. J., & Moore, K. 2014, The Astrophysical Journal, 797, 46

Shklovsky, I. S. 1967, The Astrophysical Journal, 148, L1

Sion, E. M. 1999, Publicatiosn of the Astronomical Society of the Pacific, 111, 532

Sion, E. M., & Sparks, W. 2014, The Astrophysical Journal, 796, L10

Solheim, J.-E. 2010, Publications of the Astronomical Society of the Pacific, 122, 1133

Spruit, H. C. 1998, Arxiv:astro-ph/9806141, 1

Spruit, H. C., & Ritter, H. 1983, Astronomy & Astrophysics, 124, 267

Starrfield, S. 1989, in Classical Novae, ed. M. F. Bode & A. Evans, 39–60

Starrfield, S., Iliadis, C., & Hix, W. R. 2016, Publications of the Astronomical Society of the Pacific, 128, 051001

Starrfield, S., Sparks, W. M., Truran, J. W., & Wiescher, M. C. 2000, The Astrophysical Journal Supplement Series, 127, 485

Staude, A., Schwope, A. D., Schwarz, R., et al. 2008, Astronomy & Astrophysics, 486, 899

Steiman-Cameron, T. Y., Imamura, J. N., & Steiman-Cameron, D. V. 1989, The Astronomical Journal, 339, 434

Steiner, J., & Diaz, M. 1998, Publications of the Astronomical Society of the Pacific, 110, 276

Stellingwerf, R. 1978, The Astrophysical Journal, 224, 953

Still, M., & Barclay, T. 2012, PyKE: Reduction and analysis of Kepler Simple Aperture Photometry data, Astrophysics Source Code Library, , , ascl:1208.004

Stockman, H. S., Schmidt, G. D., & Lamb, D. Q. 1988, The Astrophysical Journal, 332, 282

Strohmayer, T., & Bildsten, L. 2003, ArXiv Astrophysics e-prints, astro-ph/0301544

Strope, R. J., Schaefer, B. E., & Henden, A. A. 2010, The Astronomical Journal, 140, 34

Strüder, L., Briel, U., Dennerl, K., et al. 2001, Astronomy & Astrophysics, 365, L18

Suleimanov, V., Doroshenko, V., Ducci, L., Zhukov, G. V., & Werner, K. 2016, Astronomy & Astrophysics, 591, A35

Suleimanov, V., Revnivtsev, M., & Ritter, H. 2005, Astronomy & Astrophysics, 435, 191

Suveges, M. 2012, in Seventh Conference on Astronomical Data Analysis, ed. J.-L. Starck & C. Surace, 16

Taam, R. E. 1980, The Astrophysical Journal, 237, 142

Tapia, S. 1977, The Astrophysical Journal, 212, L125

Thorstensen, J. R., Fenton, W. H., Patterson, J. O., et al. 2002, The Astrophysical Journal, 567, L49

Thorstensen, J. R., Fenton, W. H., & Taylor, C. J. 2004, Publications of the Astronomical Society of the Pacific, 116, 300

Thorstensen, J. R., Ringwald, F. A., Wade, R. A., Schmidt, G. D., & Norsworthy, J. E. 1991, The Astronomical Journal, 102, 272

Turner, M. J. L., Abbey, A., Arnaud, M., et al. 2001, Astronomy & Astrophysics, 365, L27

Tutukov, A. V., Fedorova, A. V., Ergma, E. V., & Yungelson, L. R. 1985, Pisma v Astronomicheskii Zhurnal, 11, 123

Tutukov, A. V., & Yungelson, L. 1979, Acta Astronomica, 29, 665

Van de Sande, M., Scaringi, S., & Knigge, C. 2015, Monthly Notices of the Royal Astronomical Society, 448, 2430

Vanderplas, J., Connolly, A., Ivezić, Ž., & Gray, A. 2012, in Conference on Intelligent Data Understanding (CIDU), 47 –54

VanderPlas, J. T. 2017, ArXiv e-prints, arXiv:1703.09824

Vogt, N., Krzeminski, W., & Sterken, C. 1980, Astronomy & Astrophysics, 85, 106

Walker, M. F. 1956, The Astrophysical Journal, 123, 68

Warner, B. 1995, in Cataclysmic Variable Stars, ed. A. King, D. Lin, S. Maran, J. Pringle, & M. Ward (Cambridge: Cambridge University Press)

Warner, B. 1996, Astrophysics and Space Science, 241, 263

Warner, B. 2004, Publications of the Astronomical Society of the Pacific, 116, 115

Watson, C. A., Dhillon, V. S., & Shahbaz, T. 2006, Monthly Notices of the Royal Astronomical Society, 368, 637

Watson, C. A., Steeghs, D., Shahbaz, T., & Dhillon, V. S. 2007, Monthly Notices of the Royal Astronomical Society, 382, 1105

Webbink, R. F. 1976, The Astrophysical Journal, 209, 829

Whelan, J., & Iben, I. J. 1973, The Astrophysical Journal, 186, 1007

Wijnands, R., & van der Klis, M. 1998, Nature, 394, 344

Williams, G. 2003, Publications of the Astronomical Society of the Pacific, 115, 618

Williams, R. E., & Ferguson, D. H. 1982, The Astrophysical Journal, 257, 672

Winkler, P. F., Gupta, G., & Long, K. S. 2003, he Astrophysical Journal, 585, 324

Wynn, G. A., & King, A. R. 1992, Monthly Notices of the Royal Astronomical Society, 255, 83

Xu, X.-j., Wang, Q. D., & Li, X.-D. 2016, The Astrophysical Journal, 818, 136

Zemko, P., Orio, M., Mukai, K., et al. 2016, Monthly Notices of the Royal Astronomical Society, 460, 2744

Zorotovic, M., Schreiber, M. R., & Gänsicke, B. T. 2011, Astronomy & Astrophysics, 536, A42